

---

---

# CMB-S4 Technology Book

## First Edition

---

---

CMB-S4 Collaboration

April 28, 2022

---

---

# Contents

<b>1</b>	<b>Introduction and overview</b>	<b>1</b>
1.1	Introduction to the CMB-S4 Technology Book . . . . .	1
1.2	Overview and Status of CMB-S4 Technology Areas . . . . .	2
<b>2</b>	<b>Telescope design</b>	<b>9</b>
2.1	Introduction . . . . .	9
2.2	Current CMB telescope designs and maturity . . . . .	10
2.2.1	Current small-aperture telescope designs . . . . .	10
2.2.2	Current large-aperture telescope designs . . . . .	12
2.3	Concept for high throughput large-aperture telescope design . . . . .	12
2.4	Telescope engineering to control systematic errors . . . . .	14
2.4.1	Monolithic mirrors . . . . .	14
2.4.2	Boresight rotation . . . . .	15
2.4.3	Shields and baffles . . . . .	15
2.5	Potential future studies and development areas . . . . .	16
2.6	Optics designs for current projects . . . . .	19
2.6.1	Advanced ACTPol . . . . .	19
2.6.2	BICEP3 . . . . .	19
2.6.3	CLASS . . . . .	21
2.6.4	EBEX . . . . .	21
2.6.5	Keck Array/SPIDER . . . . .	22
2.6.6	PIPER . . . . .	23
2.6.7	POLARBEAR-2/Simons Array . . . . .	24
2.6.8	SPT-3G . . . . .	25
2.6.9	ABS . . . . .	25
2.6.10	QUIET . . . . .	26

2.6.11	CCAT-prime	28
2.7	Conclusion	28
<b>3</b>	<b>Receiver optics</b>	<b>31</b>
3.1	Introduction	31
3.2	Windows	33
3.2.1	Polyethylene windows	33
3.2.2	Zotefoam windows	35
3.3	Filters	37
3.3.1	Metal mesh filters	37
3.3.2	Laser-ablated infrared blocking filters	38
3.3.3	Nylon and Teflon filters	40
3.3.4	Alumina IR filters	41
3.3.5	Silicon substrate filters	42
3.3.6	Foam based infrared blocking filters	44
3.4	Lens material	47
3.4.1	Silicon	47
3.4.2	Alumina	48
3.4.3	Polyethylene lenses	49
3.4.4	Metal mesh lenses	50
3.5	Anti-reflection coatings	52
3.5.1	Plastic sheet coatings	52
3.5.2	Thermal spray coatings	54
3.5.3	Epoxy coatings	55
3.5.4	Diced silicon	56
3.5.5	Deep reactive ion etched silicon	57
3.5.6	Laser ablated surface	59
3.5.7	Machined plastic	60
3.5.8	Metal mesh	61
3.6	Polarization modulators	63

3.6.1	Achromatic half-wave plates . . . . .	64
3.6.2	Sapphire . . . . .	65
3.6.3	Diced silicon broadband half-wave plates . . . . .	66
3.6.4	Metal mesh polarization modulators . . . . .	68
3.6.5	Rotation mechanisms . . . . .	70
3.6.6	Variable-delay polarization modulators . . . . .	73
3.7	Characterization . . . . .	76
3.7.1	Mechanical properties . . . . .	76
3.7.2	Thermal properties . . . . .	77
3.7.3	Optical properties . . . . .	78
3.8	Conclusion . . . . .	83
3.9	Summary of optics technologies . . . . .	84
<b>4</b>	<b>Focal plane optical coupling</b>	<b>87</b>
4.1	Introduction . . . . .	87
4.2	Background . . . . .	88
4.2.1	Foreground considerations for frequency band selection . . . . .	88
4.2.2	Total bandwidth and spectral resolution . . . . .	89
4.3	Antennas . . . . .	91
4.3.1	Feedhorn coupling . . . . .	91
4.3.2	Lenslet coupled antennas . . . . .	96
4.3.3	Antenna array coupling . . . . .	101
4.3.4	Direct coupling to single and multimoded resistive absorber bolometers . . . . .	104
4.4	RF components . . . . .	106
4.4.1	Superconducting RF transmission line . . . . .	106
4.4.2	On-chip microwave filters . . . . .	107
4.4.3	Microwave cross-over . . . . .	111
4.4.4	Microstrip termination . . . . .	113
4.5	Array layout, pixel size, and wiring considerations . . . . .	116
4.6	Detector characterization . . . . .	119

4.7	Conclusion . . . . .	123
4.8	Summary of detector-RF technologies . . . . .	124
<b>5</b>	<b>Focal plane sensors and readout</b>	<b>127</b>
5.1	Introduction . . . . .	127
5.2	Transition edge sensor (TES) bolometers . . . . .	127
5.3	Microwave Kinetic Inductance Detectors . . . . .	130
5.4	Time-division multiplexing (TDM) using DC SQUIDs . . . . .	132
5.5	Frequency-division multiplexing using MHz LC resonators (DfMux) . . . . .	136
5.6	Frequency-division multiplexing using SQUID-coupled GHz resonators ( $\mu$ MUX) . . . . .	140
5.7	Room-temperature electronics for frequency-division-multiplexed readout . . . . .	143
5.8	Conclusion . . . . .	147
5.9	Summary of sensor and readout technologies . . . . .	147
<b>6</b>	<b>Conclusion and Future Work</b>	<b>149</b>

## List of Contributors and Endorsers

The following people have endorsed survey of instrumentation for the CMB as presented here. Those contributed to the writing of this document are marked with asterisk:

Kevork N. Abazajian<sup>37</sup>, Maximilian H. Abitbol<sup>\*8</sup>, Zeeshan Ahmed<sup>\*29</sup>, David Alonso<sup>48</sup>, Adam J. Anderson<sup>12</sup>, Kam Arnold<sup>38</sup>, Jason E. Austermann<sup>25</sup>, Darcy Barron<sup>\*35</sup>, Ritoban Basu Thakur<sup>\*39</sup>, Andrew Bazarko<sup>26</sup>, Amy N. Bender<sup>\*1</sup>, Bradford A. Benson<sup>\*12</sup>, Colin A. Bischoff<sup>\*40</sup>, Richard J. Bond<sup>53</sup>, Julian D. Borrill<sup>21</sup>, Francois R. Bouchet<sup>15</sup>, Michael L. Brown<sup>43</sup>, Sean A. Bryan<sup>\*2</sup>, Karen Byrum<sup>1</sup>, Giovanni Cabass<sup>28</sup>, Erminia Calabrese<sup>6</sup>, Robert Caldwell<sup>10</sup>, John E. Carlstrom<sup>\*39</sup>, Faustin W. Carter<sup>1</sup>, Thomas W. Cecil<sup>1</sup>, Clarence L. Chang<sup>\*1</sup>, Xingang Chen<sup>14</sup>, David T. Chuss<sup>\*55</sup>, Nicholas F. Cothard<sup>9</sup>, Abby Crites<sup>5</sup>, Ari Cukierman<sup>\*35</sup>, Francis-Yan Cyr-Racine<sup>14</sup>, Paolo de Bernardis<sup>28</sup>, Tijmen de Haan<sup>\*35</sup>, Marcel Demarteau<sup>1</sup>, Mark J. Devlin<sup>49</sup>, Sperello di Serego Alighieri<sup>17</sup>, Eleonora Di Valentino<sup>15</sup>, Clive Dickinson<sup>43</sup>, Matt Dobbs<sup>\*21</sup>, Jo Dunkley<sup>26</sup>, Cora Dvorkin<sup>14</sup>, Tom Essinger-Hileman<sup>\*22</sup>, Giulio Fabbian<sup>16</sup>, Farzad Faramarzi<sup>27</sup>, Jeffrey P. Filippini<sup>\*42</sup>, Raphael Flauger<sup>38</sup>, Brenna Flaugher<sup>12</sup>, Aurelien A. Fraisse<sup>26</sup>, Patricio A. Gallardo<sup>9</sup>, Ken Ganga<sup>\*3</sup>, Martina Gerbino<sup>31</sup>, Daniel Green<sup>35</sup>, Riccardo Gualtieri<sup>42</sup>, Jon E. Gudmundsson<sup>\*31</sup>, Salman Habib<sup>1</sup>, Nils W. Halverson<sup>\*41</sup>, Shaul Hanany<sup>\*46</sup>, Shawn W. Henderson<sup>\*9</sup>, Sophie Henrot-Versille<sup>19</sup>, Charles A. Hill<sup>\*35</sup>, J. Colin Hill<sup>8</sup>, Eric Hivon<sup>15</sup>, Shuay-Pwu P. Ho<sup>\*26</sup>, William L. Holzapfel<sup>35</sup>, Johannes Hubmayr<sup>\*25</sup>, Kevin M. Huffenberger<sup>13</sup>, Kent Irwin<sup>\*29</sup>, Oliver Jeong<sup>\*35</sup>, Bradley R. Johnson<sup>\*8</sup>, William C. Jones<sup>26</sup>, Brian G. Keating<sup>38</sup>, Sarah A. Kernasovskiy<sup>\*30</sup>, Lloyd E. Knox<sup>36</sup>, Brian J. Koopman<sup>9</sup>, Arthur Kosowsky<sup>50</sup>, John M. Kovac<sup>\*14</sup>, Ely D. Kovetz<sup>18</sup>, Steve Kuhlmann<sup>1</sup>, Chao-Lin Kuo<sup>30</sup>, Akito Kusaka<sup>\*20</sup>, Nicole A. Larsen<sup>39</sup>, Charles R. Lawrence<sup>23</sup>, Adrian T. Lee<sup>\*35</sup>, Marilena Loverde<sup>32</sup>, Amy E. Lowitz<sup>39</sup>, Mathew S. Madhavacheril<sup>26</sup>, Salatino Maria<sup>\*26</sup>, Silvia Masi<sup>28</sup>, Philip Mauskopf<sup>\*2</sup>, Jeff J. McMahon<sup>\*45</sup>, Alessandro Melchiorri<sup>28</sup>, Joel Meyers<sup>53</sup>, Amber Miller<sup>51</sup>, Lorenzo Moncelsi<sup>\*5</sup>, Andrew W. Nadolski<sup>\*42</sup>, Johanna M. Nagy<sup>\*7</sup>, Pavel J. Naselsky<sup>24</sup>, Tyler J. Natoli<sup>11</sup>, Michael D. Niemack<sup>\*9</sup>, Roger C. O'Brient<sup>\*23</sup>, Stephen Padin<sup>\*39</sup>, Stephen C. Parshley<sup>\*9</sup>, Guillaume Patanchon<sup>3</sup>, Julien Peloton<sup>52</sup>, Francesco Piacentini<sup>28</sup>, Michel Piat<sup>3</sup>, Damien Prele<sup>3</sup>, Clement Pryke<sup>\*46</sup>, Benjamin Racine<sup>47</sup>, Alexandra S. Rahlin<sup>12</sup>, Christian L. Reichardt<sup>44</sup>, Mathieu Remazeilles<sup>43</sup>, Natalie A. Roe<sup>\*20</sup>, Karwan Rostem<sup>\*22</sup>, John Ruhl<sup>\*7</sup>, Douglas Scott<sup>34</sup>, Erik Shirokoff<sup>39</sup>, Sara M. Simon<sup>\*45</sup>, David N. Spergel<sup>26</sup>, Suzanne T. Staggs<sup>\*26</sup>, George Stein<sup>53</sup>, Radek Stompor<sup>3</sup>, Aritoki Suzuki<sup>\*35</sup>, Eric R. Switzer<sup>\*22</sup>, Grant P. Teply<sup>38</sup>, Keith L. Thompson<sup>\*30</sup>, Peter Timbie<sup>\*54</sup>, Matthieu Tristram<sup>19</sup>, Gregory S. Tucker<sup>\*4</sup>, Sunny Vagnozzi<sup>31</sup>, Alexander van Engelen<sup>53</sup>, Eve M. Vavagiakis<sup>9</sup>, Joaquin D. Vieira<sup>\*42</sup>, Abigail G. Vieregg<sup>\*39</sup>, Benjamin D. Wandelt<sup>15</sup>, Gensheng Wang<sup>1</sup>, Scott Watson<sup>33</sup>, Benjamin Westbrook<sup>\*35</sup>, Nathan Whitehorn<sup>35</sup>, Edward J. Wollack<sup>\*22</sup>, W. L. K. Wu<sup>35</sup>, Zhilei Xu<sup>18</sup>, Ki Won Yoon<sup>\*29</sup>, Karl S. Young<sup>\*46</sup>, Edward Y. Young<sup>\*26</sup>

<sup>1</sup> Argonne National Laboratory  
<sup>2</sup> Arizona State University  
<sup>3</sup> APC Universit Paris Diderot  
<sup>4</sup> Brown University  
<sup>5</sup> California Institute of Technology  
<sup>6</sup> Cardiff University  
<sup>7</sup> Case Western Reserve University  
<sup>8</sup> Columbia University  
<sup>9</sup> Cornell University  
<sup>10</sup> Dartmouth College  
<sup>11</sup> Dunlap Institute  
<sup>12</sup> Fermi National Accelerator Laboratory  
<sup>13</sup> Florida State University  
<sup>14</sup> Harvard University  
<sup>15</sup> Institut d'Astrophysique de Paris  
<sup>16</sup> Institut d'Astrophysique Spatiale  
<sup>17</sup> Istituto Nazionale di Astrofisica  
<sup>18</sup> Johns Hopkins University  
<sup>19</sup> Laboratoire de l'Acclrateur Linaire  
<sup>20</sup> Lawrence Berkeley National Laboratory  
<sup>21</sup> McGill University  
<sup>22</sup> NASA Goddard Space Flight Center  
<sup>23</sup> NASA Jet Propulsion Laboratory  
<sup>24</sup> Niels Bohr Institute  
<sup>25</sup> NIST  
<sup>26</sup> Princeton University  
<sup>27</sup> San Francisco State University  
<sup>28</sup> Sapienza Universit di Roma  
<sup>29</sup> SLAC National Accelerator Laboratory  
<sup>30</sup> Stanford University  
<sup>31</sup> Stockholm University  
<sup>32</sup> Stony Brook University  
<sup>33</sup> Syracuse University  
<sup>34</sup> University of British Columbia  
<sup>35</sup> University of California, Berkeley  
<sup>36</sup> University of California, Davis  
<sup>37</sup> University of California, Irvine  
<sup>38</sup> University of California, San Diego  
<sup>39</sup> University of Chicago  
<sup>40</sup> University of Cincinnati  
<sup>41</sup> University of Colorado Boulder  
<sup>42</sup> University of Illinois at Urbana-Champaign  
<sup>43</sup> University of Manchester  
<sup>44</sup> University of Melbourne  
<sup>45</sup> University of Michigan, Ann Arbor  
<sup>46</sup> University of Minnesota  
<sup>47</sup> University of Oslo  
<sup>48</sup> University of Oxford  
<sup>49</sup> University of Pennsylvania  
<sup>50</sup> University of Pittsburgh  
<sup>51</sup> University of Sothern California  
<sup>52</sup> University of Sussex  
<sup>53</sup> University of Toronto  
<sup>54</sup> University of Wisconsin , Madison  
<sup>55</sup> Villanova University

# 1

---

## Introduction and overview

### 1.1 Introduction to the CMB-S4 Technology Book

CMB-S4 is a proposed experiment to map the polarization of the Cosmic Microwave Background (CMB) to nearly the cosmic variance limit for the angular scales that are accessible from the ground. The science goals and capabilities of CMB-S4 in illuminating cosmic inflation, measuring the sum of neutrino masses, searching for relativistic relics in the early universe, characterizing dark energy and dark matter, and mapping the matter distribution in the universe have been described in the CMB-S4 Science Book [1]. For CMB-S4 to be able to achieve the ambitious goals laid out in the Science Book will require a major step forward in experimental capability from the ongoing Stage-III experiments that are now starting. This CMB-S4 Technology Book is a companion volume to the Science Book and describes the status of the technology for CMB-S4.

There is range of existing technologies that are promising for meeting the challenging requirements set by CMB-S4; the optimum set of technologies has not yet been determined. While the focus of this document is on individual technologies, it is exciting to contemplate collaboration across groups, the potential for hybrid approaches that could lead to new breakthroughs, all leading towards developing the best approach to achieve the exciting science goals of CMB-S4. The diversity of approaches under development highlights the vitality of the experimental CMB community.

To guide in the compilation of the Technology Book, the community therefore agreed upon the following charge for this document:

*Summarize the current state of the technology and identify R&D efforts necessary to advance it for possible use in CMB-S4. CMB-S4 will likely require a scale-up in number of elements, frequency coverage, and bandwidth relative to current instruments. Because it is searching for lower magnitude signals, it will also require stronger control of systematic uncertainties.*

Proceeding from the sky, through the instrument, all the way to the detector data being stored to disk, we have grouped the relevant technologies into the following areas: Telescope Design; Receiver Optics; Focal-Plane Optical Coupling; and Focal-Plane Sensors and Readout. A chapter of the book is dedicated to each of these four areas. The technology choices for CMB-S4 will be inter-dependent, however. For example, the telescope will need to be designed together with the receiver optics, which in turn will need to be designed jointly with the detector arrays.

To aid in the understanding of the maturity of the technologies considered, we evaluated their current *technical readiness* with a 5-level Technology Status Level (TSL) and their *manufacturing readiness* with a 5-level Production Status Level (PSL). The criteria for these levels are described in Table 1-1. We also evaluate the effort needed to mature the technology if it is to be a viable candidate for CMB-S4.

<b>TSL Description</b>	
1	Lab test of technology to show principle
2	Lab test of technology but with full feature set and performance suitable for ground test
3	Experiment capable version built and tested in the lab
4	Deployed in a CMB experiment and data taken
5	Data fully analyzed, systematic errors understood

<b>PSL Description</b>	
1	Fabrication of a TS1/TS2 prototype demonstrated
2	Fabrication of a one or more experimental capable units
3	Conceptual plan of methods for production at scale
4	Demonstrated the critical steps for production at scale
5	Capability for production at scale exists and is demonstrated

Table 1-1: Technology Status Level (TSL) and Production Status Level (PSL) definitions.

To understand the timing of the technology development within the overall CMB-S4 schedule, a roadmap of the Critical Decision (CD) development path for the project is shown in Figure 1. Overall system design will drive all technology selections. For example, systematic error considerations can drive telescope and optics geometry which in turn impacts decisions on detector design. The strong connections between the many sub-systems in the experiment will require an iterative optimization.

In the next section we give brief overviews of the requirements for CMB-S4 and status of the technologies. The subsequent chapters of this book provide detailed descriptions of these technologies, their status (including TSLs and PSLs), and the next development steps, as follows: Chapter 2 covers Telescope Design; Chapter 3 covers Receiver Optics; Chapter 4 covers Focal Plane Optical Coupling; and Chapter 5 covers Focal Plane Sensors and Readout. Lastly, brief concluding remarks are given in Chapter 6.

## 1.2 Overview and Status of CMB-S4 Technology Areas

### Telescope Design

To achieve the ambitious science goals as set out in the Science Book, CMB-S4 will require of order  $\sim$ 500,000 effectively background-limited detectors. Since this exceeds the number of detectors that could fit in any current single telescope design, CMB-S4 will be an array of multiple telescopes. Chapter 2 reviews current telescope designs and presents promising future designs that would help meet the throughput challenges presented by CMB-S4.

At least a subset of the telescopes for CMB-S4 must have an optical beam size in the range of 1–4 arcminutes to meet many of the science requirements including those that exploit gravitational lensing, measurements of the damping tail, and galaxy cluster measurements. These large-aperture telescopes will have primary apertures in the 2–10 meter diameter range. To date, the most sensitive constraints on the degree scale inflationary recombination peak have been obtained with purpose built small-aperture telescopes in the

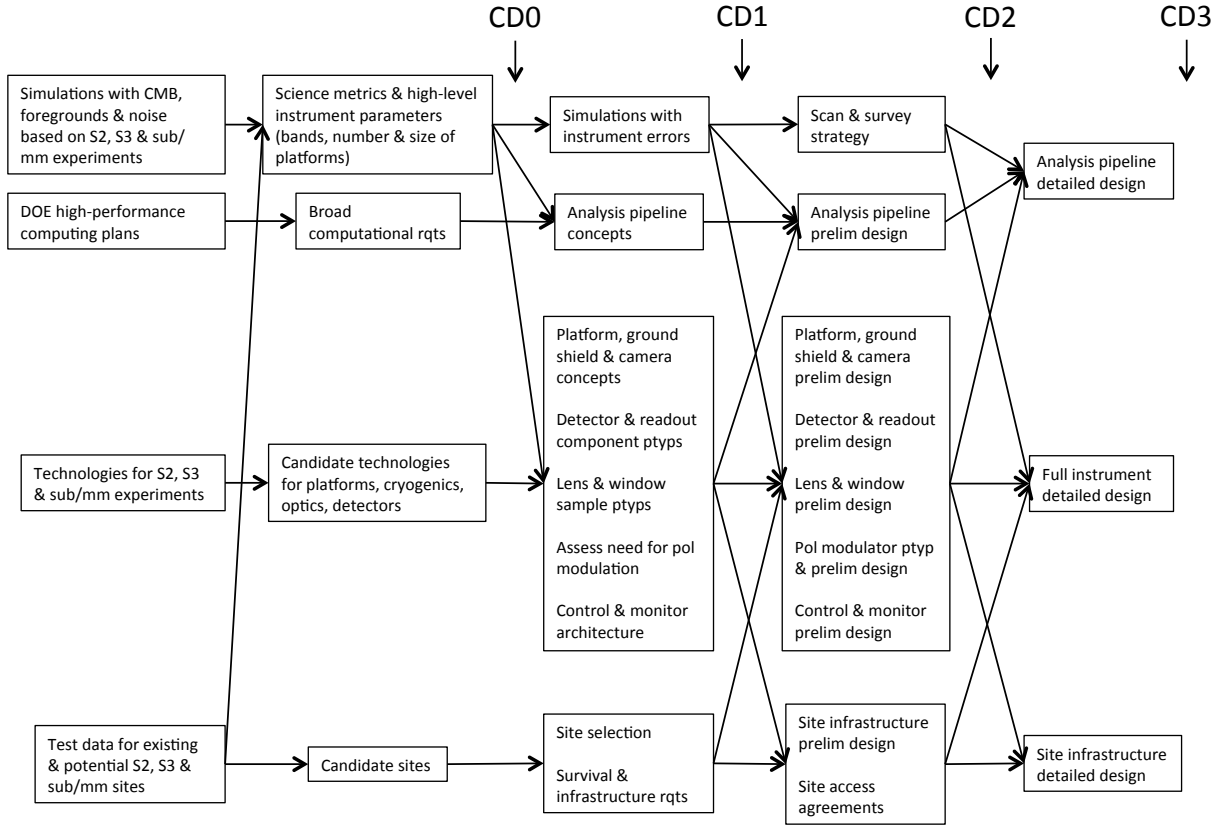


Figure 1: CMB-S4 Roadmap. Here S2 and S3 stand for Stage-II and Stage-III, respectively.

0.3–0.5 meter diameter range. Although large-aperture telescopes are, in principle, capable of high-fidelity measurements at these large scales, a conservative design of CMB-S4 would include both small and large telescopes. The large and small telescopes have different and complementary sets of systematic errors, and including both types will likely lead to the most robust results on inflation. Finally, the optics of both telescopes must be designed to minimize beam systematic uncertainties, sidelobes, and spurious instrumental polarization.

- **Small-aperture telescopes:** The small-aperture telescopes for CMB-S4 can be built with entirely cryogenic optics, reducing detector noise due to optical loading from the telescope, and suppressing the coupling of stray light onto the detectors. The optical design can be refractor-based as with BICEP/SPIDER/Keck Array or reflector-based as with ABS. BICEP3 and the BICEP Array are moving forward with high-throughput fully cryogenic optics. CLASS has a mix of cold refractive optics and ambient-temperature reflective optics. Performance from these designs will inform the design of CMB-S4.
- **Large-aperture telescopes:** Existing designs of fielded large-aperture telescopes are reviewed, as well as two attractive new large-aperture optical designs. One is a crossed Dragone design, which provides excellent image quality across a wide field of view. The final configuration will require a

detailed comparison of realistic estimates of systematic errors as well as consideration of mapping speed vs. cost.

- **Control of telescope systematic uncertainties:** Beam sidelobes that pick up spurious signals (such as those from the ground, sun and moon), beam asymmetries, and instrumental polarization can all be induced by the telescope if it is not carefully designed. Several small-aperture telescopes have demonstrated stringent control of sidelobes using a co-moving cylindrical absorptive shield. Existing large-aperture telescopes do not have the same comprehensive shielding as existing small-aperture telescopes, but it is plausible that such stringent shielding could be achieved provided that the requirement is built in at the beginning of the design process. CMB-S4 designs must also limit far-field scattering from optical surfaces including reflector-panel gaps and optical stops. To design the telescope to avoid these effects, ray tracing, as well as full beam diffraction effects can be simulated with commercial software. To further mitigate systematic uncertainties, there are also optimal mapmaker and other data analysis techniques. It will also be critical to verify with simulation and measurements that ground shields intended to limit sidelobes are not in fact adding new sidelobes themselves. Before finalizing the optical design of CMB-S4, end-to-end simulations of the telescope performance, through to simulated science data, would enable us to evaluate the impact of telescope design choices on the CMB science results.

## Receiver Optics

Advances in optical technologies have been crucial in moving the community towards realizing the full science potential of the CMB. Chapter 3 discusses the optical elements contained in CMB receivers which include lenses, filters, polarization modulators, and vacuum windows. The implementation and performance of these technologies are rapidly evolving and many new approaches are being successfully fielded on Stage-III experiments. These innovations draw on advances in materials, processing techniques, and developments in electrical engineering including metamaterial research. Examples of all of these components with relatively large diameters and broad operating bandwidths have been already successfully deployed to the field, but continued improvements on both diameter and bandwidth would be useful for CMB-S4. In Chapter 3 we summarize the current state-of-the-art and identifies development efforts that would be needed to ready each technology for CMB-S4.

- **Windows:** Vacuum windows have been built with closed-cell form sheets (Zotefoam) and from AR-coated polyethylene sheets. Work is needed to realize larger windows for the high-throughput CMB-S4 receiver designs that maintain low loss, scattering, and reflectivity.
- **Filters:** Most experiments currently use hot-pressed metal-mesh filters to help define the spectral band and to block out-of-band radiation coupling onto the detectors. Mesh filters are also used, along with infrared (IR) absorptive filters of polytetrafluoroethylene (PTFE), Nylon, and alumina ceramic, to reduce thermal loading from incident IR radiation onto the cryogenic stages. Emerging technologies for reducing the IR thermal loading include layers of laser-ablated free-standing metal mesh filters, IR-absorbing foam, and a composite of absorbing crystals and mesh filters on silicon. Further work is needed to realize large-diameter filtering schemes while minimizing in-band loss, scattering, and spurious polarization effects.
- **Anti-Reflection Coatings:** In the last five years, new approaches to multilayer coatings have emerged including: dielectric metamaterials cut by dicing saws, lasers, or etching; dielectric coatings made by casting, pressing, and thermal spray methods; and artificial dielectrics. Work is needed to realize

appropriately wide-bandwidth and large-diameter optical elements with low loss and at a practical cost for CMB-S4.

- **Polarization Modulators:** Polarization modulators are an important tool for realizing precision measurements of polarization as they mitigate systematic errors and  $1/f$  noise. Emerging approaches include anti-reflection coated half-wave plates (HWPs) fabricated from sapphire; metamaterial grooved silicon; or metamaterials realized as metal meshes; and variable polarization modulators realized by wire grids. Work is needed to realize broad-bandwidth, large-diameter, high-uniformity, and practically manufacturable modulators for CMB-S4.
- **Materials:** Low-loss dielectric materials are common to lenses, half-wave plates, IR filters, and windows. Work is needed to develop both high index of refraction alumina and silicon and relatively low index of refraction polyethylene in the large diameters required for CMB-S4.
- **Characterization:** Current approaches to optical characterization include transmission and reflection measurements using either coherent or broad-band sources of warm and cold optical elements and direct metrology. Precise characterization of the quality of the materials and performance of completed optical elements at their operating temperature is crucial to achieving the goals of CMB-S4.

## Focal-plane Optical Coupling

After the light from the sky passes through the telescope and is brought to a focus by the receiver optics, it must be coupled to the detectors. Chapter 4 discusses focal-plane coupling elements used in CMB arrays. The detector sensors themselves will be discussed in the next section. Rather than coupling the CMB signals to the sensors with simple absorbers in the traditional bolometric method, most CMB arrays use antennas. An antenna-coupled pixel has (i) an antenna that converts the free space wave to a guided wave, (ii) superconducting transmission lines, and (iii) one or several filters that define the passband(s) before the light continues on to the detector sensor(s). This approach allows simultaneous coverage of several distinct frequency bands in each spatial filter.

- **Antennas:** The antenna determines the polarization performance and beam shape of the detector. Different types of antennas permit different total bandwidths with good optical properties. Controlling the polarization and beam shape is crucial to mitigating systematic errors in the CMB measurements, while the total bandwidth impacts the total sensitivity per unit focal plane area. The three antenna types in current CMB experiments are feed horns coupled to planar orthomode transducers (OMTs), lenslet-coupled planar antennas, and planar phased-array antennas.
  - *Feed horn* arrays have been manufactured using gold-plated stacks of etched silicon wafer “platelet arrays,” reducing the manufacturing cost and complexity compared to traditional electroformed horns. Direct drilling of arrays of smooth-walled feed horns has also been demonstrated. A planar OMT in the circular waveguide at the base of each feedhorn, backed by a quarter-wave short, couples the light onto planar transmission lines leading to the detector sensors. Some earlier CMB instruments used direct absorbers in the feedhorns instead, typically operating with a single band.
  - *Lenslet* arrays using sprayed anti-reflection coatings, as well as stacked-wafer gradient index lenses, are being developed to simplify manufacturing. For these antennas, a planar superconducting antenna is on the chip under each lenslet to couple the light onto the planar transmission line.

- *Phased array* antennas use grids of small antennas, each coupled to a millimeter-wave transmission line. Each of these transmission lines travels back to the detector through a summing tree architecture, with the length of each transmission line matched such that the waves combine in phase at the detector. This lets the antenna array combine to form a main beam.
- **Multichroic Architectures:** A single-band antenna-coupled pixel has a single band-defining transmission line filter between the antenna and the lossy detector termination for each polarization mode. Multichroic pixels have filter banks (channelizers) that divide the total bandwidth of the antenna into multiple simultaneous bands each of which terminates at its own detector. The mm-wave circuitry of the pixel, including the transmission lines, crossovers, filters, and terminations need to be manufactured with stringent control of the circuit parameters and high uniformity across the array. Multichroic operation has been demonstrated for feed horn and lenslet-coupled antennas and is in the prototype stage for phased-array antenna pixels. Given that multiple frequency bands are required for foreground separation, a pixel that can measure more than one band simultaneously can provide more efficient use of the focal-plane area. Multichroic pixels require corresponding broadband receiver and telescope optics. Since the bands for each pixel are coupled through a single aperture, the pixel aperture size has to be chosen to optimize the sensitivity per band, and the improvement does not scale linearly with the number of bands. The number of bands per pixel must be determined by an experiment-wide optimization that includes the performance of all the optical elements, and the cost of the telescopes, detectors, readout electronics, and receiver optics.
- **Fabrication and Testing:** CMB-S4 will require of order 1,000 science-grade silicon detector wafers, and therefore mass manufacturing capability has to be developed. Among the DOE labs, ANL, LBNL, and SLAC are developing wafer fabrication throughput and consistency, as well as exploring hybrid fabrication using a combination of on-site and commercial foundries. Detector characterization is an essential part of the detector manufacturing process.

## Focal-plane Sensors and Readout

Chapter 5 provides a survey of the state of low-noise sensors and signal readout suitable for CMB-S4, focusing on promising scalable technologies. The order of magnitude leap in detector count from Stage-III experiments to CMB-S4 puts an emphasis on choosing a sensor and multiplexing combination that is straightforward to read out, integrate with the experiment, and manufacture.

- **Sensors:** We have identified Transition-Edge Sensors (TES) and Microwave Kinetic Inductance Detectors (MKIDs) as the leading candidates for the signal transducers in CMB-S4. TESs have a long record of well-characterized performance and CMB science results. They are a natural choice for CMB-S4 and would benefit from production scaling R&D. MKIDs are an attractive option to combine highly-multiplexed readout with signal transduction. They have demonstrated promising noise performance in laboratory measurements and millimeter-wave astronomy instruments, but are at an earlier stage of technological maturity. Areas for future MKID R&D include antenna-coupling, sensors for 100 GHz and below, and on-sky CMB measurements to verify that the detectors continue to have adequate white and 1/f noise in CMB applications.
- **Multiplexed readout:** As with Stage-III experiments, multiplexed readout will be crucial for the large detector arrays needed for CMB-S4.
  - *TES* sensors will be multiplexed using one or more of three candidate technologies: Time-division multiplexing (TDM) using Superconducting Quantum Interference Devices (SQUIDS)

as switches, frequency-division multiplexing (FDM) using in-series MHz resonators, or frequency-division multiplexing using GHz-excitation techniques ( $\mu$ MUX).

- *MKID* sensors employ frequency-division multiplexing using GHz-excitation techniques, but do not require a cold multiplexer separately from the sensor.

For CMB-S4, every TES multiplexing technology considered will benefit from an increased multiplexing factor, defined as the maximum number of sensors read out per readout channel. With some development effort, the TDM and FDM techniques for TES readout can be scaled to multiplexing factors of  $\sim 200$ . The  $\mu$ MUX TES readout technique could potentially produce MKID-like high multiplexing factors for TESs ( $\sim 1000$ ). All multiplexing techniques will also benefit from improved designs that reduce assembly complexity and provide cost and schedule savings given the large number of detectors necessary for CMB-S4.

- **Room temperature electronics:** In all of the technologies under consideration, the warm readout electronics appear scalable with development. Frequency-division techniques for both TESs and MKIDs use similar room-temperature biasing and readout electronics, enabling common development. It will be important to ensure that good individual detector performance (linearity, stability, sensitivity, and other performance parameters) continues even as multiplexing factors increase.



# 2

---

---

# Telescope design

## 2.1 Introduction

The design of the telescope has a central role in determining both the sensitivity and the level of systematic errors in a cosmic microwave background (CMB) experiment. The sensitivity of modern CMB detectors is determined by photon arrival statistics, and therefore the total sensitivity is determined by the number of detectors. CMB-S4 will require of order 500,000 detectors. Stage-III telescope designs typically contain 2,000 – 10,000 detectors, so the development of higher throughput (larger field of view) telescope designs would reduce the cost of CMB-S4. Systematic errors can be introduced by the telescope in several ways. First, the level of the telescope’s sidelobe response generated from diffraction and scattering is critical since the sidelobes will scan the 300K ground and relatively bright sky sources such as the sun, moon, and galaxy. Second, distortions of the beam (e.g., ellipticity) that depend on polarization angle, and polarization leakage from cross polarization and instrumental polarization will create false signals. Finally, pointing errors that could arise from thermal distortion of the telescope will create false signals by shifting structures on the sky.

Currently, “small-aperture” telescopes such as BICEP/Keck Array, ABS, SPIDER, PIPER, and CLASS, which typically have a primary aperture  $\lesssim 1$  m, have the best demonstrated noise and systematic error performance at the angular scales of inflationary signals ( $\ell < 200$ ). The smaller aperture size makes it practical to implement comprehensive co-moving shields, boresight rotation of the entire telescope, and polarization modulators as the first optical element. All of these features can be advantageous for control of systematic errors at the angular scales of the inflationary signals.

“Large-aperture” telescopes such as ACT, EBEX, POLARBEAR, QUIET, and SPT have demonstrated high-fidelity mapping of faint CMB structure at small angular scales, such as those from gravitational lensing, the CMB damping tail, and galaxy clusters. Given the relatively high cost of large-aperture telescopes, it is highly desirable to increase the size of the field of view (FOV) and studies have yielded Stage-IV designs that give up to a factor of 10 improvement in detector count compared to current Stage-III designs.

Given their complementary performance attributes, a plausible choice for CMB-S4 is to employ a hybrid of small- and large-aperture telescopes. However, if large-aperture telescopes could be demonstrated to give high fidelity measurements at inflationary angular scales, the use of a homogeneous array of large-aperture telescopes would reduce the cost of CMB-S4 by reducing the total number of detectors, readout, and cryogenic systems including their energy use at remote sites.

This chapter is organized as follows. In Section 2.2 we provide a general review of current telescope designs, including both small ( $\lesssim 1$  m) and large ( $\gtrsim 1$  m) apertures. In Section 2.3 we discuss a concept to achieve high throughput from a telescope. In Section 2.4 we provide a non-exhaustive list of methods that can mitigate instrumental systematic errors. In Section 2.5 we propose future studies and development areas that could expand optical designs that are viable for CMB-S4. In Section 2.6 we further review currently fielded telescope designs. We provide our final conclusions in Section 2.7.

## 2.2 Current CMB telescope designs and maturity

The current generation of CMB telescope designs incorporate lessons learned from decades of experience [2]. The ten current-generation experiments and two previous-generation telescope designs presented in Table 2-1 implement a wide variety of optical design approaches, including both refractive and reflective primary apertures, Gregorian and crossed-Dragone mirror configurations, single- and multi-camera systems, and the use or absence of polarization modulation mechanisms such as rotating HWPs, reflective variable-delay polarization modulators (VPMs), telescope boresight rotation, and sky rotation.

Small- and large-class telescope designs are discussed separately in the sections below. A table summarizing some relevant optical parameters is given in Table 2-1. A detailed description of several current telescope optical designs is given in Section 2.6.

### 2.2.1 Current small-aperture telescope designs

Small mm-wavelength CMB telescopes, with apertures  $\lesssim 1$  m, are designed to probe the inflationary gravitational wave  $B$ -mode signal at large angular scales,  $\ell < 200$ , but not the lensing signal at  $\ell > 200$ . Small telescopes reviewed here include ABS (0.25 m physical aperture), BICEP3 (0.53 m), CLASS (0.6 m), Keck Array/SPIDER (0.25 m), and PIPER (0.39 m). BICEP3 and Keck Array/SPIDER use all refractive elements, whereas the other experiments use dual off-axis reflector designs, and (with the exception of ABS) cold refractive reimaging optics.

BICEP3 (and the future BICEP Array) is an evolution of the BICEP/Keck Array optical design. Both are a simple two-lens objective/field lens design with a stop just behind the objective. The lenses and stop are cooled to 4 K. The BICEP3 telescope and each Keck Array/SPIDER telescope are single-frequency, which simplifies the anti-reflection (AR) coating implementation. Multi-frequency coverage is accomplished via the deployment of multiple telescopes. Lenses in SPIDER and the Keck Array are fabricated from HDPE plastic, whereas those in the larger, 520 mm aperture, BICEP3 telescope are alumina. A comoving absorptive conical baffle is placed in front of the telescope cryostat, and fixed reflective ground shields surround the telescopes. The telescope mount allows for full boresight rotation of the entire telescope to rotate the polarization angle sensitivity of each detector and check for polarization systematic errors. SPIDER's design is very similar, but uses a 4 K HWP rotated twice per sidereal day to modulate polarization, and reflective rather than absorbing external baffles to avoid the associated optical loading to take advantage of lower optical loading from atmosphere.

The CLASS ground-based experiment and PIPER balloon-borne experiment have similar optical layouts consisting of a VPM as the first optical element at the entrance pupil, two elliptical mirrors, cold refractive reimaging optics, and a cold stop. In CLASS, the VPM and mirrors are at ambient temperature, whereas in PIPER all optics are cooled to 1.4 K by superfluid helium boiloff. CLASS uses HDPE lenses and an UHMWPE window, whereas PIPER uses silicon lenses. Both telescopes have co-moving reflective baffles surrounding the mirrors and in front of the VPM. Similar to BICEP3 and Keck Array/SPIDER, multi-frequency coverage is accomplished for CLASS using multiple telescopes (40, 90, and 150/220 GHz telescopes) and for PIPER using multiple flights, which simplifies AR coating implementation.

ABS used a compact crossed-Dragone dual mirror design and no tertiary re-imaging optics. The mirrors were cooled to 4 K, with a cold stop preceding the primary mirror. An ambient temperature continuously-rotating HWP and co-moving reflective baffle were placed just above the AR-coated UHMWPE vacuum window.

Project	ABS	CLASS	Keck Array	BICEP3	BICEP Array	Spider	Piper
Physical aperture (m)	0.25	0.6	0.264	0.52	0.55	0.27	0.39
Illuminated aperture (m)	0.25	0.35	0.264	0.52	0.55	0.27	0.29
Telescope f/#	2.5	2, 2, 1.5, 1.5	2.2	1.6	1.6	2.2	1.55
f/# at detector array (if different)							1.6
Minimum Strehl ratio at 150 GHz	0.96		0.97	0.9576	0.942	0.97	0.97 (200 GHz)
f-lambda spacing at 150 GHz	2.6	2.42	1.8	1.63 (scaled from 95GHz)	1.63 (preliminary)	1.8	0.5
A*Omega of illuminated arrays (cm^2 sr)	50	92	5 * 24	224	4 * 337	6 * 24	6
A*Omega with Strehl > 0.8 at 150 GHz			--	404	4 * 507	--	51
Field of view per array (deg^2)	315	315	5 * 200	627.33	4 * 687	6 * 200	28
Useable field of view diameter (deg)			20 (each array)	28.26	29.6 (each array)	20 (each array)	
Number of arrays	1	4	5 (4 tiles per array)	1 (20 tiles)	4 (12 tiles per array)	6 (4 tiles per array)	
Number of telescopes	1	4	5 (1 mount)	1	4 (1 mount)	6 (1 cryostat)	2
Observation frequencies (GHz)	150	38, 93, 147, 218	95, 150, 220, 270	95	30/40, 95, 150, 220/270	(90, 150), 90,150,280	200, 270, 350, 600
Detectors on sky per frequency	480	72, 1036, 1190, 1190	5 * 512	2560	192/300, 3456, 7776, 9408/9408	(816, 1488)	272,992,1488
# Frequencies per array ("multichroic-ness")	1	1(40,90), 2(150/220)	1,1,1,1	1	2,1,1,2	1,1,1,1,1,1	1
Window Material	UHMWPE	UHMWPE	Zotefoam HD-30	HDPE	UHMWPE	UHMWPE	None
Illuminated diameter of window (m)	0.28	0.35	0.31	0.68	0.69	0.35	n/a
Lens Material	N/A	HDPE, silicon	HDPE	Alumina	Alumina	HDPE	Silicon
Temperatures of reflective optics (K)	4	300	--	--	--	--	1.4
Temperatures of refractive optics (K)	N/A	4, 1	4	4	4	4	1.4
Temperature of cold stop (K)	4	4	4	4	4	1.7	1.4
Temperature of detector arrays (K)	0.3	0.05	0.27	0.27	0.27	0.3	0.1
Year of initial (or partial) deployment	2012	2016	2012	2015	2018	(flight 1: 2015)	2016
Year of full deployment (all frequencies)	2012	2018	2013	2016	2020	flight 2: 2018	2020
Location	Chile	Chile	South Pole	South Pole	South Pole	Balloon	Balloon

Project	QUIET	EBEX	Simons Array	Adv. ACTPol	CCAT-Prime	SPT-3G
Physical aperture (m)	1.4	1.5	2.5	6	6	10
Illuminated aperture (m)		1.05	2.5	5.6	5.5	8
Telescope f/#	1.65	1.9	1.9	2.5	3	1.7
f/# at detector array (if different)		1.9	1.9	1.35	1.5	1.7
Minimum Strehl ratio at 150 GHz		0.9	0.85	0.8 (1 array), 0.93 (2 arrays)	0.81	0.99
f-lambda spacing at 150 GHz		1.74	1.8	1.8	1.3	2
A*Omega of illuminated arrays (cm^2 sr)				180	-2700	425
A*Omega with Strehl > 0.8 at 150 GHz				379	-3000	600
Field of view per array (deg^2)	39, 53		4 deg on sky	0.8	0.9	2.8
Useable field of view diameter (deg)	7.0, 8.2			2.3	7.5	1.9
Number of arrays	2 (in series)	14	1	3	up to 50	1
Number of telescopes	1	1	1	1	1	1
Observation frequencies (GHz)	42, 90	150, 250, 410	90, 150, 220, 280	28, 41, 90, 150, 230	90 GHz - 1 THz	90, 150, 220
Detectors on sky per frequency	76 diodes, 360 diodes	504, 342, 109	7588, 7588, 3794, 3794	88, 88, 1712, 2718, 1006	up to ~10^5	5420, 5420, 5420, 5420
# Frequencies per array ("multichroic-ness")	1	1	2	2	2 or 3	3
Window Material	UHMWPE	UHMWPE	Zote Foam	UHMWPE		HDPE
Illuminated diameter of window (m)		0.28	0.5	0.31		0.6
Lens Material	N/A	UHMWPE	alumina	silicon		alumina
Temperatures of reflective optics (K)	300	300	300	300	300	300
Temperatures of refractive optics (K)	N/A	4, 1	4	4, 1		4
Temperature of cold stop (K)	N/A	1	4	1		4
Temperature of detector arrays (K)	20K, 27K	0.25	0.25	0.1	0.1	0.25
Year of initial (or partial) deployment	2008	2009 (test flight)	2017	2016	2020	2017
Year of full deployment (all frequencies)	2009	2013	2017	2018	TBD	2018
Year of full deployment (all frequencies)	Chile	Balloon	Chile	Chile	Chile	South Pole

Table 2-1: Table of telescope and instrument parameters for current and recent projects sorted by primary aperture size. Descriptions of each of these projects are presented in Section 2.6.

### 2.2.2 Current large-aperture telescope designs

Large-aperture mm-wavelength CMB telescope designs,  $\gtrsim 1$  m diameter, can be used to measure the CMB lensing signal at  $\ell > 200$ , and  $> 5$  m designs can also measure arcminute-scale secondary anisotropies such as the Sunyaev-Zeldovich effect from galaxies and galaxy clusters, emission from dusty galaxies and active galactic nuclei. Large aperture designs reviewed here include AdvACT (6 m physical aperture), EBEX (1.05 m), Simons Array (2.5 m), SPT-3G (10 m), and QUIET (1.4 m). All large telescope designs with the exception of QUIET use ambient temperature dual-mirror off-axis Gregorian configurations and cold refractive reimaging optics to form a cold stop and flat (telecentric) image plane. In contrast to the small-aperture designs, the large-aperture telescopes are all designed to conduct simultaneous observations in multiple frequency bands.

The AdvACT receiver design consists of three independent optics tubes for each of three frequency pairs (28/41, 90/150, and 150/230 GHz). Each optics tube uses a UHMWPE vacuum window and has three cold AR coated silicon lenses and a 1 K cold stop to control illumination of the primary. AdvACT will use ambient temperature continuously rotating half-wave plates (HWPs) just outside each optics tube's vacuum window. The ACT telescope has a co-moving reflective shield and a stationary reflective ground shield. The large primary aperture is comprised of small panels separated by gaps.

The Simons Array (three telescopes) and SPT-3G share a similar optical design consisting of a single receiver (per telescope) with three cold alumina lenses and a 4 K cold stop. SPT-3G uses a HDPE window whereas the Simons Array receivers (called the POLARBEAR-2 receivers) each use a 10-inch thick laminated Zotefoam window. The first POLARBEAR-2 receiver will have an ambient temperature continuously-rotating HWP just outside the receiver window, whereas the second and third receivers will have 50 K HWPs inside the cryostat window. SPT-3G does not have plans to use a HWP. Both the Simons Array telescopes and SPT-3G use a prime focus baffle and reflective co-moving shields, but no fixed ground shields. The Simons Array primary mirrors are monolithic, while the SPT primary mirror is comprised of small ( $\sim 0.7$  m) panels separated by small gaps.

EBEX operated at 150, 250, and 410 GHz using a receiver containing five plastic (UHMWPE) lenses, a co-located cold stop, and a continuously rotating HWP at 1 K. Polarization sensitivity was achieved by using a polarizing grid inside the receiver cryostat and two focal planes of non-polarization sensitive detectors. Each focal plane consisted of seven detector wafers, with each wafer sensitive to a single frequency band (150, 250, or 410 GHz), defined by reflective filters above the feedhorns and the cylindrical waveguides between the feedhorns and detectors.

QUIET was a crossed-Dragone telescope operating at 42 and 90 GHz. The two mirrors were at ambient temperature, and no tertiary optics were used in front of the cryogenic focal plane of feedhorns. Unlike ABS, it did not use a stop above the primary mirror. Instead, the feeds were sized to under-illuminate the mirrors to minimize spillover. Sidelobes were also mitigated by using an absorbing baffle in front of the entrance aperture and surrounding the telescope.

## 2.3 Concept for high throughput large-aperture telescope design

As described in the CMB-S4 science book, several of the science goals require arcminute-scale resolution, which roughly translates to telescope apertures between a few and ten meters at 150 GHz. This requirement has motivated designs with lower levels of systematic error (e.g., cross polarization) and larger throughput

than existing telescopes with the potential for illuminating a much larger number of detectors than current telescopes.

For CMB-S4, the number of detectors required is nearly two orders of magnitude larger than the number in a typical Stage-III telescope. It is critical, therefore, to develop telescope designs with much higher throughput than Stage-III designs. Fortunately, there are a number of candidate designs including the crossed-Dragone, the three-mirror anastigmat, and commonly-used offset Gregorian but implemented with a secondary mirror of similar size to the primary mirror. Of these, the crossed-Dragone has been studied the most and will be described in detail below as an example case.

The example concept is based on a crossed-Dragone design with higher  $f/\#$  than had been studied previously [3, 4]. Specifically, previous studies of crossed-Dragone CMB telescope designs focused on systems with focal ratios closer to  $f/1.5$  and with the detector arrays at the telescope focus [4–8]. For ground-based telescopes, controlling spillover with this approach generally requires either severely under-illuminating the primary mirror [6] or cooling the entire telescope to cryogenic temperatures [5], which is not practical for a large telescope.

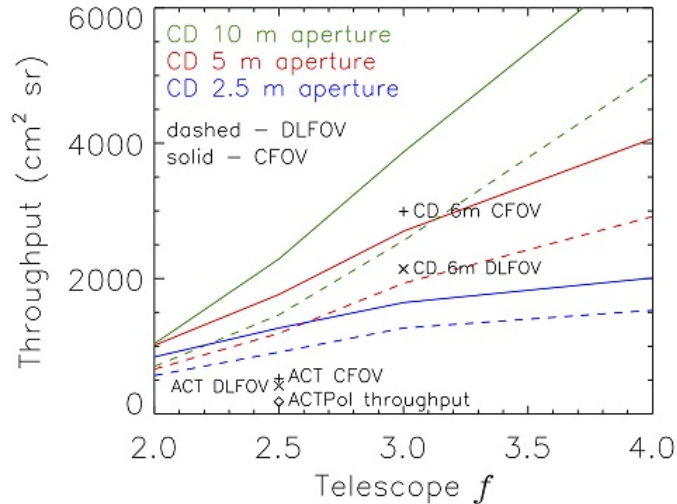


Figure 2: Optical throughput comparison for large-aperture crossed-Dragone telescopes with different  $f/\#$  and apertures compared to the off-axis Gregorian ACT design [3]. Dashed lines are diffraction limited field of view (DLFOV) and solid lines are correctable field of view (CFOV)

The new crossed-Dragone concept instead controls spillover past the mirrors using cryogenic refractive optics similar to those used in the existing large-aperture telescopes ACT [9], Simons Array [10], and SPT [11]. Refractive optics naturally couple to telescopes with larger focal ratios, which also increases the available optical throughput as shown in Figure 2. This crossed-Dragone design has recently been adopted for the CCAT-prime submillimeter astronomy project to study cosmic origins of stars, planets and galaxies. Preliminary designs and potential systematic error advantages of this design are shown in Figure 14 and discussed in Section 2.6.11. When combined with closely-packed optics tubes, a 6 m telescope based on this design is capable of providing a diffraction-limited field of view for more than  $10^5$  detectors, which is roughly ten times more detectors than will be deployed on upcoming Stage-III telescopes [3].

As mentioned above, there are several telescope designs that may be capable of providing a similar scale of diffraction-limited field of view. For example, adding an optimized tertiary similar in size to the primary for

a more traditional off-axis Gregorian design results in a relatively large field of view, and this design should be studied in further detail. As described in Section 2.5, such alternate designs represent a high priority area of study for CMB-S4.

## 2.4 Telescope engineering to control systematic errors

CMB-S4 will require exquisite control of systematic errors, and therefore the telescopes must be designed to have low sidelobe pickup, stable optics, and have the capability to scan fast enough to minimize atmospheric brightness fluctuations without introducing vibrations that cause microphonics pickup or temperature instability in the cryogenics. It may also be necessary to measure systematic errors that are fixed relative to the instrument, e.g., by rotating the camera or the entire telescope about boresight. CMB-S4 will build on experience with existing telescope designs, but the scale of CMB-S4 may allow approaches that were deemed impractical for current experiments. Some of these approaches are described below; all will require design and manufacturing studies to assess their viability for CMB-S4.

The level of systematic error induced by sidelobe pickup depends on a number of optical aspects that will have to be studied extensively for CMB-S4. To give a sense of the rough order of magnitude involved, the EPIC, a proposed CMB polarization satellite mission, 1.4 m aperture design was expected to have about  $-80$  dB sidelobes ( $-20$  dBi), which corresponds to approximately  $0.1$  nK rms polarized pickup from the galaxy at  $150$  GHz [12]. There are two approaches for controlling pickup: (i) reduce scattering, which means using off-axis optics with enough clearance to avoid sidelobes due to clipping the beam, and smooth optical surfaces to avoid scattering from gaps between mirror segments, and selecting low-scatter windows and filters; and (ii) control what does get scattered, which requires reflecting shields and/or absorbing baffles to eliminate pickup in far sidelobes.

The pointing requirements for CMB-S4 will be stringent: we estimate that pointing reconstruction will need to be accurate at the level of  $1\%$  of beamwidth or about  $1.5''$  for the large-aperture telescopes [13], so the telescope structures must be stiff. Limiting spurious signals from flexing of the optics also require stiff structures and schemes to keep the optical surfaces free of water, snow, and ice.

### 2.4.1 Monolithic mirrors

The use of a monolithic primary mirror for large-aperture telescopes would avoid the structured sidelobe response that is seen with all telescopes with segmented primary mirrors. The POLARBEAR/Simons Array telescopes have 2.5 meter diameter monolithic mirrors made from machined cast aluminum. Fabrication of a monolithic, millimeter-wavelength mirror larger than a few meters in diameter is challenging however, and therefore 6-10 meter diameter CMB telescopes (i.e., ACT and SPT) have mirrors made of  $\sim 1$  m segments with about 1 mm gaps between segments. Scattering from the gaps generates sidelobes, which account for approximately  $1\%$  of the telescope response [14]. It is difficult to make the gaps smaller because some clearance is needed for assembly and manufacturing tolerances. Various gap cover/filler schemes have been attempted, but a robust solution has not yet been demonstrated.

The key issues for monolithic mirrors are: (i) fabrication errors; and (ii) thermal deformation. Figure 3 shows surface error contributions for a monolithic, aluminum mirror, which is an obvious choice for low cost. A 5 m diameter,  $\lambda = 1$  mm mirror seems possible if thermal gradients through and across the mirror can be kept within 1 K, which is what the  $\sim 1$  m diameter and 50 mm thick Caltech Submillimeter Observatory

primary mirror segments achieve at night. Keeping thermal gradients below 1 K in a large aluminum mirror will require insulation on the back of the mirror, a reflective front coating for daytime operation, and maybe active control (e.g., cooling the back of the mirror even at night). A carbon fiber reinforced polymer (CFRP) mirror would have an order of magnitude better thermal performance, but it is technically challenging to fabricate a large monolithic CFRP mirror with the required surface accuracy.

### 2.4.2 Boresight rotation

A few experiments (e.g., DASI, CBI, QUAD, QUIET, BICEP, Keck Array) have included boresight rotation to measure and potentially cancel systematic errors that are fixed with respect to the instrument (e.g., instrumental polarization) and vary slowly (on timescales of tens of seconds). All these experiments have or had small telescopes, or arrays of small telescopes; the largest boresight rotator was the 6 m diameter platform of the CBI. Boresight rotation on a off-axis 6m telescope would be technically challenging, but it could play an important role in achieving the systematic error control required to reach CMB-S4 sensitivity levels.

The key issues for boresight rotation are: (i) balancing the telescope structure while also providing adequate range of motion; and (ii) protecting the drive mechanisms from the weather.

A mount that supports boresight rotation can wrap around the outside of the telescope, which allows full range of motion with a naturally balanced structure (no counterweight), but results in a massive, expensive mount with large mechanisms that are difficult to protect. Alternatively, a compact, inexpensive, enclosed mount can be placed behind the telescope, but this requires a counterweight which results in limited range of motion because the counterweight interferes with the mount. Figure 4 shows a concept for a compact mount with boresight rotation. The design provides an optical bench that can support a single, large, off-axis telescope, or an array of smaller telescopes inside a deep baffle. The compact drive mechanisms can be enclosed and are accessible from below, which is appropriate for a site that has severe snow storms or very low temperatures.

Another approach under study that offers partial boresight rotation is having the telescope elevation axis aligned with the chief ray between the secondary and the tertiary (or between the secondary and the instrument if a tertiary is not used). This approach offers other potential advantages of not tilting the instruments in elevation and enabling instrument rotation independent of the telescope, and it is being pursued by the CCAT-prime project (see Section 2.6.11 for details).

### 2.4.3 Shields and baffles

Co-moving reflective shields and/or absorbing baffles that fully shield the optics will be needed to control pickup in the far sidelobes. Stringent shielding is a key ingredient in the success of small CMB telescopes making measurements at low  $\ell$ , but a full shield or baffle may also be practical for a large telescope. For example, the mount in Figure 4 can accommodate a 5 m telescope inside a deep, cylindrical baffle that is supported by a light, CFRP spaceframe.

The key issues for shields and baffles are: (i) maintaining adequate mechanical stability to avoid time-varying pickup, e.g., due to wind buffeting; (ii) keeping surfaces clear of water, snow, and ice, which change the optical loading; (iii) limiting baffling temperature variations, which cause variations in optical loading; and (iv) ensuring the survival of absorbing coatings.

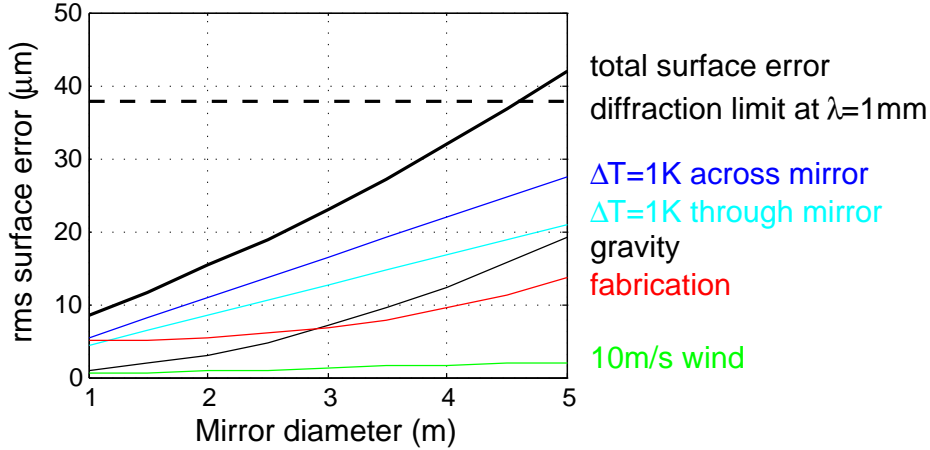


Figure 3: Surface error vs. diameter for a monolithic aluminum mirror with thickness = diameter/4. Temperature gradients across the mirror change the thickness, while a temperature gradient through the mirror causes cupping. The gravitational deformation model represents the deflection of a simply supported plate, and wind-induced deformation is the gravitational deformation scaled by the ratio of wind pressure to mirror weight per unit area. The fabrication error model has 50  $\mu\text{m}$  rms for a 10 m mirror, with error scaling as the square of diameter, combined in quadrature with a setup error of 5  $\mu\text{m}$  rms. The model is based on the OVRO 10.4 m primary mirrors, which were machined as a single piece, and the 1 m segments for SPT. The horizontal dashed line corresponds to 80% Strehl ratio ( $\lambda/27$  rms surface error) at 300 GHz.

Mechanical stability is more challenging for a reflective shield because any part of the surface that sees scattered light must be stable. For an absorbing baffle, the rim must be stable, but the rest of the baffle can move relative to the telescope beam as long as the baffle is truly black. There is no practical experience with large absorbing baffles, so the effect of temperature variations needs consideration. Some work must also be done to identify or develop a light, robust, weather-resistant absorber.

## 2.5 Potential future studies and development areas

The CMB-S4 effort would profit from a variety of studies with respect to telescope and receiver design. A comprehensive list is beyond the scope of this document, but we list a few potential studies and areas of research that could significantly help in the course of designing the CMB-S4 telescopes.

**Comprehensive optical design study for large-aperture telescopes** It has been shown that crossed-Dragone designs can provide substantially larger throughput than current large-aperture telescopes (Section 2.3). However, current telescopes were not designed with the goal of maximizing throughput, and therefore it is important to perform a comprehensive study to determine if modifications to more traditional off-axis Gregorian or Cassegrain designs, such as implementing a larger secondary mirror, could achieve similar performance. As mentioned, the three-mirror anastigmat (TMA) is a well known design that can have very high throughput that should be investigated. Introducing higher-order correction terms to the mirrors of a conventional crossed-Dragone also has the potential to increase diffraction-limited throughput.

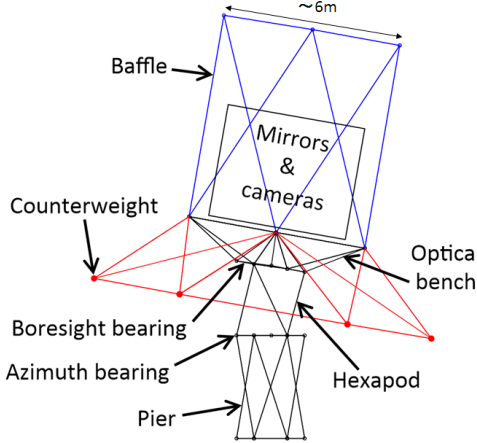


Figure 4: Concept for a telescope mount with boresight rotation. The mount provides a large, flat optical bench that can accommodate various arrangements of cameras and off-axis mirrors. Standard, slewing-ring bearings allow fast scanning in azimuth and rotation about boresight to modulate/measure polarization. Zenith angle motion is controlled by a hexapod that provides a stiff connection between the azimuth and boresight slewing rings. The blue structure is a lightweight CFRP spaceframe that supports an absorbing baffle to reduce pickup. Dimensions in the diagram are based on a 6 m diameter optical bench and 2 m diameter slewing rings.

**Optimization study for number of aperture sizes for CMB-S4** Given the strong relationship between cost and telescope diameter, an optimization study should be performed to determine the number of aperture sizes to include in CMB-S4. By including two or more telescope sizes, resolution could be matched to some degree over the roughly factor of ten range in frequency to be measured by CMB-S4. However, the savings in telescope construction cost must be balanced against additional design and logistics costs of a larger number of telescope types.

**Study on measuring inflationary angular scales with large-aperture telescopes** This study is critical since significant cost savings are possible if large-aperture telescopes can cover at least the degree angular scales of the Inflationary recombination peak. ACT (Section 2.6.1), the Simons Array (Section 2.6.7), and SPT (Section 2.6.8) are currently making measurements aimed at the recombination peak with different combinations of HWPs and scan strategies, but none have published high-fidelity results. Some new large-aperture telescope designs have a FOV approaching that of small-aperture telescopes (e.g.,  $\sim 8^\circ$  for CCAT-prime, Section 2.6.11), which could be beneficial for measuring degree-scale polarization, although results may not be available before a CMB-S4 telescope is designed.

**Study on the feasibility of reionization peak measurements by CMB-S4** Measurements of both *E*-mode and *B*-mode polarization of the reionization peak would be highly valuable for increasing the confidence in the detection of an inflation signal and to improve the error on the sum of neutrino masses by improving constraints on the optical depth to reionization. CLASS (Section 2.6.3), PIPER (a NASA balloon, Section 2.6.6), and GROUNDBIRD are the only current sub-orbital projects targeting this largest angular scale range. CMB-S4 science can be pursued independently of these measurements, but it may be worth expanding the CMB-S4 science case if these projects produce compelling results down to  $\ell \approx 5$ .

**Tradeoff study between segmented and monolithic primary mirrors** As mentioned earlier, the gaps between panels in the segmented primary and secondary mirrors generate sidelobe structure in large-aperture telescopes. A study should be made of the impact of these sidelobes for CMB-S4 science. Additional simulations and calculations are needed to better understand the impact of the sidelobes and the potential benefit of monolithic primary mirrors. Also, this study would address the cost and feasibility of large-diameter ( $\geq 5$  m) monolithic mirrors (Section 2.4.1).

**Study of baffle design for CMB-S4 telescopes** There is currently diversity in the design of optical baffling for CMB telescopes. Both absorptive and reflective baffles are common. It is important to study the optimal design of baffles, especially in the case of co-moving baffles on large-aperture telescopes (Section 2.4.3). It is particularly important to understand how to control systematic errors and to minimize spillover onto absorptive baffles. Spill over onto absorptive baffles gives additional optical loading and the consequent increase in photon noise.

**Study of systematic error mitigation with boresight rotation** Boresight rotation of the entire telescope is very effective in reducing systematic errors from beam shape imperfections. Boresight rotation has been implemented only on  $\leq 1.5$ m-aperture telescopes. Additional simulations including a variety of sources of systematic error could help address whether the additional cost of implementing full boresight rotations or partial boresight rotations (Section 2.4.2) on large-aperture telescopes is worthwhile.

**Study of optimal receiver envelope** As the physical aperture of receiver windows increases, more cooling power is needed to remove the additional radiative loading. Improved cryogenic modeling would help to assess the trade-offs in the amount of optical throughput per receiver, and in particular the trade-off in single versus multiple receivers for large-aperture telescopes. The study would include the effect of cooldown time on testing efficiency and explore methods to reduce the cooldown time of large-envelope receivers such as the implementation of an integrated liquid nitrogen pre-cool system.

**Optimization study on the number and diameter of optics tubes per receiver** There are a set of trade-offs on the number and diameter of optics tubes per receiver for large-aperture telescopes. A choice of larger diameter optics tubes reduces the number of tubes required arguably giving a reduction in system complexity. A single optics tube is currently used by Simons Array (Section 2.6.7) and SPT-3G (Section 2.6.8). However, the optical bandwidth of those systems is limited to that achievable with practical anti-reflection coatings, and the systems have additional loss due to having relatively thick refractive optics.

Having many optics tubes enables each one to be optimized for a different wavelength range, and relaxes space constraints around each detector array (e.g., Section 2.6.1 and Section 2.6.11); however, it can lead to increased cryogenic complexity and requires fabrication of more refractive optical elements. Use of many optics tubes also appears to increase the usable field of view [3]. It is important to understand the optical design and implementation trade-offs between these options and, relatedly, the optimal diameter of each tube in the multiple-tube design.

## 2.6 Optics designs for current projects

### 2.6.1 Advanced ACTPol

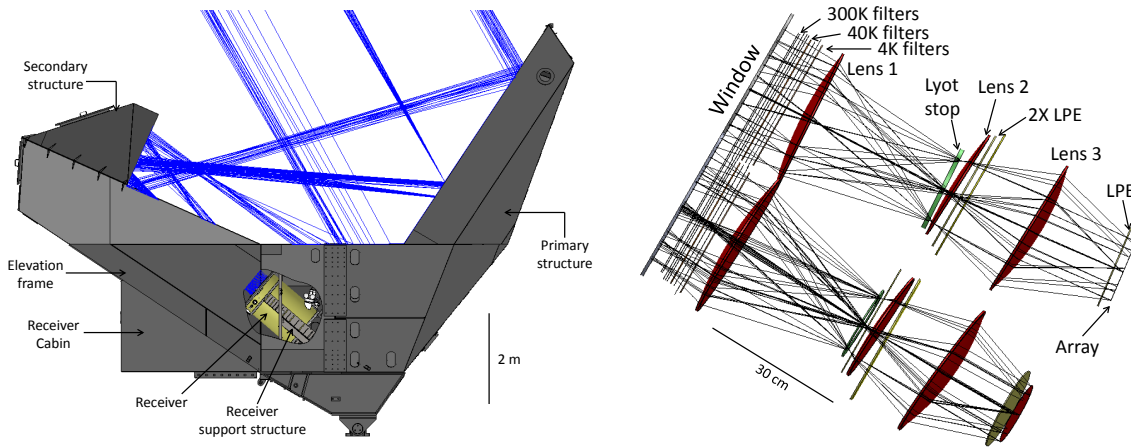


Figure 5: Left: ACT telescope optics and mechanical structure. Right: Ray trace of Advanced ACTPol receiver optics, which includes three optics tubes: one on the top and two symmetric tubes on the bottom [15].

AdvACT is the third instrument upgrade for the 6 m ACT. The 6 m primary and 2 m secondary are arranged in a compact off-axis Gregorian configuration to give an unobstructed image of the sky. The details of the telescope optics design are presented in [16], while the ACTPol and AdvACT receiver optics designs are presented in [15, 17]. Figure 5 shows a ray trace through the ACT mechanical structure as well as through the AdvACT receiver optics. Illumination of the primary mirror is controlled using a 1K Lyot stop. To minimize ground pickup during scanning, the telescope has two ground screens. A large, stationary outer ground screen surrounds the telescope and a second, inner ground screen connects the open sides of the primary mirror to the secondary mirror and moves with the telescope during scanning.

ACTPol and AdvACT use the same receiver with three independent optics tubes. Both use large silicon lenses with two and three layer metamaterial anti-reflection (AR) coatings [18]. These coatings offer the advantages of negligible dielectric losses (< 0.1%), sub-percent reflections, polarization symmetry equivalent to isotropic dielectric layers, and a perfect match of the coefficient of thermal expansion between coating and lens. Each optics tube focuses light onto a two-frequency multichroic detector array at one of the following frequency pairs: 28/41 GHz, 90/150 GHz, or 150/230 GHz [9]. The AdvACT reimaging optics have  $f/1.35$  at the array focus. A pixel-to-pixel spacing of 4.75 mm in the recently deployed 150&230 GHz array leads to approximately 1.8&2.5  $f\lambda$  spacing. A UHMWPE vacuum window is used combined with metal mesh filters to control out of band radiation.

### 2.6.2 BICEP3

BICEP3 is a cryogenic refractor of aperture 0.52 m, with two alumina lenses [19, 20] in an  $f/1.6$  system. The main cryostat volume is 29 inches in diameter and 95 inches high. It operates at 95 GHz on a three-axis

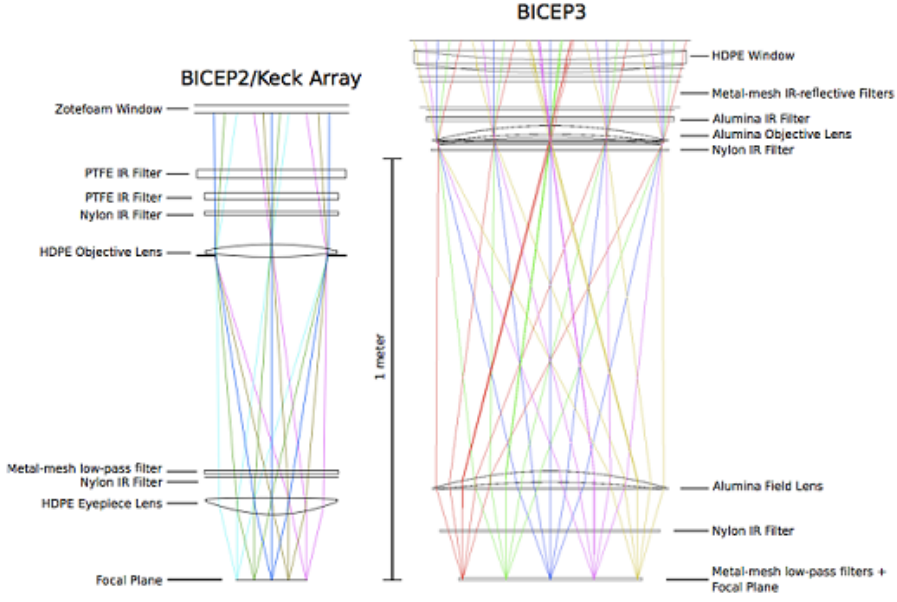


Figure 6: Left: BICEP2/Keck Array ray trace. Right: BICEP3 ray trace.

mount at the South Pole. The field used is  $14.1^\circ$  half-opening angle, nearly the unvignetted FOV. At 2 mm wavelength the design gives  $\text{Strehl} > 0.96$  over the full unvignetted field (top-hat illumination assumed).

The lenses are 99.6% pure alumina. The lenses and stop are at 4 K. The window is made using HDPE. The optical filters consist of metal mesh filters at (nominal) ambient temperature, an alumina filter at 50 K, another mesh filter below that, two Nylon filters at 4 K, and Ade edge filters at 250 mK over each detector module. The window, alumina components, and Nylon filters are single-layer AR coated; the alumina AR is built from an epoxy mix. A co-moving absorptive forebaffle and a reflective groundshield mitigate ground source contamination.

Starting in the 2016 season, BICEP3 has 2400 light detectors. The pixels are phased slot antenna arrays with tapered weighting to approximate Gaussian beams [21]. The  $1/f$  noise knee after atmospheric common-mode rejection from detector pair differencing is well below the degree-scale science band [22, 23]. Beam systematic errors are averaged down by boresight rotation and residual temperature to polarization beam leakage is removed by deprojection [24]. Thus, a (fast) polarization modulator is not used in BICEP3 (as is also true with BICEP2 and Keck Array).

The mount (originally built for BICEP) provides elevation down to  $\sim 50^\circ$ , full azimuth and boresight rotation of  $255^\circ$ . The latter provides full  $Q/U$  discrimination and cancellation of several beam related systematic errors. Mapping is performed with a sequence of constant elevation scans at  $2.8^\circ/\text{s}$  in azimuth.

The BICEP Array receivers will be substantially the same as BICEP3, with small improvements planned to windows, filters, and optical throughput.

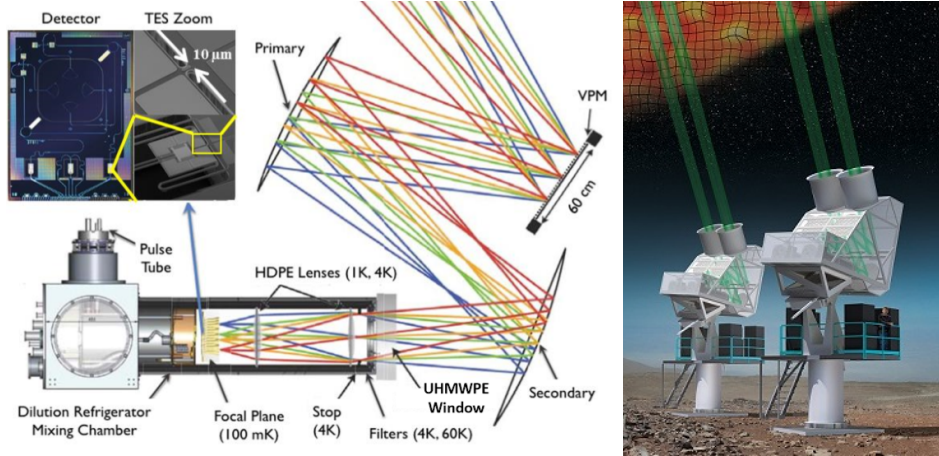


Figure 7: Left: CLASS system overview. Right: CLASS site rendering, showing the two mounts with four telescopes.

### 2.6.3 CLASS

The CLASS experiment consists of four telescopes sharing similar optical layouts [25]. One telescope operates at 40 GHz, two at 90 GHz, and the final telescope is a dichroic 150/220 GHz, hereafter the high-frequency (HF) telescope. A 60 cm-diameter VPM is the first element in the optical chain, providing approximately 10 Hz front-end polarization modulation [26]. Ambient-temperature, off-axis, elliptical, 1-meter primary and secondary reflectors reimaging the cold stop of the receiver at 4 K onto the VPM. Cryogenic reimaging lenses, one at 4 K and one at 1 K, focus light onto the focal plane of feedhorn-coupled TES bolometers. The CLASS design emphasizes per-detector efficiency and sensitivity with 10 dB edge-taper illumination of the cold stop. The CLASS telescopes provide diffraction-limited performance over a large, 20° FOV with resolutions ranging from 90' at 40 GHz to 18' at 220 GHz. Three-axis mounts give azimuth, elevation, and boresight rotations, with two telescopes on each of two mounts (See Figure 7). Co-moving ground shields and baffles reduce ground pickup.

The lenses for the 40 and 90 GHz telescopes are made of HDPE, while the HF telescope employs silicon lenses. All of the lenses are AR coated with simulated dielectrics cut directly into the lens material. The receivers have vacuum windows approximately 50 cm in diameter made of UHMWPE. A combination of capacitive-grid metal-mesh filters, absorptive polytetrafluoroethylene (PTFE) filters, and Nylon filters reject infrared radiation.

### 2.6.4 EBEX

The EBEX telescope was a balloon-borne CMB polarimeter observing at 150, 250, and 410 GHz. The EBEX design achieved flat telecentric focal planes, a large diffraction limited FOV defined as Strehl ratio  $> 0.9$ , a cold stop to control sidelobe response, as well as a continuously-rotating achromatic HWP [27] and polarizing grid to provide polarimetry, all while remaining sufficiently compact to fit on a balloon payload [28].

To achieve this, the EBEX optical system consisted of a 1.05 m,  $f/1.9$ , ambient temperature, Gregorian Mizuguchi-Dragone [29,30] reflecting telescope and a cryogenic receiver containing five UHMWPE re-imaging

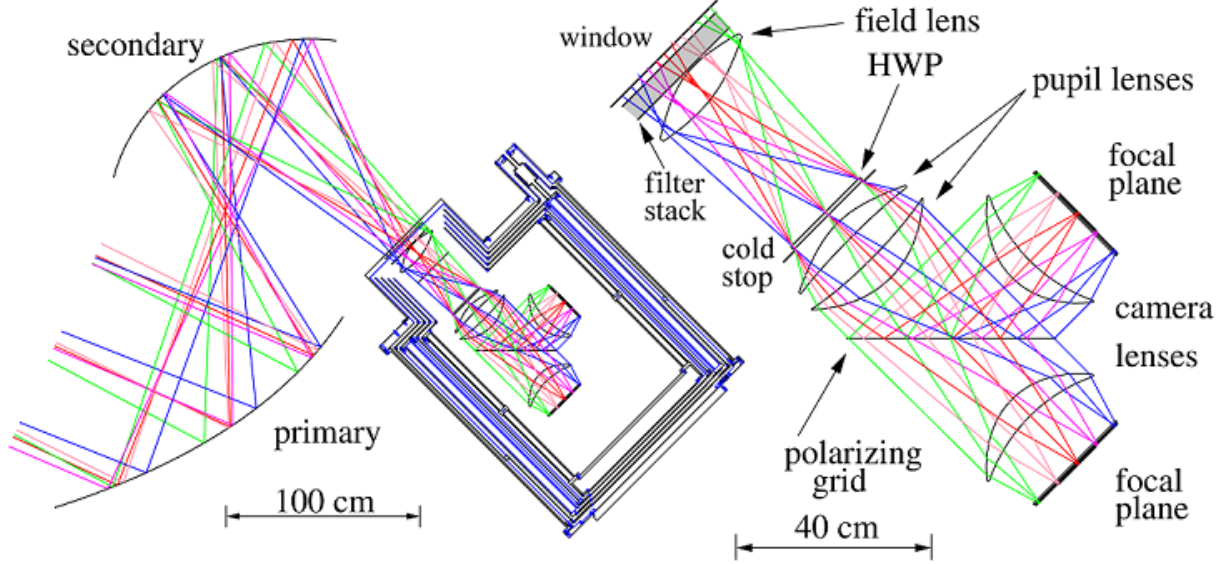


Figure 8: EBEX optical design ray trace schematic consisting of two ambient temperature reflectors in an off-axis Gregorian configuration and a cryogenic receiver (left). Inside the receiver (right), cryogenically cooled polyethylene lenses formed a cold stop and provided diffraction limited performance over a flat, telecentric,  $6.6^\circ$  FOV. A continuously-rotating achromatic HWP placed near the aperture stop and a polarizing grid provided the polarimetry capabilities.

lenses (see Figure 8). The mirrors were oversized to suppress sidelobe pickup; the illuminated aperture is 1.05 m while the physical aperture is 1.5 m. The reimaging lenses preserved the  $f/\#$  of the system while forming a 1 K cold stop, the location of the continuously-rotating achromatic HWP, enlarging the diffraction limited FOV to  $6.6^\circ$ , and forming two flat, telecentric focal planes [28, 31]. On the focal planes conical feedhorns coupled the detectors, TES bolometers, to free space. Each focal plane consisted of seven wafers, four at 150 GHz, two at 250 GHz, and one at 410 GHz.

### 2.6.5 Keck Array/SPIDER

The Keck Array and SPIDER are close relatives of BICEP and BICEP2. Both consist of multiple cryogenic refractors with an approximately 250 mm aperture and  $f/2.2$  of essentially the same optical design as BICEP2 [32]. Both use JPL dual-polarization slot antenna array coupled TES bolometers [21].

Keck consists of five telescopes co-aligned in their ground-based mount at the South Pole, each in its own independent vacuum jacket. Individual telescopes have been assigned each observing season to different frequency bands from 95 to 270 GHz [33]. Apertures are 264 mm and FOVs are  $15^\circ$  [34].

The Keck telescopes have 120 mm thick Zotefoam windows, 50 K PTFE and Nylon filters, 4 K HDPE lenses and a Nylon filter, and Ade edge filters [33, 34]. The lenses and filters (except the edge filter) are single-layer AR coated, matched to the frequency band of the detector in use. The stop is at 4 K, on the bottom of the first lens. Absorptive co-moving forebaffles surround each telescope aperture, and along with a reflective groundscreens minimize ground pickup.

The Keck Array is on a three-axis mount (built for DASI). Mapping is performed by a sequence of constant EL scans at each of eight boresight rotation angles, four pairs of  $180^\circ$  complements for complete  $Q/U$  discrimination and mitigation of beam systematic errors. The azimuth scan speed is  $2.8^\circ/\text{s}$ . The  $1/f$  noise knee after atmospheric common-mode rejection from detector pair differencing is well below the degree-scale science band [22, 23]. Beam systematic errors are averaged down by boresight rotation and residual temperature to polarization beam leakage is removed by deprojection [24]. Thus, a (fast) polarization modulator is not used in Keck (as with BICEP2 and BICEP3).

SPIDER is a balloon experiment with six co-aligned telescopes in one large LHe cryostat [35, 36]. It has some optical differences from the Keck Array (and BICEP2) to take advantage of the lower sky loading at float altitude (35 m). Specifically, the filter stack is predominantly comprised of reflective metal mesh (vs. absorptive) filters at 250 K, 130 K and 35 K, with multi-layer mesh lowpass edge filters at 4 K and 2 K, and an absorptive Nylon filter at 4 K. The optical sleeve baffles are cooled to 1.6 K. This configuration led to less than 0.35 pW optical loading on the detectors.

The detectors (for the first circum-Polar flight in January, 2015) are slot antenna array-coupled TES bolometers, with 95 and 150 GHz bandpasses. The detector  $1/f$  noise knee is low [35], the science goals for  $10 < \ell < 300$  are accommodated with available scan rates (see below), and fast polarization modulation is not needed, as with the Keck Array and the BICEP2 and 3 instruments (see also [37]). The second circum-Polar flight is planned to include feedhorn arrays and orthomode transducer (OMT)-coupled detectors [38].

The gondola provides for AZ and EL scanning. It does not have boresight rotation, but uses cryogenic waveplates (rotated  $22.5^\circ$  every 12 sidereal hours) for  $Q/U$  discrimination and polarization modulation, with a contribution as well from sky rotation.

### 2.6.6 PIPER

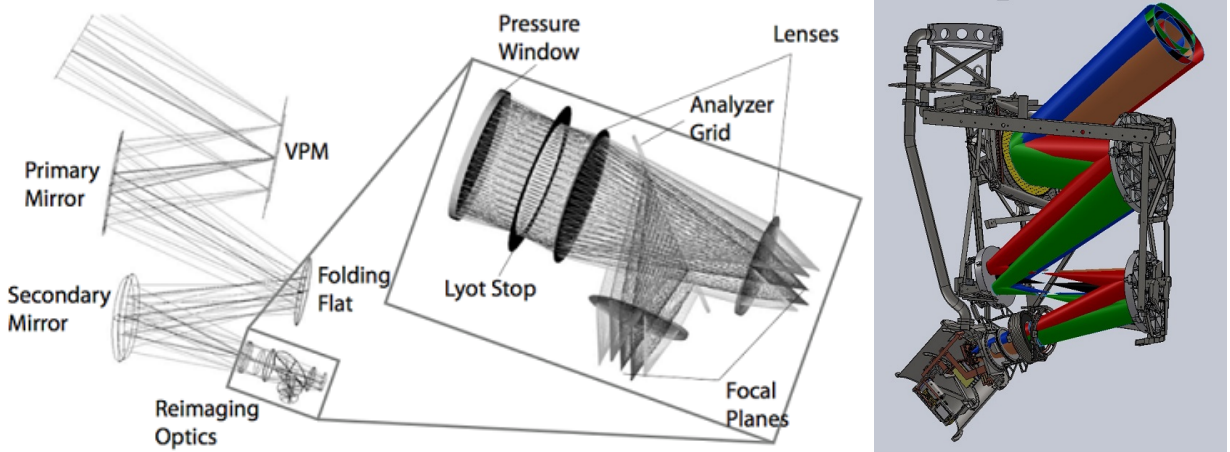


Figure 9: PIPER. Left: Ray trace of original PIPER optics design. Right: Current PIPER implementation.

PIPER is a balloon-borne instrument to observe CMB polarization at 200, 270, 350 and 600 GHz [39]. Twin co-pointed telescopes survey Stokes  $Q$  and  $U$ . Like CLASS, the first optical element of each telescope is a VPM. The VPM separates sky signal from instrument drifts by modulating the incoming polarized signal

at 3 Hz, aiding reconstruction of the polarized CMB sky on the largest angular scales. The VPM efficiently mitigates instrument polarization systematic errors by being the first optical element. Each of the PIPER VPMs have a 40 cm clear aperture with  $36\text{ }\mu\text{m}$  wires at  $115\text{ }\mu\text{m}$  pitch. PIPER uses the bucket dewar from ARCADE, which carries 3000 L of liquid helium. Helium boiloff allows operation without emissive windows. Superfluid fountain effect pumps draw LHe to cool all optics to 1.4 K. Cold optics and the lack of windows reduce photon noise and allow PIPER to take full advantage of the float conditions (especially at high frequencies) and to conduct logically simpler, conventional flights from Palestine/Ft. Sumner and Alice Springs. Each flight is optimized for one band, and flights from the northern and southern hemispheres cover 85% of the sky.

Two aluminum mirrors image a 12 cm diameter cold aperture stop (1.4 K) onto the central region of the front-end VPM. The entrance pupil is 29 cm in diameter and is undersized to limit edge illumination of the VPM (33 dB edge taper). The stop is a corrugated stack of Eccosorb. The 1.4 K environment of the bucket dewar mitigates stray light and acts as a co-moving ground screen. The reflective fore-optics feed silicon re-imaging optics that use metamaterial anti-reflection layers [18]. The off-axis nature of the fore-optics creates aberrations that can be corrected by de-centering the reimaging lenses. The reimaging lenses remain planar to the stop and are oversized to retain cylindrical symmetry for diamond turning. The final lens focuses light onto a  $32 \times 40$  free-space backshort-under-grid detector array at  $f/1.6$ . The resolution at 200 GHz is  $21'$  and its Airy disk spans approximately six bolometers. The minimum Strehl ratio within the  $6 \times 4.7^\circ$  FOV is 0.97 [40]. PIPER uses a common detector array for all frequencies. Between flights, the VPM throw, band-defining filters, and (when necessary) lenses are swapped. This strategy is facilitated by a backshort that is optimized for 200 GHz and is less efficient at high frequencies where the atmosphere and dust emission are brighter. A narrower passband toward higher frequency also limits loading.

### 2.6.7 POLARBEAR-2/Simons Array

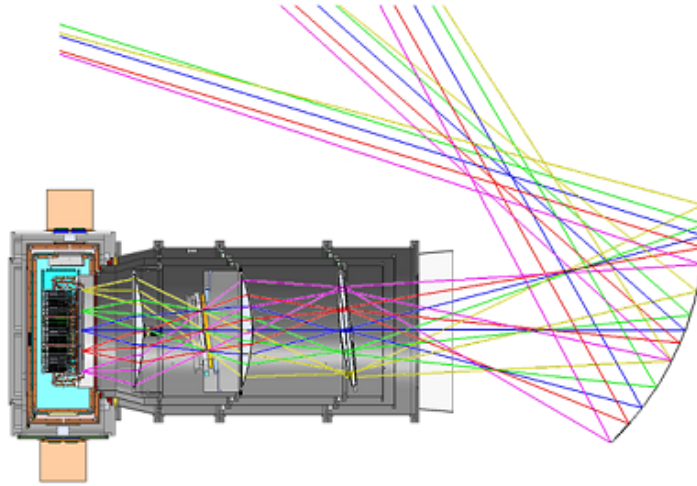


Figure 10: Ray trace of the POLARBEAR-2 and the Simons Array optics. Secondary mirror and cryogenic receiver are shown. The length of the cryogenic receiver is 2 m. The diameter of the three cryogenic lenses are 500 mm.

The three telescopes that comprise the Simons Array are identical off-axis Gregorian designs that utilize a 2.5 m monolithic primary mirror [10]. The telescope and receiver optics are designed to provide a flat,

telecentric focal plane over a wide diffraction-limited FOV. The angular resolution of the telescope is  $5.2'$ ,  $3.5'$ , and  $2.7'$  at 95, 150 and 220 GHz, respectively. Relative positions of the primary mirror and the secondary mirror obey the Mizuguchi-Dragone condition to minimize instrumental cross-polarization [41]. Each telescope has a co-moving shield to prevent sidelobe pickup from ground emission and an optical baffle around prime focus to block stray light from reaching the window and scattering into the receiver. The first telescope comprising the Simons Array — the Huan Tran Telescope — was installed in Chile in 2011 and has been operating nearly continuously with the POLARBEAR-1 experiment since. The second and third telescopes were installed in early 2016.

The receivers have windows made out of laminated 10-inch thick Zote foam. Radio-Transmissive Multi-Layer Insulation and a 2-mm thick AR coated alumina plate are anchored to the 50-K stage as infrared filters [42, 43]. The first POLARBEAR-2 receiver, POLARBEAR-2a, will deploy with ambient temperature continuously-rotating HWPs [44]. The second and third POLARBEAR-2 receivers, POLARBEAR-2b and POLARBEAR-2c, will have cryogenically cooled HWPs at the 50-K stage. All three receivers have three 500 mm diameter alumina re-imaging lenses cooled to 4-K. The high index of refraction of alumina allowed for an optics design with lenses that have moderate radii of curvature. The first lens is a double convex lens, whereas the second and third lenses are plano-convex. The optics design has a cold stop between the second (aperture) lens and the third (collimator) lens. Metamaterial infrared blocking filters and a Lyot stop are mounted at the stop. The final  $f/\#$  of the focal plane is 1.9. The optics design provides diffraction limited illumination that extends over the 365 mm diameter of the focal planes. The Strehl ratio at the edge of the focal plane is 0.95 for 95 GHz and 0.85 for 150 GHz.

### 2.6.8 SPT-3G

SPT-3G is a third generation wide-field trichroic (95, 150, 220 GHz) pixel camera for the South Pole Telescope (SPT), a 10-m off-axis Gregorian telescope first fielded in 2007 [11, 45]. The new optical design features a 4 K Lyot stop with a 7.5 m primary illumination, Strehl ratios  $> 0.97$  at 220 GHz across the  $1.9^\circ$  linear FOV, and angular resolutions of  $1.4'$ ,  $1.0'$ , and  $0.8'$  at 95, 150, and 220 GHz, respectively. The telescope is fitted with a reflective primary guard ring, side shields, and a prime focus baffle to mitigate far sidelobe pickup.

SPT-3G employs a new optical design consisting of a warm 1.8-m off-axis ellipsoidal secondary mirror positioned at the Mizuguchi-Dragone angle [29, 30], a tertiary folding flat mirror, and a single receiver with three 720-mm diameter 4 K plano-convex alumina lenses which serve to form a 4 K Lyot stop and a flat telecentric  $f/1.7$  focal plane (see Figure 11). The usable FOV is limited by vignetting from the lens apertures, not optical aberrations. The 6.8-mm pixel pitch translates into a pixel spacing of  $1.3f\lambda$ ,  $2.0f\lambda$  and  $2.9f\lambda$  at 95, 150, 220 GHz, respectively, and was chosen to optimize mapping speed given readout constraints.

The vacuum window is 600-mm inner diameter HDPE with a triangular-grooved AR coating. IR filters consist of multiple layers of closed cell polyethylene foam behind the window, an alumina IR blocker and metal mesh IR shaders at 50 K, and low-pass metal mesh IR filters at 4 K and 300 mK. The lenses are three-layer AR coated using alumina plasma spray [46] and laminated expanded PTFE.

### 2.6.9 ABS

The ABS telescope consists of 60-cm, cryogenic primary and secondary reflectors in a crossed-Dragone configuration held at the 4 K stage of the receiver (see Figure 12) [5]. This optics design was chosen for

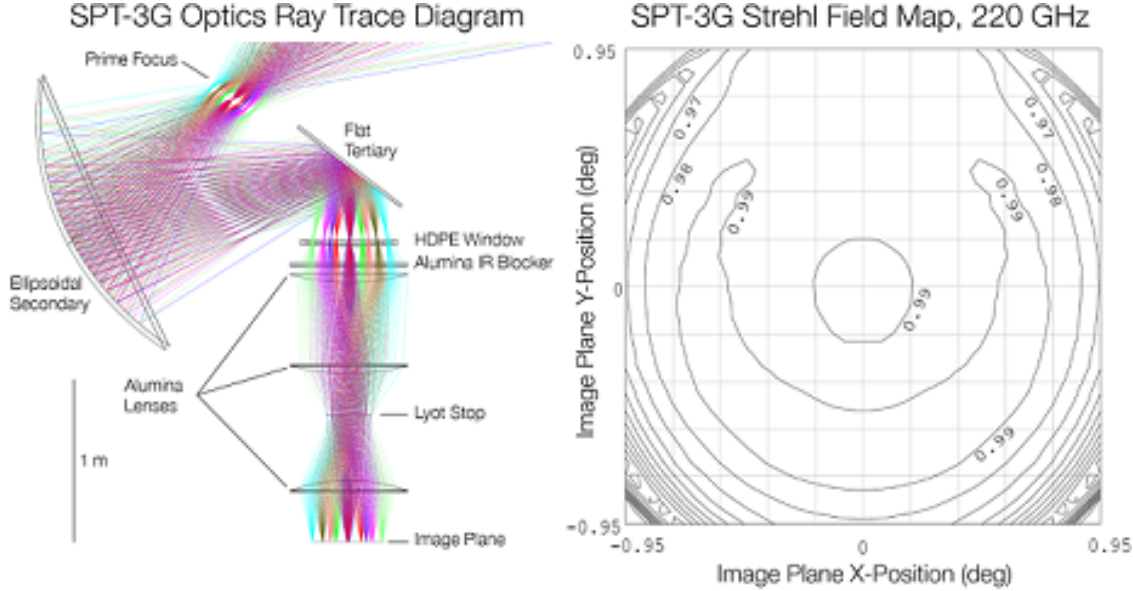


Figure 11: Left: SPT-3G optics ray trace diagram. The new optics include a warm secondary and flat tertiary mirror, and three cold 4 K alumina lenses which serve to form a 4 K Lyot stop and a flat telecentric  $f/1.7$  focal plane. Right: Strehl ratio field map of the  $1.9^\circ$  diameter image plane at 220 GHz. The Strehl ratio is  $> 0.97$  at 220 GHz across the usable 430-mm image plane diameter.

its compactness for a given focal-plane area and low cross-polarization. The reflectors were machined out of single pieces of aluminum. A 25-cm stop at 4 K limits illumination of warm elements. The reflectors couple the 25-cm-diameter array of 240 feedhorn-coupled, polarization-sensitive, TES bolometer pairs (480 detectors) operating at 145 GHz to the sky with  $33'$  FWHM beams over a  $20^\circ$  FOV. The telescope is an  $f/2.5$  system. The polarization directions of the detectors within groups of ten adjacent detectors were oriented to minimize cross-polarization and each group was tilted to minimize truncation on the cold stop. Although neither the orientations of the ten elements within each group nor the orientations of different groups are parallel, the detectors are largely sensitive to polarizations  $\pm 45^\circ$  to the symmetry plane of the optics.

An ambient-temperature, 33-cm-diameter continuously-rotating HWP is placed at the entrance aperture of the receiver [47]. The HWP is made of 3.15-mm-thick  $\alpha$ -cut sapphire AR coated with  $305\ \mu\text{m}$  of Rogers RT-Duroid 6002, a fluoropolymer composite. An air-bearing system provided smooth rotation of the HWP at 2.55 Hz and polarization modulation in the detector timestreams at 10.20 Hz. Infrared blocking is provided by capacitive-grid metal-mesh filters patterned on  $6\ \mu\text{m}$  Mylar with grid spacings of 150 and 260  $\mu\text{m}$ , along with absorptive 2.5-cm PTFE filters AR coated with porous PTFE at 4 K and 60 K. A 0.95 cm Nylon filter AR coated with porous PTFE at 4 K provides additional filtering below 1 THz. The receiver has a 3-mm thick UHMWPE vacuum window AR coated with porous PTFE. A reflective baffle, shown in Figure 12, and a co-moving ground shield reduce ground pickup.

### 2.6.10 QUIET

QUIET was a crossed-Dragone telescope and receiver sited in Chile with 1.4 m diameter mirrors [6, 48]. It operated with 42 and 90 GHz receivers using corrugated feedhorns (19 and 91 feeds, respectively) and no

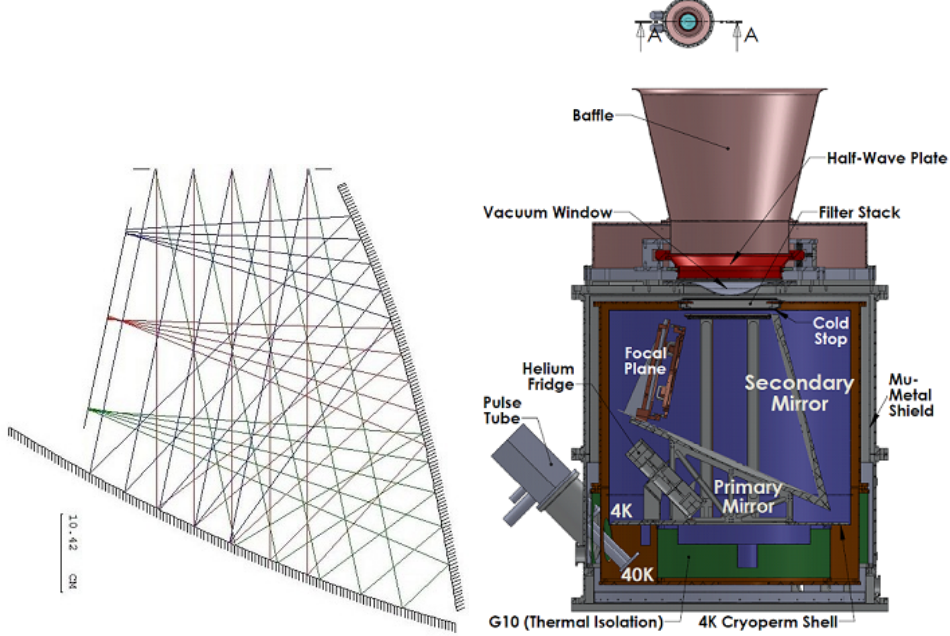


Figure 12: Left: Ray trace of ABS optics. Right: Overview of the ABS Receiver.

tertiary optics. It did not have a stop above the primary mirror; the absorptive entrance aperture was large enough to miss any ray-traced beam from the receiver and only intercepted scattered or strongly diffracted radiation. Above the entrance aperture an absorptive fore-baffle caught several known sidelobes.

At a wavelength of 2.0 mm, the design would give a Strehl  $> 0.8$  across a field size (assuming uniform illumination at  $f/1.65$ ) of about  $6.6^\circ$  half-angle. When considering realistic detector beams the Strehl-limited field size was considerably larger.

The receivers had slow feeds to minimize spillover through the telescope, with FWHM of  $7\text{--}8.6^\circ$  (for the two edges of the 90 GHz band, similar for the 42 GHz band). The resulting beam sizes on the sky were  $0.5^\circ$  for the 42 GHz band and  $0.22^\circ$  for the 90 GHz band. The unvignetted  $f$ -ratio for the 90 GHz receiver's feed locations was 1.65 (full angle  $33.7^\circ$ ), resulting in less than 0.25% spillover for any feed in the 91 pixel 95 GHz receiver (modeled, not measured). The telescope was surrounded by a box of Eccosorb (HR-10 on sheet aluminum, protected by Volara foam), so that all spillover was intercepted at ambient temperature except the small percentage that made it through the entrance baffle onto the sky or back into the receiver itself. The cross-polar response of both the telescope and the feed horns was also exceptional [49]. A larger receiver with 397 identical feeds in the same hex pattern on an unmodified QUIET telescope would reach about 2.2% spillover for the edge feeds. However, redistributing the feed pattern and widening the mirrors out of the plane of symmetry would reduce that number. The design is not Strehl-limited.

The QUIET telescope was operated on the CBI mount, with three axes including boresight rotation.

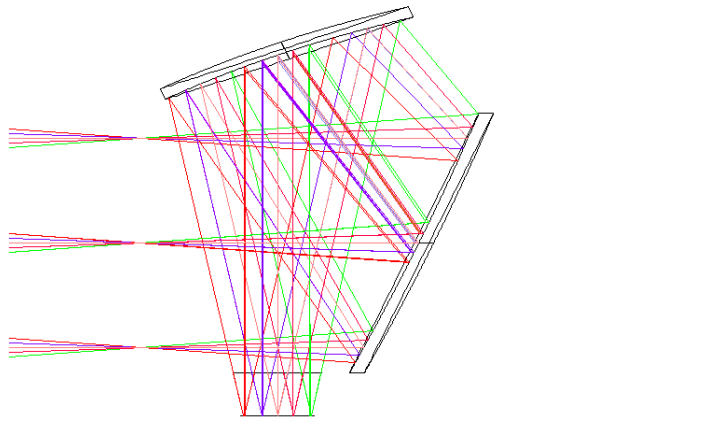


Figure 13: QUIET ray trace.

### 2.6.11 CCAT-prime

The crossed-Dragone telescope design presented in [3] and described in Section 2.3 has recently been adopted by the CCAT-prime project and is being studied in greater detail as a candidate telescope design for CMB-S4. A preliminary CCAT-prime engineering study is shown in Figure 14. This design offers a large increase in diffraction-limited field of view compared to existing large aperture telescopes, with a  $\sim 8^\circ$  diameter usable field of view. The compact nature of this design enables an unusual optical layout in which the elevation axis is aligned with the optical axis between the secondary and tertiary (or between the secondary and the instrument for designs without the flat tertiary), providing a single Nasmyth-like position for instruments. A fixed, flat tertiary can be used to fold the focal plane down, keeping the overall size compact while improving stability for heavy instruments by shifting them down, closer to the azimuth platform. A design without the flat tertiary is also being considered to reduce loading from the optics. The instruments only rotate with the azimuth structure; they are not required to tip in elevation. This simplifies instrument design and allows for implementation of an instrument rotator to help control systematic errors. Due to the symmetric nature of the telescope mount, the bore sight can be flipped on the sky by rotating in elevation beyond zenith ( $> 90^\circ$  elevation, see Figure 14) and coming back around  $180^\circ$  in azimuth. Some baffling is inherent in the structure, as the optics are mounted inside it, and more baffling or a co-moving ground screen would be straightforward to add. A clear advantage of having the optics “buried” inside the mount is lower wind loading on the mirrors as they are effectively inside an enclosure, and elimination of the typical secondary support structure. The design also lends itself to having an integrated shutter to provide protection from weather during poor observing conditions.

## 2.7 Conclusion

The telescope design(s) for CMB-S4 can likely be drawn from the set of existing and new design concepts already available. For each CMB-S4 science goal, telescopes have been demonstrated with good control of systematic errors, although further study and measurements will be required to prove the designs at the sensitivity level of CMB-S4. Large-aperture designs with up to a factor 10 larger optical throughput than

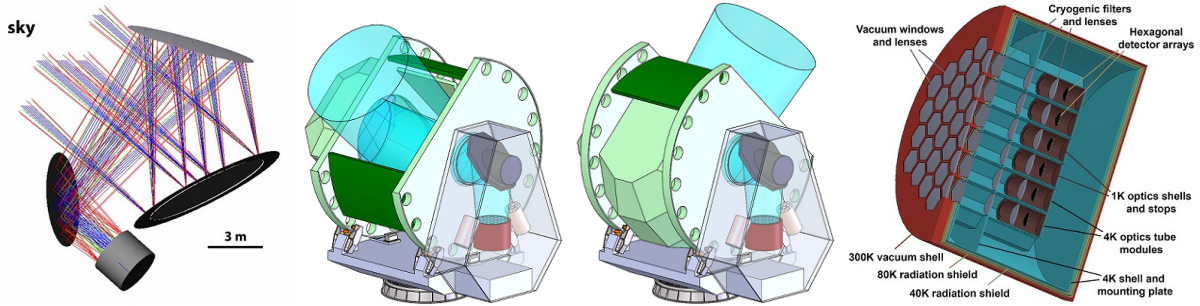


Figure 14: Left: Preliminary high-throughput crossed-Dragone telescope design [3]. The CCAT-prime telescope design evolved from this. Middle pair: A preliminary design for the CCAT-prime telescope provides a 180° elevation range without tilting the cryogenic instruments. This is accomplished by rotating the telescope in elevation about the optical axis between the secondary and flat tertiary; the telescope is shown at 45° and 135° elevation. The extended elevation range enables the equivalent of one telescope boresight rotation at each observing elevation. These two telescope boresight positions could be combined with an instrument rotator that provides arbitrary boresight rotations for the cryogenic instrument. Right: Concept for a CMB-S4 receiver with 50 optics tubes that could each illuminate between 2,000–3,000 detectors, providing more than  $10^5$  detectors on a single telescope.

Stage-III designs exist, and these designs have the potential to greatly reduce the telescope cost for CMB-S4. We have identified a set of studies to improve our understanding of the trade-offs for choosing the final configuration of telescopes for CMB-S4. These studies will feed into a global systems engineering process that will include the relationship of the telescope design with other design choices in areas such as cryogenics, detectors, and readout electronics.



# 3

---

---

## Receiver optics

### 3.1 Introduction

The science requirements for CMB observations are driving rapid progress in millimeter wave optical technology. Unambiguous detection of the B-mode signal from inflationary gravitational waves (IGW) requires broad frequency coverage to handle foregrounds and tight control over beam systematic errors. The need for sensitivity drives the push for high efficiency and wide bandwidth optics to compliment multiband detector technologies. Similarly, polarization modulators can be used to mitigate multiple detector systematic errors that are associated with differences between two orthogonally polarized detectors, and it can also be used to eliminate atmospheric  $1/f$  noise that currently degrades sensitivity on large angular scales where the IGW B-mode signal peaks. The optical and infrared blocking requirements for the system can be met with a combination of technologies including vacuum windows, polarization modulators, IR filters, high index of refraction lenses, and advanced optical coatings.

Stage-II and Stage-III CMB experiments have developed numerous innovative solutions to address these instrumental challenges. Table 3-1 summarizes these receiver optics choices. Advanced ACTPol uses the transparency and high dielectric constant of Silicon to implement receiver optics with broadband lenses and polarization modulators. BICEP3 achieved low optical loading from the cryostat by using simpler single band optics and only instrument rotation as the polarization modulator. POLARBEAR/Simons Array and SPT-3G designed large aperture broadband optics with high purity alumina. POLARBEAR will deploy with

	<b>AdvACT</b>	<b>BICEP3</b>	<b>CLASS</b>	<b>PB/SA</b>	<b>SPT-3G</b>
<b>Window</b>	HDPE	HDPE	UHMWPE	Zotefoam	HDPE
<b>Pol Mod</b>	Silicon HWP + Sky Rot	Instrument Boresight Rot	VPM + Sky Rot + Boresight Rot	Sapphire HWP + Sky Rot	
<b>IR Filter</b>	Silicon MMF	LAIS Alumina Nylon	MMF	RT-MLI Alumina MMF	Zotefoam LAIS MMF
<b>Lens</b>	Silicon	Alumina	HDPE / Silicon	Alumina	Alumina
<b>AR Coating</b>	Meta-Material	Epoxy	Meta-Material	Thermal Spray Epoxy	Thermal Spray Plastic

Table 3-1: Summary of optical elements for ground based Stage-III experiments.

a polarization modulator whereas SPT-3G has no polarization modulator and no sky rotation. CLASS uses plastic lenses with proven performance from past CMB experiments, as well as Variable Polarization Modulators (VPMs), a polarization modulation scheme currently unique to their system. The fact that most of these technologies did not exist five years ago illustrates the vitality of the field. The fact that no two experiments have chosen to use identical technologies illustrates the complexities of optical design. Developing and optimizing these optical design approaches further is a critical goal of the CMB-S4 effort.

In this write up, we survey state-of-the-art optical technologies for CMB polarimetry experiments. This includes windows (Section 3.2), IR filters (Section 3.3), lenses (Section 3.4), coatings (Section 3.5), and polarization modulators (Section 3.6). For this survey, research groups prepared notes on their technologies which give a basic introduction to each technology, descriptions of existing implementations, and suggestions for necessary research and development to achieve the technological readiness required to meet CMB-S4's scientific goals. This survey seeks to present the current technological landscape in order to aid in the development of optimized optical system designs for CMB-S4.

## 3.2 Windows

Receiver windows maintain the cryostat vacuum and maximize the transmission of mm-wave radiation. The first condition requires a robust material and the second requires materials with low dielectric losses and small reflections in the band of interest. The required clear diameter (i.e. the diameter through which light can pass, necessarily smaller than the diameter of any mounting rings or hardware) ranges from tens of centimeters to a meter or more depending on the optical design. In this section we review the state of the art in mm-wave window technology.

### 3.2.1 Polyethylene windows

**Description of the technology** Polyethylene windows maintain vacuum over large ( $> 400$  mm) clear apertures and can be made thin to minimize dielectric losses.

Polyethylene is manufactured in multiple grades, broadly divided into 3 categories: low density (LDPE), high density (HDPE), and ultra high molecular weight (UHMWPE). These have similar and somewhat overlapping physical and optical properties.

**Demonstrated performance** UHMWPE has high impact strength allowing for the use of very thin sheets as windows which minimizes absorption losses without sacrificing strength. Absorption loss is often quoted as loss-tangent  $\tan \delta = \epsilon_i/\epsilon_r$  which is the tangent of the angle between the real and imaginary components of the dielectric function. UHMWPE has a loss tangent,  $\tan \delta < 3 \times 10^{-4}$  at 150 GHz [50], and lab measurements of the windows built for SPIDER show that the mm-wave photon scattering is less than 1% for those windows. Additionally, UHMWPE has a relatively low refractive index,  $n = 1.525$ , allowing simple anti-reflection coatings with expanded Teflon glued with LDPE to be effective over wide observing bands [48,51]. Because the windows are thin, they plastically deform when holding a vacuum. This deformation occurs the first time vacuum is pulled on the windows. For the windows used on SPIDER there was no measurable creep after 48 hours under vacuum, even after repeated pressure cycles. Figure 15 shows a cross-sectional view of a window that successfully held vacuum for three months. It was then cut in half for visual inspection, but no signs of damage were found. For lab testing and deployment, the windows were mounted on the cryostat in a recessed structure, and a cross sectional view of a window assembly is shown in Figure 15. UHMWPE has a low coefficient of friction, making it difficult to hold the windows in place with clamping force alone. To provide additional gripping force, concentric teeth were milled into the clamp which push into the plastic material, as shown on the right of Figure 15.

The QUIET Q-band and W-band vacuum windows were composed of Teflon-coated UHMWPE [48]. The cryostat windows were 22 inches in diameter. Multiple tests proved that 2 mm thick UHMWPE could withstand multiple cycles with 75 mm of bowing. The Teflon coating was adhered by melting a layer of LDPE between the Teflon and the UHMWPE in a large vacuum chamber and pressing the materials together. The UHMWPE thickness was chosen from commercially-available stock (6.35 mm for W-band, 9.53 mm for Q-band) to be close to an integer wavelength in the material. The QUIET window was anti-reflection coated with expanded Teflon (Zitex) because it has a well-matched index of refraction ( $\sim 1.2$ ) for an anti-reflection coating for polyethylene, and the required thickness of  $\lambda/4$ . All windows and coatings maintained physical integrity during receiver testing in the laboratory and 1-2 years of deployment in Chile.

The calculated reflection coefficients gave transmission minima of 84% for uncoated windows, while the Teflon AR-coated window has minimum transmission of 95% for the W-band window and 98% for the Q-

band window. The absorptive losses increase the noise temperature by 4 K for the W-band window and 3 K for the Q-band window. The reflection values for the coated windows were confirmed in VNA tests of small samples, and the noise temperature value was confirmed in laboratory measurements by placing a second window in front of the receiver. Finally, GRASP<sup>1</sup> simulations were performed to estimate the level of induced polarization from the curvature of the window. For the QUIET window, the central feedhorn had negligible instrumental polarization while the off-center pixel had instrumental-polarization induced by the window curvature of 0.01%, occurring only at the edge of the bandpass.

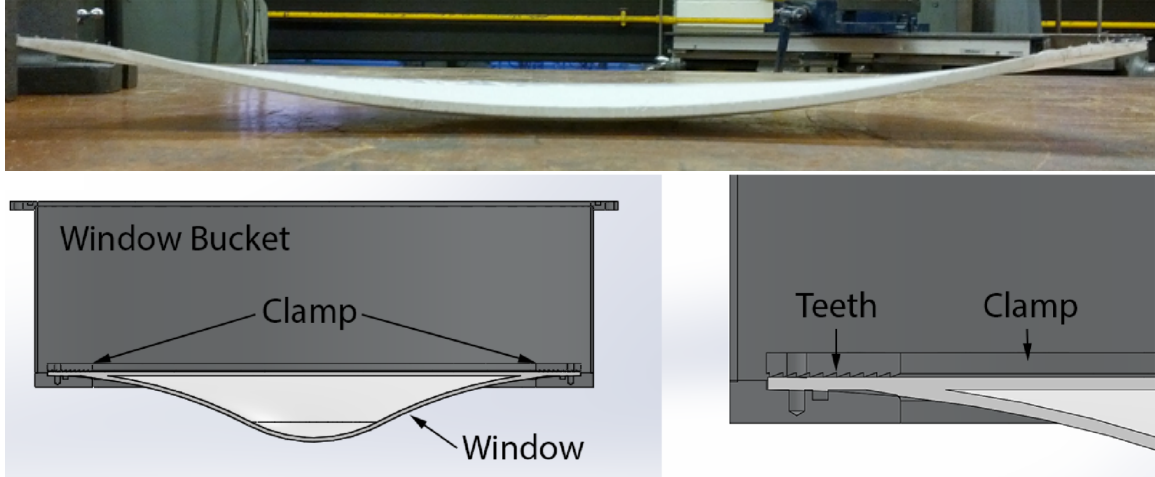


Figure 15: (Top) A window sliced in cross section after 3 months of continuous use. (Bottom) On the left is a cross section of the window bucket which holds the UHMWPE window. The window is held down using the clamp ring which is screwed into threaded holes at the bottom of the window bucket. On the right is a zoom in on the interface between the clamp and the window. Note the teeth milled into the clamp ring. AR coating not drawn.

HDPE is also used as vacuum window by CMB experiments. The BICEP3 team considered both UHMWPE and HDPE for the receiver window. The window was required to be thick enough not to bow down into the volume occupied by the nearby infrared thermal blocking filters. Testing showed that HDPE and UHMWPE had similar performance (the former's slightly higher room temperature absorption was offset by its slightly higher stiffness and strength), so HDPE was chosen as it had been used within the collaboration for lenses (BICEP, BICEP2, Keck Array). The window is a conservative 31.75 mm thick, with a span of 684.53 mm. It bows under vacuum by  $\sim$ 35 mm. The AR treatment is the same as described above, although a different source for the ePTFE was chosen since Porex (described in Section 3.5.1) is not wide enough to cover the clear aperture in one sheet-width.

The BICEP3 window was designed to be conservatively thick to be robust and reliable, but it therefore contributes a measured  $\sim$ 6 K of in-band loading. Plans are in place to replace it with a thinner window, following on the successful SPIDER and QUIET experience.

**Prospects and R&D path for CMB-S4** A “catenary” style window like SPIDER and QUIET could in principle be linearly scaled to larger aperture diameters. The window material is under nearly pure tensile stress, and if the thickness increases along with the diameter (and circumference), the same (scaled) bowing should be seen and the same maximum material stresses should result. This natural scaling means that in

<sup>1</sup>Commercially available software for electromagnetic simulations, <http://www.ticra.com/products/software/grasp>.

principle a new material is not required to increase to a larger diameter. As with the currently deployed windows, careful design of the supporting ring and gripping mechanism will be necessary.

Other polyethylene variant materials may prove useful, given that the plastics industry continually develops new materials. Polyethylenes with embedded high-strength fibers may also prove interesting if the index of refraction of the fibers is sufficiently close to that of the polyethylene to minimize scattering. Investigating these options would require a modest dedicated effort to procure samples and test them both optically and mechanically. Further investigations that could be carried out are measuring the polarization qualities of highly stressed polyethylene to determine the expected instrumental polarization contribution, and understanding any potential changes in optical properties over time and/or with ambient and temperature.

The technology status level of the solid plastic window is 5. QUIET and the series of BICEP experiments has analyzed data taken with plastic windows. Many Stage-III experiments deployed with solid plastic windows.

The production status level of the solid plastic window is also 5. As mentioned above, design can be challenging. But once design is complete it can be manufactured in large quantity. Plastic is readily available commercially, and industrial machining can be utilized to fabricate machined part quickly.

### 3.2.2 Zotefoam windows

**Description of the technology** Closed-cell foam has been considered as a window material for microwave and radio receivers since as early as 1992 [52]. The first foam CMB receiver windows used Zotefoam PPA-30 (Zotefoams PLC, Croyden, UK), a polypropylene based foam, expanded with nitrogen gas ( $N_2$ ). Zotefoam has been used on CMB receivers ACBAR, BICEP, BICEP2, Keck Array, POLARBEAR-1, SPT-SZ, and SPTpol. In recent years, since the supply of PPA-30 dwindled given a halt in manufacture, HD-30 has been used, which is based on high density polyethylene.

**Demonstrated performance** PPA-30 and HD-30 have substantial appeal given (i) their very high transparency in the mm band, and (ii) their near-unity indices of refraction, eliminating the need for anti-reflection treatment. The practical diameter limit is of order 500 mm, approached by the POLARBEAR-2 receiver, due to the low modulus of elasticity and strength. For example, the POLARBEAR-2 receiver uses  $\sim$ 200 mm thick laminated HD-30 Zotefoam. The low thermal conductivity of Zotefoam also helps cryogenic receiver performance, with the cold side of a foam window cooling to of order 200 K or less.

**Prospects and R&D path for CMB-S4** At higher frequencies PPA-30 (and presumably HD-30) becomes lossy [53], suggesting more limited application for broadband or high frequency instruments. The scattering of the material is significant enough that SPT-3G and BICEP3 (2017 season) will both use HD-30 as a low-pass FIR filter (i.e. the RT-MLI filters described in Section 3.3). Smaller cell foam could reduce scattering losses, but its mechanical strength is not as strong as commonly used HD-30. With current commercially-available foam thicknesses, multiple laminated layers of foam are required to hold vacuum on a window of  $\sim$ 200 mm diameter or greater. These laminations provide a mechanical advantage, but are known to increase loss at higher frequencies. The ideal foam material for a receiver window would be a thick closed-cell foam without lamination. Both the use of smaller cell size and the elimination of lamination would lead to lower scattering losses.

The technology status level of the Zotefoam window is 5. Many Stage-II experiments used the Zotefoam windows.

The production status level of the Zotefoam window is also 5. As long as foam thickness is less than 10 inch, it can be purchased commercially. Cutting foam into desirable shape can be done easily. Making window from the Zotefoam requires epoxying the foam to metal frame. It is a simple process that can be parallelized to fabricate large quantities of windows simultaneously.

### 3.3 Filters

CMB detectors are subject not only to in-band photon loading, but also to radiative IR loading from warm optical elements such as the window, lenses, and telescope and receiver structures. The in-band contribution increases photon noise on the detectors, reducing mapping speed. Additionally, there may be loading from the cold stages which could compromise the bath temperature seen by the detectors, or reduce the efficiency or duty cycle of the sub-Kelvin cooler that maintains the bath temperature. Various reflective and absorptive optical filter technologies are employed in current CMB experiments to mitigate this infrared radiation from the 300 K, 50 K, 4 K and sub-Kelvin stages. In the case of wideband CMB detectors, the photons of interest might also be selected using optical bandpass filters. Below we review the performance of these filters and the prospects for their use in CMB-S4.

#### 3.3.1 Metal mesh filters

**Description of the technology** For many years mm and sub-mm experiments have employed multilayer metal-meshes embedded in polymeric dielectrics to define detector passbands, reject unwanted optical/near IR (NIR) radiation, and control the thermal environment in cryogenic instruments. By employing several such filters at sequential temperature stages it is possible to reject optical/NIR radiation while maintaining the transmission performance of the filter stack to  $> 80\%$ . These filters are composed of patterned metal-mesh layers which essentially act as reflectors of the high-frequency radiation, thus rejecting thermal power that would otherwise be absorbed, and therefore reducing the thermal loading in the instrument.

**Demonstrated performance** By using multiple layers of inductive, capacitive, or resonant metal mesh patterns and combinations thereof it is possible to achieve high-pass, low-pass, and band-pass optical filtering, respectively [54–56]. Heritage from lab measurements, and modeling with commercial software (e.g., HFSS and CST), enables precise filter design. The technology for all such filters relies upon highly accurate and reproducible photolithography performed on Cu layers on a polypropylene substrate, with standard patterns composed of elements with feature sizes ranging from 1 to 1000  $\mu\text{m}$  or greater. The basis of a composite filter is the accurate embedding of many such metal-mesh layers (typically 6 to 12) within a solid polypropylene disc, through a hot-pressing technique. The same technology has been used to produce filters for operation from 30 GHz to 25 THz. Good band-pass filters and dichroic beam splitter performance can be achieved over an octave, whereas other devices (low- and high-pass filters) can perform excellently in transmission or reflection over much broader ranges. Photos of several metal-mesh devices are shown in Fig. 16, and lab spectral measurements are shown in Fig. 17. The devices are stable and robust and have been cryogenically-qualified for wide use in space and suborbital missions. Finally, high-pass filters can be installed just above the detectors at the focal plane to mitigate radio-frequency interference originating outside of the receiver.

Thermal filtering of optical/NIR radiation is needed for cryogenic instruments to minimize the cryogenic cooling requirements. Here it is vital to reject as much excess heat from the cryogenic chain as early as possible, since the re-emission of heated dielectric components in the optics would lead to excess thermal loading onto the detectors. A combination of very thin scattering and single-layer metal-mesh devices have been designed, built, and deployed at various temperature stages to reject optical and NIR radiation. The porous material scatters most of the incident optical/NIR radiation for wavelengths equivalent to the pore size of the material, while the metal mesh reflects longer NIR wavelengths. As a result the composite device maintains high transmission ( $> 95\%$ ) for mm-waves. The in-band millimeter wave absorption loss in these devices is typically  $\ll 1\%$  [57].

**Prospects and R&D path for CMB-S4** CMB receivers are using larger detector arrays, necessitating larger-diameter optics and filters. Metal mesh filters can currently be manufactured with excellent uniformity and reproducibility with an optically-active diameter up to 300 mm. Expansion of fabrication capability up to 530 mm diameter is under way for Stage-III experiments [58]. CMB-S4 is likely to require receiver optics and filters of diameter  $\sim$ 500–1000 mm. To increase metal-mesh filter diameter further, R&D is necessary and should include establishment and verification of high-fidelity photolithography and uniform thermal pressing of multilayer metal-mesh structures up to 1000 mm diameter. No major technical challenges are foreseen for this R&D effort.

The technology status level of the metal mesh filter is 5. Every Stage-II and Stage-III experiments has been deployed with some metal mesh filters.

The production status level of the metal mesh filter is 3. Many metal mesh filters were produced for Stage-II and Stage-III experiments, but request for metal mesh filter production the production needs have been spread out over time. Depending on receiver design for CMB-S4, the project may require a large number of metal mesh filters in short a amount of time.

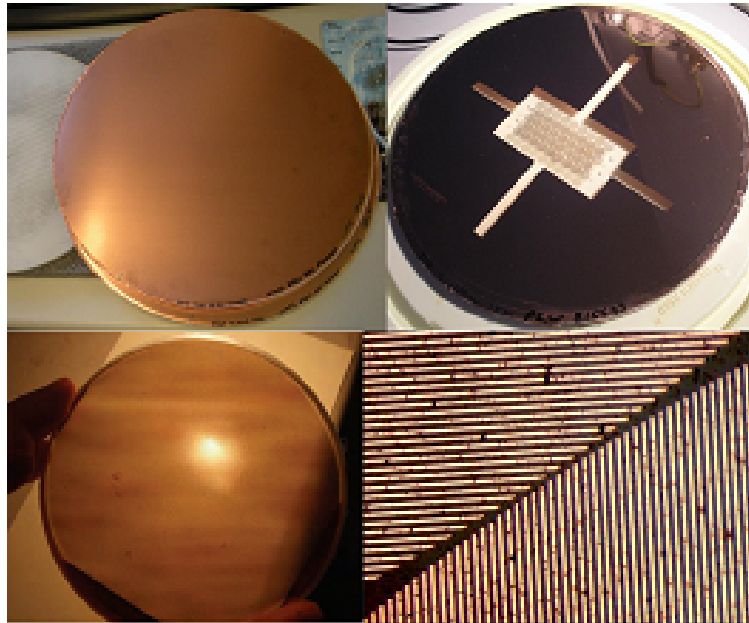


Figure 16: Top left: two hot-pressed low-pass filters; top right: photolithographed polarizers used in BLASTPol; bottom right: macro detail of BLASTPol polarizers; bottom left: metal-mesh HWP.

### 3.3.2 Laser-ablated infrared blocking filters

**Description of the technology** An alternative technique to photolithography for metal mesh filter fabrication is laser ablation, which is a standard industrial process. In this approach, a single- or double-sided metal-coated dielectric such as aluminized Mylar or copperized BOPP film is mounted on a precision XY linear translation stage. A 355 nm NdYAG laser with a beam waist of  $\mathcal{O}(10)$   $\mu\text{m}$  is focused on the metal and pulsed at  $\mathcal{O}(100)$  Hz. The translation stage controller moves the substrate while the laser pulses to ablate away lines of metal in the two perpendicular axes, leaving behind metal squares on the dielectric

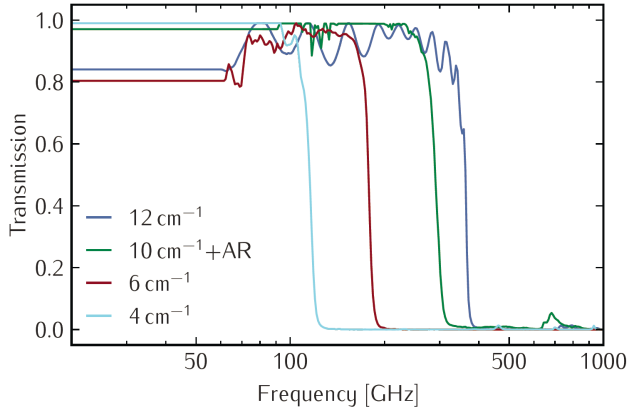


Figure 17: Typical measured transmission coefficients at 300 K for a series of hot-pressed low-pass filters. For clarity, the data has been extrapolated with a horizontal line below the minimum measurement frequency.

substrate [59]. A typical pattern of  $40\text{ }\mu\text{m}$  squares separated by  $15\text{ }\mu\text{m}$  spacing achieved using this technique is shown in Figure 18 and has a reflection resonance around 1 THz.

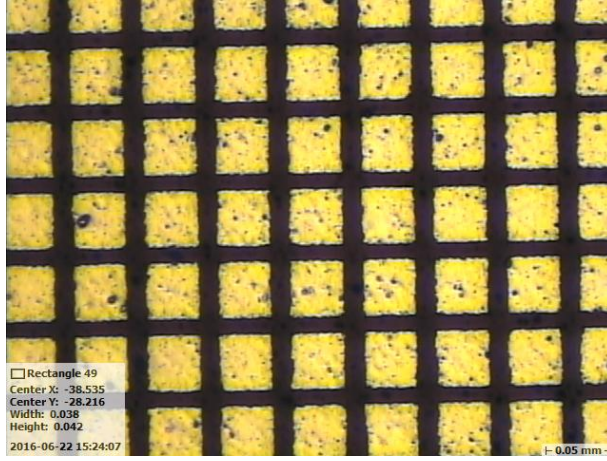


Figure 18: Microphotograph of laser-ablated metal mesh features on infrared shaders. Squares are  $400\text{ nm}$ -thick aluminum  $40\text{ }\mu\text{m}$  on a side with  $15\text{ }\mu\text{m}$  pitch.

**Demonstrated performance** Laser-ablated FIR shaders with optically-active diameters of  $\sim 600\text{ mm}$  were successfully fabricated and used in BICEP3 [19]. Installing a stack of these filters at ambient temperature leads to an  $\sim 85\%$  reduction of IR power absorbed by the second-stage absorptive alumina filter. The filter stack consisted of ten  $3.5\text{ }\mu\text{m}$ -thick Mylar filters with  $400\text{ nm}$ -thick aluminum squares of side  $40\text{ }\mu\text{m}$  on a  $15\text{ }\mu\text{m}$  pitch. In-band mm-wave transmission of  $\sim 98\%$  and reflection of  $\sim 1.5\%$  was measured at 95 GHz.

**Prospects and R&D path for CMB-S4** 800 mm optically-active diameter shaders are currently in fabrication for SPT3G [11], and diameters of up to 1 m are possible without significant technical challenges. Laser ablation provides a solution for fabrication of large-area metal mesh filters where feature sizes smaller

than  $\mathcal{O}(10)$   $\mu\text{m}$  are not necessary. This technique has not been demonstrated with sufficient feature tolerance for use in band-defining filters where  $\mathcal{O}(1)$   $\mu\text{m}$  tolerance is necessary. Beam-waist shaping of the laser could improve filter tolerances. Additionally, a program of IR and mm-wave measurements of transmission, reflection, and loss will be necessary to validate the choice of technology for CMB-S4.

The technology status level of the laser ablated filter is 5. The laser ablated aluminum filter was deployed for a single color receiver in BICEP-3.

The production status level of the laser ablated filter is 3. Aluminized mylar and laser ablation are done commercially, and in principle the technology is scalable. No explicit steps were taken to demonstrate mass production, thus PSL of 3 is assigned.

### 3.3.3 Nylon and Teflon filters

**Description of the technology** Nylon and Teflon (DuPont, trade names; generically, a class of polyamide, and polytetrafluoroethylene or PTFE, respectively) have strong absorption in the THz and IR region, yet acceptable transparency to mm-waves, making them useful for absorptive IR filtering [32]. Teflon has a higher frequency cutoff and also higher mm-wave transparency and thus has often been used as a first stage filter, held at 77 K or some other intermediate temperature. Nylon has a lower frequency cutoff but also higher in-band losses, so it is generally used on colder stages [60].

**Demonstrated performance** Several CMB receivers have used one or both of these filter materials in lab and on the sky. BICEP, BICEP2, and Keck Array, for example used thick PTFE filters at the intermediate stage and thin Nylon filters at the 4 K stage [61]. The thickness of the PTFE filters was driven by the need for thermal conductance to carry the heat out, and not by the optical opacity at high frequencies. BICEP3 exchanged the PTFE filters for an alumina filter given its higher thermal conductivity, but still had two Nylon filters [62]. POLARBEAR, on the other hand, used a porous PTFE filter in combination with mesh filters, its waveplate, and its Zotefoam window for thermal IR blocking [63].

SPIDER uses a 2.8 mm thick Nylon 6/6 filter mounted at 4 K and located just skyward of the primary lens. Nylon 6/6, one of commercially available type nylon, was selected for its excellent balance of strength, ductility and availability. This filter has a clear diameter of 285 mm and is AR coated with Porex ePTFE (expanded Teflon) using the LDPE vacuum bonding technique described in Section 3.2.1. The induced polarization was constrained to be less than 1% by warm 90 GHz measurements in samples of Quadrant extruded Nylon 6/6, Quadrant cast Nylon 6, and Tecamid extruded Nylon 6/6. Although a second Nylon filter was considered for SPIDER’s 30 K stage, it was not used for flight because of the potential for high emission due to poor heat sinking and the redundancy of the filter stack [64].

**Prospects and R&D path for CMB-S4** The limited thermal conductivity of plastic means that the center of a large-diameter plastic filter can be heated by its absorption of the incident IR radiation, causing the filter itself to re-radiate. This makes it difficult for these filters to manage IR power for larger receivers. This absorbed power also loads the cryogenic cooling system. In contrast, reflective and/or scattering filters reject the incident power back to the outside of the cryostat, meaning these filters have a cryogenic advantage for large filter diameters. To design for and control these effects, accurate measurements of the frequency-dependent absorption and thermal conductivity of these materials are needed.

The technology status level of the plastic filter is 5. Many Stage-II experiments used plastic filters. For example, series of BICEP receivers used both teflon and nylon filters to reduce infrared loading successfully.

The production status level of the plastic filter is also 5. Large quantity of plastic can be easily purchased from vendors. It simply needs to be cut to necessary diameter. Also its low dielectric constant makes application of AR coating simple.

### 3.3.4 Alumina IR filters

**Description of the technology** Alumina IR filters are attractive for CMB experiments due to the high mm-wave transmission, high IR absorption, and high thermal conductivity of alumina at cryogenic temperatures. In particular, the high conductivity prevents the center of the filter from heating when loaded with incident radiation. Standard industrial manufacturing processes can be used to make filters that are larger than 1 meter in diameter. The optical and thermal properties, as well as the commercial availability of large diameter plates make alumina a promising IR blocking filter candidate for future CMB experiments.

**Demonstrated performance** The current state-of-the-art alumina manufacturing process can produce alumina with a loss tangent less below  $10^{-4}$  at 100 K. Measurements in [43] show >95% transmission at 95 and 150 GHz in bands with 30% fractional bandwidth, limited by the AR coating and not the loss tangent. Multiple methods for AR coating alumina are discussed in Section 3.5. Alumina has high IR absorption with a rapid cutoff frequency near 1 THz. The high thermal conductivity of the material ( $\sim 100$  W/m·K at 50 K, roughly three orders of magnitude greater than PTFE) allows for a smaller temperature gradient across the filter, even when placed near the cryostat window. For example, a 50 K alumina IR filter design of 2 mm thickness and 500 mm diameter for POLARBEAR-2 has a measured temperature gradient of <6 K between the center and edge [43]. Lastly, the technology should be scalable in size, since companies have been identified that can make alumina plates larger than 1 meter in diameter.

BICEP3, POLARBEAR-2, and SPT-3G use alumina absorptive IR filters at 50 K [11, 19, 65]. These experiments apply the same AR coating between alumina reimaging lenses and alumina IR filters to maximize mm-wave transmission while efficiently absorbing IR photons. Figure 19 shows the measured absorptive performance of a one-layer AR-coated, 2 mm thick alumina IR filter, with a 3 dB cutoff frequency of 450 and 700 GHz at 300 and 30 K respectively.

**Prospects and R&D path for CMB-S4** In-band transmission and out-of-band absorption have both been shown to vary with different alumina powders. This means that continuing to explore various powder compositions may further improve the performance of alumina filters.

The technology status level of the alumina filter is 5. The alumina filter was deployed for single color receiver in BICEP-3, and it was deployed for multichroic operation in SPT-3G. Alumina filter is also being prepared for POLARBEAR-2 for dichroic operation.

The production status level of the alumina filter is 3. Alumina plates are available from commercial companies with high throughput production rate. Application of broadband anti-reflection coating may become throughput limiting aspect of the technology. There are R&Ds for rapid application of broadband AR coating as discussed in Section 3.5.

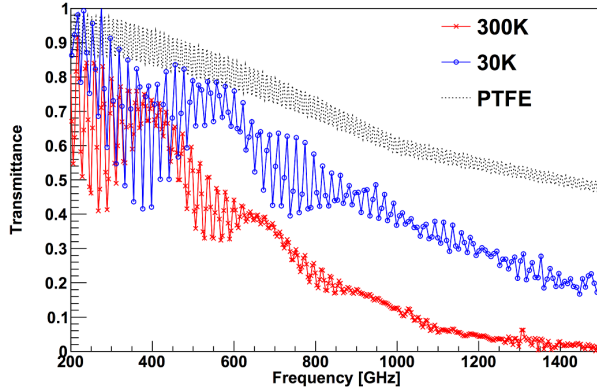


Figure 19: Measured spectra of a 2 mm thick IR filter with a single-layer AR coating at 300 K (red) and 30 K (blue). For comparison, a calculated spectrum for a 20 mm thick PTFE filter is also shown [43].



Figure 20: Photographs and an overview drawing of a silicon-substrate composite filter. In the filter pass-band the metamaterial AR coated silicon couples light into and out of the filter stack from free space. In the stop-band, a set of lithographically patterned reflective metal features reflect a significant portion of the incident light, and an absorptive and scattering layer of optical epoxy loaded with powdered Reststrahlen materials blocks much of the remaining light.

### 3.3.5 Silicon substrate filters

**Description of the technology** A silicon substrate infrared filter is a hybrid filter based on reflective frequency-selective structures patterned on silicon substrates, scattering/absorptive layers consisting of crystal powders embedded in an epoxy binder, and metamaterial AR coatings to reduce in-band reflections from the vacuum-silicon interfaces.

Figure 20 shows a conceptual drawing and photographs of a composite absorptive/reflective IR-blocking filter. Proceeding from top to bottom, the first surface is a groove metamaterial AR coating cut into a silicon wafer. A lithographically-defined frequency-selective surface is patterned on the bottom of this wafer. Below that is a  $\sim 25 \mu\text{m}$  layer of an absorptive mixture of epoxy and Reststrahlen (frequency selective reflective) powders. Finally, below that is another frequency-selective surface, patterned on another silicon wafer, with another groove metamaterial AR coating cut into the very bottom of the entire stack. At

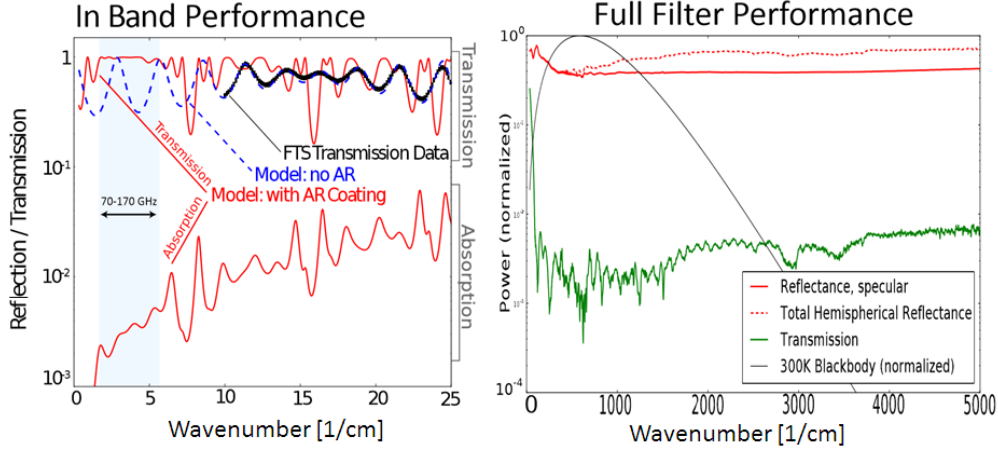


Figure 21: Measured and calculated performance of composite filter parts. Left: The measured (black dots), and simulated (blue dashed) low frequency performance for a single  $75\ \mu\text{m}$  layer of Reststrahlen powder mix, in epoxy, on a silicon wafer. Additionally shown are the best fit simulated performance (transmission and absorption) for a stack consisting of AR coated silicon on either side of a  $75\ \mu\text{m}$  powder mix layer. The target transmission band for the AR coating is 70-170 GHz and is marked with the blue band on the plot. Right: The IR blocking performance of a full composite filter is shown, with a 300 K blackbody overlaid.

IR wavelengths, light is reflected off the front silicon wafer and the frequency selective surface. The front metamaterial surface specularly and diffusely scatters light at frequencies above the single-moded limit of the metamaterial structure. IR light not reflected by the metal mesh is subject to both scattering and absorption by the powder-epoxy composite layer. The second metal-mesh layer reflects most of the remaining light back into the epoxy-powder layer, boosting absorption and (to a lesser extent) reflection. This approach reduces the load on the cryogenic stage by reflecting a significant portion of the IR power, and also uses an absorbing layer to further attenuate IR power passing the first reflective layer even at non-normal incidence angles.

At mm- and sub-mm wavelengths the frequency-selective surfaces have high transmission, and since the absorbing layer is much thinner than a wavelength it has low in-band absorption [18].

**Demonstrated performance** The performance of composite filters was evaluated using Fourier transform spectrometer (FTS) measurements, as well as integrated measurements made with a disk bolometer in a cryostat receiving radiation from a 300 K blackbody. The IR blocking performance of these filters was measured on an FTS up to 150 THz, giving a full characterization of the transmission across the spectrum of a 300 K blackbody. In these measurements, the composite filter specularly reflected  $>40\%$  of the light incident from the 300 K blackbody (indicating reflection off the front silicon surface and metal mesh features), and diffusely reflected another  $\sim 10\%$ , indicative of backscattering off the powder layer. It transmitted  $<1\%$  of the 300 K blackbody in FTS tests, and  $<2\%$  in an integrated cryostat test, confirming excellent IR blocking performance.

The low frequency performance of a  $75\ \mu\text{m}$  layer of the powder filter component was measured down to 300 GHz using an FTS. These data were then fit with a simple transmission line model. This model was then used to extrapolate down to the mm-wave band and to simulate the effect of adding a three-layer antireflection coating. This model shows that the filter introduces minimal loss (dominated by the epoxy

carrier) in a signal band from 70-170 GHz, and that an instrument-band transmission of >99% should be achievable for a filter using this technology with the total transmission limited by the AR performance.

It is a known phenomenon that some Reststrahlen materials have absorption that significantly decreases when the material is cooled down. In particular, alumina ( $Al_2O_3$ ) is known to have a section of its absorption band (between 30 and 300 microns) that decreases at temperatures of tens of Kelvin [66, 67]. A powder filter consisting of a mixture of calcium carbonate ( $CaCO_3$ ) and magnesium oxide ( $MgO$ ) was measured in an FTS at a range of temperatures between 4 K and 300 K to confirm that there is not a significant performance change upon cooling. An integrated test of the composite filter performance was carried out in a cryostat, to measure the total blocking efficiency of a 150 mm diameter prototype. For this filter, there was no measurable heating when the filter was cooled to 20 K and used to block the power from a 70 mm diameter window open to 300 K. In this configuration, the power deposited on a carbon disk bolometer at  $\sim 5$  K was measured, and this measurement yielded the lower limit that at least 98% of the ambient 300 K blackbody radiation was blocked. This limit is in agreement with the FTS measurements of the full composite filter.

**Prospects and R&D path for CMB-S4** In addition to forming effective free-space IR blocking filters, this filtering approach offers several novel possibilities for silicon-substrate optical elements. Lower frequency-selective metal elements can be incorporated into these filters to aid in defining the instrument signal band. These filters can also be easily and inexpensively integrated into other optical components, such as silicon lenses.

To scale this technology for CMB-S4, demonstrations of a full scale prototype, of merging this approach with a silicon lens, and of band defining filters are required. Also diffraction and scattering from these filters should be explored for wider frequency bands. The first generation prototype filter has smaller than expected reflection of IR power (40% vs 90% predicted). This could be attributed to a near-field coupling of IR power into the absorbing layer. Further study would be helpful to reveal origin of this discrepancy.

The technology status level of the silicon substrate filters filter is 2 and the production status level is 1. Laboratory testings were performed to demonstrate the IR blocking properties of the filter. A filter suitable for deployment in a CMB experiment should be fabricated and demonstrated.

### 3.3.6 Foam based infrared blocking filters

**Description of the technology** Foam based infrared blocking filters, such as stacks of Zotefoams and radio multi-layer insulation (RT-MLI)-based filters are constructed using commercially-available thermally-insulating foam [68]. The insulator is transparent to mm-waves but absorptive to IR radiation as shown in Figure 22. The working principle is similar to conventional aluminized-Mylar multi-layer insulation (MLI) used for cryostat thermal isolation. Heat sinking to a cryogenic stage is not required for this filter to work effectively, simplifying the installation process.

Figure 22 shows the working principle of the RT-MLI filter. A stack of  $N$  isolated layers of the material is assembled, and each intermediate layer is allowed to reach radiative equilibrium. Just as with conventional aluminized-Mylar MLI, to first order this has the effect of reducing the thermal radiation by a factor of  $N+1$ . When the simplified formula is compared to measured load on the RT-MLI, the measured radiation tends to be even smaller than predicted by this formula because of thermal gradients inside each layer. A more accurate model [68] can be built by simultaneously solving  $N+1$  coupled equations for radiative equilibrium between the layers, and accounting for the thermal gradients inside each layer.

Since RT-MLI filters do not rely on heat sinking to a temperature stage, or on thermal conduction radially across filter layers, the filters should work as well for large-aperture systems as for small-aperture systems. Therefore, RT-MLI is naturally suitable for large-aperture systems, a major advantage for future CMB receivers. Because this technology relies on passive cooling, maximum performance is obtained by attaching the RT-MLI on the cold side of the space between two surfaces.

**Demonstrated performance** In general, any material that is transparent to radio frequency but opaque to infrared radiation can be used as a filter material. The low index of refraction of foamed polystyrene makes an anti-reflection coating unnecessary. Figure 22 shows measurements of 2 mm layers of this material, verifying its performance as an effective IR blocking filter. The transmission through an  $N$ -layer stack of this material is approximately  $0.997^N$  at 200 GHz, i.e., 97% in the case of 10-layer RT-MLI stack. So far, GroundBIRD [69], and the POLARBEAR-2a receiver for the Simons Array [65] employ this technique. GroundBIRD uses RT-MLI with a metal mesh filter in a 300 mm aperture in the space between the 300 K window and the 50 K filter, as well as in the space between 50 K and 4 K. POLARBEAR-2a uses RT-MLI behind the vacuum window (500 mm diameter). RT-MLI is also used at SRON, RIKEN, and NAOJ, in laboratory test cryostats. In addition, KUMODES uses RT-MLI for a cryostat that houses a cold calibration source [70].

**Prospects and R&D path for CMB-S4** RT-MLI is expected to work equally well for large apertures, but building larger diameter systems to test their cryogenic performance will be informative. Evaluations of the performance of different RT-MLI materials, studies to determine the optimal number of foam layers, and further development of stack assembly techniques are some additional developments that are required to develop this technology further for CMB-S4.

The technology status level of the foam filter is 3. Foam filter deployed in SPT-3G receiver. It is also implemented in POLARBEAR-2 and GroundBIRD receivers.

The production status level of the foam filter is 5. Foam used for foam filters is available commercially. No AR coating is required because of its low dielectric constant. Also cutting foam into required diameter is very easy and fast.

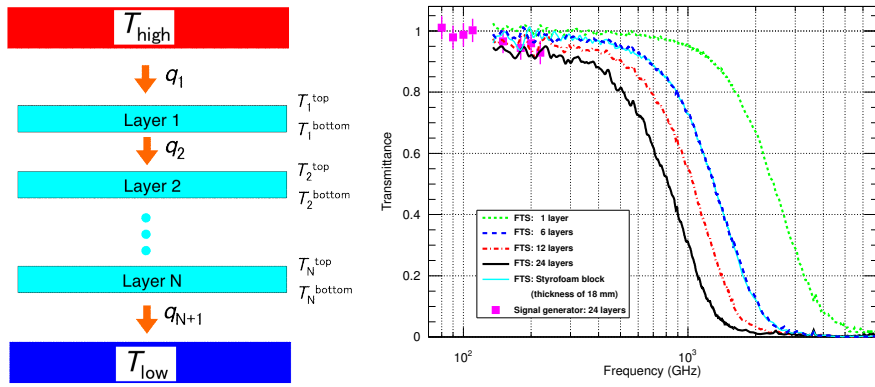


Figure 22: Left: Conceptual drawing showing the principle behind RT-MLI. The exchange of thermal radiation between each intermediate layer is balanced, and thermal gradients develop within each individual layer. These two effects permit each layer to have a colder bottom side, and to float to successively lower temperatures, reducing the heat flow from  $T_{\text{high}}$  to  $T_{\text{low}}$  by at least a factor of  $N + 1$ . Right: Measured transmission of RT-MLI at room temperature. Using an FTS, we measured four different configurations: the number of layers in each configuration was 1, 6, 12, and 24. We also measured the transmittance of a styrofoam block for comparison. Below the 220 GHz region, the transmission through a 24-layer sample was also measured using signal generators.

## 3.4 Lens material

Multiple design studies have found that high index of refraction lenses ( $n \gtrsim 3$ ) are required for refracting re-imaging optics to realize large fields of view on  $> 3$  m telescopes and to maximize the number of detectors per telescope in fully-refracting telescope systems. This does not imply that plastic lenses (in particular polyethylene) are not suitable for some of the optical components in CMB-S4, but it does mean that the high index materials currently being used in Stage-III telescopes will likely play a role in CMB-S4.

Silicon, alumina, and sapphire are naturally occurring materials which have high index of refraction and low dielectric losses, and for which AR coatings are currently in use and under further development. These materials have trade-offs that drive their use for different applications. Sapphire has extremely low dielectric loss (loss tangent  $\lesssim 10^{-4}$ ) and is available in single crystal pieces up to 510 mm in diameter, but it is birefringent. Its birefringence makes it useful for waveplates, but unsuitable for lenses. Silicon has a high index of refraction ( $n = 3.4$ ) and extremely low dielectric loss (loss tangent below  $7 \times 10^{-5}$ ), but is only available in pieces up to 460 mm in diameter. Alumina also has a high index of refraction ( $n \sim 3$ ), reasonably low dielectric loss (loss tangent below  $1 \times 10^{-4}$ ), and has the advantage that it can be fabricated as a single piece for parts up to  $\sim 0.78$  m in diameter. Alumina's material property could vary depending on impurities and sintering method. Using alumina as optical element requires accurate characterization of actual alumina being used. These differences in performance and availability drive the application of these materials in different optical systems. For example, ACTPol requires lenses only up to 330 mm diameter and uses silicon to take advantage of its machinability and low loss, while BICEP3, SPT-3G and POLARBEAR use alumina since they require larger diameter lenses.

### 3.4.1 Silicon

**Description of the technology** Silicon is an excellent material for the fabrication of millimeter wave optics. It has good strength, a high index of refraction ( $n = 3.4$ ), high thermal conductivity, and low dielectric loss tangents. Its low hardness (6 on Mohs scale) permits machining with diamond tooling. For the highest purity silicon crystals, grown with the float zone process, the loss tangent at 300 K can be  $\sim 10^{-5}$ , and for Czochralski (CZ) grown crystals it is typically  $\sim 10^{-4}$ . When cooled most samples realize good loss tangents in the  $10^{-5}$  range where the measurements are limited by the difficulties of cryogenic mm-wave testing.

Currently CZ silicon can be fabricated in boules up to 460 mm in diameter, while float zone silicon is restricted to 200 mm by the limits of surface tension in the zone refining process. The CZ process introduces a number of oxygen defects into the lattice that could increase absorption loss. However with thermal donor annihilation the impact of these defects can be mitigated to the point where the material approaches the performance of float zone silicon.

**Demonstrated performance** 300 mm diameter silicon lenses were deployed for ACTPol and Advanced ACTPol receivers.

**Prospects and R&D path for CMB-S4** The primary challenges for CMB-S4 are acquiring larger diameter samples and further reducing the dielectric losses. It may be possible to contract with a company to develop the capability to grow boules larger than 460 mm. A lower cost alternative is to develop the

ability to glue multiple single crystal wafers together to form a larger diameter composite piece. The glue process that has been developed for the silicon metamaterial HWP<sub>s</sub> as described above could be adapted for this purpose and direct wafer bonding may offer a higher performance alternative which could be pursued. If even lower loss material is required in large diameters, requiring the CZ growth process, there are processing techniques such as neutron doping which could be applied to fabricate that material.

The technology status level of the silicon lens is 5. Silicon lenses were deployed in ACTpol and Adv-ACT receivers for single color and multichroic operation. Data from the experiment was analyzed in detail.

The production status level of the silicon lens is 3. Commercial vendors are available to provide silicon ingots and to machine them. Large production throughput that can meet CMB-S4's demand is yet to be demonstrated.

### 3.4.2 Alumina

**Description of the technology** Alumina is a suitable lens material for CMB polarimetry applications due to its commercial availability, high index of refraction, low loss tangent, and high thermal conductivity at cryogenic temperatures. Its high index of refraction ( $\sim 3$ ) allows for higher optical power with lower curvature lens surfaces, resulting high-throughput lens systems that can fit in a compact cryostat. Its low loss tangent ( $\leq 10^{-4}$  at 4 K) results in low absorption of in-band photons for high optical efficiency. Current state-of-the-art alumina reduces the loss tangent even further below  $10^{-4}$ . Its high thermal conductivity facilitates easier cooling and lowers the operating temperature of the optics, which in turn lowers the loss tangent and thermal emission of the optics. Alumina has a thermal conductivity of  $\sim 100$  W/m·K at 50 K, which is three orders of magnitude better than typical plastics used for CMB optics. Alumina also has high strength with a fracture toughness of 4 MPa·m<sup>1/2</sup> so that the alumina refractive elements are mechanically robust. In addition to its excellent physical properties, alumina lens fabrication is extremely precise (25  $\mu$ m accuracy on aspheric surface) and relatively inexpensive (\$10,000 per lens).

**Demonstrated performance** Experiments such as BICEP3 [19], POLARBEAR-2 [65], and SPT-3G [11] currently use or plan to use alumina with high purity ( $\geq 99.5\%$ ) for their refractive elements. The material has also been used to make cryogenic filters [43]. Unlike silicon, alumina lenses are not limited in diameter or thickness, with the largest existing lens being one of the SPT-3G reimaging lenses which is 720 mm in diameter and 65 mm thick.

**Prospects and R&D path for CMB-S4** Alumina is an attractive lens material since it is the material that is currently enabling the largest lenses. Manufacturing throughput and the consistency of material properties should be further studied for CMB-S4. In order to support accurate optical design, precision setups for measuring the index and loss-tangent of alumina at operating temperatures should be developed.

The technology status level of the alumina lens is 5. BICEP-3 has taken data with receiver with alumina lens. SPT-3G also deployed receiver with three alumina lenses. POLARBEAR-2 is preparing alumina lens for 2017 deployment.

The production status level of the alumina lens is 3. Alumina lens is fired and machined at a commercial company. The company has many production lines to work on lens in parallel. Large production is possible in principle, but it has not been demonstrated.

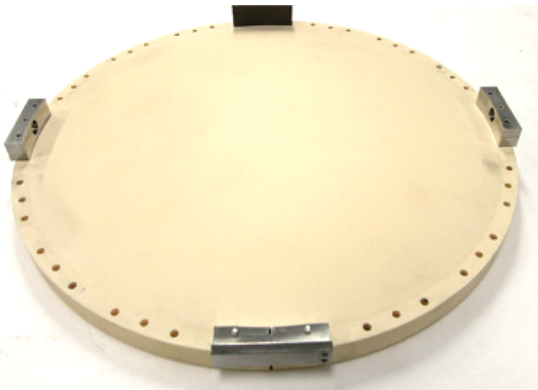


Figure 23: 500 mm diameter POLARBEAR-2 Alumina reimaging lens.

### 3.4.3 Polyethylene lenses

**Description of the technology** Polyethylene has been successfully used as a lens material for multiple CMB experiments. Polyethylene is manufactured in multiple grades, broadly divided into 3 categories: low density (LDPE), high density (HDPE), and ultra high molecular weight (UHMWPE). These have similar physical and optical properties.

The materials have moderate indices of refraction  $n \sim 1.53$ , which makes AR coating relatively easy. Large ( $> 500$  mm, 100 mm or more thick) plates of all grades are easily available, and have good machinability. Since LDPE has a slightly lower melting point, it may be used in a hot-press process to adhere ePTFE AR coatings to HDPE and UHMWPE lenses. Alternately, antireflection grooves, pyramids, or posts can be machined directly onto lens surfaces.

The low thermal conductivity of polyethylene makes the cryogenic design challenging for the larger diameter optics. Also, the moderate index of refraction puts practical limits on the refraction power of any particular lens, since higher power (thick) lenses may have too high an absorption, too steep a curvature, and/or too long a thermal time constant for some applications.

Due to the moderate index of polyethylene, a single thick HDPE or UHMWPE lens with front and back surfaces can have individual aspheric surfaces to reduce aberrations, whereas an alumina or silicon lens would be in the “thin lens” limit. Also, for polyethylene, a single AR layer may be adequate over a very broad band, while for the higher index dielectrics a multi-layer AR coating would be needed. Finally, the cost of polyethylene and its fabrication is considerably lower than the high index materials.

**Demonstrated performance** APEX-SZ, QUaD, BICEP, BICEP2, Keck Array, and SPTpol successfully deployed cryogenic receivers with multiple HDPE lenses. POLARBEAR-1 and EBEX deployed with UHMWPE lenses. These lenses are up to 350 mm in diameter and 100 mm thick. APEX-SZ deployed lenses with anti-reflection grooves on their surfaces, while the others deployed with bonded expanded Teflon anti-reflection coatings.

There have been some cryogenic challenges with UHMWPE lenses. For example, the lenses were the last optical elements to get cold during a cool down for the POLARBEAR-1 receiver. Also in the POLARBEAR-2 receiver optics design, it was not possible to design large FOV optics using UHMWPE due to its low index of refraction. BICEP3 experienced similar cooling problems with a set of HDPE back-up lenses used only in

the lab, although the HDPE optical design had nearly the same performance as the deployed alumina lens design excepting its (uncertain) absorptive losses.

**Prospects and R&D path for CMB-S4** The CMB community has extensive experience with polyethylene (HDPE and UHMWPE) lenses. Polyethylene continues to be a good candidate material to consider for CMB-S4 lenses, especially for small aperture optics where thermal conductivity might not be as important and total lens thickness is smaller. Good machinability, low cost, and transparency to mm-waves also makes it a good lens material candidate for lab test setups, particularly for laboratory measurements where AR coatings are not required.

An advancement that would benefit CMB-S4 would be to make comprehensive low temperature transmission and index measurements of the commonly used grades and brands of polyethylene. Although some exist in the literature (e.g. [51]), from grade to grade and manufacturer to manufacturer we expect some variation. Removing that uncertainty would make the best polyethylene materials more appealing to the optical designer.

The technology status level of the UHMWPE lens is 5. UHMWPE lenses were used by nearly every Stage-II experiments that successfully detected B-mode polarization.

The production status level of the UHMWPE lens is also 5. Bulk UHMWPE is readily available from commercial companies. Also it is easy to machine to desired shapes.

### 3.4.4 Metal mesh lenses

**Description of the technology** Metal mesh technology has been recently used to realize flat devices with focusing properties similar to conventional curved dielectric lenses. This can be achieved either by manipulating the effective refractive index of the medium [71] or the phase across the surface of the lens. In the latter case, a mesh-lens can be imagined as a simple planar transmissive device that changes a planar wavefront into a converging wavefront by locally modifying the phase of the radiation across its surface. The mesh-lens is spatially discretized into pixels optimized to provide a phase-shift relative to the lens center with the required frequency dependence. Each pixel is a column of aligned high-transmission capacitive unit-cells designed like a normal mesh-filter.

**Demonstrated performance** A 54 mm diameter,  $\sim 2.3$  mm thick mesh lens for the 75 – 110 GHz band has been designed, built, and tested [72]. The beam measurements show very good agreement down to the fourth sidelobe. This device did not require anti-reflection coatings and the overall modeled transmission was above 97%. The diameter of these lenses (currently 10-50 mm) can be in principle increased by adopting a Fresnel-lens like approach. This should only modestly increase the lens thickness, of order one wavelength. Although the operational frequency ranges are in principle the same as those of successful existing mesh filters ( $\sim 30$  – 300 GHz), misalignments and grid non-idealities can affect the performance at the higher frequencies of interest.

**Prospects and R&D path for CMB-S4** Metal mesh lenses are in an early stage of development although results are promising. While demonstrations have occurred on small scales, large-area fabrication requires R&D similar to that of metal mesh filters (Section 3.3.1). CMB-S4 is likely to require receiver optics and filters of diameter  $\sim 500$ –1000 mm. To increase metal-mesh lens diameter further, R&D is necessary and

should include establishment and verification of high-fidelity photolithography and uniform thermal pressing of multilayer metal-mesh structures up to 1000 mm diameter.

The technology status level of the metal mesh lens is 1. Laboratory demonstration shows good agreement with simulation. On-sky demonstration would further advance technology status level.

The production status level of the metal mesh lens is also 1. Demonstration of large diameter lens and fast production rate would further advance production status level.

## 3.5 Anti-reflection coatings

Broad-band AR coated lenses are required for nearly all of the currently proposed CMB-S4 optical designs, including small-aperture refracting telescopes and high angular resolution telescopes using reimaging lenses. Similar optical coatings can also be used to realize efficient HWP polarization modulators which could dramatically improve the ability of CMB-S4 to measure polarization on large angular scales. They can also be used to coat vacuum windows. Various approaches for AR coating are explored such as adding stack of sheets of dielectric layers, modifying the dielectric constant of surfaces by modifying material density, and stacks of metal mesh layers. Broad-band detector designs have evolved such that 2:1 ratio bandwidth detectors have been deployed, 3:1 ratio bandwidth detectors will soon be deployed, and even broader bandwidths are envisioned. In this note we review the requirements for these coatings, discuss the state of the art, and outline the next steps required to prepare these technologies for the CMB-S4 project.

### 3.5.1 Plastic sheet coatings

**Description of the technology** Plastic sheets with a wide range of dielectric constants are commercially available, making them an attractive AR coating option. The dielectric constant of a plastic sheet can be tuned by changing its porosity or by adding high dielectric constant filler material. CMB experiments have explored PTFE, expanded PTFE (Teflon), loaded PTFE, polyimide (Kapton) and polyetherimide (Ultem) as AR coating materials. A list of plastic AR coating materials is given in Table 3-2.

Material	$\epsilon_r$	$\tan \delta [\times 10^{-3}]$	Description
ePTFE	1.1 - 2.0		expanded PTFE
PTFE	2.1		Teflon [51]
RO3035	3.5	1.7	PTFE loaded with high dielectric ceramics [73]
RO3006	6.5	1.6	PTFE loaded with high dielectric ceramics [73]
RT/Duroid	2.9		Glass-reinforced, ceramic-loaded PTFE [73]
TMM	3.3 - 12.9	2.0	Loaded plastics. Thermoset laminates [73]
Cirlex	3.4	0.8	Pressure-formed laminate of polyimide [74]
Skybond	2.1	2.5	Skybond foam is an expanded polyimide [75]
Polyetherimide	3.15		Ultem [76]

Table 3-2: Summary of plastic AR coating materials. The loss tangent values shown here are room temperature values that may decrease upon cooling to cryogenic temperatures.

There are several methods to bond multiple plastic sheets onto a lens. Since the melting temperature of LDPE is below that of commonly used plastics for AR coating, a thin layer of LDPE can be melted between plastic AR coat layer(s) and the lens material. Multiple groups have also used Stycast 1266 epoxy to adhere a plastic layer to a lens. It is possible to bond the various PTFE layers directly into a single, monolithic sheet (self-bonding) through a controlled heating and cooling cycle as shown in Figure 24. This technique eliminates any intermediate bonding layers which could cause additional loss and unexpected coating performance.

Application of plastic sheets to a lens requires a uniform adhesive layer across the lens, and the sheet must be applied without any wrinkles. This is especially challenging on a curved surface. If the plastic is soft, such as expanded PTFE, it can simply be stretched over the curved surface. Some plastics, such as polyetherimide, can be thermoformed before coating [76]. Other plastics, such as PTFE, are not suited to thermoforming processes. Consequently, a spring loaded press was designed to mold PTFE; the SPT-3G experiment is using this technique to coat lenslet arrays. Cirlex has been machined to the correct shape before being adhered to a silicon lens [74]. Otherwise, for low radius of curvature shapes, vacuum-bagging produces a uniformly adhered, smooth coating.

Differential thermal contraction between plastic and other common lens materials such as silicon, alumina, and sapphire is problematic for cryogenic operation. Adhesion promoter, such as Lord AP-134, helps to increase the epoxy bond strength to make a bond strong enough to withstand thermal contraction. Dicing stress relief grooves into plastic sheets also helps to mitigate the thermal contraction issue as shown in Figure 41. Multilayer plastic coatings of sizes up to 300 mm in diameter are robust to violent thermal cycling without dicing. The mechanical modulus of expanded PTFE lowers as the material becomes more porous. A lower modulus helps to mitigate the delamination problem that occurs as a result of differential thermal contraction.

**Demonstrated performance** Many deployed instruments have successfully used this technology to AR coat a range of optical devices. Expanded PTFE sheets were glued with LDPE to an UHMWPE cryostat window and reimaging lenses for the SPIDER, POLARBEAR and EBEX experiments as shown in Figure 24 [63, 77, 78]. The HWP for the ABS experiment was coated with Rogers RT/Duroid using rubber cement as a glue layer [79]. The 150 GHz HWPs for the SPIDER experiment were coated with hot-pressed Cirlex using HDPE as an adhesion layer, and this is baselined for the 285 GHz SPIDER HWPs as well [80]. Machined Cirlex was adhered to a silicon lens with Stycast 1266 and Lord AP-134 adhesion promoter for the ACT experiment [74]. The measured performance from the coating is shown in Figure 24. A sheet of Skybond foam was attached to an alumina IR filter that was coated with a thermal sprayed mullite ceramic layer to cover the 90 GHz and 150 GHz bands simultaneously [75]. Multiple sheets of Roger's corporation's TMM laminates and expanded PTFE were used to coat a broadband HWP of the EBEX experiment which covers 150 GHz, 220 GHz and 410 GHz simultaneously [81].

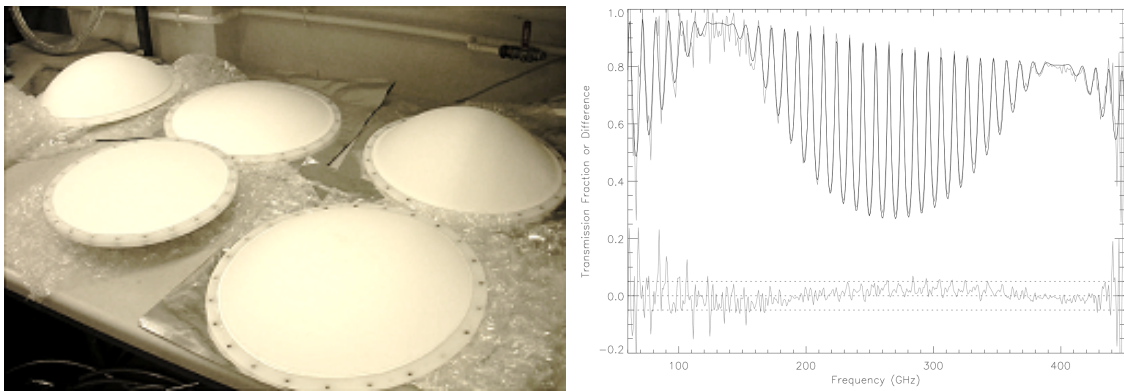


Figure 24: Examples of plastic AR coated optical devices. The left panel shows lenses made for the EBEX experiment with the AR-coatings applied. The right panel shows a measured spectrum of the AR coating used on an ACT lens.

**Prospects and R&D path for CMB-S4** The performance of plastic sheet AR coatings is primarily limited by the commercial availability of suitable materials. It is possible to custom order loaded PTFE sheets with different types of dopant to optimize the dielectric property of the material. Such an idea was not practical for smaller scale Stage-III experiments, but with larger commercial orders, it may become feasible for CMB-S4.

The technology status level of the plastic coating is 5. Plastic AR coating was used for multiple Stage-II experiments on UHMWPE lens. Plastic AR coating has not been used for high dielectric lens such as silicon lens and alumina lens. For multi-chroic application, 5 layer plastic coating was applied on sapphire for a cryogenic half-wave plate.

The production status level of the plastic coating is 5. Stage-II experiments demonstrated that coating is relatively easy to apply once proper jig is setup.

### 3.5.2 Thermal spray coatings

**Description of the technology** Plasma spray AR is a process by which a base material of alumina and silica is melted with a plasma jet and sprayed onto a lens surface, cooling immediately upon impact to form a strongly adhered coating without the need for any glue or adhesion promoters. The ability to tune the dielectric constant by varying porosity within the coatings, as shown in Figure 25, and the low loss-tangent (below  $10^{-3}$  at 140 K) of plasma sprayed coatings allow for AR coatings with the range of dielectric constants suitable for broadband multi-layer applications [46]. The spraying process is technically straightforward. The alumina-silica coating material has a matching coefficient of thermal expansion to the alumina optics, meaning it is robust against cryogenic delamination. Additionally, the robotic arm that controls the spraying allows for a fast and accurate programmable spraying pattern to uniformly coat a variety of surface profiles, whether they are flat filters or waveplates, curved lenses ( $\sim 700$  mm diameter), or a large array of small hemispherical lenslets ( $\sim 6.35$  mm diameter).

**Demonstrated performance** The POLARBEAR-2 receiver will be deploying alumina infrared filters coated with this approach. The SPT-3G receiver will be deploying with a 720 mm diameter infrared filter and lenses, with multi-layer sprayed AR coatings that simultaneously cover the 90, 150, and 220 GHz bands [11]. For a broadband AR coating, it is desirable to have some layers with an index of refraction as low as 1.25. The lowest index currently achieved by the plasma spray technique is 1.6. SPT-3G and POLARBEAR-2 experiments combined plasma sprayed layers with a porous plastic sheet (index of 1.25) to create the broadband AR coating shown in Figure 25.

**Prospects and R&D path for CMB-S4** Having dielectric layer with an index below 1.4 facilitates design with low level of reflection for a broadband AR coating. Currently, the lowest demonstrated index for alumina ceramic thermal spray is 1.6. The spray process has several variables that could be tuned to further lower the index, such as the powder feed rate, spray distance and flame temperature. Other dielectric powders compatible with the spray process should also be explored, to explore if the index can be lowered using this existing process but a different material.

The technology status level of the thermal spray AR coating is 3. Multilayer anti-reflection coating with thermal spray coating and expanded kapton sheet was applied on POLARBEAR-2 lenses. POLARBEAR-2 lenses are on going through integration test for 2017 deployment. SPT-3G used thermal spray coating for bottom two layers of three layer anti-reflection with plastic layer as top layer. Second and third receivers

for Simons Array and SPT-3G is planning upgrade of alumina lens anti-reflection coating with fully thermal sprayed lenses.

The production status level of the thermal sprayed AR coating is 3. Production rate was demonstrated on POLARBEAR-2 lens, and development is on going for thermal spray coating to cover required range of dielectric constant.

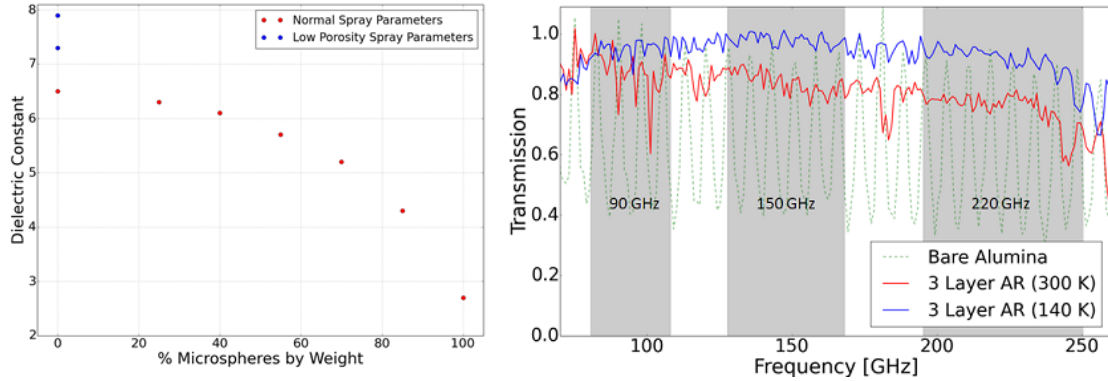


Figure 25: Left: Tunability of dielectric constant (i.e. the square of the index of refraction) for plasma spray AR technologies. The dielectric constant of an alumina-based coating is controlled by mixing hollow microspheres (red) and/or varying plasma energy with different spray parameters (blue), such as the flow rate of plasma gas [46]. Right: Measured transmission of a three layer AR coating on two sides of a 6 mm thick slab of alumina. The bottom two AR layers were thermal spray coatings. The top AR layer was expanded Teflon adhered to the alumina with LDPE.

### 3.5.3 Epoxy coatings

**Description of the technology** Epoxy can be used as an AR coating material [82]. Different types of epoxies have different indices of refraction, and the index can be tuned by mixing two epoxies in various ratios. For example, Styccast 1090 and Styccast 2850 FT have indices of refraction of 1.43 and 2.23, respectively. Even higher indices have been obtained by mixing other powdered material, such as strontium titanate, into the epoxy. The tunability of the index and the low loss of epoxy-based coatings at cryogenic temperatures are shown in Figure 26. An epoxy-based AR coating can be applied on a lens with a negative mold to coat the lens surface, and then after the epoxy hardens the surface can be precisely machined to the correct thickness with a computer numerical controlled (CNC) milling machine. Laser machined stress relief grooves have been shown to relieve mechanical stress between the epoxy AR coating and lens due to the thermal contraction mismatch. The groove width can be made smaller than 25 microns to prevent scattering.

**Demonstrated performance** An epoxy-based dielectric single-layer AR coating was applied to the 600 mm diameter IR filter and lenses of the 95 GHz BICEP3 receiver [19]. A multi-layer AR coat on 500 mm diameter lenses will be deploying on the POLARBEAR-2a receiver covering the 95 and 150 GHz bands [65]. The thicknesses of each coating were assessed by measuring the profile of the lens before and after coating with a coordinate measuring machine, showing that the thickness of the coatings were machined to 10 to 20 micron accuracy. The loss tangent of epoxy and epoxy-filler mixture increases at frequencies above the CMB

passbands, which means that the AR coating itself provides additional IR filtering when used with alumina infrared filters or lenses [43].

**Prospects and R&D path for CMB-S4** For single-layer and two-layer AR coatings of alumina, a combination of Styccast 1090 and Styccast 2850-FT provides the necessary range of dielectric constants with low levels of absorption loss. For three- or more layer AR coatings, an index above 2.23 is required for some of the layers, which has been achieved by adding the strontium titanate powder to the mix. While it has performed well in a three layer coating, unfortunately the loss tangent of a mixture of Styccast 2850-FT and strontium titanate mixture is relatively high. It would therefore be useful to develop a high index filler powder with a lower loss tangent. Silicon and alumina should be explored to see if they will reduce the total loss tangent of the mix to below  $5 \times 10^{-4}$ .

The fabrication process for epoxy AR coatings requires a somewhat laborious process of moulding and machining, which may limit its applicability for high volume fabrication. Furthermore, epoxy-based AR coating requires a large CNC to machine large diameter lens coatings. A dedicated machining center, or potentially an industry contract, could solve these scalability challenges.

The technology status level of the epoxy AR coating is 5. Epoxy coated alumina lens has been deployed on BICEP-3 receiver. Multichroic version of epoxy coated alumina lens is prepared for POLARBEAR-2 deployment, and it is in final stage of integration and test. The production status level for the epoxy AR coating is 2. Although it was successfully deployed for Stage-III experiment, epoxy coating requires laborious coating and machining process.

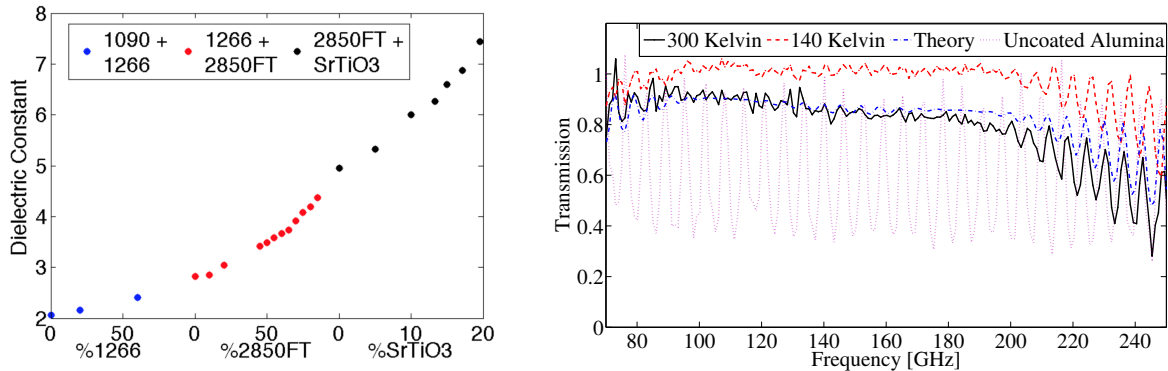


Figure 26: Tunability of the dielectric constant for epoxy-based AR coatings. The dielectric constant is controlled by mixing different Styccasts and  $\text{SrTiO}_3$  [82]. The spectra in the right panel show that the coatings have low loss when cooled to 140 K or lower.

### 3.5.4 Diced silicon

**Description of the technology** Diced silicon metamaterial AR coatings are fabricated by cutting sub-wavelength features into surfaces of refractive optical elements. Since AR coatings are machined directly into the surface of the cryogenic optical element, there are no concerns about thermal contraction mismatch or delamination during cryogenic cycling. The fill factor tunes the dielectric constant of the machined layer. Multi-layer coatings can be produced by cutting progressively deeper and thinner square grooves centered

on the wider first layer, creating a stepped pyramid as shown in Figure 27. [18] Alternatively, a single pass using a bevelled dicing saw blade produces smooth sided pyramids, Figure 28, which provide a continuous gradient in index. [83]

**Demonstrated performance** Stepped coatings, Figure 27, with micron level accuracy have been produced using a three-axis dicing saw. [18] Twelve lenses were deployed on the ACTPol and the AdvACT experiments and lenses have been delivered to the PIPER experiment. The largest lens produced is 330 mm in diameter, but lenses up to the maximum diameter available for single crystal silicon, 460 mm, can be fabricated. Coatings on both concave and convex surfaces have been demonstrated. Current stepped coatings achieve  $\sim 0.1\%$  average reflections in bands centered on 90 GHz and 150 GHz. Coatings using smooth sided pyramids, Figure 28, have been demonstrated with 97% fractional bandwidth. [83]

**Prospects and R&D path for CMB-S4** The primary challenge for applying this technology to CMB-S4 is reducing the time it takes to AR coat a single lens. Currently, fabricating the stepped coatings takes roughly two weeks per lens. Automating some of the most time intensive setup tasks, it could be possible to build a machine that reduces that time to 1-2 days. Alternatively, the number of cuts required to produce a coating could be reduced by using bevelled blades.

It is possible to design silicon pyramids for wider bandwidth. Using pyramids, a three-layer coating designed for 1% reflection could achieve 3:1 ratio bandwidth. Wider bandwidth (5:1) may also be achieved by exploring more pyramid profile options. A prototype five-layer AR coating covering 75-300 GHz has been fabricated, and optical performance measurements will be made soon.

The technology status level of the diced stepped silicon metamaterial AR coatings is 5. Diced silicon metamaterial AR coatings on silicon lenses have been deployed on the ACT-pol and Adv-ACT receivers. The technology status level of the coatings using smooth sided pyramids is 1. These smooth pyramid coatings cut using bevelled saws have been demonstrated on flat samples.

The production status level of the diced stepped silicon metamaterial AR coatings is 3. Current dicing method takes non-negligible time to complete a lens, but an upgrade for the dicing setup is planned to speed up production rate. The production status level of smooth sided pyramid coatings is 1; prototypes have been fabricated.

### 3.5.5 Deep reactive ion etched silicon

**Description of the technology** Deep reactive ion etching (DRIE) has recently been developed [84, 85] as an alternative to dicing saw machining to produce diced silicon AR coatings as described in previous section [18]. This approach is significantly less mature than the dicing saw approach, and has only thus far been fully demonstrated on flat 100 mm diameter silicon wafers for a wavelength of  $350\ \mu\text{m}$ .

DRIE offers the potential for significant advantages for optics as large as 300 mm diameter. Specifically, the DRIE process acts on the entire wafer simultaneously, unlike the dicing saw and laser ablation approaches which cut individual grooves or holes. Simultaneous processing of entire 300 mm wafers should make this approach easier to scale to fabrication of hundreds of lenses.

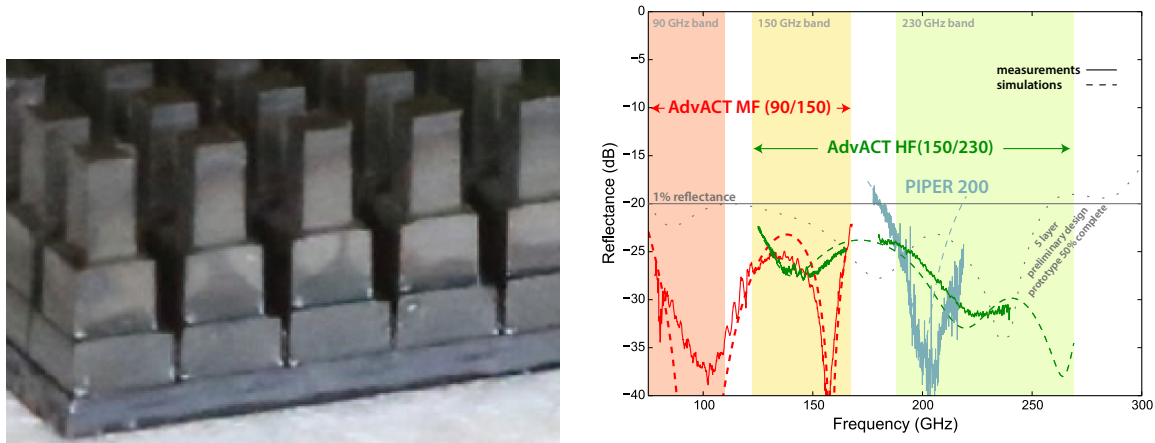


Figure 27: Left: Photograph of a mechanical prototype of a three-layer coating for 75 – 165 GHz. The top cut is  $250\text{ }\mu\text{m}$  wide, and  $500\text{ }\mu\text{m}$  deep. The middle layer is  $110\text{ }\mu\text{m}$  wide,  $310\text{ }\mu\text{m}$  deep. The last layer is  $25\text{ }\mu\text{m}$  wide,  $257\text{ }\mu\text{m}$  deep. The pitch between the sets of cuts is  $450\text{ }\mu\text{m}$ . Right: Performance of metamaterial silicon AR coatings fabricated on lenses that have been or will soon be fielded including: the medium frequency (MF) (90/150 band) lenses for ACTPol, the HF (150/220 band) lenses for AdvACT, and the soon-to-be-deployed PIPER 200 GHz lenses. Simulations are shown as dashed lines and measurements are shown as solid lines. The MF and HF lenses use three layer AR coatings while the PIPER lenses use a single layer coating. A preliminary design for a five layer coating is shown by the gray dashed line. A prototype of this five layer coating has been fabricated on one side of a 250 mm diameter test wafer.

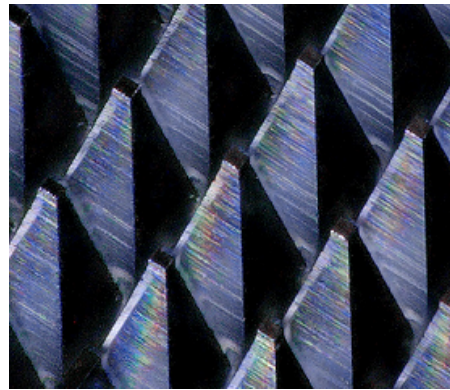


Figure 28: Photograph of smooth sided pyramids cut on silicon using a bevelled dicing saw. The pyramids are  $1000\text{ }\mu\text{m}$  tall, have flat tops  $50\text{ }\mu\text{m}$  wide, and a pitch of  $350\text{ }\mu\text{m}$ .

**Demonstrated performance** The DRIE approach has been demonstrated for single layer AR coatings on flat 100 mm diameter silicon wafers for a wavelength of  $350\text{ }\mu\text{m}$ . Preliminary results of this work are presented in [84]. Results of high-efficiency double-sided coatings including silicon bonding of two samples and a prototype two-layer coating are presented in [85].

**Prospects and R&D path for CMB-S4** The primary challenges for this technology include: (i) bonding silicon wafers with DRIE coatings onto curved lenses and (ii) demonstrating this approach at the 300 mm scale. A final requirement for this technology is to demonstrate performance at longer wavelengths; however, this is expected to be straightforward for wavelengths up to  $\sim 3\text{ mm}$ . The largest diameter wafers that could be coated using this approach are limited to 300 mm by the size of available DRIE machines. This may be sufficient for optics designs that use modular optics tubes (e.g., [3]).

The technology status level of the DRIE etched silicon metamaterial AR coatings is 1. Laboratory demonstration has been done on flat silicon wafer.

The production status level of the diced silicon metamaterial AR coatings is 1. Laboratory demonstration has been done, but deployable model has not been demonstrated.

### 3.5.6 Laser ablated surface

**Description of the technology** Laser ablation has been used to fabricate metamaterial AR coatings similar to the dicing saw and DRIE techniques described in previous sections. Since hard materials are difficult to process with mechanical machining, laser ablation is advantageous when working with materials such as alumina or sapphire. Producing structures on any material with features smaller than  $\sim 25$  microns is challenging with mechanical machining, but laser ablation can readily make features down to nearly 1 micron, approximately the scale of the laser spot diameter.

**Demonstrated performance** Matsumura et al. [86] recently demonstrated laser ablated pyramidal structures on sapphire and alumina; see Figure 29. The structures were produced by repeated raster scanning of the sample using a pico-second laser operating at green wavelengths (515 nm) with total power of 30 W. There is reasonably good agreement between the designed and as-built structures, and between the measured and predicted transmission; see Figure 29. Young et al. [83] demonstrated similar structures on silicon using the same laser system at 28 W.

**Prospects and R&D path for CMB-S4** For CMB-S4, several areas can benefit from further development. Plastics can be explored to see if laser ablation can be used on those materials. Investigating smaller features for higher frequencies, and higher aspect ratio structures for wider bandwidth, are both useful areas for future study. Finally, it would be advantageous to work to increase the ablation rate of the process to decrease the cost and increase the speed of fabrication.

The technology status level of the laser ablation on sapphire, alumina, and silicon is 1. Development is still in the early stages. Laser ablated AR coatings have been demonstrated on flat samples of all three materials in the laboratory.

The production status level of the laser ablation on sapphire, alumina, and silicon is also 1. Although this technology is an attractive way to achieve low loss and wide bandwidth AR coatings, ablating over large surface areas still takes non-negligible time.

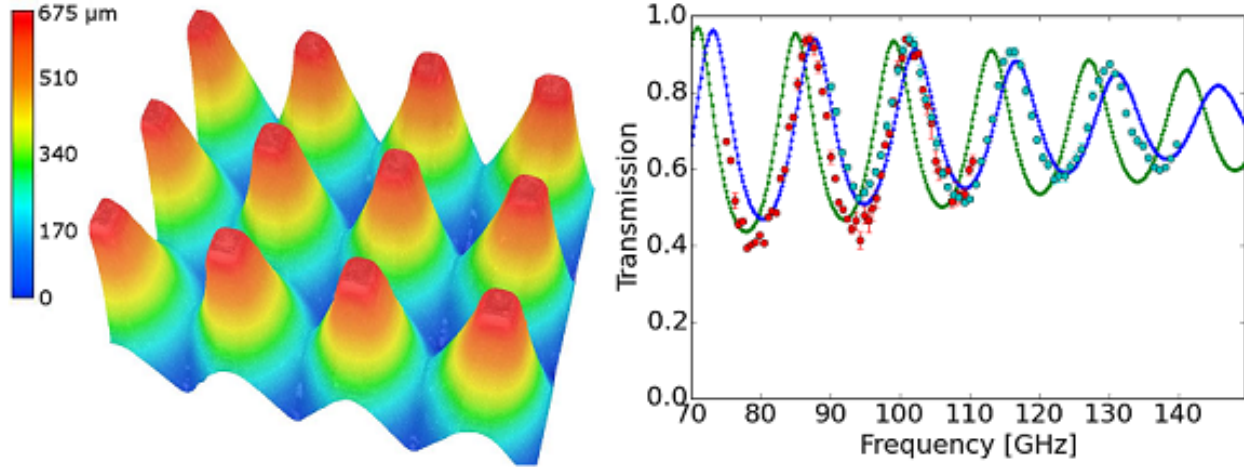


Figure 29: Left: Image of a laser-ablated sub-wavelength AR coating fabricated on sapphire. The patterned pitch is  $320\text{ }\mu\text{m}$  and the height is  $700\text{ }\mu\text{m}$ . Right: Measured transmission for this structure between 75 and 110 GHz (red) and 90 and 140 GHz (cyan) matches predictions that are based on the tallest (blue) and shortest (green) structure measured on this sample. The data is normalized to the blue curve at 87 GHz.

### 3.5.7 Machined plastic

**Description of the technology** Metamaterial AR coatings, as shown in Figure 30, have been created using a grid of sub-wavelength holes cut into the surface of plastic cryogenic optics. The hole diameter and grid spacing are tuned for the frequency band and the required index of refraction. These AR coatings are machined on a conventional CNC milling machine with minimal alterations and standard tooling.

**Demonstrated performance** Simulated dielectrics were used to AR coat sixteen 140 mm HDPE lenses for CAPMAP [87]. More recently, simulated dielectrics were applied to two 400 mm diameter HDPE lenses, three flat Teflon filters, and one Nylon filter for the CLASS 40 GHz telescope [88]. The lenses and filters for the two CLASS 90 GHz telescopes are also AR coated with simulated dielectrics and are currently in production. AR coating for HDPE window for SPT-3G is CNC machined pyramidal grooves on its surface. Two orthogonal groove patterns were machined on opposite sides of HDPE window. Pyramidal grooves were designed for broadband AR coating application that covers 90 GHz, 150 GHz, and 220 GHz.

**Prospects and R&D path for CMB-S4** The size of the optics AR coated in this fashion is only limited by the travel of the CNC mill used in fabrication and standard commercial machines have sufficient range for 600 mm diameter pieces. Demonstration of broadband coating over curved surface would make this method more versatile.

The technology status level of the machined plastic coating is 4. Broadband AR coated plastic window has been deployed on SPT-3G.



Figure 30: A 400 mm diameter CLASS 40 GHz lens that is AR coated using a grid of sub-wavelength holes (top) to create a simulated dielectric layer of lower mean density and tuned index of refraction.

The production status level of the machined plastic coating is 5. Machining of SPT-3G window demonstrated that broadband AR coating on plastic lens can be applied easily with CNC mill.

### 3.5.8 Metal mesh

**Description of the technology** There are cases where the refractive indices required for AR coatings are hard to obtain. In these cases quarter-wavelength layers made of artificial dielectrics can be synthesized and used for very broadband applications, more than 100% in bandwidth. Artificial dielectrics have been realized by loading dielectric materials with stacked metal-mesh grids. In addition to the requirement of having sub-wavelength structures as in mesh-filter-type applications, the periodic grids need to be stacked within their near field distances. The stacked grids will look like a uniform medium to the electromagnetic radiation passing through them. The equivalent refractive index will depend on the number of grids and their spacing. The effective index can be tuned by modeling with commercial software such as HFSS, compared with previous experience in metal mesh filter design, and measured in the lab after fabrication.

**Demonstrated performance** Refractive indices ranging from 1.2 to 4 can be easily achieved with negligible losses [89]. Measurements of a two-layer AR coating with artificial dielectrics and porous PTFE (PPTFE) on both sides of a quartz substrate are shown in Figure 31.

**Prospects and R&D path for CMB-S4** Broadband metal-mesh AR coatings are in an early stage of development. While demonstrations exist on small scales, large-area fabrication requires R&D similar to that for metal mesh filters (Section 3.3.1). CMB-S4 is likely to require receiver optics and filters of diameter  $\sim$ 500–1000 mm. To increase the diameter of metal-mesh AR coatings further, R&D is necessary and should include establishment and verification of high-fidelity photolithography and uniform thermal pressing of multilayer metal-mesh structures up to 1000 mm in diameter.

The technology status level of the metal mesh AR coating is 1. Demonstration of dichroic AR coating was demonstrated, but it has not deployed on CMB experiment yet.

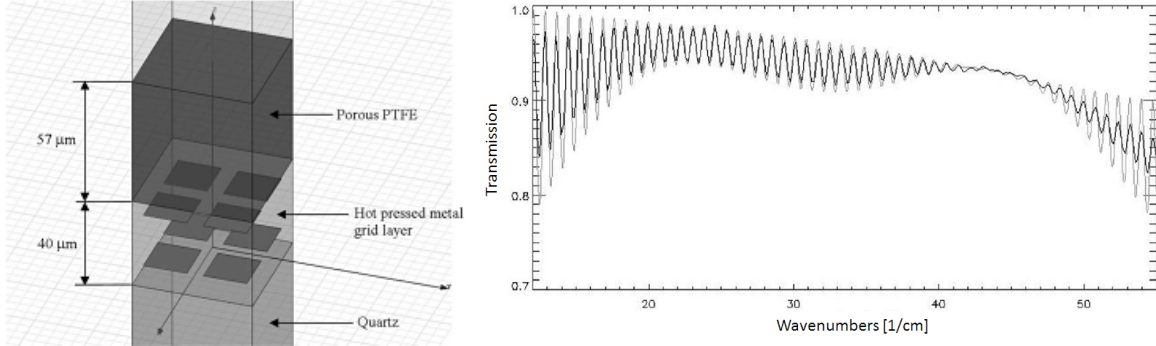


Figure 31: Left: Full model of an AR coating on both sides of a quartz substrate. Right: Measured transmission spectrum of the stack (PPTFE-ADMquartz-ADM-PPTFE). The black line is the best fit of a scattering matrix model with varying optical constants to fit the data as a function of frequency [89].

The production status level of the metal mesh AR coating is 1. Metal mesh infrared filters have been used by multiple CMB experiments successfully. Basic production concept is similar, however, production of metal mesh AR coating has not been demonstrated beyond laboratory level.

## 3.6 Polarization modulators

Polarization modulation is a generic term for all techniques that are used to change the orientation of instrument's polarization sensitivity, relative to fixed sky coordinates. This is a powerful technique that enables consistency checks to reveal and mitigate several kinds of systematic errors in the instrument. Effects that can be mitigated with a suitably-implemented modulator include beam systematic errors, performance differences between each detector in a polarized pixel, and spurious temperature-to-polarization and polarization-polarization coupling in the instrument. Moving towards the specific implementation, it is useful to consider two different regimes of modulation speed: one that is much slower (i.e. stepped rotation), and the other much faster (i.e. continuous rotation), than the characteristic  $1/f$  knee of the detector+atmospheric noise spectrum. The modulator can be installed either at ambient temperature or inside the cryostat. In both cases, there are several different places in the optical chain that modulators have been used. Conventional motors dissipate a fraction of a watt of heat, meaning that installing the drive mechanism inside the receiver cryostat has required special consideration. Several mechanical design solutions and their associated instrumental challenges are reviewed in Section 3.6.5.

At mid-latitude and equatorial observing sites, a significant degree of polarization modulation happens naturally through the daily rotation of Earth. Rotating the entire instrument is also possible, and has recently been used by the BICEP/Keck Array teams. In this section, we will discuss polarization modulation by motion of an optical element in the light path. The rotation of a half-wave plate (HWP), realized either through (a) crystalline plate(s) or metamaterial, and the translation of a mirror in front of a polarizer (VPM) are among the standard techniques to achieve modulation with an optical element in the light path. Polarization modulation using these approaches have been implemented by a number of CMB experiments [9, 27, 44, 77, 79, 90–94].

Continuous rotation modulates the polarization signal up to higher audio frequencies in the detector, which reduces the impact of atmospheric fluctuation noise that can be polarized by instrumental effects. ABS and other instruments have shown that atmospheric noise can be reduced this way. So far, this has been done with the instrument scanning slowly, such that there is more than one complete modulator rotation in the time it takes to scan a single beamwidth across the sky. This slow scan meant that atmospheric fluctuations added excess noise to the CMB temperature data. Since temperature maps are still important to achieve lensing and other science goals, it has been proposed (and testing is underway with ACT) to scan the instrument much faster than this to enable simultaneous temperature and polarization mapping with a rapid modulator.

Stepped modulation changes the sensitivity angle of the instrument periodically. The instrument then scans rapidly to make a map in this configuration. Data taken at several modulator states are combined in software to yield polarized maps, as well as allowing for assessment and removal of systematic errors. The SPIDER balloon mission used a stepped half wave plate, and the BICEP/Keck Array instruments used stepped instrument rotation. In this approach, the temperature and polarization data appear at the same audio frequencies. Detector differencing was used in BICEP/Keck Array to remove atmospheric fluctuation noise, instead of using rapid modulation to remove atmospheric fluctuation noise.

The rotation of the HWP, at a mechanical frequency  $f$ , completely rotates the polarization vector of each pixel of the observed sky at twice that rate. This means that after passing through a polarized detector, polarized signals from both  $Q$  and  $U$  appear in the detector timestreams at a frequency of  $4f$ . Spurious signals from HWP emission and non-uniformity appear at  $2f$  and other frequencies [79, 95]. Instruments using stepped rotation also take advantage of this separation between polarization signal and systematic errors [96]. The HWP can be located at room temperature at the entrance aperture of the entire telescope [44, 79] or nearby the Lyot stop at cryogenic temperatures [81]. In the first case, since it is the first optical element

seen by the incoming light, it completely separates the instrumental polarization from the sky polarization. In the second case the thermal emission of the HWP is reduced, but it will unfortunately be unable to fully separate instrumental and sky polarization. Several experiments have demonstrated data analysis techniques to separate the two in software.

In the following sections, we review the technical issues and outline the challenges to implementing these polarization modulation techniques for CMB-S4, focusing on HWPs and VPMs. Subsections 3.6.1–3.6.5 describe elements of HWP systems. Subsection 3.6.1 describes the principles and properties of AHWP, which achieves wide bandwidth required for CMB-S4 and can generically be applied to both of two types of HWP materials discussed later: sapphire (Section 3.6.2) and metamaterial silicon (Section 3.4.1). Subsection 3.6.4 describes a metal-mesh HWP, which also achieves wide-band polarization modulation. All of these HWPs require rotation mechanisms; subsection 3.6.5 discusses them. Subsection 3.6.6 describes the VPM, for both working principle and mechanical implementation.

The Section concentrates on technical issues in implementing specific technologies, not on sources of systematic errors. It also ignores technical solutions that require rotation of the entire instrument.

### 3.6.1 Achromatic half-wave plates

**Description of the technology** A crystalline, single-plate HWP is a narrow-band, birefringent optical element whose thickness is tuned to give a precise half-wave difference in the phase of the electric field traversing the two orthogonal optical axes. The half-wave difference only occurs at a single frequency. A Pancharatnam AHWP is a stack of several single plates, each oriented at an angle relative to the next to give a half-wave difference over a broad range of frequencies. This makes AHWP suitable for multi-frequency CMB polarization experiments [97].

An AHWP consists of an odd number of identical “single HWPs” stacked in an optimized orientation [98]. A useful approximation for considering the performance of an AHWP is to treat it as rotating incoming light with linear polarization fraction  $P_{in}$  by twice the angle  $\theta_{in}$  with respect to the principle axes of the AHWP, plus a frequency-dependent phase  $\phi(\nu)$ , and with a frequency-dependent modulation efficiency  $\epsilon(\nu)$  [99].

$$\Delta\theta = 2\left[\theta_{in} + \phi(\nu)\right] ; \quad \epsilon(\nu) = \frac{\sqrt{Q_{out}^2 + U_{out}^2}}{\sqrt{Q_{in}^2 + U_{in}^2}} \quad (3.6.1)$$

The calculated modulation efficiency and phase for various AHWP stacks is shown in Figure 32. A greater number of plates gives increased polarization efficiency and decreased phase variation across a larger bandwidth. However, the larger the number of plates leads to a thicker device, and therefore increased absorption loss and thermal emission. This could be reduced by operating the waveplate at cryogenic temperatures, however this has thermal and mechanical challenges.

**Demonstrated performance** The implementation of the AHWP technology is relatively new to CMB polarization experiments but has shown early promise. During an 11-day balloon observation of 150, 250, and 410 GHz in 2012/2013, EBEX flew a cryogenically cooled five-stack sapphire AHWP that completed a half-million revolutions at 4 K [81]. Advanced ACTPol (AdvACT) has deployed a three-stack, ambient-temperature silicon metamaterial AHWP on their 90/150 GHz receiver and is planning to utilize this technology on future AdvACT receivers [9]. Simons Array will deploy an ambient-temperature three-stack sapphire AHWP on POLARBEAR-2a to observe at 90 and 150 GHz starting in 2017 [44].

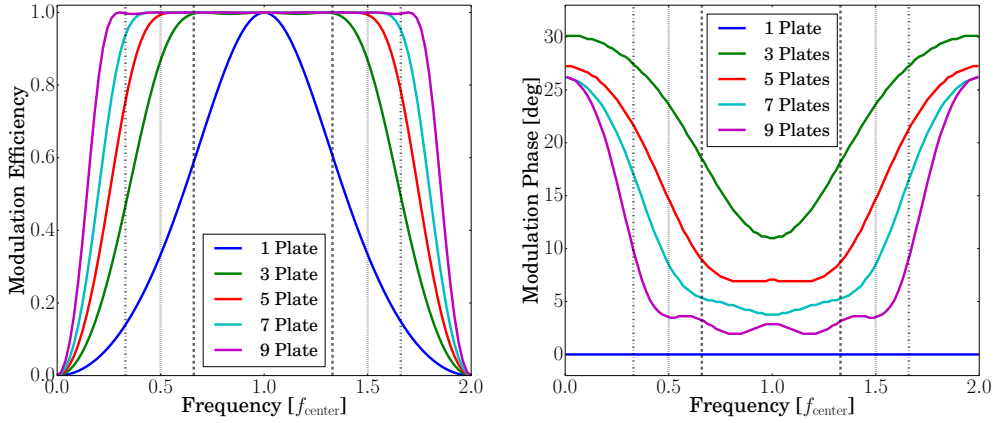


Figure 32: The calculated modulation efficiency and phase for various AHWP stacks, referenced to the modulator’s central frequency. Increasing the number of plates increases the polarization efficiency and decreases the phase variation across an increasing bandwidth. Various percent bandwidths are shown for reference: 2:1 (dash), 3:1 (dot), and 5:1 (dash-dot).

**Prospects and R&D path for CMB-S4** The primary technological advances required for implementing AHWP s for CMB-S4 include the availability of large-diameter birefringent plates, the development of broadband AR coatings, mitigation of increased absorption and thermal emission due to multi-plate stacks, and control of frequency-dependent effects such as modulation efficiency and phase [44]. Each of these topics is being actively addressed within the CMB community.

Various birefringent materials — including sapphire, metamaterial silicon, and metal-mesh substrates — have been suggested for large-diameter AHWP design [9, 100, 101]. Additionally, various anti-reflection techniques — such as laser-ablated sub-wavelength structures, thermal-sprayed ceramic, and epoxy — have been suggested for large-bandwidth AHWP construction [46, 82, 102]. Cryogenic rotation stages have been developed to facilitate AHWP cooling and suppress thermal emission [27, 44, 103, 104]. Hardware and analysis techniques have been proposed to control AHWP frequency-dependent effects [105, 106]. Lessons from EBEX and AdvACT HWP data analysis, from in situ characterization of the POLARBEAR-2a AHWP, and from HWP R&D associated with other broadband CMB experiments such as LiteBIRD will help define the role and construction of AHWP polarization modulators for CMB-S4 [107].

### 3.6.2 Sapphire

**Description of the technology** Sapphire is an appealing HWP candidate due to its low loss tangent ( $\tan\delta \sim 10^{-4}$  at 300 K,  $\tan\delta < 10^{-6}$  at 50 K) and large differential index ( $n_o \sim 3.1$ ,  $n_e \sim 3.4$ ) at millimeter waves [108, 109]. Additionally, sapphire has already been successfully demonstrated on several CMB polarization modulators [63, 79, 81, 90, 110]. For example, the polarization modulation efficiencies measured for the AHWP s of the POLARBEAR-2a and EBEX experiments are shown in Figure 33 [31, 44, 111].

**Demonstrated performance** The Heat Exchanger Method (HEM) is the standard growth technique for large sapphire boules [112]. As shown in Figure 33, GHTOT (in China) is now reaching > 500 mm diameters while achieving low levels of impurities and crystal defects via their Advanced HEM method [113]. Arc-

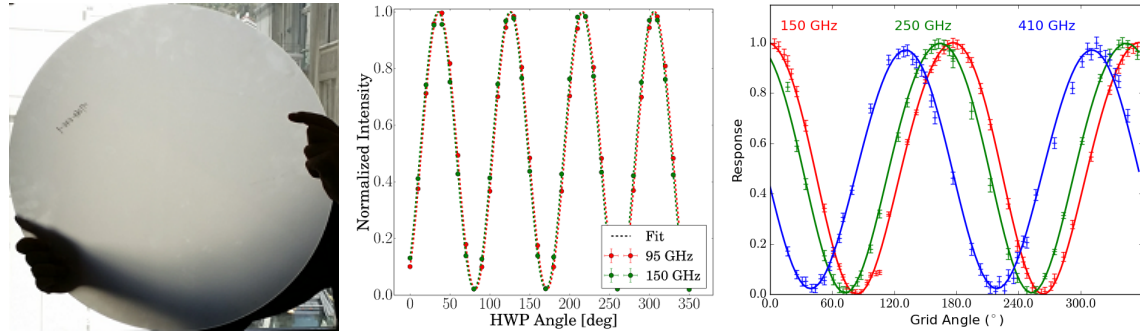


Figure 33: (Left) 512 mm-diameter sapphire plate cut from a 200 kg ingot of HEM sapphire grown at Tuizhou Haotian Optoelectronics Technology in China. (Center) Polarization modulation performance of a three-layer sapphire AHWP for the POLARBEAR-2a receiver. Polarization modulation efficiencies are 99% and 98% for 90 GHz and 150 GHz band, respectively. (Right) Polarization modulation performance of a five layer sapphire AHWP for the EBEX experiment. Polarization modulation efficiencies are 98%, 98%, and 92% for 150 GHz, 250 GHz, and 410 GHz band respectively.

Energy has developed a Controlled Heat Extraction System (CHES) furnace which controls seed orientation during HEM growth to push beyond 500 mm [114]. Despite its successes producing HWPs for Stage-III CMB experiments [44], the HEM process is limited by its need for large chambers that are difficult to clean and inherent thermal gradients that tend to cause crystal defects.

**Prospects and R&D path for CMB-S4** In reaction to demand for larger plates, industry is developing alternative sapphire growth techniques. The edge-defined, film-fed growth (EFG) method aims to create plates during growth rather than via post-process machining by drawing the crystal through shaping aids [112]. The clear, large aperture sapphire sheets line of EFG products at Saint-Gobain crystals reach 300 mm. Kyocera (in Japan) can go up to 200 mm and is pushing towards larger diameters [115, 116].

In the event that single-crystal growth does not meet its diameter and purity requirements, CMB-S4 can turn to other sapphire solutions, including composite plates. For example, sapphire bonding is a common technique that can be pushed to large diameters for low-stress applications [117]. Combining the power of precision dicing and novel bonding techniques may further accommodate large fields of view in CMB-S4 optical systems.

The technology status level of the sapphire plate for polarization modulator is 4. Sapphire was used as birefringent material for EBEX, ABS and POLARBEAR-1 polarization modulator. ABS and POLARBEAR-1 used single plate for single color operation. EBEX used multiple sapphire plates for broadband operation.

The production status level of the sapphire plate for polarization modulator is 5. Sapphire ingot is commercially available. It can be purchased at desired thickness.

### 3.6.3 Diced silicon broadband half-wave plates

**Description of the technology** Birefringent metamaterial silicon is fabricated by making asymmetric features in the surface of Silicon plates. There are several advantages of this technology. First, the difference in the index of refraction between the two principal axes can be made large ( $\Delta n > 1$ ). Second, the loss

of this material can be extremely low as silicon has a low loss tangent and with the high  $\Delta n$  each HWP layer can be made very thin. The warm loss tangent of silicon is typically  $10^{-4}$  which drops to  $\sim 10^{-5}$  at cryogenic temperatures. Larger achievable  $\Delta n$  with diced silicon half-wave plate technique allows thinner substrate, which in turn helps to reduce absorption loss.

**Demonstrated performance** A three-layer metamaterial Silicon broadband HWP with a Pancharatnam geometry and three-layer AR coatings on both sides was fabricated as shown in Figure 34. The HWP layers consist of a set of evenly spaced grooves cut into the silicon. The AR layers consist of two orthogonal sets of grooves, leaving rectangular cross-sectioned stepped pyramids. The coating is designed to be birefringent, to better match to the birefringent of the HWP itself, which in turn will minimize the polarization dependence of reflections. To make a three-layer HWP, the central HWP layer is cut into one side of the thickest Si wafer. The patterned side of the thickest silicon and a thinner silicon layer are then glued together, and the outer layers are cut. The HWP layers just touch, leaving no interstitial silicon, so small holes permeate the entire plate. Despite this, the assembly is mechanically robust.

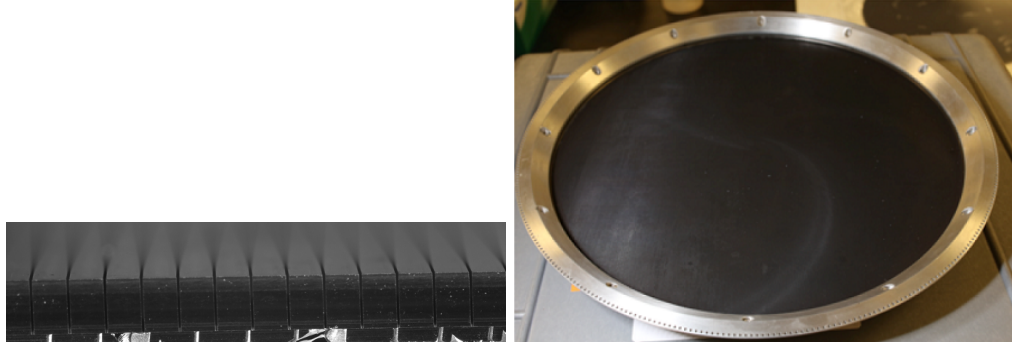


Figure 34: (Left) Birefringent silicon is cut only in one direction, with evenly spaced cuts. To form the three-layer HWP, one silicon wafer is cut all the way through, leaving only strips which remain in place due to the glue layer between the two wafers. By varying the width and depth of the cuts, the index of refraction can be tuned within a range. (Right) Pictured is the fully fabricated HWP currently deployed on ACT. It is placed in an encoder ring to measure the angle of the HWP as it rotates in front of the telescope.

One broadband HWP has been deployed on the Atacama Cosmology Telescope as part of the Advanced ACTPol upgrade. The HWP had a diameter of 340 mm, was optimized for the 75-165 GHz range, and operates at ambient temperature in front of the cryostat. In lab, it was demonstrated to have a modulation efficiency larger than 90% (see Fig. 35) and reflections averaging less than 3%. On the telescope, it was measured to have emission equivalent to approximately 2 and 4 K at 90 and 150 GHz, respectively. Analysis of polarized astrophysical sources confirms that it functions as a polarization modulator.

**Prospects and R&D path for CMB-S4** The potential challenges for this approach include: (i) extending beyond 460 mm diameters, (ii) frequency scaling, (iii) bandwidth and (iv) fabrication efficiency.

Diameters beyond 460 mm could be achieved by tiling silicon, but this would need to be developed. Frequency scaling for the CMB-S4 science bands (25-300 GHz) will soon be demonstrated: the AdvACT HF array covers 120-280 GHz and its HWP is nearly complete; and the AdvACT low frequency (LF) array which will cover 24-50 GHz will be fabricated in the coming year. Increasing the bandwidth is possible by adding additional layers to the broad-band stack; however our design process, which relied on full wave simulations with a carefully chosen square superlattice, would need to be expanded to handle these new layers. Given that

a five-layer AR coating has already been successfully demonstrated, the broadband coatings needed for a waveplate with more layers should be tractable.

The major challenge to overcome scaling this technology to CMB-S4 level production is the fabrication time and yield. The current system can fabricate one HWP in approximately three weeks. A fully automated system (as described in Section 3.5.4) could get the fabrication time down to three days. More development on the gluing procedure and associate cleaning procedure would mitigate the risk of delamination of the two silicon plates during the fabrication process which so far has reduced the yield to 50% for the first two HWPs produced.

The technology status level of the diced silicon for polarization modulator is 4. Silicon half-wave plates were deployed for ACTpol and Adv-ACT. Data is currently being analyzed.

The production status level of the diced silicon for polarization modulator is 3. Silicon ingot can be purchased, and it comes sliced at desirable thickness. Dicing setup is being upgraded to dice larger silicon at faster pace.

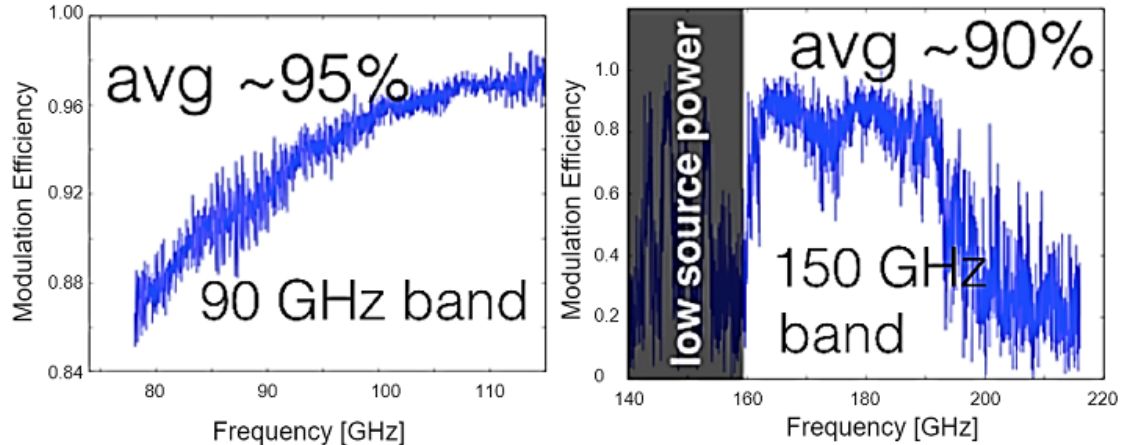


Figure 35: Measured modulation efficiency of a metamaterial silicon HWP in two bands. The modulation efficiency was found to be approximately 90% in the high band (120-185) GHz and 95% in the low band (75-110) GHz. These measurements should be interpreted as lower limits due to the presence of a small amount of uncleansed wax in the grooves at the time of the measurement. Since the wax has  $n > 1$  it reduced the modulation efficiency. The wax was fully cleaned before shipping it to the field. Initial on-sky measurements show promising performance, and measurements and observing is underway. The modulation efficiency of the next AdvACT HWP will be measured in more detail to inform future applications of this technology.

### 3.6.4 Metal mesh polarization modulators

**Description of the technology** Anisotropic patterns of conducting material, similar to the isotropic structures used in metal mesh filters (discussed in Section 3.3.1), have been used to create birefringent metamaterials. Parallel continuous lines and parallel dashed-lines are examples of structures with strong inductive and capacitive reactance to incident mm-waves of one polarization, yet they are almost transparent to the orthogonal polarization. By appropriately stacking capacitive and inductive grids in orthogonal directions, it is possible to create an arbitrary relative phase-shift between the two polarizations as shown in Figure 36. The overall effect is similar to that introduced by the ordinary and the extra-ordinary axes

in birefringent crystals and so, by using the appropriate number of grids and geometries, it is possible to realize phase retarders. These, in turn, can be used to manipulate the polarization state of the light.

**Demonstrated performance** Quarter-Wave Plates: A stack of three capacitive and three inductive grids is enough to achieve  $90^\circ$  differential phase-shift between two orthogonal axes, which was used to make a metal-mesh quarter wave-plate (QWP) used to convert linear polarization into circular and vice-versa. Mesh QWPs used in combination with polarizers have been used to rotate the polarization angle. Bandwidths ranging from 30% to 90% can be achieved [118].

**Half-Wave Plates:** Differential phase-shifts of a half-wave can be achieved using capacitive and inductive stacks made of four to six grids, depending on the bandwidth required. The challenge of the large bandwidths potentially required by CMB-S4 is to maintain high in-band transmission while keeping the differential phase-shift close to  $180^\circ$ . The first mesh-HWPs had bandwidths of the order of  $\sim 30\%$  [119–121]. More recent broadband realizations have exceeded 90% bandwidths.

**Reflective Half-Wave Plates:** Simple reflective HWPs can be built by locating a polarizer at a quarter-wavelength distance from a plane mirror. These are also called VPMs, and a specific application is also discussed in Section 3.6.6. These devices work only within periodic narrow bands. However, it is possible to realize dielectrically-embedded reflective HWPs with bandwidths larger than 150% by using polarizers and artificial dielectrics [122].

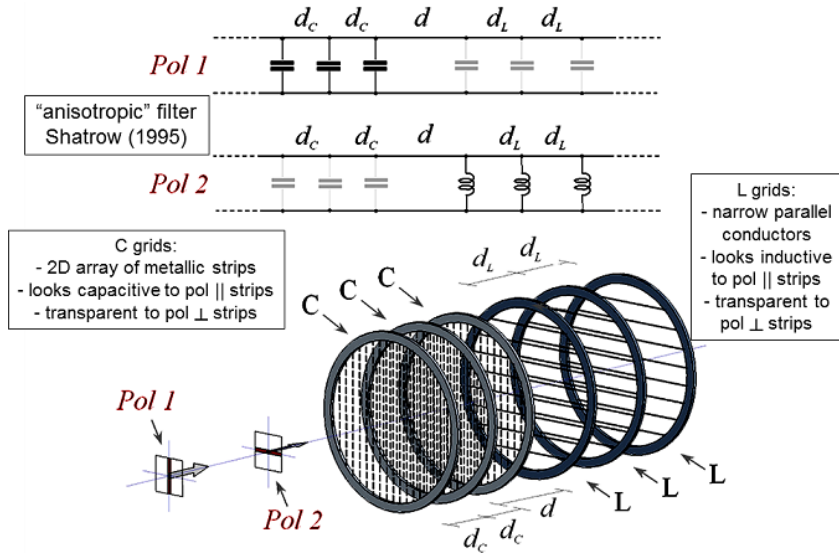


Figure 36: Transmission-line model and grid configuration for metal-mesh HWPs [119].

**Prospects and R&D path for CMB-S4** Broadband metal-mesh HWPs are under active development. R&D similar to that of metal mesh filters (Section 3.3.1) is necessary to increase size of structures as CMB-S4 is likely to require receiver optics and filters of diameter  $\sim 500\text{--}1000$  mm. To increase metal-mesh HWP diameter further, R&D is necessary and should include establishment and verification of high-fidelity photolithography and uniform thermal pressing of multilayer metal-mesh structures up to 1000 mm diameter.

The technology status level of the metal mesh polarization modulator is 3. The metal mesh polarization modular is designed and fabricated for QUBIC experiment.

The production status level of the metal mesh polarization modulator is 2. Metal mesh technology was used in almost every CMB experiment, however demonstration of large throughput production for metal mesh polarization modulator has not modulation done.

### 3.6.5 Rotation mechanisms

**Description of the technology** Stepped and continuous rotation mechanisms have been deployed for CMB experiments. Mechanical design and engineering challenges are very different between room temperature and cryogenic HWP. As reviewed in the introduction to Section 3.6, continuous rotation could potentially offer additional benefits than stepped rotation, and a HWP mounted at cryogenic temperatures will have less thermal emission (and therefore contribute less to detector noise and/or spurious signals) than a room temperature one. However from the mechanical engineering and system integration perspective, continuous and/or cryogenic systems are more challenging than stepped and/or room temperature systems. The optimal solution will take both the benefits and challenges into consideration. In this subsection we discuss three different rotation mechanisms: cryogenic step rotation, cryogenic continuous rotation, and room-temperature continuous rotation.

In addition to rotating the modulator, the rotation mechanism must also measure the rotation angle. The absolute accuracy and repeatability requirement for both stepped and continuous rotation mechanisms is stringent, set by the sensitivity of the experiment, and would likely be of order  $0.1^\circ$  for CMB-S4. Even though such stringent control was not needed by the current generation of CMB experiments, rotation mechanisms have been successfully deployed that meet all of these requirements, and will be reviewed in this section.

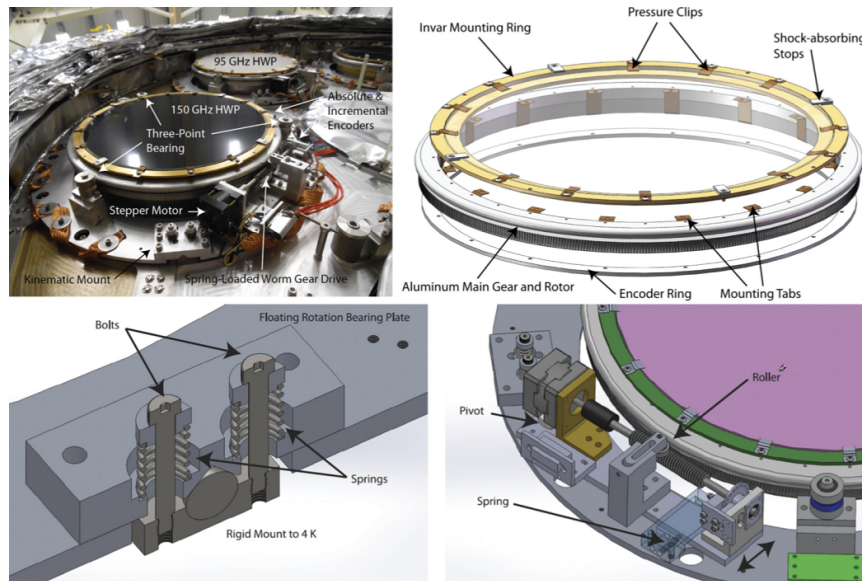


Figure 37: The SPIDER HWP rotation mechanism: the rotator in the SPIDER flight cryostat (top left), detailed view of the HWP mount (top right), close view of the mechanical system (bottom) [103].

**Demonstrated performance** *Ambient-temperature continuous rotation* In ABS [79], a 330 mm diameter HWP, at the entrance aperture of the telescope, rotated in front of the cryostat window by means of an air bearing system. Compressed air, forced through three porous graphite pads around an aluminum rotor, suspended the HWP so it could be rotated at a frequency of 2.5 Hz. The angle was monitored by an incremental encoder disk with 2.4' resolution. Based on this success, ACTPol has implemented this strategy for rotating the HWP and Advanced ACTPol is planning to do the same.

POLARBEAR-1 observed with a 300 K continuously rotating HWP and POLARBEAR-2a is planning to use the same rotator strategy, a 500 mm diameter HWP rotating at 2 Hz. A mechanical system based on rails, rotational stages, thin-section ball bearings, and an AC servo motor rotates the HWP. The AC servo avoids electrical switching noise present in typical stepper motors. Independent rubber sandwich mounts tangentially and axially oriented to the HWP rotation axis isolate the HWP vibrations from the telescope, while a thin rubber gasket isolates the sapphire from vibrations in the bearing.

*Cryogenic stepped rotation* In January 2015 the SPIDER balloon experiment successfully deployed six cryogenically stepped HWPs rotating at 4 K. [103] A worm gear driven by a commercially available modified cryogenic stepper motor rotated the HWP, and the rotation angle was monitored with a custom-built optical encoder with an absolute accuracy of 0.1°. Each HWP was supported by three bearings positioned equidistant around its circumference. For each HWP, the rotation mechanism was estimated to boil off 4 ml of helium per 22.5° of motion. [103] POLARBEAR observed the sky with a stepped HWP cryogenically cooled down to 80 K [63] for first season observation.

*Cryogenic continuous rotation* The balloon-borne EBEX experiment [31, 81] demonstrated, with a flight in 2013, continuous rotation of the HWP at 4 K using a superconducting magnetic bearing (SMB). A ring-shaped permanent magnet and the HWP constituted the rotor which was levitated 3.2 mm above the stator (a high temperature, 80 K, superconductor YBCO ring) [27, 31]. The HWP, mounted inside the magnetic ring, rotated continuously at a frequency of 1.235 Hz. A motor mounted outside the cryostat was connected to a shaft that went through the cryostat wall and turned the rotor with a tensioned kevlar belt. The HWP angle was monitored with an encoder system to better than 0.02°. The absence of stick-slip friction did not produce vibrations. POLARBEAR-2b and POLARBEAR-2c are planning to use the same cryogenic bearing strategy for a 500 mm diameter HWP rotating at 2 Hz. Drive mechanism for the rotators are magnetic driven system.

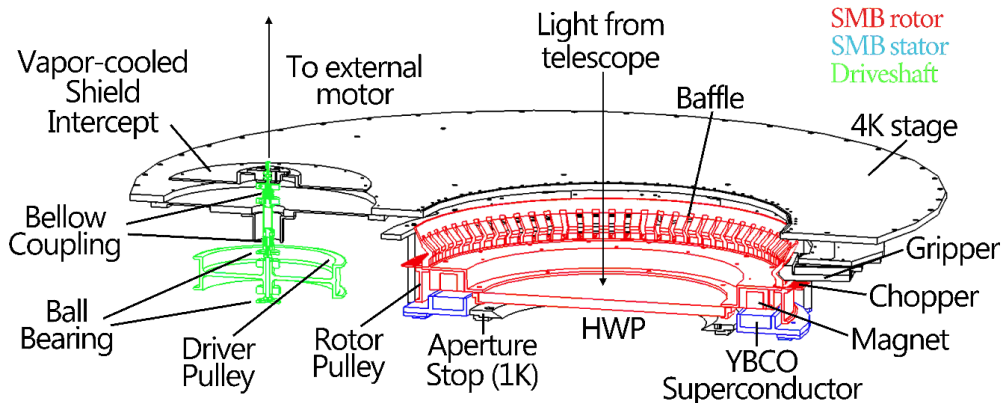


Figure 38: Cross section view of the EBEX HWP rotation mechanism which exploits magnetic levitation [31].

POLARBEAR observed the sky with a stepped HWP cryogenically cooled down to 80 K [63]. POLARBEAR-1 observed with a 300 K continuously rotating HWP and POLARBEAR-2 is planning to use the same rotator

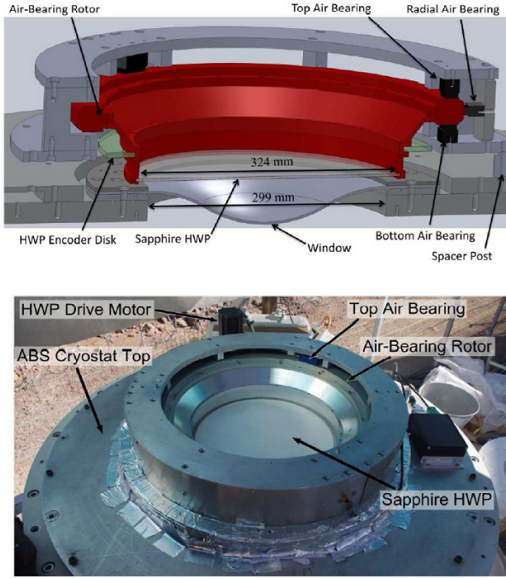


Figure 39: The ABS rotation mechanism. Cross-section drawing of the air-bearing system (Top), the rotation mechanism on the ABS cryostat at the Chilean site HWP and air-bearing system showing the 3.2 mm thick UHMWPE vacuum window, sapphire HWP mounted in its rotor, air bearings, encoder disc, and the overall HWP support. (Bottom) Photograph of the HWP installed on the ABS cryostat at the Chilean site [79].

strategy, a 500 mm diameter HWP rotating at 2 Hz. A mechanical system based on rails, rotational stages, thin-section ball bearings, and an AC servo motor rotates the HWP. The AC servo avoids electrical switching noise present in typical stepper motors. Independent rubber sandwich mounts tangentially and axially oriented to the HWP rotation axis isolate the HWP vibrations from the telescope, while a thin rubber gasket isolates the sapphire from vibrations in the bearing.

**Prospects and R&D path for CMB-S4** CMB-S4 may require a HWP with a diameter larger than current experiments, and scaling up a rotation mechanism creates challenges. Dissipated power from the HWP rotation typically scales linearly with diameter. Large cryogenic bearings may be difficult to buy or produce; the SPIDER mechanism avoids this scaling issue since it has a three point bearing, no moving parts span the entire circumference. A larger CMB-S4 HWP rotator needs more powerful motor(s) with larger inertia and will be heavier. Increased vibrations in a large mechanism could damage the HWP or introduce systematic errors. A large HWP will likely have a longer thermalization time as well as increased thermal gradients and thermal fluctuations, controlling these will impact the choice of rotation mechanism.

The technology status level of the ambient rotation mechanism is 4. ACTpol, ABS and POLARBEAR-1 have taken data with rotating half-wave plate. Analysis on large angular scale data is on going.

The production status level of the ambient mechanism is 3. Parts are available commercially. Also once mechanical design is finalized, machining can be done at industrial scale machine shop. Assembly of the POLARBEAR-1 half-wave plate was done on a short time scale.

The technology status level of the continuous cryogenic rotation mechanism is 4. A continuously rotating cryogenic half-wave plate was used successfully on the EBEX balloon flight, and one is currently being assembled for the second receiver of POLARBEAR-2. .

The production status level of the continuous cryogenic rotation mechanism is 3. A continuously rotating cryogenic HWP was implemented on EBEX. Superconducting magnetic bearings are commercially available. Lead time could be many month, but it could be planned such that bearing won't be a bottle neck in the process.

### 3.6.6 Variable-delay polarization modulators

**Description of the technology** VPMs modulate polarization by introducing a controlled, variable phase delay between linear orthogonal polarizations [123, 124]. VPMs have been implemented with a wire grid polarizer and a mirror that is positioned behind and parallel to the polarizer. In this configuration, the polarization component of the incoming light that has its electric field parallel to the grid wires is reflected by the wires without delay; the perpendicular component passes through the wires and is reflected by the mirror, with that extra distance inducing a phase delay. The output polarization state is determined by the incoming state and the delay introduced by the path difference between the grid and the mirror (see Fig. 40). This electrical delay can be modulated by varying the separation between the grid and the mirror. Alternately, the delay can be fixed, and the entire device can be rotated.

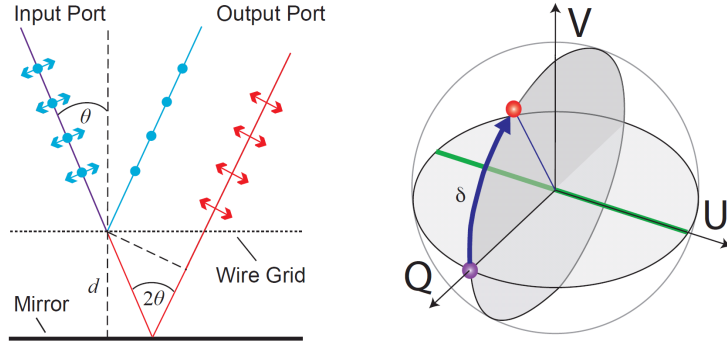


Figure 40: (Left) The VPM introduces a variable phase delay between orthogonal linear polarizations as the distance,  $d$ , is varied [125]. (Right) As the phase delay,  $\delta$ , changes, the polarization state transitions from  $Q \rightarrow V \rightarrow -Q$  with no mixing between  $Q$  and  $U$ .

In the variable-distance mode, as the grid-mirror separation is changed, the VPM will modulate between the linear polarization oriented at an angle of  $45^\circ$  with respect to the grid wires (taken to be defined as Stokes  $Q$ ) and circular polarization (Stokes  $V$ ). In this way, VPMs can be used to switch an instrument's sensitivity between  $Q$  and  $-Q$ . There is no conversion between Stokes  $U$  and  $Q$  during the modulation cycle, so residuals in the phase delay couple to the  $V$  mode, which is expected to be negligible for the CMB. This has the consequence of avoiding  $U \rightarrow Q$  leakage due to non-zero cross-polarization across the telescope beam [126]. This is important because  $U \rightarrow Q$  leakage leads to systematic  $E \rightarrow B$  leakage. While the motion profile can be selected to reduce the impact of this effect, since the CMB is not expected to be circularly polarized, for CMB polarimetry the inherent  $V$  sensitivity of the VPM is a sensitivity disadvantage. Also, the  $Q$  to  $U$  modulation of other modulators enables simultaneous detection of both linear Stokes parameters, VPM-based instruments require a combination of instrument and sky rotation to fully sample the linear polarization space. Performance modeling and design of the VPM requires physical optics modeling, similar to dielectric and metal-mesh HWPs [124].

An advantage of VPM-based systems includes the capability of potentially building the modulator sufficiently large to be positioned at the primary aperture of a  $\sim$ meter-scale CMB experiment. As apertures and modulators get larger, it may be easier to implement the small linear motions associated with a VPM than to implement rotational motion required for a wave plate. Scaling the freestanding wire grid to large diameters would then become the limiting engineering challenge. A VPM built with a freestanding wire grid does not require AR coating. Since thermal emission only arises due to the finite conductivity of the wires and metal mirror, low thermal emission is achieved even at room temperature. In addition, for space applications, VPMs can be implemented without the use of high quality dielectrics that are vulnerable to damage from electrons.

The modulation scheme of VPM-based systems can be tuned to trade sensitivity to Stokes  $V$  for increased sensitivity to linear polarization ( $Q$ ). The limit of this is a square wave motion of the mirror for which polarization sensitivity of the instrument is rapidly switched between the  $Q$  and  $-Q$  state with little time being spent in the  $V$  state. For sinusoidal mirror strokes, a polarization modulation efficiency of  $\sim$ 85% has been realized for a  $\sim$ 26% bandwidth [127], with a decrease in efficiency similar to that for a single-layer HWP for broader bands when used in this mode. Birefringent and metal-mesh HWPs use multiple layers to broaden the modulation bandwidth. Since something similar can not naturally be done with a VPM system, strategies for using VPMs for broader bandwidths and for multichroic focal planes are under development. One strategy includes the optimization of bands to operate at the harmonics of a common VPM modulation function. VPM-based systems could also in principle be used as polarization spectrometers [124] as their polarization transformation is similar to a Martin-Puplett interferometer.

**Demonstrated performance** VPMs were prototyped in the submillimeter using the Hertz polarimeter [128]. These devices utilized kinematic double-bladed flexures [129] to maintain parallelism between the mirror and grid. Piezoelectric drives were used to actuate the mirror, and capacitive sensors were implemented to measure the distance and provide feedback to the control system. The construction of large ( $>0.5$  m) polarizing grids has been developed [130] for the implementation of VPMs as the first optical element of CMB polarimeters. CLASS [127] and PIPER [131] are utilizing VPMs in this capacity. PIPER employs 39 cm diameter VPMs on each of its two telescopes, enabling it to modulate and measure Stokes  $Q$  and  $U$  simultaneously. The VPMs have been constructed to be cryogenically compatible and will operate at 1.5 K [132]. The grid-mirror separation is actuated via a linear voice coil. The parallelism is maintained using a double-blade flexure similar to that used for Hertz, but with a larger operating throw to accommodate the longer wavelengths.

The CLASS VPMs are 600 mm in diameter and are operated at ambient temperature. Because of the longer wavelengths (CLASS operates down to 38 GHz), a four-bar-linkage flexure was used in place of the single-material flexures. A voice coil is used for actuation and an optical encoder is used to measure the distance and close the feedback loop. To fully cover the  $Q - U$  space, CLASS employs instrument rotation around the boresight.

The characterization of the Hertz prototype VPM has led to an improved understanding of the transfer function of VPMs [26]. The resulting model enables the characterization of non-ideal properties of the VPM, including its emission properties. These effects have informed simulations of ground-based, VPM-modulated CMB surveys [133]. These forecasts have provided guidance for survey implementation.

**Prospects and R&D path for CMB-S4** CLASS is currently observing in the Atacama desert, and the first flight of PIPER will be soon. These experiments will inform and refine the data analysis pipeline and systematic error mitigation for VPM-based systems. Beyond CLASS and PIPER, for potential inclusion in CMB-S4 and in a space mission, one of the key aspects of technology maturation would be to scale the VPMs

up to larger sizes to accommodate larger focal planes and higher angular resolution. VPMs can likely be developed up to  $\sim$ 1 meter diameters using current grid manufacturing techniques and flexure technologies (perhaps larger with some development). Strategies for operating VPM-based systems over broader bands would need to be explored and developed.

The technology status level of the VPM is 4. VPM has been deployed in CLASS telescope for 40 GHz operation.

The production status level of the VPM is 2. For a wire grid production, once the machinery (CNC or other) is set up, grids can be made fairly rapidly and reliably. For apertures approaching 2 meters, development efforts to maintain grid flatness and grid-mirror parallelism will need to be undertaken.

## 3.7 Characterization

Accurate characterization of optical elements is crucial for designing high performance CMB receivers. Mechanical, thermal and optical properties of optical elements need to be carefully measured. To reflect actual operation conditions, most of the optical elements need to be characterized at cryogenic temperatures. Most material properties vary enough between manufacturers and grades that literature values can only be used as a guide. However, cryogenic measurements are challenging, and often values are extrapolated from either room temperature or liquid nitrogen temperature, and old property values are adopted in the design of new receivers. In this section, we review material properties that are important for CMB receiver optics, and examples of measurement techniques will be presented.

### 3.7.1 Mechanical properties

**Vacuum windows** A vacuum window needs to support atmospheric pressure while being transmissive to millimeter-wave photons. Because optical loading from room temperature optical material can be significant, it is usually desirable to make the window material as thin as possible, but this requirement works against making it mechanically robust. 3-D mechanical simulators such as ANSYS and COMSOL have been used to study mechanical stress on CMB windows. It is straightforward to model if a window is a simple circular solid plate of a well known plastic, though some subtle details such as the curvature of the inner edge of the supporting ring requires some effort to study properly. The scenario can become complicated for laminated layers of foam or solid plastic with machined features.

To confirm these models and guide the design, multiple experiments have built simple vacuum chambers to test windows for mechanical performance. This allows testing of a fully built window assembly independently of the receiver, and allows observation and study of window failure modes and life testing without putting the receiver itself at risk. It would also be helpful if the fundamental mechanical properties of potential window materials were better understood, which will in turn guide the 3D and pen-and-paper simulations.

**Material defects** Stage-III experiments are using silicon, alumina and sapphire as lens and half-wave plate material. These materials have desirable optical and thermal properties, but both silicon and alumina are brittle. Stage-III experiments that use these materials developed flexible metal mounting schemes to relieve mechanical stress from differential thermal contraction while maintaining optical alignment. One problem with these materials is that they are very strong *as long as there is no material defect*. It is hard to find defects and cracks in these materials, although a low-tech technique (application of ink followed by solvent cleaning) can be useful in cases where the surface is already smooth. Identifying techniques to produce single crystal silicon, large alumina blanks and sapphire boules with low defect rates is important. However, as CMB-S4 expects to use so much of these materials, screening both material and finished optical elements for defects may be helpful. X-ray and ultrasound are used to find such defects, but so far no demonstration of such techniques were done on stage-III lens materials.

**Delamination** Differential thermal contraction is a challenge for anti-reflection coatings. Some methods, such as silicon dicing and thermal spray of ceramic powder, get around this problem by using the same material as the lens. Epoxy coating and plastic coating relies on bonding strength to overcome mechanical stress from thermal contraction as shown in Figure 41. This problem is mitigated by choosing a plastic that has small difference in thermal contraction relative to the optical element material, and in other cases stress

relief grooves have been cut into some plastic coatings to relieve mechanical stress. Further benefits result from details of the application of the AR material, such as surface preparation, use of adhesion promoter, and exact conditions of the cure or fusion of the parts. Due to lack of knowledge of adhesion properties at cryogenic temperatures and mechanical stress from thermal contraction, stage-III experiments cryogenically tested anti-reflection coating delamination on witness samples. To build enough confidence for deployment, it is always desirable to test on a full-size optical element. Such a test is very expensive if failure means the lens or filter is no longer usable, and also adds time to the development phase. It would be useful to build a setup to measure mechanical stress and adhesion properties at cryogenic temperature such that mechanical/cryogenic performance can be predicted.

**Profile** Stage-III experiments used highly accurate bridge type coordinate measuring machines (CMM) at national labs to measure profiles of lenses and thickness of anti-reflection coatings, as shown in Figure 41. There exist CMM machines at national labs that have a large enough throw and accuracy at the micron level, easily able to meet CMB-S4's requirements for cryogenic optics. However, CMM operation requires trained technicians to operate, setup can take a significant time, and it is expected that they will be shared facilities in large labs, so this phase could easily become a bottleneck for CMB-S4.

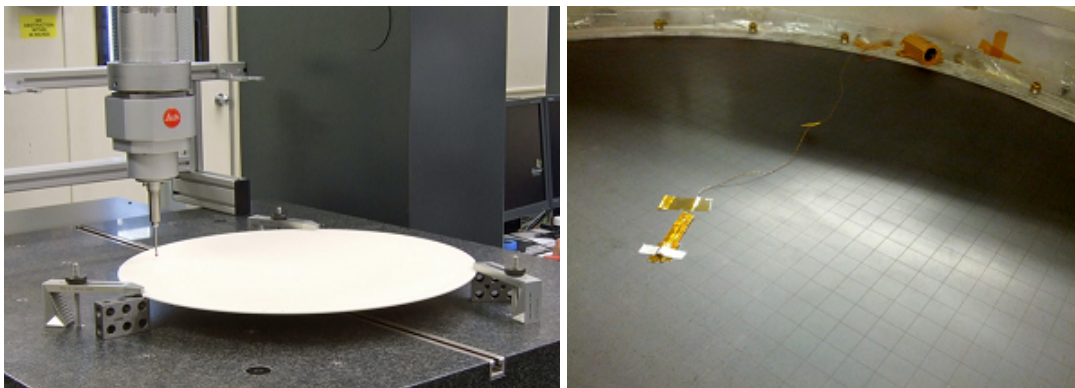


Figure 41: **Left:** Bridge-type coordinate measuring machine used to measure the profile of a lens before and after applying anti-reflection coating. **Right:** Photograph of laser-diced, machined-epoxy, anti-reflection coating.

### 3.7.2 Thermal properties

Stage-III experiments are using silicon, alumina, plastics and copper mesh filters as optical elements. Understanding thermal conductivity, emissivity, and scattering at infrared frequencies are necessary to calculate accurately the final temperature of these optical elements. For detector sensitivity calculations, emission from filters anchored at higher temperature stages can be a significant contribution to in-band loading, and for thermal design the out of band loading on the cold stages from these “warm” filters is also critical.

Thermal conductivity measurement at 4 K and 50 K are routinely done with a heater and well-calibrated thermometers. The community does have a compendium of material property values that do inform us in the design phase, but some aspects, like the performance of material interfaces between dielectrics and metal, are not well-established. Some additional testing will be beneficial to CMB-S4, including filling out thermal

conductivity and specific heat vs. temperature tables for some materials, and determining optimum use of interface materials like indium, Apiezon-N grease, and varnish on our various dielectrics.

### 3.7.3 Optical properties

**Cut-off frequency** Key parameters for an infrared filter are emissivity at infrared frequencies, thermal conductivity, and bandpass parameters. The latter consist of in band transmission, cut-off frequency, roll-off speed and out-of-band attenuation and scattering. These are essential inputs to calculations of sensitivity and cryostat thermal performance. Fourier transform spectrometers (FTS) can be used to characterize the optical performance of filters. A schematic drawing of a setup is shown in Figure 42. A broadband signal from the FTS is transmitted through the sample and detected at a detector (often a cryogenically cooled, NTD-Ge bolometer with JFET readout). Measurements are made with and without a sample in the optical path, the latter to normalize the response of the former, giving transmission as a function of frequency. An example of such plot is shown for the RT-MLI section in Figure 22. From the plot, it is possible to extract in band transmission, cut-off frequency, roll-off speed and out of band attenuation.

**Dielectric constant** Dielectric constant (alternatively, index of refraction) is necessary for optics and anti-reflection coating design. The dielectric constant of a material can be measured accurately with an FTS or a frequency tunable coherent source. The measurement setup with an FTS can be the same as that used for infrared filters described above, although the source and detector may be optimized for in-band performance. Fabry-Perot (FP) fringes in frequency space are generated by interference between the direct pass-through of radiation and the portion of the E-field that reflects band and forth on the sample surfaces. An example of a measurement of an alumina sample with an FTS is shown in Figure 42.

A measurement setup with a frequency tunable coherent source involves the source, a diode detector, and lenses or mirrors to collimate the radiation to pass through the sample and then refocus for the detector. Just like a measurement with an FTS, the measurement with a sample is divided by one without the sample to normalize the response. An example of a measurement of an alumina sample with a coherent source setup is shown in Figure 29. As with the FTS example, the spectral features of FP fringes in transmission data are used to determine the dielectric constant.

The index of refraction of a dielectric material can also be determined by measuring the focal length of a lens of known shape, or the angular deviation of a prism of known geometry, with lower precision.

**Absorption** Absorption loss in the optical elements hurt sensitivity of an instrument by decreasing in-band optical efficiency and increasing optical loading on the detectors. Loss-tangent can be calculated from transmission versus frequency curve from a FTS measurement or frequency tunable coherent source measurement as shown in Figure 43. It can also be calculated by measuring transmitted power as a function of thickness of a sample at single frequency.

**Dielectric Characterization with Fabry-Perot Resonators** An alternative FTS scheme used is to place the sample in the collimated beam between the beamsplitter and the fixed mirror. For materials with slowly varying transmission through the band, this allows simultaneous determination of transmission loss, dielectric constant, and optical sample thickness. The key is that the absolute phase shift as a function of frequency is measured through the sample as well as the Fabry-Perot fringes, thus adding additional information to the analysis.

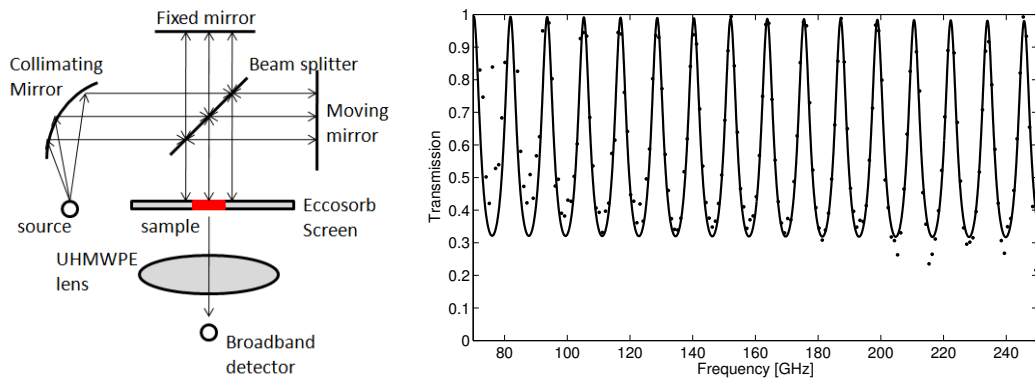


Figure 42: **Left:** Fourier transform spectrometer example. The sample also may be placed between a collimating mirror and beamsplitter, or (as described below) in one of the arms. **Right:** Spectrum of an alumina sample from an FTS scan. The high frequency oscillations are Fabry-Perot fringes from interference associated with surface reflections, and their spacing and amplitude indicate index of refraction when combined with knowledge of the sample thickness. The difference between unity and the values at the peaks of the fringes represent losses in the material, and one can derive the loss tangent as a function of frequency with an accurate measurement.

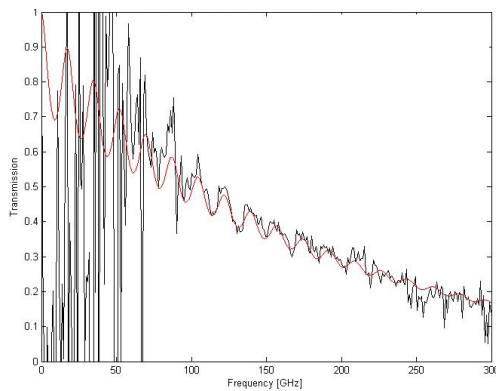


Figure 43: Transmission measurement of epoxy loaded with titanium oxide. Transmission as a function of frequency is fitted with a model to extract the absorption coefficient (and therefore the loss tangent) of a material

The technique can also be used to measure the index of refraction of near-unity materials like Zotefoam when combined with mechanically measured thickness. They have such small surface reflections that FP fringes are unmeasurable while the net phase shift through the material can still be measured, thus allowing determination of refractive index.

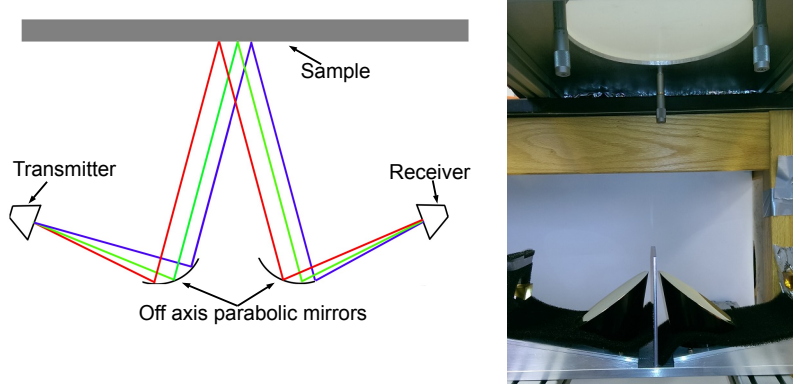


Figure 44: Reflectometer setup at University of Michigan. The reflectometer uses a variable microwave source to measure the reflection off a flat sample. An off-axis parabolic mirror collimates the beam from the source and directs the beam at the sample. Another mirror collects the beam and directs it at a horn-coupled photodiode. Calibrating with known highly reflective sources, this set-up can measure absolute reflection down to 0.1%, with a relative accuracy of a few percent.

**Reflection** Reflection measurements are important for characterization of anti-reflection coatings and absorbers. An example of a reflectometer is shown in Figure 44. In the setup, two off-axis parabolic mirrors are used to collimate and re-focus the beam from a coherent source. A goniometer stage, a stage for the precise manipulation angles, is used to align sample to measure reflection accurately.

There is also metrology techniques for reflectometry which rely on phase modulation of the sample [53, 134, 135]. These approaches enable characterization of smaller reflectances if desired.

**Scatter** Scatter of in-band optical signal from porous material could increase parasitic optical loading on the detectors. It is a special concern for higher frequency bands, where scattering from irregularities in the granularity of various materials (such as metal mesh infrared shaders) may cause an increase in Rayleigh scattering at higher frequencies, which scales rapidly with increasing frequency as  $\sim \nu^4$ . Even a small level of scattering from room temperature optics or those near the aperture of a receiver affect detector sensitivity strongly. The expected level of scattering from candidate optical materials is usually low, since we have already rejected any materials with significant in-band losses. A candidate infrared filter at 50 K with 1% in-band loss, for example, may be acceptable if it is all from absorption (adding 0.5 K loading), but may be intolerable if it were from scattering (adding up to 3 K loading if the scattered rays terminate on an ambient temperature surface), and this does not even take into account spurious polarization effects, for which we are particularly sensitive. The small signal that is nonetheless critical makes scattering measurements challenging. A bright, coherent source such as a Gunn diode can be used to illuminate a test sample, while a detector is placed off-axis from the line of sight to measure the scattered signal. In this setup, the measured signal is weak since the detector catches scattered light within a limited solid angle. An integrating sphere may be used to improve sensitivity. For the wide spectral range coverage required for CMB-S4, the ability to characterize scattering will be important.

Stanford's prototype scattering test setup is shown in Figure 45. Only a 1-D sweep of angle is measured, reducing the sensitivity to total power scattered and introducing uncertainties since 2D beam shapes must be estimated based on incomplete information. Also, the beam from the source convolved with the beam seen by the detector is several degrees across, so small-angle scattering is difficult to measure. Nonetheless it can put limits on scattering. A next-generation prototype is envisioned making use of larger optics to narrow the beams and a 2D gimbal hinge to measure a greater fraction of the full sphere. An alternate setup is considered having a Winston cone to capture broader solid angles to increase detection sensitivity off-axis. Enclosure of the entire rig in an absorber-lined box may be needed.

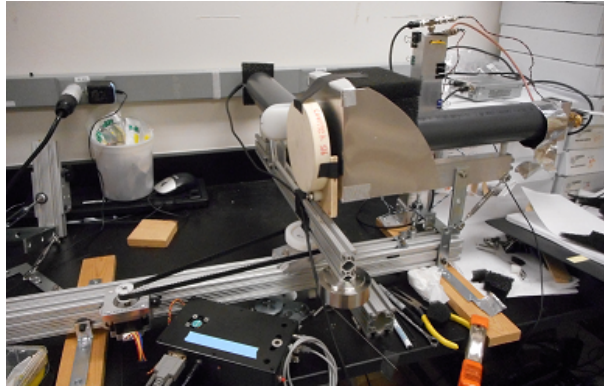


Figure 45: Stanford scattering test prototype. Gray tubes to the right and on the far side are, respectively, the source collimator and the detector camera. Both are absorber-lined tubes with HDPE lenses. Installed are a 95 GHz broadband source and detector, both linearly polarized. A 25 mm aperture in the aluminum shield just upstream of the sample (not seen in photo) defines the beam. As seen, the detector camera is mounted on a motorized swing-arm to sample a 1D cut through the forward-scattering hemisphere. A large absorber (to left, out of the photo) absorbs most of the un-captured, un-scattered radiation. To sample a more complete fraction of the hemisphere, one can in principle rotate source, detector, and sample through various angles and re-scan the 1D arc, but this procedure is cumbersome, thus motivating a more sophisticated setup. See text.

**Cryogenic sample testing** CMB receivers cryogenically cool optical elements to take advantage of improved material properties at cryogenic temperatures. For example, silicon, alumina, and sapphire's absorption losses decrease significantly at cryogenic temperature. Thermal conductivity also changes strongly with temperature, and the refractive index of some materials change significantly as a function of temperature as well. Since many optical elements are used at cryogenic temperatures, characterizing properties of material at cryogenic temperatures is essential for predictable design of a receiver. There are multiple challenges associated with measurement of a sample at cryogenic temperature.

For testing at temperatures above 77 K, LN2-cooled atmospheric-pressure sample chambers have been used in several labs. Introduction of dry nitrogen (or the LN2 evaporation) keeps the sample dry, otherwise water vapor, CO<sub>2</sub>, etc. will condense on the sample under test. A setup that was used to cool samples to approximately 100 K is shown in Figure 46. For larger samples and those with lower thermal conductivity such as polyethylene, additional infrared blocking becomes necessary or the sample will not become sufficiently cold.

Lenses for the CMB receivers are mounted at 4 K, and cooling a sample to approximately 4 K in a test chamber is more challenging. One approach is to immerse samples and detector in liquid helium, as shown in Figure 46. An optical signal is transmitted to a sample through a light pipe, and mechanical feedthrough

allows rotation of sample holder immersed in liquid helium. To perform measurement with and without samples, mechanical motion at 4 K is required. A cryogenic stepper motor, or a mechanical feedthrough can be installed in a dewar to move a sample. While this LHe direct contact technique is good for absorption loss measurements, it is more difficult for dielectric constant measurements since the LHe optical properties must be accounted for. A vacuum 4 K system, with significant infrared blocking, is important for the latter.

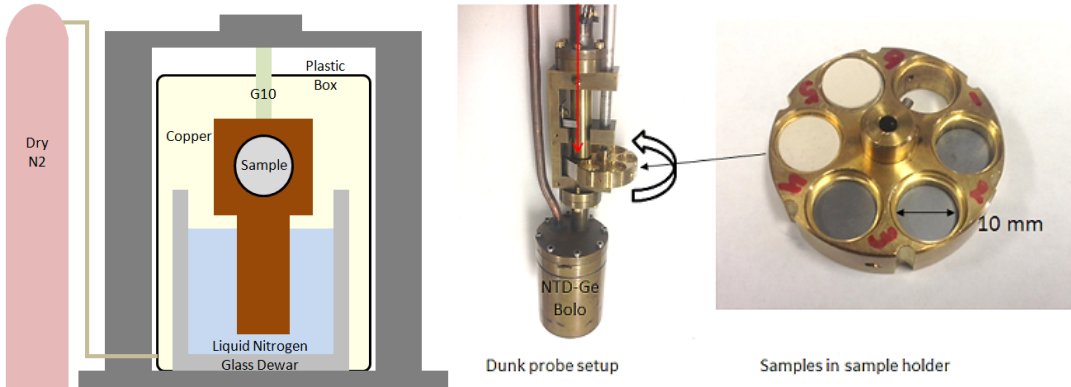


Figure 46: **Left:** In this setup, a sample is conductively cooled through a copper holder that is immersed into liquid nitrogen. Dry nitrogen fills plastic container around the sample to keep the sample dry. A Zotefoam window was added to the plastic box to let millimeter wave signal through.

## 3.8 Conclusion

Optical technologies for observations of the CMB are rapidly evolving with many exciting approaches reaching full maturity through deployments on Stage-III experiments. Work is needed to select and optimize the optical materials needed for CMB-S4 as was discussed in each of the technology sections.

While this document has focused on presenting the current state of the art, there are opportunities for new ideas to develop during the CMB-S4 process including synergistic combinations of approaches. For example, combinations of metamaterials with low loss dielectrics could result in wave plates, lenses, and filters with superior optical properties and simplified manufacturing. This document represents the first step in the initiation of a community-wide conversation about how to implement the optical system for CMB-S4. We look forward to the exciting technological developments that will come out of this process.

### 3.9 Summary of optics technologies

	Lab Demonstration	Sky Demonstration	Path to CMB-S4	Section	T/PSL
<b>Window</b>					
UHMWPE	✓	ABS/ BICEP3/CLASS/EBEX SPIDER/SPT-3G, 700 mm ACTBICEP2/PB/SPT, 500 mm	large diam, emission	3.2.1	5/5
Zotefoam	✓	ACTBICEP2/PB/SPT, 500 mm	large diam, scatter	3.2.2	5/5
Cryowindow	Foam/alumina	-	full scale lab demo	3.2.2	1/1
<b>IR Filters</b>					
MMF	✓	Mult. exp. < 300 mm	530 mm dia, prod rate	3.3.1	5/3
Laser Ablated	✓	BICEP3/SPT-3G	prod rate	3.3.2	5/3
Plastic	✓	BICEP2, BICEP3	temp/emission	3.3.3	5/5
Alumina	✓	BICEP3/PB2/SPT-3G, 700 mm	large dia, prod rate	3.3.4	5/3
Silicon	300 mm	-	Prod rate, diameter	3.3.5	2/1
RT-MLI	✓	PB2, GroundBIRD, SPT3G	✓	3.3.6	3/5
<b>Lens</b>					
Silicon	✓	ACTPol < 480 mm	Size, AR prod rate	3.4.1	5/3
Alumina	< 880 mm	BICEP3/PB2/SPT-3G < 700 mm	loss	3.4.2	5/3
Plastic	✓	Stage-II, CLASS < 300 mm	low index	3.4.3	5/5
MML	Measured beam	-	530 mm, prod rate	3.4.4	1/1

	Lab Demonstration	Sky Demonstration	Path to CMB-S4	Section	T/PSL
<b>AR Coating</b>					
Thermal Spray	PB-2 in prep ✓	SPT-3G (deployed)	low dielectric outer layer	3.5.2	3/3
Epoxy	3:1 bandwidth PB-2 in prep ✓	BICEP-3	CNC fabrication	3.5.3	5/2
Diced Silicon	4:1 bandwidth: ✓	ACTPol/AdvACT	efficient fabrication	3.5.4	5/3
DRIE Silicon	1.5:1 bandwidth: ✓	-	apply to curved surfaces	3.5.5	1/1
Laser Ablated	3:1 bandwidth ✓	-	larger areas / lower freq	3.5.6	1/1
Plastic	✓	EBEX (on sapphire)	application on high $\epsilon$ lens	3.5.1	5/5
Machined Plastic	CLASS 90 GHz ✓	SPT-3G window	application for curved lens	3.5.7	4/5
MMARC	✓	-	on sky demo	3.5.8	1/1
<b>Pol Mod</b>					
Sapphire	✓	PB, ABS, EBEX	broad-band / large diameter	3.6.2	4/5
Silicon	✓	ACTPol	efficient fabrication / improve glue	3.4.1	4/3
MMPolMod	✓	-	design / 60 cm fabrication	3.6.4	3/2
AmbRotation	✓	PB, ACT/ABS	reliability / encoder	3.6.5	4/3
CryoRotation	PB-2 ✓	EBEX	electronic drive electronics	3.6.5	4/3
VPM	✓	CLASS	large diameter, efficient fabrication	3.6.6	4/2
<b>Characterization</b>					
reflection	✓		cover all CMB-S4 bands		
transmission			improve accuracy		
metrology			extend to larger diameters		
scattering			improve sensitivity		
emission			measure emission of cold optics		

# 4

---

## Focal plane optical coupling

### 4.1 Introduction

The performance of a CMB experiment depends critically on the design of the focal plane. The focal-plane feed determines the shape and polarization properties of the pixel beams and therefore plays a strong role in controlling systematic errors. The feed design also can determine the total bandwidth and number of photometric bands of each pixel, which is important for the efficient use of a telescope’s focal plane area. This chapter discusses the detector system from the focal-plane feed up to the power detection element. Chapter 5 discusses the detector itself (TES or KID) and the readout multiplexing system.

There are a number of successful approaches that have been or are being implemented by different experiments. They include using a telescope with a receiver observing at a single frequency band with single-color lenslet-coupled antennas or with corrugated horns (POLARBEAR-1, ABS) [63, 79], using one telescope with multiple receivers each observing at one frequency with corrugated horns (ACTPol) [136], using multiple telescopes each observing at a single frequency with antenna-array feeds or with horn-coupled antennas (Keck Array, BICEP Array, CLASS 40 & 90) [127, 137, 138], using a multichroic receiver observing on one telescope with single color corrugated horns or smooth wall profiled horns (SPTpol, CLASS 150/220) [127, 139], or using a multichroic receiver observing on one or more telescopes with multichroic lenslet-coupled detectors (POLARBEAR-2, SPT-3G, Simons Array) or with feedhorns (ACTPol, Advanced ACTPol) [9–11, 65]. Experiments with single color detectors first successfully detected B-mode polarization, and multichroic detectors have since been deployed and years of data has been collected. The diversity of detector designs used in these experiments emphasizes the complexity of global experimental optimization. In this chapter, we survey the current state of technologies for antennas and RF circuit architectures developed for CMB polarization experiments. In each section, we give a basic introduction to the technology, describe the current implementation, and identify necessary research and development to bring the technology to a readiness level required for CMB-S4.

## 4.2 Background

### 4.2.1 Foreground considerations for frequency band selection

For a ground-based microwave telescope, the atmospheric transmission profile defines four discrete frequency windows that are useful for observation: a low-frequency band that extends from  $\sim 30$ – $50$  GHz, mid-frequency bands from  $\sim 75$ – $110$  GHz and  $\sim 130$ – $170$  GHz, and a high-frequency band above  $\sim 190$  GHz as shown in Figure 47 [140]. These windows are separated by molecular oxygen lines at 60 and 120 GHz and a water line at 183 GHz. Above 200 GHz, atmospheric transmission and sky noise get steadily worse. There may however be useful bandwidths for mapping dust foregrounds up to the 325 GHz water line if the level of dust foregrounds increases faster than atmospheric noise. While mapping speed considerations would favor designing instruments that cover as much of this bandwidth as possible, the problem of separating the CMB signal from astrophysical foregrounds will require CMB-S4 to feature a number of somewhat narrower frequency bands.

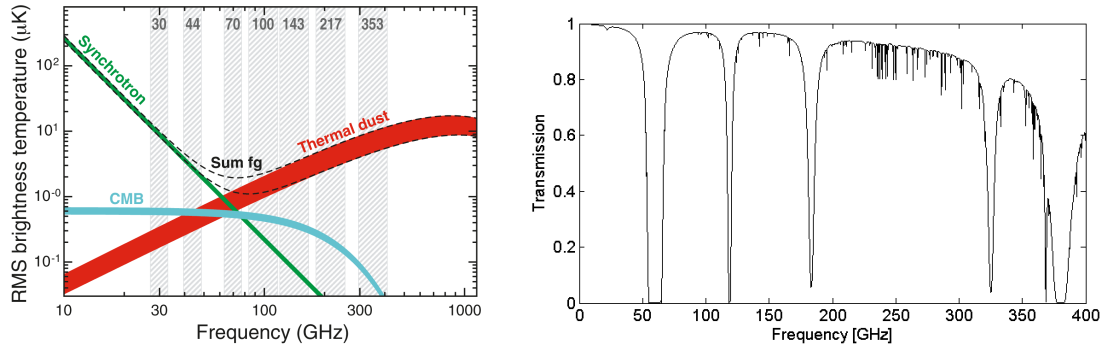


Figure 47: (Left) Root mean square (RMS) brightness temperature for polarization as a function of frequency and astrophysical component [141]. (Right) Atmospheric transmission coefficient for a precipitable water vapor level of 1 mm and an observing elevation angle of 60 degrees [142].

The two dominant polarized astrophysical foregrounds for CMB observations are synchrotron emission from free electrons and thermal emission from microscopic dust grains. Foreground emission can be distinguished from the CMB by its spectrum. Relative to the  $2.73\text{ K}$  blackbody of the CMB, synchrotron emission grows brighter at low frequencies while dust is brighter at high frequencies as shown in Figure 47. Multi-frequency data allows us to identify and remove foreground signals. Indeed, the science goals of CMB-S4 lead to stringent requirements on the accuracy and precision of foreground separation. Even over a small region of clean sky, the power spectrum of polarized dust at 95 GHz exceeds the  $r = 0.001$  tensor spectrum by more than an order of magnitude, highlighting the difficulty of this problem (see Figure 7 in Reference [1]).

With current data, we are just beginning to be able to measure the properties of polarized foregrounds at high Galactic latitude [143]. As the signal-to-noise ratio on foregrounds improves, we will likely find that the simple parametrizations in use today are inadequate, for instance due to spatial variation of the spectral index or frequency-dependent variation of the polarization angle [144]. Failure to account for the full complexity of the foreground signals could lead to bias on cosmological parameters. The job of detecting and constraining these foregrounds requires better frequency resolution. To account for this yet unknown complexity, the projections for inflation science from tensor modes with CMB-S4 make a baseline assumption of eight frequency bands, splitting each atmospheric window into two sub-bands [1, Section

2.3]. Our understanding of this problem will improve with data from Stage-III experiments, but CMB-S4 sensitivity will remain at the leading edge of our ability to separate components.

### 4.2.2 Total bandwidth and spectral resolution

Current bolometric detector technology has reached the noise limit set by CMB photon noise. Once individual detectors are limited by photon noise, the mapping speed for a fixed field of view can be increased by use of multichroic detectors. Designing an array of diffraction-limited, multi-chroic pixels in a limited field of view introduces a sensitivity optimization challenge. Optimizing pixel size given a fixed focal plane area must balance two competing effects: small pixel diameter allows for more detectors but degrades aperture illumination efficiency while large pixel diameter improves aperture illumination efficiency but reduces the detector count. The product of these opposing effects gives a mapping speed peak at some optimal pixel diameter.

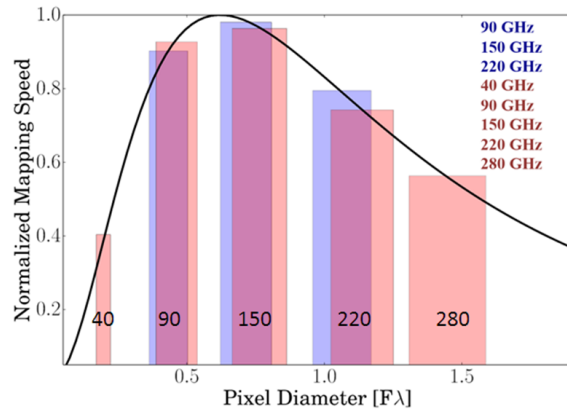


Figure 48: Mapping speed (CMB spectrum) versus pixel size in units of  $F/\lambda$ , where  $F$  is the final  $F/\#$  at the focal plane and  $\lambda$  is the observation wavelength. We assume a fixed focal plane area filled with diffraction limited multi-chroic pixels. Plotted mapping speed is from a 10K telescope with a 100 mK focal plane. We show example band locations for a three (90/150/220 GHz) and five (40/90/150/220/280 GHz) -band receiver. Band positions for given a pixel diameter are chosen to optimize integrated mapping speed with more weight on CMB bands. The optimal pixel size for a three band detector and five band detector is shifted due to this optimization.

Figure 48 shows mapping speed (referenced to a CMB) as a function of detector pixel diameter assuming multi-chroic receiver with a  $\sim 10$  K telescope temperature and a 100 mK focal plane of fixed area [145]. This calculation shows that given a single observation wavelength  $\lambda$  and a  $F/\#$  “F” at a focal plane, one ought to set the pixel diameter at small  $F\lambda$ , near  $\sim 0.6$ . However, given multiple observation bands on a single multi-chroic detector pixel, the optimal pixel size at some frequencies will be different from others.

Also, example band locations for a three/five-band receiver given a pixel diameter that optimizes integrated mapping speed across the experiment’s bandwidth are shown in Figure 48. As an experiment adds more total bandwidth, there is a decrease in mapping speed in channels away from the optimal frequency. Therefore, even though building multi-chroic detectors can improve sensitivity by enhancing foreground removal and total optical throughput, the relative sensitivity in each frequency channel should be considered carefully when choosing the total bandwidth of a pixel.

As discussed in Section 4.2.1, dividing the atmospheric windows into sub-bands helps resolve foregrounds using their spectral dependencies. On-chip multi-chroic band pass filter techniques that are used to divide broadband signals into sub-bands are described in Section 4.4.2. There are challenges associated with packing spectral bands close together, such as increasing the number of bands introduces readout challenges, including the possibility of a greater multiplexing factor, more complicated wiring schemes, and higher interconnect density. Therefore, the experiment's design should be optimized to find a balance between the capability of a focal plane and the complexity of a design.

## 4.3 Antennas

The choice of microwave antenna influences the angular response, polarization properties, bandwidth and efficiency of a detector. An ideal antenna has a polarization-symmetric beam pattern across its entire spectral bandwidth.

Multiple antenna technologies have been used for CMB experiments: horns, lenslet-coupled antennas, antenna arrays, and direct absorber coupling. Broadband horn antennas have been observing the CMB on the ACTPol and Advanced ACTPol experiments. Broadband lenslet coupled antennas were deployed on SPT-3G in early 2017, will be deployed on POLARBEAR/Simons Array in 2017, and cover two to three atmospheric windows with one pixel. Single-band antenna arrays are being used on BICEP2/Keck Array/BICEP3 experiments, and development aimed at increasing the bandwidth for antenna arrays is ongoing. Direct absorber detectors are being developed for future balloon and satellite CMB experiments.

This section will review the basic properties and current state of these detector along with supporting technologies. Demonstrated performance and future prospects are given for each topic.

### 4.3.1 Feedhorn coupling

Feedhorns have been widely used in radio astronomy. Horn antenna defines angular response of a detector. Planar ortho-mode transducer (OMT) probe can be used to couple RF power to microwave circuit on a chip. RF sensitive detectors, can be placed directly at one end of a horn for direct detection or behind microwave circuit after on-chip signal processing. In this subsection, technologies for feedhorn-coupled detectors designed for CMB polarimetry experiment is described.

#### 4.3.1.1 Feedhorns

**Description of the technology** Feedhorns have been a work horse of radio astronomy for generations as they offer the ability to minimize polarization systematic errors and adjust the detector beam size with no need for AR coatings. The leading approach for control of beam systematics has been the corrugated feed which produces a nearly Gaussian beam shape with small polarization leakage over a wide band [146–148] (see Figure 49). Recently, advances in computer driven optimization have facilitated new feed designs based on a smooth spline-profiled taper [149]. These spline-profiled designs can achieve beam properties comparable to what has been demonstrated with corrugated feeds, while providing opportunities to optimize for a combination of beam systematic errors and increased array packing densities. Both spline-profiled and corrugated feeds have been demonstrated with more than an octave of bandwidth. Other feedhorn design approaches, including dielectric-loaded feeds, offer paths to extend this technology to achieve broader bandwidth while maintaining attractive beam shapes and low beam systematic errors.

**Demonstrated performance** Feedhorns have been used widely in observatories for the CMB including COBE, WMAP, PLANCK, SPTpol, ACTPol, and many other experiments. The ACT collaboration has recently deployed two dichroic arrays using feedhorns to define the detector coupling over more than an octave of bandwidth. The first array of 256 horns was deployed in early 2015 and covered (75-165) GHz using ring-loaded corrugated feeds [150]. The second array was comprised of 503 spline-profiled horns that covered the (120-280) GHz observation band and deployed in mid-2016 [148]. These horn arrays were

fabricated out of stacked silicon wafers that are each etched with a pattern of holes and plated in gold after assembly. The use of silicon wafers eliminates the need to account for differential thermal contraction between the horn array and the silicon detector wafers and has lower mass than metal horn arrays. Further, the use of photolithography allows for tight tolerances of  $1\text{-}2\ \mu\text{m}$  over 150-mm wafer. The spline-profiled feeds were optimized to maximize the packing density of the feed array while controlling beam systematic errors to the level required for the AdvACT experiment. The 90/150 GHz spline-profiled feedhorn designed for AdvACT improves the mapping speed of the array by a factor of  $\sim 1.8$  over the 90/150 GHz corrugated ACTPol array and has a cross-polarization lower than  $-18\text{ dB}$ . The analysis of the data from these arrays is ongoing, but simulations of estimated polarization leakages show that the feeds are not expected to limit the measurements.

**Prospects and R&D path for CMB-S4** The technology status level of the feed horn system is 5 for single frequency operation and 4 for dichroic design. Feed horn detector array has deployed in SPT-pol and ACT-pol. Data from dichroic horn system from ACT-pol is currently being actively analyzed. The production status level for the current feed horn system is 3 due to challenges associated with scalability of silicon platelette fabrication.

Several technical aspects of producing feedhorns will need to be addressed for CMB-S4. Current methods of fabricating platelets (a stack of micro-machined silicon wafers) can be time consuming, and production is currently limited to 150 mm wafers. Mass producing platelets on wafers up to 305 mm is achievable, but needs to be demonstrated. The deep reactive ion etch (DRIE) rate dictates that a typical feedhorn array requires  $\sim 20$  hours of etching to produce all platelets. Additional time is also required for etch preparation and post-etch wafer cleaning. Such work can be outsourced to an industrial micro-electromechanical (MEMs) facility. Laser etching could further expedite the processing time for wafers and can be considered as an alternative. In addition, improved methods of platelet metalization are likely required. On the design side, if broader bandwidth is desired, it is possible to further optimize the spline-profiled design or develop new approaches including a dielectric-loaded feed based on silicon metamaterials. The current OMT design limits the bandwidth ratio (ratio of the highest frequency and the lowest frequency) to  $\sim 2.3:1$ , but the use of a quadridge architecture (a horn with four internal “fins”) in combination with dielectrically-loaded feeds could open the possibility of  $6:1$  bandwidth coupling. Finally, there are trade-offs between beam systematic errors and coupling efficiency, especially at small aperture sizes, that must be evaluated based on a system level optimization that includes the telescope and detector array design.

**Lab Demonstration:** 2.3:1 bandwidth, round beam,  $<-18\text{dB}$  cross-pol. 90/150/220/350 GHz

**Sky Demonstration:** Multichroic horns 90/150 GHz (ACTPol) 150/230 GHz (AdvACT)

**Path to CMB-S4:** Speed up production rate, advance spline-profile design

#### 4.3.1.2 Planar OMT coupling

**Description of the technology** A feedhorn couples to a planar circuit on a silicon wafer by use of a broad-band, planar OMT comprised of four niobium probes fabricated on a low-stress, silicon nitride membrane as shown in Figure 50. These fins separate the two orthogonal polarizations and launch radiation onto superconducting coplanar waveguide (CPW) transmission lines (TLs). A wide bandwidth stepped impedance transformer is used to switch from CPW to low impedance micro-strip lines that travel to diplexers comprised of resonant stub filters that separate the two frequency bands. Light from each pair of opposite OMT probes within a given frequency band are symmetrically fed into a hybrid tee [152–154] that differences the two

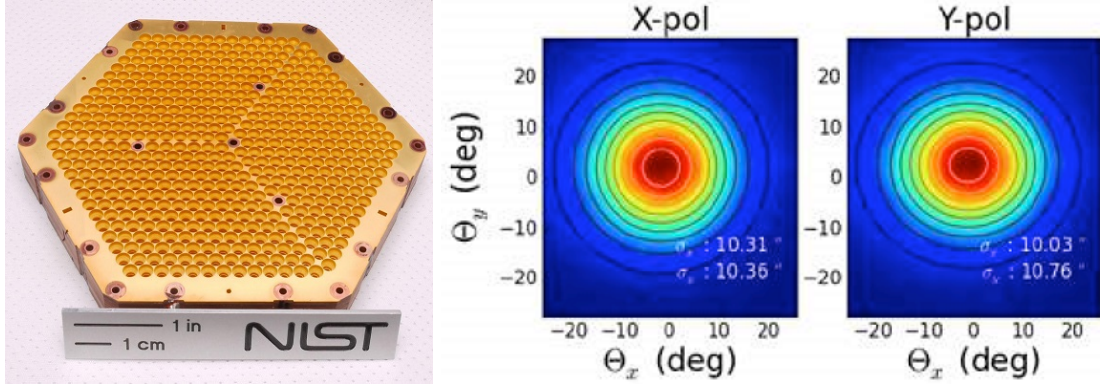


Figure 49: (Left) A photograph of the fully assembled and gold coated 150/230 GHz AdvACT feedhorn array. The array consists of 503 spline-profiled feeds that were optimized for low beam systematic errors and high coupling efficiency with a small aperture. (Right) 2D angular response measurements of an ACTPol single-pixel detector consisting of a single corrugated feedhorn and a single 90/150 GHz dichroic pixel [151]

signals and leads to single-moded (TE11) output over 2.3:1 ratio bandwidth. Unwanted higher order modes are dissipated on the substrate and relative power changes from the lowest order waveguide mode are sensed with TES bolometers. Details of planar OMT coupling can be found in [153, 155], and in [156–159] for implementation on single-crystal silicon for the CLASS focal planes.

**Demonstrated performance** Multiple experiments have been deployed with single color planar OMT coupled feed horns [79, 127, 136, 139]. A multichroic polarimeter array covering the 90 and 150 GHz bands was deployed in 2015 as part of the ACTPol experiment and has logged 2 seasons of observations [9, 136]. In mid 2016, a second 150/230 GHz array was deployed on the ACT telescopes as the first installment of the Advanced ACTPol instrument. The beams are defined by feedhorns, which offers flexibility to optimize sensitivity and control of systematic errors, and the OMT defines a frequency independent polarization angle offering an advantage for control of polarization mixing effects. Multiple deployments of experiments with single colored OMT coupled horns and multichroic OMT coupled horn arrays represent full system demonstrations of this technology and all the ancillary systems, paving the way for their use on even more ambitious future experiments.

**Prospects and R&D path for CMB-S4** The technology status level and production status level for OMT coupling carries over from the horn coupled detector system. The technology status level of the feed horn system is 5 for single frequency operation and 4 for dichroic design. Feed horn detector array has deployed in multiple CMB polarimetry experiments. Data from dichroic focal plane is currently being actively analyzed. The production status level for the current feed horn system is 3 due to challenges associated with scalability of silicon platelet fabrication.

CMB-S4 requires frequency coverage from roughly 30-300 GHz with potentially finer spectral resolution than what has been deployed to date. Frequency scaling above 300 GHz has been demonstrated with OMT coupled feedhorns. Work must be done to fully demonstrate detectors with (i) improved spectral resolution, (ii) a low enough frequency limit, and (iii) improved optical coupling efficiency through design and control of dielectrics.

OMTs based on a quadruple ridge wave guide are under development to increase the bandwidth of this technology. Quad ridge wave guide has been demonstrated in systems with single mode performance in excess of 6:1 ratio bandwidth into Vivaldi style feeds. The current design is based on the eVLA 1-2 GHz receiver and achieves 3.3:1 bandwidth, in line with the current bandwidth limits of our feed horns.

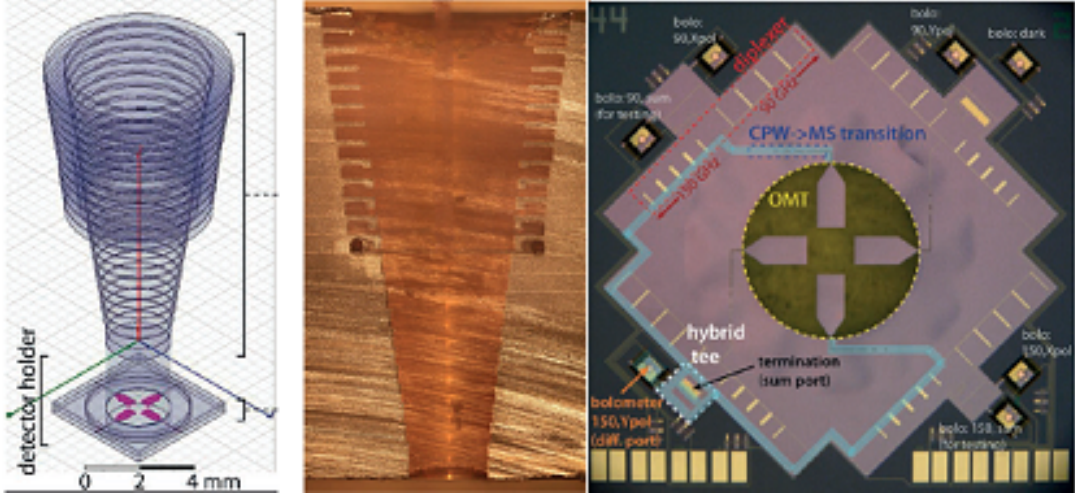


Figure 50: The dual-band, dual-polarization sensitive pixel consists of a silicon-platelet corrugated-feedhorn (cross-section of an actual horn shown) coupled to a polarimeter chip containing Nb probes, diplexers, hybrid tees and TES bolometers.

<b>Lab Demonstration:</b>	SiN dielectric feed achieved 70% efficiency
<b>Sky Demonstration:</b>	90/150 GHz (ACTPol) 150/230 GHz (AdvACT)
<b>Path to CMB-S4:</b>	Improved spectral resolution, low frequency, coupling efficiency

#### 4.3.1.3 Direct kinetic inductance detector coupling

**Description of the technology** Two RF coupling strategies are currently being developed for MKIDs: (i) Horn-coupled, multichroic MKIDs and (ii) dual-polarization lumped-element KID (LEKIDs), which are shown in Figure 51. For the multichroic MKIDs, RF coupling is achieved with an OMT-coupled feedhorn design as described in Sections 4.3.1.1 and 4.3.1.2 [161]. Multichroic MKID detectors share common RF circuit elements with multichroic TES detectors between the OMT coupling and the RF termination. RF termination design for MKID detectors is described in Section 4.4.4. LEKIDs are placed directly at output of a horn. It makes direct polarization sensitive detection of RF power without on-chip RF signal processing. For the dual-polarization LEKIDs, the planar resonators are made from a thin aluminum film deposited on a silicon substrate, and they consist of two orthogonal inductors connected to inter-digitated capacitors (IDCs). Each resonator is capacitively coupled to a TL, which carries a GHz probe tone that drives each resonator at its resonant frequency. The inductor in the resonator acts as the absorber, which is fed by a horn that is perpendicular to the silicon substrate. Each inductor is naturally polarization sensitive, preferentially absorbing radiation with the E-field aligned to the thin inductor traces. The dimensions of the inductor are optimized so the wave impedance is well matched to the incoming radiation [162]. Millimeter-wave photons from the sky absorbed in the inductor break Cooper pairs, which changes the quasiparticle density. The

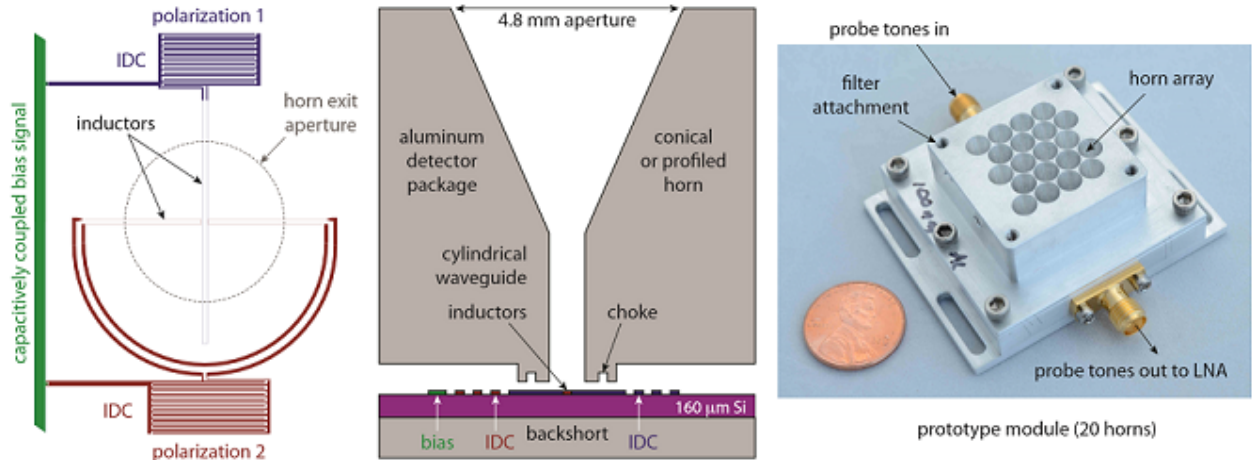


Figure 51: (Left) Schematic of LEKID that is sensitive to one spectral band centered on 150 GHz [160]. The *LC* resonator sensitive to the horizontal polarization is colored red, while the resonator sensitive to the orthogonal polarization is colored blue. The inductor in the resonator is the photon absorber. The dotted circle represents the waveguide exit aperture at the back of the horn. The resonators are driven by a probe tone capacitively coupled to a TL for read out, which is colored green. (Center) A cross-sectional view of a single array element. (Right) A photograph of a 20-element dual-polarization LEKID module.

quasiparticle density affects the kinetic inductance and the dissipation of the superconducting film, so a changing optical signal will cause the resonant frequency and internal quality factor of the resonator to shift. These changes in the properties of the resonator can be detected as changes in the amplitude and phase of the probe tone.

**Demonstrated performance** LEKID detectors that are sensitive to polarized millimeter wave signal were deployed to study galactic magnetic field at 140 GHz and 260 GHz by NIKA [163].

The 150 GHz LEKID technology for CMB polarimetry observation has been extensively studied in the laboratory [160, 164, 165], but not yet demonstrated on the sky. Similar 1.2 THz devices are being developed for BLAST-TNG [166, 167]. Prototype arrays of the multichroic MKIDs will be fabricated starting in the summer of 2016. Laboratory studies of these prototype arrays will follow.

**Prospects and R&D path for CMB-S4** The multiplexing factor, which is one of the key advantages of MKIDs, is largely determined by the quality factor of the resonator and the bandwidth of the readout. In terms of scalability, it should be possible to make the required multi-kilo-pixel arrays of the dual-polarization LEKIDs now given the manufacturability of the design.

On sky demonstration of 1.2 THz LEKID detectors for BLAST-TNG, and further demonstration of 150GHz LEKID detector will reveal competitiveness of this technology.

The technology status level of the LEKID detector system is 2. LEKID system has been demonstrated in laboratory, but deployable focal plane with LEKID detector has not been fabricated and demonstrated. The production status level for the current feed horn system is 3. Demonstration of simplicity in microfabrication shows that LEKID is promising technology bring scalability to CMB-S4. PSL for LEKID will advance once the fabrication of large pixel-count LEKID arrays has been demonstrated.

Horn coupled MKID

**Lab Demonstration:** Design is complete. Fabrication will start soon

**Sky Demonstration:** -

**Path to CMB-S4:** Scalability is KID detector's strength. Lab demonstration of scalability

Horn coupled LEKID

**Lab Demonstration:** 150 GHz LEKID studied in the laboratory

**Sky Demonstration:** 1.2 THz devices are being developed for BLAST-TNG, 140/230 GHz NIKA

**Path to CMB-S4:** Scalability is KID detector's strength. Lab demonstration of scalability

### 4.3.2 Lenslet coupled antennas

Lenslet coupled planar antenna is used in millimeter and sub-millimeter frequencies. In this subsection, performance of lenslet coupled broadband antenna and manufacture challenge for anti-reflection coated lenslet array will be discussed.

#### 4.3.2.1 Lenslet coupled broadband antennas

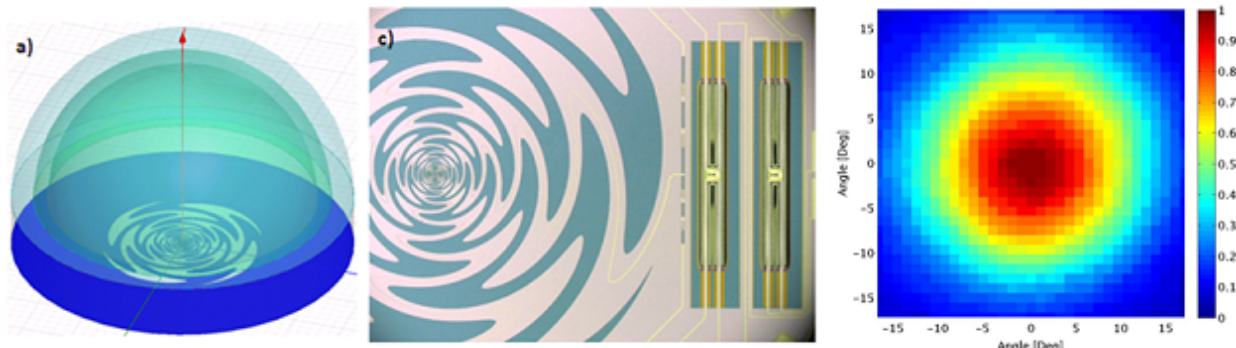


Figure 52: (Left) A CAD drawing of a lenslet coupled sinuous antenna designed to cover 90 GHz and 150 GHz. The lenslet in this drawing is AR coated with two layers of dielectric. The lenslet is 5.68 mm in diameter, and the sinuous antenna is 3 mm in diameter. (Center) A microscope photograph of a fabricated sinuous antenna detector. (Right) A measurement of the beam of the 150 GHz channel with a two layer anti-reflection coated silicon lenslet.

**Description of the technology** Using a contacting lens to increase a planar antenna's gain has been a common technique over a wide range of frequencies, including millimeter and sub-mm wavelengths [168]. In the ray-optics limit, an elliptical lens collimates rays from a point source placed at the far focus of an ellipse. However, a true elliptical lens is difficult and expensive to fabricate. To approximate an elliptical lens, it is common to synthesize a lens that is a combination of a hemisphere and an extension. Coupling this style of

lenslet to a planar antenna has multiple benefits. First, it increases the antenna's forward gain, efficiently coupling the antenna to the telescope optics. Second, a planar antenna placed in a space filled with half air and half dielectric favorably radiates into the dielectric, and the fraction of energy that radiates into the dielectric increases with increasing dielectric constant. Third, the required antenna size for a given frequency also becomes smaller with a higher surrounding material dielectric constant, freeing up wafer real estate for RF filters, detectors, and inter-pixel wiring. A high dielectric constant lens needs an anti-reflection (AR) coating to suppress reflections, and broadband AR coatings for high dielectric constant lenslets have been developed [169]. AR coated lenslet arrays are discussed in Section 4.3.2.2.

A slot antenna is preferred over a wire antenna for the on-chip integrated circuit design because the slot antenna and TL can share a ground plane. This ground plane also provides continuous RF shielding for cryogenic readout electronics. A lenslet-coupled double-slot dipole antenna was deployed for single-frequency observations that cover a  $\sim 30\%$  fractional bandwidth [63, 170]. For broadband applications, a lenslet-coupled sinuous antenna was developed [171, 172]. The sinuous antenna is in a class of antennas called log-periodic antennas, for which the antenna's characteristics repeat every log-frequency cycle. The sinuous antenna's lowest and highest operation frequencies are set by the largest and smallest radius of the antenna respectively, so there are no theoretical limits on the operable frequency range of a sinuous antenna. Practical limits, such as finite lithography resolution and finite bandwidth of the AR coating on the lenslet, restrict the frequency range [173]. Log-periodic antennas are known to have a linear polarization axis that oscillates as a function of frequency, but the amplitude of this oscillation for a sinuous antenna is relatively small ( $\sim \pm 5^\circ$ ) [171], and data analysis technique has been developed to deal with this effect [174, 175]. Hardware mitigation has also been implemented in the POLARBEAR-2 and SPT-3G detector array design; two types of pixels, each with the opposite handedness of sinuous antenna, were used in the detector array, canceling the polarization rotation effect.

**Demonstrated performance** The POLARBEAR-1 experiment has been observing in the 150 GHz atmospheric window with a focal plane filled with double-slot dipole antennas with silicon lenslets [63, 176]. The ellipticity of the feed is  $< 1\%$ , and the cross-polar response is better than -20 dB in a plane 45 deg rotated from polarization angle where cross-polar response is expected to be highest (D-plane). The POLARBEAR-2/Simons Array and SPT-3G are deploying with lenslet coupled sinuous antennas [173]. Each POLARBEAR-2 pixel covers the 90 GHz and 150 GHz bands; each SPT-3G pixel covers the 90 GHz, 150 GHz, and 220 GHz bands. The lenslet-coupled sinuous antenna has been demonstrated from the 40 GHz band to the 350 GHz band [177], and has been shown to have a round beam with an ellipticity of  $\sim 1\%$  [169] and a measured cross-polar response of  $\sim 1\%$  [178].

**Prospects and R&D path for CMB-S4** The technology status level of the single frequency band lenslet coupled antenna detector system is 5. Single band lenslet-coupled antenna detector was deployed in POLARBEAR-1. Systematic errors were studied in detail using on-sky data for the polarization result. The technology status level for multichroic version of lenslet coupled antenna detector with sinuous antenna is 3. Multichroic version has been deployed for SPT-3G, and multichroic focal plane for POLARBEAR-2 is in final stage of integration for deployment. The production status level for the current lenslet coupled antenna system is 3. Large quantity ( $\mathcal{O} 100$ ) of lenslet coupled detector wafers were fabricated for the stage-III experiments. Production rate shows promise to meet high demand ( $\mathcal{O} 1000$ ) from CMB-S4.

As described in Section 4.2.2, small pixel size (in unit of  $F\lambda$ ) is preferred for a ground based experiment. A lenslet-coupled antenna's sensitivity to beam and polarization systematic errors as a function of radius of a lenslet and wavelength should be studied in detail with 3D EM simulators such as HFSS. A scale model test at lower frequency ( $\sim 10$  GHz) should also be performed [171].

The sinuous antenna's polarization oscillation amplitude can be reduced by decreasing period of fractal repetition as a function of frequency [171], but micro-fabrication becomes more challenging as the expansion factor becomes smaller. Fabrication of a sinuous antenna at a smaller expansion factor is possible for low frequency (< 100 GHz) with current fabrication methods, and sub-micron lithography can be explored for sinuous antennas with smaller expansion factors for higher frequencies.

An on-sky demonstration of lenslet-coupled sinuous pixels is happening in 2017 with the POLARBEAR-2 and the SPT-3G experiments. A detailed study of systematic errors with actual on-sky data will be important for the development.

**Lab Demonstration:** 5:1 bandwidth. 40 GHz to 350 GHz band. 2,3, and 7 band pixels.

**Sky Demonstration:** 90 GHz /150 GHz PB-2 (2017). 90/150/220 GHz SPT-3G (2017).

**Path to CMB-S4:** On sky demonstration and systematic error study

#### 4.3.2.2 Lenslet arrays

**Description of the technology** An array of lenslets coupled to planar antennas increases the gain of the antenna array as described in Section 4.3.2.1. In this section manufacturing challenge for anti-reflection coated lenslet array will be discussed. POLARBEAR/Simons Array and SPT-3G use silicon ( $\epsilon_r = 11.7$ ) and alumina ( $\epsilon_r = 9.6$ ) lenslets respectively, and a broadband AR coating is applied to the lenslets to suppress reflections. The details of the AR technologies are given in the AR coating section of the optics chapter (Section 3.5.3 and 3.5.1). The fabrication and assembly processes for a monolithic lenslet array will be described in this section.

**Demonstrated performance** Figure 53 and Figure 54 show lenslet arrays and assembly jigs for the POLARBEAR and SPT-3G experiments respectively [169]. Both methods populate silicon hemispheres in  $\sim 100 \mu\text{m}$  deep circular pockets etched by micro-fabrication process. Two layers of AR coating made of Styccast 2850 FT and Styccast 1090 are applied with metal molds [82, 169], and the application of the AR coating and the assembly of the lenslet array are done manually.

For the plastic sheet method, three types of loaded PTFE sheets are laminated together with a thermal cycling process, and the laminated sheets are molded to conform to the populated lenslet array with a screw-driven die press and system of molds. Once the coating has been molded, it is attached to the populated lenslet array using a calibrated volume of Styccast 1266 and allowed to cure. The final 3 mm-thick molded AR coating is repeatable to  $\sim 20 \mu\text{m}$ . A 30W CO<sub>2</sub> laser was used to cut relief cuts between lenslets to mitigate delamination from differential thermal contraction between the AR coating and the lenslet.

**Prospects and R&D path for CMB-S4** The technology status level of the lenslet array for lenslet coupled antenna detector system is 5 for single frequency band system and 3 for multichroic detector. As mentioned in previous section, lenset coupled antenna detector was deployed in POLARBEAR-1. Systematic errors were studied in detail using on-sky data for the polarization result. Multichroic version has been deployed for SPT-3G, and multichroic focal plane for POLARBEAR-2 is in final stage of integration for deployment. The production status level for the current lenslet coupled antenna system is 3. Large quantity ( $\mathcal{O} 30$ ) of lenslet coupled detector wafers were fabricated for the stage-III experiments at production rate of approximately 1 array per week. Current production method still involves manual labor, which may limit throughput for mass production in future.

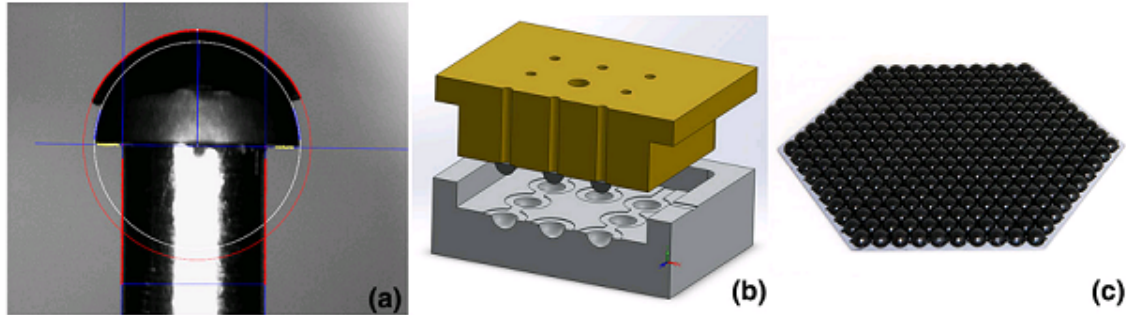


Figure 53: (Left) Photograph of a single layer AR coating on a silicon lenslet under a microscope. Photographs were used to inspect the shape of the AR coating. The solid red line indicates a fit to the AR coating and the solid white line indicates a fit to the hemispherical lens. (Middle) The mold for one layer of coating is shown in cross section. The hemispherical lens, which is placed on the seat, is also shown in the drawing. (Right) A photograph of the fully populated broadband AR-coated hemispherical lenslets on the 150 mm wafer.

Several improvements can be made to the lenslet array fabrication process in order to increase throughput and repeatability.

At present, populating the silicon lenslet array is performed by hand. While by-hand assembly is feasible now—for experiments with  $\mathcal{O}(10,000)$  pixels—it will not be feasible for future experiments with  $\mathcal{O}(100,000)$  pixels. Many, if not all, of the epoxy dispensing steps in the fabrication process can be adapted for computer numerical controlled devices, increasing precision and repeatability, and decreasing the time spent in fabrication.

The plasma spray technique described in Section 3.5.2 can also be used to AR-coat lenslet arrays. The process is fast and fully automated, and is a scalable technology for CMB-S4. R&D is required to verify coating thickness uniformity across a lenslet array.

<b>Lab Demonstration:</b>	Silicon and alumina lenslet array. Epoxy AR coating and plastic AR coating
<b>Sky Demonstration:</b>	90/150 GHz PB-2, 2017. 90/150/220 GHz SPT-3G, 2017
<b>Path to CMB-S4:</b>	Increase production rate with automation and faster AR coating method

#### 4.3.2.3 Metamaterial lenslet arrays

**Description of the technology** As an alternative to hyper-hemispherical lenslet arrays, planar lenslet arrays using metamaterials can be fabricated using silicon wafers. Instead of curved optical surfaces, the lenslets consist of a stack of silicon wafers each patterned with a periodic array of subwavelength features. Two approaches can be used, gradient index (GRIN) lenslets produced by etching radially varying holes in the wafers, and metal-mesh lenslets produced by depositing a radially varying metal mesh grid that acts as a series of TL lumped element filters to control the wavefront phase delay across the lenslet. Metamaterial lenslets can be fabricated using standard lithographic techniques on silicon wafers in only a few steps, they are precise, repeatable, and scalable to mass production, and the flat optical surface lends itself to a variety of broadband AR coating techniques, including impedance matching to free space using the metamaterial itself.

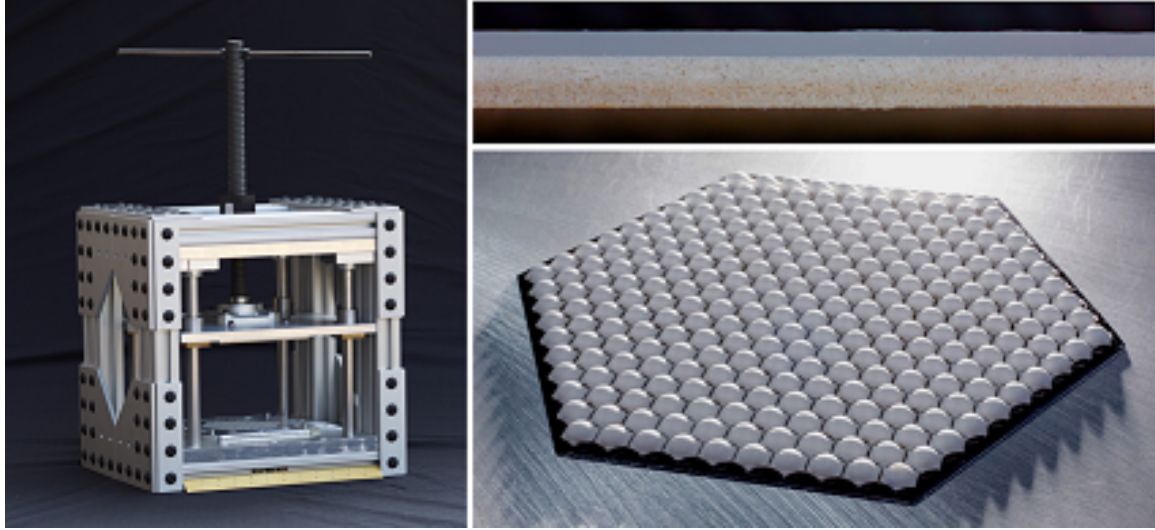


Figure 54: (Left) Photograph of the press used for the molding process (Top Right) Cross-sectional image of laminated loaded Teflon sheets. Laminates are Teflon, RO3035, and RO3006. RO3035 and RO3006 are dielectric loaded plastic sheet from Roger Corporation. (Bottom Right) Photograph of a lenslet array for the SPT-3G experiment with 271 lenslets. The Teflon laminates are laser ablated to physically separate lenslets from each other.

Also, since both the detector arrays and lenslet arrays are patterned on silicon, there is no differential thermal contraction between the two, and this allows them to be designed together in close proximity, accounting for electromagnetic interactions.

**Demonstrated performance** Only recently have grooved or perforated dielectrics been studied to produce GRIN lenses at submillimeter wavelengths. For example, a single-layer etched GRIN was tested as a candidate lenslet array at  $350\text{ }\mu\text{m}$  wavelength with the MAKO [180] instrument (Chris McKenney, private communication), and a single wafer GRIN lenslet array using a  $120\text{ }\mu\text{m}$  hole pitch on a  $100\text{ }\mu\text{m}$  thick silicon wafer has been demonstrated with broadband operation from  $0.3\text{--}1.2\text{ THz}$  [181]. Recently, a 19-element prototype GRIN lenslet subarray was designed and fabricated for mm-wave application (Fig. 55, left panel). The prototype array is being optically tested using a single-pixel prototype POLARBEAR-2 sinuous-antenna coupled dual-polarization  $90/150\text{ GHz}$  TES detector. Preliminary measurements show that the optical efficiency is similar to that of the same detector mounted to a conventional AR-coated hemispherical lenslet.

Single meshes or combinations of different grids have long been used to form low-pass, high-pass, band-pass, and dichroic spectral filters (see, e.g., [54]), and the same technology has been further developed to realize phase retarders such as mesh half-wave plates and mesh quarter-wave plates [182]. Recently, a metal-mesh metamaterial lens was developed [179]. A 54-mm diameter W-band ( $70\text{--}115\text{ GHz}$ ) metal-mesh lens was demonstrated by using stacks of spatially varying inhomogeneous grids (Figure 55, center panel). The lens does not need an AR coating since all the cells of the surface are optimized to be impedance matched to free space. Experimental measurements of the mesh lens beam pattern agree well with HFSS simulations (Figure 55, right panel).

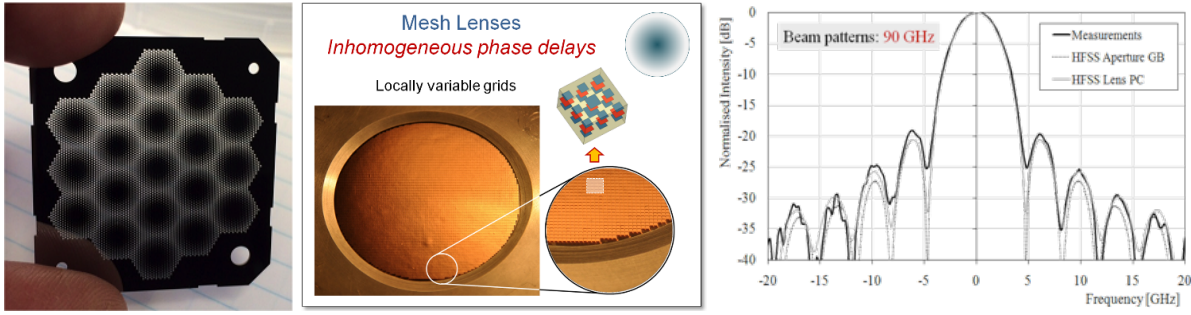


Figure 55: (Left) Photograph of a single GRIN lenslet array layer showing the etched hole pattern. Eight wafers are stacked together to form the prototype 19-element GRIN lenslet array. Each lenslet is 6.8-mm diameter. (Center) 54-mm diameter metamaterial metal-mesh lens photograph and concept [179]. (Right) Experimental measurements of the beam created by the mesh lens. Notice the agreement between models and data down to the fourth sidelobes [179].

<b>Lab Demonstration:</b>	Fabricated 19-element lenslet array. Efficiency is similar to hemispherical lenslet
<b>Sky Demonstration:</b>	-
<b>Path to CMB-S4:</b>	Demonstrate metamaterial lenslet arrays with antenna-detector array

**Prospects and R&D path for CMB-S4** In principle, the technology is scalable to mass production. For both the etched-hole and metal-mesh lenslets, stacking and alignment will be performed using alignment features and notches fabricated on the individual wafers to align the layers, and the layers will then be glued together using Styccast in vertical channels on the edge of the stack, similar to the method developed for the silicon corrugated feed arrays.

The technology status level for the technology is 2. Laboratory test has been done to show that technology works at small array level. Demonstration of deployable size array with study of beam and polarization systematics will push the technology status level to next level. The production status level for the technology is 1. Fabrication of proto-type 19 pixel model for demonstration of technology status level 1 and 2 has been done.

### 4.3.3 Antenna array coupling

**Description of the technology** To facilitate rapidly deploying over 10,000 detectors in the BICEP, Keck Array, and SPIDER experiments, planar antenna-array coupled detectors have been developed. This design eschews large bulk coupling optics such as horns or contacting lenses and instead synthesizes a beam from coherently fed sub-antennas [183], all fabricated entirely through photolithographic means. Figure 56 shows the design of the antenna array from one pixel. The sub-antennas are slots carved into a superconducting niobium film and their waves are captured and summed in an integrated niobium microstrip circuit that uses the metal around the slots as a ground plane.

Each pixel contains two interleaved co-centered antenna arrays that receive the two orthogonal linear polarizations and couples them to two independent microstrip feeds. The feed combines waves in microstrip T-junctions. It is possible to control the optical mode to which the detectors couple by choosing the impedance of the lines at the junctions as well as the length of line to the adjacent junctions. This design

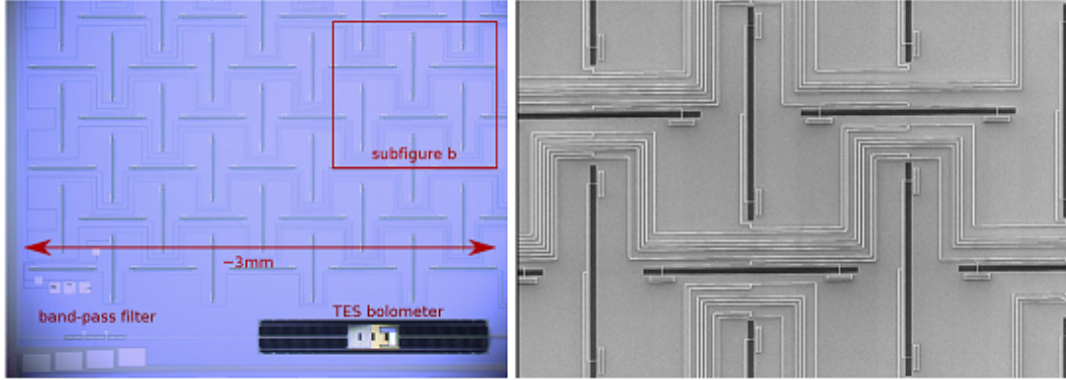


Figure 56: (Left) Pixel design of the antenna array. (Right) a zoom in of the left-hand panel. Dark lines are slots in Nb ground plane.

avoids microstrip cross overs, simplifying the fabrication by reducing the number of required depositions and etches as well as obviating superconducting vias between layers.

**Demonstrated performance** The antenna-array coupled design is mature, thanks to deployment of 88 tiles into scientific experiments where they were subjected to exhaustive analysis. These measurements have demonstrated an antenna band that is nearly 50% wide, but limited to 30% by integrated band-defining microstrip filters centered at 90, 150, and 220 GHz. The end-to-end optical efficiencies are 40% in the deployed cameras. Detectors have been developed that cover the 40 GHz and 270 GHz bands for the BICEP Array that will deploy in 2018.

Early designs used a top-hat illumination of the antenna, which couples to sinc-patterned modes in the detectors' far field. While these are acceptable for BICEP-style refracting telescopes with a well-controlled cold 4-K aperture, other optical design require lower-sidelobe levels to limit detector loading from warmer surfaces. Detectors in the BICEP3 telescope have a Gaussian illumination, controlled through the impedance of the transmission lines at the T-junctions. These receive more power in the center than edge, dropping side-lobe levels by nearly 10 dB [184]. Figure 57 shows a comparison of the feeds' performance. In principle, it is possible to match to more exotic illuminations, such as sinc-patterns that overlap between pixels in the illumination tails and synthesize top-hats in the telescope aperture, providing very high optical throughput. However, implementing such a design would require multiple ground planes and myriad microstrip cross-overs.

**Prospects and R&D path for CMB-S4** The technology status level of the antenna array system is 5. The antenna array system has been deployed in multiple CMB polarimetry experiments (series of BICEP experiments and SPIDER). Detailed systematic error studies have been done for published results. The production status level for the current feed horn system is 4. Large quantity of antenna arrays have been fabricated and deployed to multiple experiments. Lithographed beam forming elements that is unique to this technology provides scalability to the technology.

Mode coupling can be further customized by altering the relative phase between sub-antennas. For example, by increasing the length of the lines leading to the sub-antennas in a way that linearly increases across a pixel's array, it is possible to couple to modes whose boresight is angled away from the focal-plane's normal vector. In this way, the detector naturally accommodates non-telecentric optical designs. The phase could

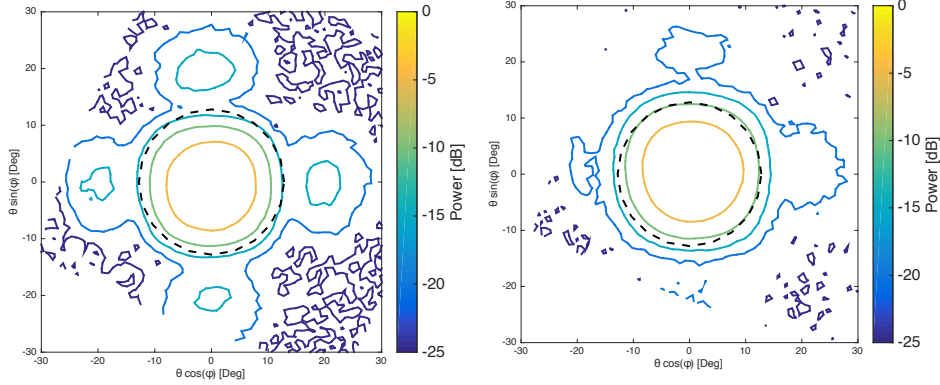


Figure 57: Measured beam patterns for pixels formed from antenna arrays, without refracting optics. (Left) Antenna beam pattern from an antenna array with top hat illumination pattern. (Right) Antenna beam pattern with Gaussian illumination pattern.

be varied quadratically across the pixel, which would allow pixels to couple to waves that have a waist off the physical detector tile locations, accommodating optics with curved focal surfaces as well. Detectors with linear phase shifts have been fabricated, but we have yet to fabricate higher order phase profiles.

Multiple antenna-array designs have been explored to extend detector bandwidth. Arrays of “figure-eight” antennas, reminiscent of bow-ties, can provide in excess of an octave bandwidth—more than enough for multi-color pixels. These are currently under development. Another far more ambitious possibility is building focal planes where slot array from two orthogonal polarizations and frequency bands are interleaved. If the detectors are all at the edge of such an array, then the beams from different frequency bands could be independently tuned to match the optics, providing a highly efficient use of focal plane real estate. Implementation of this concept presents similar engineering challenges as for the sinc-illuminations described above.

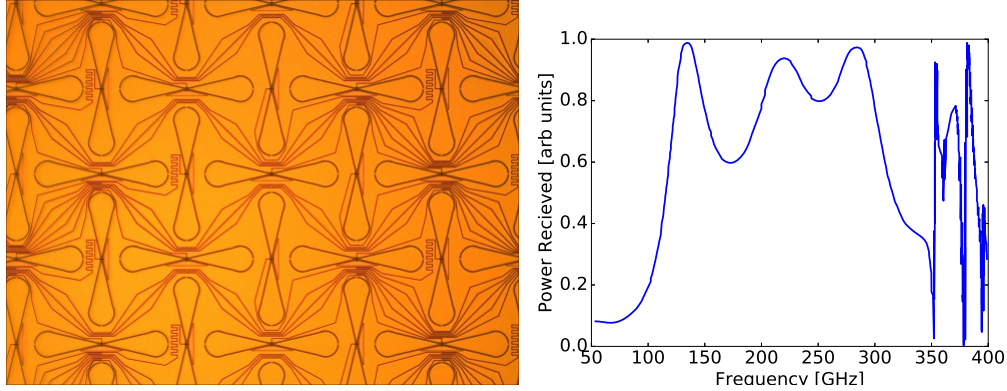


Figure 58: (Left) Photograph of a broadband antenna array. (Right) Simulation of received power by the broadband antenna array as a function of frequency.

<b>Lab Demonstration:</b>	Design and fabricated broadband (2:1) antenna array
<b>Sky Demonstration:</b>	Deployed 90, 150, 220, 270 GHz in the BICEP, Keck Array, and SPIDER
<b>Path to CMB-S4:</b>	Beam steering with customized phasing for non-telecentric coupling

#### 4.3.4 Direct coupling to single and multimoded resistive absorber bolometers

**Description of the technology** To meet the evolving demands of CMB science, technological advancements have focused on improving array sensitivity. Rather than increase the number of sensing elements in the focal plane, multimode devices use fewer, larger absorbing structures to collect photons in more than one spatial mode. The simplest such absorber is a resistive sheet. Depending on the optical coupling between the absorber and the sky, such a sheet can be operated in single-moded or multimoded configurations.

**Demonstrated performance** As an example of a single-moded implementation, the Millimeter Bolometric Array Camera (MBAC) on the Atacama Cosmology Telescope used pop-up bolometers with impedance-matched solid silicon sheet absorbers [185]. More generally, planar absorbers can be realized on a thin membrane, i.e. SiN or  $\text{SiN}_x$ , or solid dielectric substrate. This technology was first used by the SHARC-II instrument for the Caltech Submillimeter Observatory [186]. A further evolution of the pop-up design, the Backshort-Under-Grid (BUG) detector array with individual absorber backshorts has found use in sub-mm and IR polarimetric experiments when combined with a polarizing wire-grid analyzer. Examples are the HERTZ polarimeter [187], the polarimeter for SCUBA-2 [188], the SHARC polarimetric instrument SHARP [189], and the CMB instrument PIPER [190].

In contrast, a multimoded polarimeter can be formed from inherently polarization-sensitive sheet absorbers. For the PIXIE mission [191], a freestanding grid of doped silicon wires forms the detecting element of a space-based FTS. This “harpstring” absorber enables broadband detection of polarized optical power between 30 GHz and 6 THz. The detectors would achieve low levels of crosspolar response, measured as individual detector response to incoming orthogonal polarization, when two orthogonally-sensitive harpstring detectors are mounted together [192].

**Prospects and R&D path for CMB-S4** The technology status level of the direct coupling to single and multimoded resistive absorber bolometer system is 3. Experimental capable version has been fabricated and tested in laboratory for CMB instrument PIPER. The production status level for the current feed horn system is 3. Fabrication for resistive absorber bolometer is done using micro-fabrication technique. Such technique is suitable for scalable fabrication. The production status level will advance once mass fabrication for this type of detector has been demonstrated.

Polarization-sensitive multi-moded detector pairs can also be formed into arrays. Using many fewer detectors, such arrays would achieve equivalent sensitivity to current or future kilopixel arrays [193]. The reduced angular resolution of a multimode detector would not affect a target of measuring B-modes at large angular scales sourced by primordial gravitational waves. Current detector development is focused on verifying thermal transport and optical response of the harpstring absorber. Initial results for prototype bolometers reported on performance of ion-implanted semiconductor thermistors in the harpstring frame [194].

<b>Lab Demonstration:</b>	Direct absorber with wiregrid polarizer, BUG Detector for PIPER, PIXIE
<b>Sky Demonstration:</b>	MBAC, SHARC-II
<b>Path to CMB-S4:</b>	Fabricate polarization-sensitive multi-moded detector array Verify thermal transport and optical response of the harpstring absorber

## 4.4 RF components

Contemporary CMB detectors typically employ low-loss superconducting TL to convey the optical signal from the RF feed to the detector where the signal is thermalized and measured. The use of planar TL enables implementation of traditional RF circuit elements for signal processing prior to detection. Realized applications include beam synthesis as part of phased antenna arrays, mode rejection and passband definition with the latter including channelizing the signal into multiple passbands. Applying these RF engineering techniques to CMB applications is now a mature technology having been successfully implemented in Stage-II and upcoming Stage-III experiments. The RF circuit design needs to occur within the broader context of detector fabrication and testing in order to yield structures that can be reliably and uniformly fabricated without repercussions to other detector components. In this section, we survey different RF circuit components employed across multiple CMB experiments.

### 4.4.1 Superconducting RF transmission line

**Description of the technology** Microfabrication of CMB detectors on silicon wafers with lithography technique enabled on-chip RF signal processing. Typical RF circuitry used in CMB detectors utilizes both CPW and microstrip TLs where the conducting metal is a superconducting film, typically  $\sim 300$  nm of Nb. To maximize detector performance, impedance, absorptive loss, and radiative loss of TLs should be carefully thought through. CPW structures have higher impedance and typically lower loss compared to microstrip. Radiative losses are important for CPW structures and need to be minimized through design considerations. Microstrip TLs have substantially less radiation compared to CPW, but suffer from losses in the dielectric material separating the conductor strip from the ground plane. A review of superconducting planar TL technology detection of the CMB is given by U-yen, Chuss and Wollack [195].

**Demonstrated performance** Low-loss TL is essential for providing flexibility in the detector RF circuit design. The dielectric loss can be parameterized by the loss tangent, defined as  $\tan \delta = \epsilon''/\epsilon'$ , where  $\epsilon = \epsilon' + i\epsilon''$  is the complex dielectric constant. Fielded systems have typical loss tangents of  $\tan \delta < 5 \times 10^{-3}$ . Current CMB detectors have explored a number of dielectric materials including: silicon oxide, silicon nitride and single crystal silicon. Silicon oxide is the most common dielectric and has a dielectric constant of  $\sim 3.8$  and loss tangent of  $\sim 5 \times 10^{-3}$ . Increasing the silane-to-oxygen ratio during plasma-enhanced chemical-vapor deposition of the silicon oxide improves the dielectric loss-tangent from  $6 \times 10^{-3}$  for stoichiometric silicon dioxide to  $2 \times 10^{-3}$  for a more silicon-rich silicon oxide [196]. Similar to silicon oxide, silicon nitride, which has a dielectric constant of  $\sim 7.0$ , can also be made silicon-rich thus reducing the dielectric loss tangent from  $1.2 \times 10^{-3}$  to  $2.5 \times 10^{-5}$  [197]. For example, the 150/230 GHz Advanced ACTPol array with low-loss SiN dielectrics and appears to have a dielectric efficiency in line with the predictions of  $\sim 70\%$ . Single crystal silicon has a dielectric constant of  $\sim 11.7$  and loss tangent of  $\sim 1 \times 10^{-5}$  or better. Microstrip TL can be fabricated with single crystal silicon dielectric by using Silicon-on-Insulator (SOI) wafer [198,199] processing. Detectors fabricated for the 38 GHz channel of the CLASS experiment have been demonstrated to achieve feed-to-detector efficiency of  $\sim 90\%$  [157–159]. Single-crystal silicon has a predictable EM performance [191] and provides uniformity in microwave properties and substrate thickness over wafer batches [200].

The typical conducting material for the RF TL is niobium, a superconductor with superconducting transition temperature  $\sim 9$  Kelvin. Changes in quality of Nb from various effects such as film stress, contamination and temperature can change loss and the kinetic inductance of the superconducting niobium TL. Most CMB detectors use compressive Nb films where the stress is tuned to be around  $0 \sim 500$  MPa.

For a microstrip line, as the dielectric constant increases, the impedance of the TL drops as approximately  $1/\sqrt{\epsilon_r}$ . To compensate for this effect, either the thickness of the dielectric needs to be increased or the stripline needs to be made thinner. A balance is required between the two because a thicker dielectric increases the amount of field fringing whereas micro-fabrication capabilities limit the width of the stripline.

**Prospects and R&D path for CMB-S4** The technology status level of the superconducting RF transmission line is 5. Every CMB experiment uses micro-lithographed superconducting RF transmission line as part of detector system. Multiple scientific results were published with systematics effect that came about due to transmission line coupling problem. This problem was understood, simulated and solution to mitigate that problem was found and demonstrated.

The production status level for the superconducting RF transmission line is 5. Hundreds of detectors were fabricated for stage-III experiments. During fabrication for stage-III experiments, we learned various ways performance of superconducting RF transmission line could degrade. Prevention methods were found for these problems, and large quantity of stage-III detector arrays were fabricated without problem with superconducting transmission line.

Low-loss TL is essential for providing flexibility in the circuit design and improving detector efficiency. A reliable dielectric constant is important for predictable RF circuit performance and dielectric films with loss tangent lower than  $1 \times 10^{-3}$  are needed for dielectric loss to be negligible. Silicon nitride and single crystal silicon have desirable properties, and multiple Stage-III experiments are going to deploy detectors with these dielectrics. Demonstration of detector fabrication with these films will pave the way for the CMB-S4 detector fabrication.

Reliable fabrication of high quality niobium films requires a dedicated Niobium sputter machine that is under tight control. Multiple CMB detector fabrication facilities already have dedicated niobium sputtering systems for superconducting film process. A similar degree of control needs to be implemented for CMB-S4 detector fabrication to realize predictable detector performance.

**Lab Demonstration:** Improved efficiency with silicon nitride dielectric

**Sky Demonstration:** Multiple CMB experiments deployed with  $\text{SiO}_2$  microstrip line

**Path to CMB-S4:** Improve efficiency with low-loss dielectric such as SiN and single crystal Si

#### 4.4.2 On-chip microwave filters

**Description of the technology** Many experiments employ band-defining filters on the detector wafer [159, 176, 201–206]. These are planar microwave structures that lie between the antennas and the detectors are typically composed of sections of microstrip lines and coplanar waveguides. Most current ground-based experiments design for bandwidths of  $\sim 30\%$ . An example passband is shown in Figure 59.

Typically, the filters are modeled by an ideal circuit composed of exclusively reactive elements (e.g. see Figure 60). The number of degrees of freedom in the filter design is often referred to as the number of *poles* and is related to the order of the polynomial that describes the passband. A higher-pole filter has, by definition, more degrees of freedom and is, therefore, able to achieve a steeper roll-off in the passband. The disadvantage of a higher-pole filter is that dielectric loss is more severe due, heuristically, to multiple reflections within the filter, so that the loss is much greater than would be incurred by an equivalent length

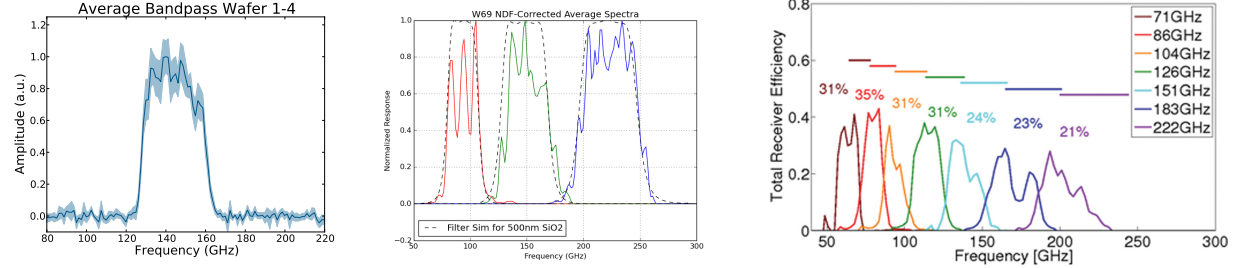


Figure 59: Example passbands (Left) Horn coupled band pass filter from ABS 150-GHz passband [205]. (Center) Passbands for the SPT-3G 90/150/220-GHz triplexer [204]. (Right) Channelizer bands for the pixel shown in Figure 60 [207].

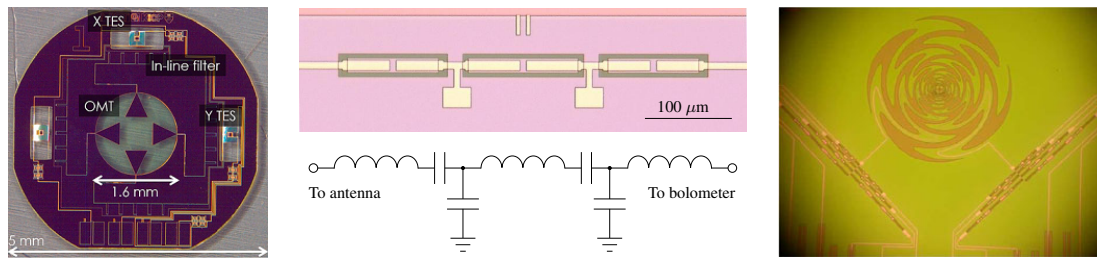


Figure 60: Photographs of RF filters from CMB detectors. (Left) ACT-Pol pixel with 5-pole single-band 150-GHz stub filters [176]. (Center) BICEP2 single-band 150-GHz lumped-element filter with corresponding circuit diagram [201]. (Right) Log-periodic lumped-element channelizer with 7 contiguous bands between 50 and 230 GHz [207].

of transmission line. For a microstrip filter with a dielectric loss tangent of  $3 \times 10^{-3}$ , the expected loss is  $\sim 5\%$  for a 3-pole filter and  $\sim 10\%$  for a 5-pole filter. In designing a microwave filter, then, a balance must be struck between efficiency and band shape.

There are two main strategies for implementing a given filter circuit. One is to use quarter-wavelength short-circuited TL stubs. These types of microwave structures are sometimes called distributed filters, because they do not consist of discrete circuit elements but instead exploit the similarity in behavior of *LC* resonators and quarter-wavelength TL stubs. The degrees of freedom translate to the impedances of the stub sections, which are usually controlled by microstrip width. The other main approach is to use lumped circuit elements. In this paradigm, each geometric structure corresponds to a specific circuit element, e.g., an inductor or a capacitor.

In implementing an on-chip filter, it is vital to have good knowledge and control of the material properties. Most current experiments use a microstrip paradigm, which involves a metal-dielectric-metal tri-layer stack. The metals are superconducting, e.g., Nb, which eliminates resistive losses for high quality films. The kinetic inductance of the superconductor, however, can affect the impedance of the TL. The dielectric constant of the middle layer controls the impedance as well, and the loss tangent of this dielectric is often the limiting factor in transmission efficiency. Some typical microstrip dielectrics include  $\text{SiO}_2$  with  $\tan \delta \sim 10^{-3}$ ,  $\text{Si}_3\text{N}_4$  with  $\tan \delta \sim 10^{-4}$  and single-crystal Si with  $\tan \delta < 10^{-5}$ . Lower-loss dielectrics allow for higher-pole filters. A 6-pole filter with  $\tan \delta = 3 \times 10^{-3}$  dissipates  $\sim 10\%$  of the incident power, whereas the same filter with  $\tan \delta = 3 \times 10^{-4}$  would dissipate  $\sim 1\%$ . A comparison of filters is shown in Figure 61.

**Demonstrated performance** The POLARBEAR, POLARBEAR-2, BICEP2 and SPT-3G experiments use 3-pole filters [176, 201, 204, 206]; the ACTPol experiment uses a 5-pole filter [203]. ACTPol, CLASS, and POLARBEAR are using distributed filters; an example passband is shown in Figure 59. The CLASS detectors also employ filters to reject out-of-band radiation coupling to the microstrip circuit [156–159]. The BICEP2 experiment and the upcoming POLARBEAR-2 and SPT-3G experiments are using lumped-element filters; an example is also shown in Figure 59.

Recently, the ACTPol experiment deployed a diplexing 90/150-GHz distributed filter, which is essentially a T-junction with a different bandpass filter on each branch. The POLARBEAR-2 experiment will deploy a 90/150-GHz lumped-element diplexer, and the SPT-3G experiment will deploy a 90/150/220-GHz lumped-element triplexer (see Figure 59).

Two separate arrays of multichroic detectors have been deployed and additionally several experiments are near deployment with multichroic detector focal planes [203, 204, 206]. Also laboratory demonstration was made on filter designs that increase the bandwidth even further [207, 208].

**Prospects and R&D path for CMB-S4** In [208], some 3- and 4-band filters are achieved by sprouting several bandpass filters from a common node. If the passbands are not overlapping, a given frequency is admitted by at most one of the branches, so that there is very little interaction among the filters. This is the paradigm used in the SPT-3G triplexer, whose passbands are shown in Figure 59. Another method, which is shown in Figure 60, is to construct a “channelizer,” in which the bandpass filters branch off log-periodically from a TL trunk. The channelizer produces an arbitrary number of contiguous bands; the design shown in Figure 60 has 7 filters, and the passbands are shown in Figure 59.

An extreme version of the channelizing filter is a filter bank that subdivides the telluric windows into many channels, either to provide additional spectral information for foreground characterization and removal or to pursue ancillary science opportunities. Today several groups are designing compact, on-chip spectrometers

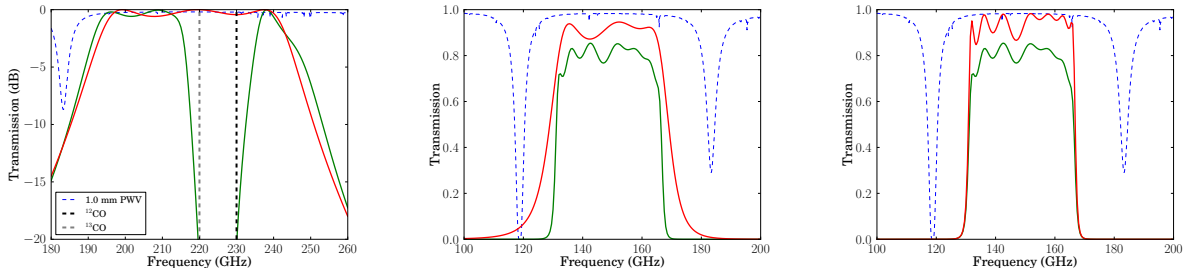


Figure 61: (Left) Simulated performance of bandstop filter. A bandstop filter can be used to notch out unwanted frequencies within a band, e.g., CO lines. Shown is a three-pole bandpass filter in series with a three-pole bandstop filter. (Center) Comparison of roll off speed for different number of poles. A lower-loss dielectric allows for higher-pole filters. Shown is a simulated comparison of a three-pole filter (red) and a seven-pole filter (green) on dielectric with  $\tan \delta = 3 \times 10^{-3}$ . The higher-pole filter has a more rapid roll-off of the passband, but loss increases. (Right) Simulated band with different dielectric loss tangent. The effect of dielectric loss on a seven-pole filter. The red curve is from a simulation with  $\tan \delta = 3 \times 10^{-4}$ ; the green is with  $\tan \delta = 3 \times 10^{-3}$ .

that use either superconducting transmission line resonators as filter elements or phased delay lines to create a grating-waveguide analogue [209–212]. Laboratory demonstrations have shown excellent rejection of out-of-band direct pickup and NEPs suitable for background limited performance at  $R = \nu/\Delta\nu \lesssim 100$  for ground-based operation at mm-wavelengths, and on-sky demonstrations are planned within the coming year.

Bandstop filters can be implemented to reject certain frequencies, e.g., atmospheric or CO lines. The design approach is similar to that for bandpass filters with the main difference being in the ideal circuit model. Bandstop filters can be implemented in series with bandpass filters to notch out unwanted frequencies. An example is shown in Figure 61, in which a 3-pole bandstop filter notches out the 220- and 230-GHz CO lines while leaving the rest of the 220-GHz band mostly intact.

The technology status level of the on-chip microwave filter is 5. Multiple CMB polarization results were published using detector system that uses on-chip microwave filters to define its spectral response. The technology status level of the multi-chroic on-chip filter is 4. Technology is deployed on ACT-pol, Adv-ACT and SPT-3G.

The production status level for the on-chip microwave filter is 5. On-chip microwave filter is part of lithographed detector architecture. Large quantity of detector array was fabricated for stage-III experiments with on-chip microwave filter. It was demonstrated that process step to define on-chip microwave filter is not limiting throughput of detector fabrication.

For better spectral resolution, the atmospheric windows can be subdivided into multiple bands. This is illustrated in Figure 62 for both three- and seven-pole Chebyshev filters. Subdividing the atmospheric window does not reduce overall transmission and there is only a small gain from increasing the number of poles. Integrated bandwidths are given in the captions of Figure 62. Realizing these narrower-band filters presents some challenges. For stub filters, the impedance of each stub is proportional to the fractional bandwidth. For a microstrip implementation, this requires wider stubs for narrower bands. When the stub width is comparable to  $\lambda/4$ , the stubs can no longer be treated as quarter-wave resonators and will not produce the designed passband. For lumped-element filters, the required inductances are roughly inversely

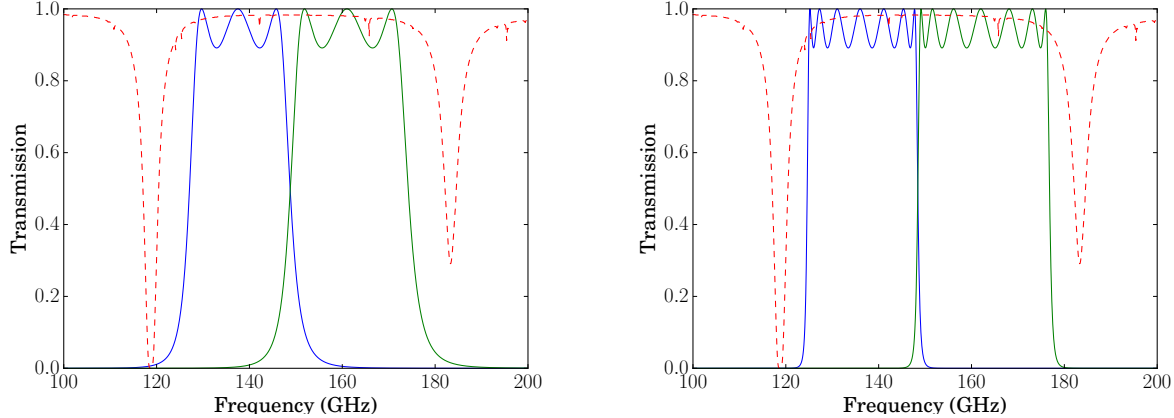


Figure 62: Subdividing the 150-GHz for better spectral resolution. In this case, higher-pole filters do not provide a substantial increase in transmitted power, but they do help to isolate the bands and, thereby, avoid mutual coupling. A proper treatment would involve a simulation of the microwave circuit as, e.g., a diplexer where the power can be shared between the two filters, but the raw Chebyshev transmission curves give a good approximation of what to expect from these simulations. (Left) 3-pole Chebyshev bandpass filter with 0.5-dB ripples. The combined integrated bandwidth is 47 GHz. (Right) 7-pole Chebyshev bandpass filter with 0.5-dB ripples. The combined integrated bandwidth is 50 GHz.

proportional to the fractional bandwidth. It is difficult to realize a large inductance while keeping the effective length much smaller than a wavelength, i.e., maintaining the lumped-element approximation. These challenges are not insurmountable but will undermine the naive application of current techniques.

**Lab Demonstration:** Triplexer, tetraplexer and 7-band channelizer filter

**Sky Demonstration:** Single and dual band filter deployed with multiple CMB detectors

**Path to CMB-S4:** High-Q band to sub-divide atmospheric window

#### 4.4.3 Microwave cross-over

**Description of the technology** Microwave cross-overs allow two transmission lines to cross on a wafer. It provides flexibility for detector design. It is important to design cross-over with high transmission efficiency and without coupling between orthogonal lines. Cross-overs are used on most dual polarization-sensitive CMB detector arrays [159, 176, 198, 203–206, 213, 214], except for the antenna array detector design (used in the BICEP series of experiments), which avoids the cross-over process. Planar RF cross-over designs are well established, with multiple experiments implementing cross-over designs that are compatible with the rest of the detector fabrication steps.

A typical microstrip cross-over uses two metal wiring layers separated by an insulator; a microscope photograph and the simulated performance of a cross-over design is shown in Figure 63. In this approach, the lower layer is a common ground plane with a section cut out in the area of the “cross-over.” The top wiring layer carries the primary runs of microstrip, and the line which “crosses under” connects down to

the lower layer through vias. In the area of the ground plane cut-out, neither line truly has a ground plane, introducing a deficit of capacitance to ground, which is compensated for by adding “wings”, small sections of widened trapezoidal transmission lines, to both lines. Simulations of this “cross-under” predict cross-talk and reflection below -30 dB over nearly all of the 30-300 GHz range.

POLARBEAR-2 and SPT-3G use a design that has additional insulator and metal layers that form a cross-over [204, 206]. In this design, the conductor at the cross-over is narrowed to minimize capacitive coupling between the two orthogonal channels. The extra inductance introduced by the short narrow section is compensated for by widening the transmission line section via wings, similar to the cross-over shown in Figure 63.

It is also possible to design a cross-over without using a via, a vertical short to connect two conductors at different layers, demonstrated for narrow-band applications [214]. The CLASS detectors employ a via-less crossover design. A broadband version of the via-less design has been recently reported [158]. In addition, an air-bridge crossover, extending the bandwidth to  $\sim$ 500 GHz has been fabricated [158, 215]. A via-less cross-over has the benefit of simplifying fabrication.

**Demonstrated performance** Multiple Stage-II CMB experiments successfully deployed detector arrays with cross-overs [63, 136, 139]. There is no measurable difference in efficiency between the two orthogonal polarizations and the differential spectra between two orthogonal polarization channels are small indicating that cross-overs work well. There are multiple Stage-III CMB experiments that have designed and demonstrated cross-overs spanning multiple frequency bands. The cross-over for the POLARBEAR-2 experiment was designed to cover the 90 GHz and 150 GHz band [178]. Microwave cross-unders targeting the frequency range 60-300 GHz were deployed for the AdvACT experiment in 2016. Cross-unders targeting 240-340 GHz have also been designed and fabricated, and will be deployed in the SPIDER experiment.

**Prospects and R&D path for CMB-S4** The technology status level for microwave cross-overs is 5. Multiple Stage-II CMB experiments successfully deployed detector arrays with cross-overs. There is no measurable difference in efficiency between the two orthogonal polarizations and the differential spectra between two orthogonal polarization channels are small indicating that cross-overs work well. The production status level for microwave cross-over is also 5. Microwave cross-overs are a mature technology that is compatible with other detector fabrication steps. There are well established designs that achieve reflection and cross-talk below -30 dB and there are no scaling issues for CMB-S4.

For a receiver configuration that does not use polarization modulation, fabricating symmetric detectors for the two orthogonal polarizations will be important. The dominant issue for implementing cross-overs is quality control during fabrication, an issue which would benefit from developing a simple method for validating cross-over performance without necessitating a full optical test.

**Lab Demonstration:** Multiple designs robustly designed

**Sky Demonstration:** With via, via-less cross-filters demonstrated in multiple CMB experiments

**Path to CMB-S4:** Technology is mature. Detail systematic error study for asymmetric cross-over

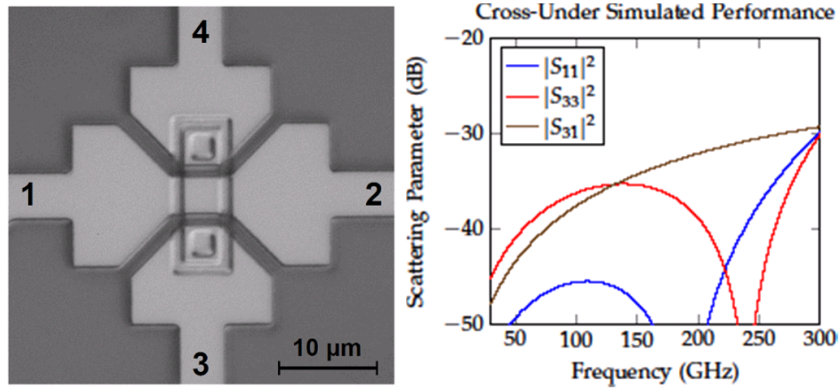


Figure 63: (Left) Optical microscope image of a microstrip cross-under. (Right) Simulated Performance of a microstrip cross-under.

#### 4.4.4 Microstrip termination

**Description of the technology** In most current-generation experiments, the incident radiation couples to an antenna which is fed by a microstrip line. The signal then passes through bandpass filters and/or mode rejectors on its way to the bolometer island, where the power is dissipated as heat for the bolometer to detect. A resistive element is used to dissipate the heat. There are two common techniques in the field: a lossy meandering microstrip line and a lumped resistor.

Most experiments use superconducting metals and low-loss dielectrics for their microstrip lines in order to minimize attenuation of the microwave signal. At the bolometer island, however, it is necessary to dissipate the power. This can be achieved by transitioning to a non-superconducting, purposefully resistive metal. The signal will be attenuated along the length of this non-superconducting microstrip line, and the power will be dissipated as heat. The microstrip can be designed to meander so that the path length is large while occupying a relatively small area on the bolometer island. The resistivity of this non-superconducting metal must be relatively low in order to prevent an impedance mismatch between the incoming superconducting microstrip line and the lossy meandering microstrip line. Since the resistivity is low, the attenuation per unit length is relatively small; therefore, the meander must have a large path length in order to dissipate most of the power. This tends to make the lossy meanders large, which also increases the size of the bolometer island. A desirable property of this termination is that it requires only a signal unbalanced microstrip line coming in to the bolometer island. The end of the meander can be left open-circuited, since the reflected power is heavily attenuated by the lossy metal. Since different frequencies pass through a different number of wavelengths in the meander, the absorption efficiency is frequency dependent.

The other main type of termination is a lumped resistor. The incoming microstrip line is terminated by an impedance-matched resistor, and the power is then dissipated as heat on the bolometer island. An advantage of this paradigm is that a lumped resistor tends to be relatively small and represents a minor contribution to the size of the bolometer island. The lumped resistor typically consists of a short section of high-resistivity metal, where the particular geometry is important in determining the lumped resistance. For a single unbalanced microstrip line, the lumped resistor should be shorted to ground; the disadvantage here is that a via is required. For two balanced microstrip lines, the resistor can be differentially fed and, if its resistance is chosen to be twice the microstrip impedance, will dissipate all of the power without a via. Another advantage of the differentially fed termination is that it accepts odd modes but rejects even modes.

The lumped-resistor paradigm is relatively insensitive to the termination resistance, because the reflected power goes as

$$|\Gamma|^2 = \left| \frac{R_0 - R_L}{R_0 + R_L} \right|^2, \quad (4.4.1)$$

where  $\Gamma$  is the reflection amplitude,  $R_0$  is the characteristic impedance of the microstrip line and  $R_L$  is the termination (load) resistance. The reflection increases relatively slowly as  $R_L$  deviates from  $R_0$ . Even when the termination resistance differs from the microstrip impedance by a factor of 2, the reflection is only  $\sim 10\%$ .

RF termination for MKID detectors also uses lossy metal to generate quasi-particles, but its implementation is slightly different from terminations used for TES bolometers. The coupling scheme for RF termination is shown in Figure 64. A microstrip line feeds a standard broadband microstrip-to-slotline transition, where the slotline is formed in the niobium ground plane that is common to the microstrip and the MKID CPW. The two slotlines are then brought together and become the gaps of the CPW transmission line, where it dissipates by exciting quasiparticles and thereby changes the resonant frequency of the device. The slotline is electrically short at the resonant frequency of the MKID, and thus it does not impact the microwave characteristics of the resonators. Each CPW resonator is capacitively coupled to a transmission line and driven by a probe tone; sky signals are detected as changes in the amplitude and phase of this probe tone. HFSS/Sonnet simulations show the expected absorption efficiency of the detector is approximately 90%.

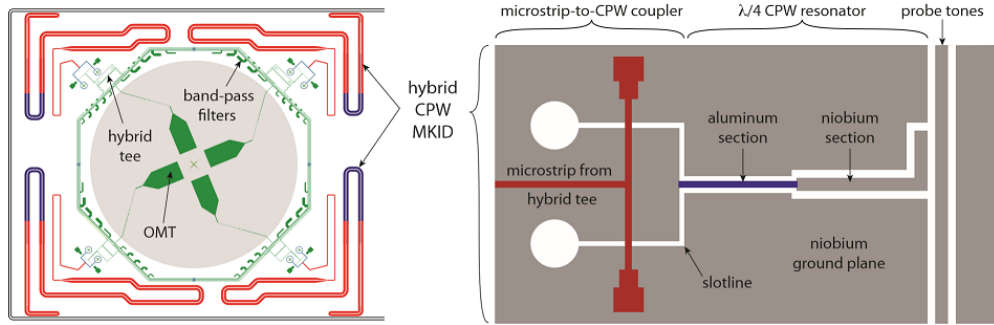


Figure 64: A schematic of the microstrip-to-CPW coupling schematic for MKID detectors. The millimeter-wave power is coupled from the microstrip output of the hybrid tee to the CPW of the MKID using a novel, broadband circuit [216].

**Demonstrated performance** Experiments that use lossy meanders include BICEP2, ABS, ACTPol and SPTpol [201, 205, 217, 218]. Gold is a popular low-resistivity metal for this purpose.

Experiments that use lumped resistors include POLARBEAR, POLARBEAR-2, SPT-3G and CLASS [63, 159, 173, 204]. Titanium is a popular high-resistivity metal for this purpose. The critical temperature of titanium, which is  $\sim 500$  mK, is low enough for frequencies above  $\sim 40$  GHz to break Cooper pairs and see titanium as an effectively normal metal. A bolometer island is shown in Figure 65, where the lumped resistor can be seen. Notice that the lumped resistor is substantially smaller than the lossy gold meander.

**Prospects and R&D path for CMB-S4** The technology status level of the RF termination for TES bolometer is 5. Multiple CMB polarization results were published using microwave coupled TES bolometers.

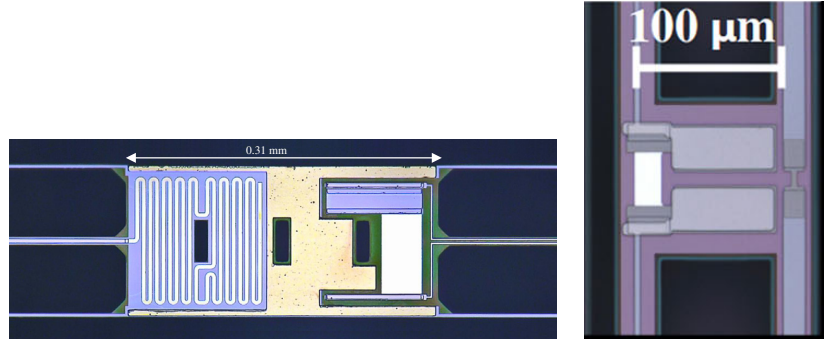


Figure 65: Example microstrip terminations for TES bolometers. (Left) BICEP2 bolometer island with a lossy gold meander and TES [201]. (Right) POLARBEAR-2-style bolometer island with a lumped titanium resistor (right) and TES (left) [208].

The production status level for the RF termination for TES bolometer is also 5. RF termination is micro-fabricated as part of the standard detector fabrication process. Large quantity of detector array was fabricated for stage-III experiments to demonstrate scalability.

The technology status level of the RF termination for CPW coupled MKID detector system is 1. A laboratory demonstration of the RF termination scheme described above with multichroic MKIDs will happen in 2017

The production status level for the RF termination for CPW coupled MKID detector system is 1. MKID technology is designed to provide high throughput necessary for CMB-S4. Demonstration in 2017 will inform the scalability of the technology.

**Lab Demonstration:** RF termination for MKID detectors

**Sky Demonstration:** Lumped and distributed termination deployed successfully with high efficiency

**Path to CMB-S4:** Technology is mature for TES coupling

MKID termination could provide additional path for scalability

## 4.5 Array layout, pixel size, and wiring considerations

**Description of the technology** Finding an optimal pixel size is a complex problem that requires balancing the sensitivity of a detector array, the finite size of RF components, and the density of interconnects. Sensitivity of the detector array as a function of pixel size can be determined by calculating the sensitivity of each pixel and the number of pixels in a focal plane. For ground-based experiments that have to observe through the atmosphere, an optimal pixel size for a fixed field of view typically is in the range 0.5 to 1.5  $f\lambda$ . Knowing the  $f/\#$  of the optics at the focal plane and the wavelength of interest translates pixel size in  $f\lambda$  units to a physical pixel size. The challenge is then to find a balance between the desire to have smaller pixels and the need to fit RF components within a limited space.

For example, a multichroic pixel from AdvACT covers the 150 GHz and 230 GHz bands. The  $f/\#$  of the AdvACT optics at the focal plane is 1.35, so  $f\lambda$  for the center frequency (185 GHz) is 2.2 mm. If the optimal pixel size is between 0.5 to 1.5  $f\lambda$  (see Figure 48), the pixel spacing should be around 1.1 mm to 3.3 mm. Figure 66 shows a proto-type pixel for the AdvACT experiment that has one side of the rhombus at 4.75 mm. Inside the pixel, the OMT feed is the largest element in the pixel, and there is not much freedom to tune antenna size, as it is constrained by wavelength. Lenslet-coupled antennas use the fact that the wavelength is shorter inside a dielectric to shrink the antenna size for a given frequency. As the number of bolometers increases, the filters and bolometers start to take up significant space. It is possible to ease the pixel size challenge in isolation by designing optics with a larger  $f/\#$ ; however, increasing the  $f/\#$  has multiple consequences, such as an increase in the number of detector wafers that need to be fabricated and a need for larger optical components.

Interconnects between detector wafer and readout electronics become challenging as the number of bolometers on a wafer increases. CMB detectors make the connection between a wafer and the readout cable at the perimeters of the wafer. A larger wafer is more challenging because the pixel count increases as length-squared, whereas the length of perimeter grows as length. A multi-chroic detector multiplies the number of required interconnects by the multiplexing factor. Stage-III experiments use automatic wire bonders to make wire-bond connections at  $\sim 100\mu$  pitch. As shown in Figure 66, the current bond pad size is approaching the size of the wire bonding tip.

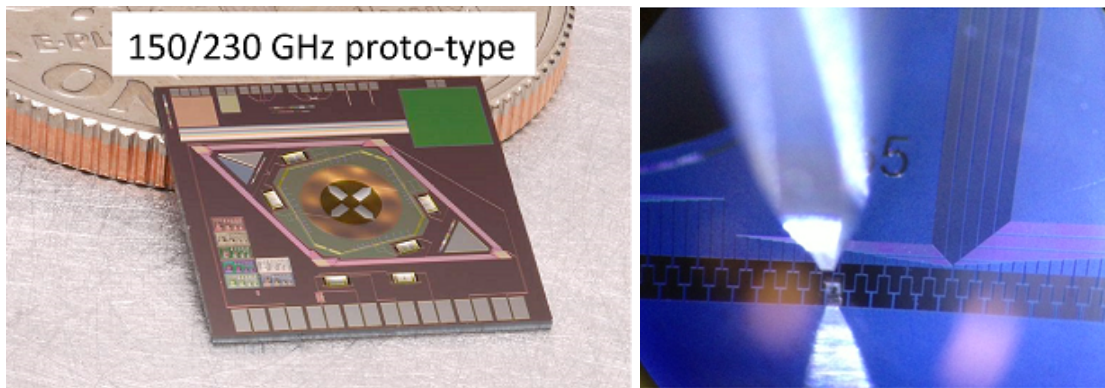


Figure 66: (Left) Advanced ACTPol pixel for 150 GHz and 230 GHz dual-color dual-polarization pixel. Pixel spacing is 4.75 mm. (Right) Array of wire bond pads for the POLARBEAR-2 detector array with a wire bond head. Pads are 90 micron wide with 10 micron gap between pads.

**Demonstrated performance** POLARBEAR-2/Simons Array (90 and 150 GHz) and the SPT-3G (90, 150, and 220 GHz) detector array have 6.789 mm spacing fabricated on a 150 mm diameter wafer. Each hexagonal detector array has 271 hexagonal-shaped pixels with a total of 1,626 bolometers. The largest RF element in the pixel is a sinuous antenna that takes up 3 mm in diameter. Both experiments use a lumped filter design since it takes up less space compared to the equivalent distributed stub filter design. There are six TES bolometers per pixel that are each roughly 100 micron x 1000 micron. Readout wiring is routed between hexagonal pixels and consists of a 5 micron wide line with a 5 micron spacing between lines. An automatic wire bonder makes wire bonds between Nb pads on the wafers to a flexible cable at 100 micron pitch.

The Advanced ACTPol detector array (150 and 230 GHz) was also fabricated on a 150 mm wafer [213]. A pixel is shown in Figure 66; the array has tiles of rhombus-shaped pixels. Wiring from each pixel travels between rhombuses with a 5 micron wide line with 1 micron spacing. There are 503 pixels on a wafer with 2,012 bolometers per array [9]. The bond-pad size is 120 microns wide with a 140 micron pitch, and bond-pads are staggered, so the separation between two wire bonds is 70 microns. Wire bonding with an automatic wire bonding process [219].

**Prospects and R&D path for CMB-S4** Pixel size optimization is a global optimization problem. It is important to understand the pros and cons to come up with a good design for CMB-S4.

For example, there is a trade-off between smaller pixel size and beam performance of a pixel. Also as the density of pixels and wiring increases, cross-talk between detectors needs to be studied carefully. EM simulations would be helpful to study these effects for various pixel sizes.

As the number of pixels on a wafer increases, physical space that inter-pixel wiring takes up becomes a problem. One idea to increase readout wiring density is to run readout lines on top of each other, requiring a pin-hole free dielectric layer to prevent shorts between two lines. Increased detector count also makes the detector to readout cable interconnect challenging. An alternative to wirebonding for high-density interconnections is bump bonding, which was used on SCUBA-2 and will be used on PIPER. It is generally less reversible than wirebonding; however, it warrants further study because wirebonding becomes difficult to reverse when thousands of wirebonds have been installed on large format detector arrays.

Dead space between detector modules due to mounting hardware could hurt coupling efficiency. A modular optics tube that physically separates adjacent detector modules allows mounting hardware to be present between detector modules. This approach is used in Advanced ACTPol. The same approach could be improved by matching the shape of the first refractive optic to the hexagonal shape of the detector array (e.g [3]). This approach seems to reduce the detector array constraints in exchange for increasing the refractive optics constraints. It facilitates deploying additional frequencies on the same telescope though, because each optics tube can easily be used for different frequencies.

Integrating a multiplexing circuit with a detector wafer will greatly reduce the number of wire bonds required, as shown in Figure 73. Such resonators can be coupled to  $\mu$ MUX or high frequency DfMux readout as outlined in Chapter 5. Currently 50-100 MHz resonators are being developed for DfMux readout. The same method can be used to fabricate  $\sim$ 1 GHz resonators for  $\mu$ MUX readout, which would be significantly smaller and take less space on a wafer.

Because array packing density problem is global optimization problem, it is hard to come up with the technology status level for the topic. We assigned TSL level 4, since multiple experiments successfully deployed with densely packed focal plane. However, this does not guarantee focal plane density won't be a problem for CMB-S4. Small f-number at focal plane, physically small pixels for high frequency channels, and multichroic pixel could pose new level of packing density challenge for CMB-S4. We assigned slightly lower status level for the production status level. The production status level is 3. There are new ideas such

as bump bonding to solve interconnect challenge, but these new approaches have not been demonstrated ability to be mass produced at scale of CMB-S4.

**Lab Demonstration:** 90/150/220 GHz lenslet detector array packed 1,600 bolometers on a wafer

**Sky Demonstration:** 150/230 GHz horn array packed 2,000 bolometers on a wafer

**Path to CMB-S4:** High density interconnect, integrate multiplexer on chip, new telescope design

## 4.6 Detector characterization

**Introduction** Detector testing is an essential part of detector fabrication, a common need for all the technologies discussed in this paper. Detector testing is challenging for two fundamental reasons: (i) CMB detectors utilize superconducting technology and can only be fully characterized using sub-Kelvin testbeds, and (ii) complete optical characterization of CMB detectors requires broadband incoherent light sources spanning  $\sim$ 1–3 mm wavelengths, a spectrum where there is little or no commercial instrumentation. As such, the testing and feedback associated with developing detector RF architectures can only be fulfilled through research groups at universities and national labs. In this section, we review common methods and challenges associated with characterizing RF performance.

**“Room temperature ( $>1$  K)” inspection** Room temperature measurements are typically used as a first pass assessment of fabrication quality. These measurements include visual inspection and electrical resistance measurements, where the latter provides some information regarding electrical connectivity (or isolation) and materials properties. In general, these measurements primarily help with preparing devices for cryogenic testing. The critical limitation to these measurements arises from the fact that the CMB detectors need to be superconducting in order to operate. Similarly, measurements at  $\sim$ 70 K are limited in their utility. There is some benefit to measurements at 4 K, as at this temperature, the detector microstrip structures are functional. Though it isn’t possible to characterize the integrated performance of a detector at 4 K, it is possible to understand generic microstrip properties using dedicated test structures. For example, it is possible to measure a microstrip test device that couples radiation from one polarization, transmits that signal through an RF test circuit (including filters and calibration structures), and then re-radiates the signal into the orthogonal polarization. This test structure can be cooled to 4 K and analyzed using more conventional room temperature network analyzers.

**Sub-Kelvin testbeds** The necessary measurements for developing the detector RF design require operating devices at temperatures below the detector critical temperature with base temperatures ranging from  $\sim$ 50 mK-300 mK. Current test beds (see Figure 67) include smaller cryostats, often using liquid cryogens, and larger cryostats typically cooled using cryogen-free pulse tube coolers (PTC)s. The advantage of the smaller cryostats is that they can typically reach base temperature in less than 12 hours allowing for rapid turnaround. If cooled using liquid cryogens, the small size efficiently utilizes the liquid cryogens, though regular servicing and monitoring is required to keep the system cold. PTC-cooled cryostats are now commercially available, though they have higher startup costs and require careful design to minimize electrical and microphonic pickup. The advantage of PTC systems is in their low operating overhead, which makes them efficient for tests requiring large cryogenic volumes.

	He-3 Adsorption	ADR	Dilution
Operation	One-shot	One-shot or Continuous	Continuous
Stages [Kelvin]	2, 0.35, 0.25	1, 0.5, $< 0.1$	1, $< 0.1$
Cooling power [ $\mu$ W]	$\sim 5$	$\sim 5$	$\sim 100$

Table 4-1: Comparison of sub-Kelvin cooler

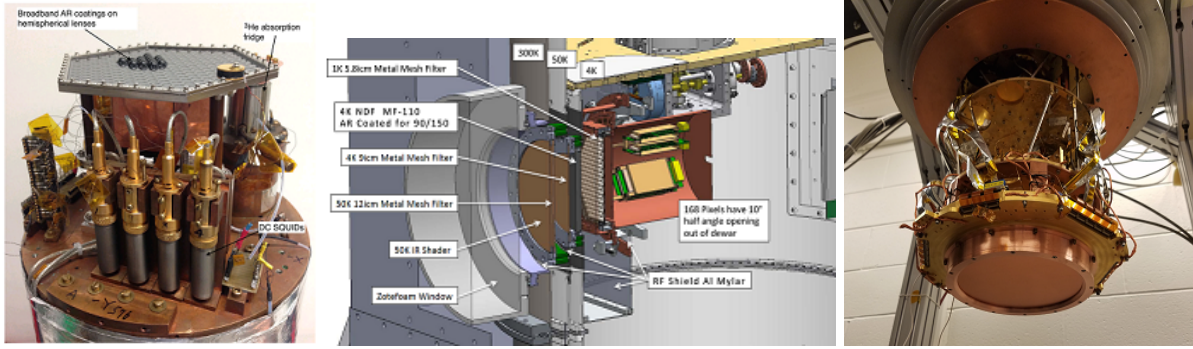


Figure 67: (Left) Photograph of a 8-inch wet dewar with a He-3 adsorption refrigerator. TES bolometers are read out by commercially available DC SQUID. (Middle) Cross-section of PTC cooled detector test cryostat with ADR. (Right) Photograph of a PTC cooled dilution refrigerator with an Advanced ACTPol array installed prior to deployment.

CMB detector test beds achieve sub-Kelvin operating temperatures using either a Helium-3 adsorption refrigerator, an ADR, or a dilution refrigerator. Comparison of refrigerator characteristics are tabulated in Table 4-1.

The cryogenic testing technology for CMB detector development is mature and well understood. The primary challenge for CMB-S4 detector development is in the sparsity of this critical resource. Investment into building up sub-Kelvin testing capabilities at universities and national labs is a high priority for CMB-S4 R&D.

**Detector loading** The difference in optical power loading between actual observation and the laboratory environment places requirements on the detector characterization procedure in the lab. To prevent optical power from the calibration source from saturating CMB detectors, a cold attenuating filter is often installed inside the dewar. A commonly used attenuating filter is MF-110, a castable mm-wave absorber. There is literature on emissivity of MF-110, but the exact details of the filter performance depend on its temperature and AR coating. The attenuator has a steep attenuation profile versus frequency, so a filter optimized for one frequency band is not suitable for testing other bands.

Another way to characterize the RF performance is to couple the RF circuit to a detector that is designed for high optical loading. A TES bolometer can be fabricated to accept a higher optical load by increasing the transition temperature of the thermistor. The BICEP2/Keck Array/BICEP3 experiments and POLARBEAR-1 had a high T<sub>c</sub> superconducting metal (Aluminum) in series with a superconducting metal with transition temperature tuned for observations. The detector is biased onto the high T<sub>c</sub> superconducting metal for laboratory testing, and the detector is biased to the low T<sub>c</sub> superconducting metal during actual observation. This method has the benefit of not requiring a special attenuating filter at the cost of having to fabricate an additional TES for each detector for lab testing. In-situ testing of the final optical system, including beam and bandpass calibrations, also benefit from having a second, high-loading detector.

**Beam** Angular response of feed is characterized by sweeping a source in front of a detector. Simple beam mapping approach is to sweep unpolarized temperature modulated incoherence source with circular aperture in flat 2-dimensional linear stage. More elaborate setup involves linear translation stages with a

source antenna attached to multi-axis rotation head. A CAD drawing of a multi-axis system is shown in Figure 68.

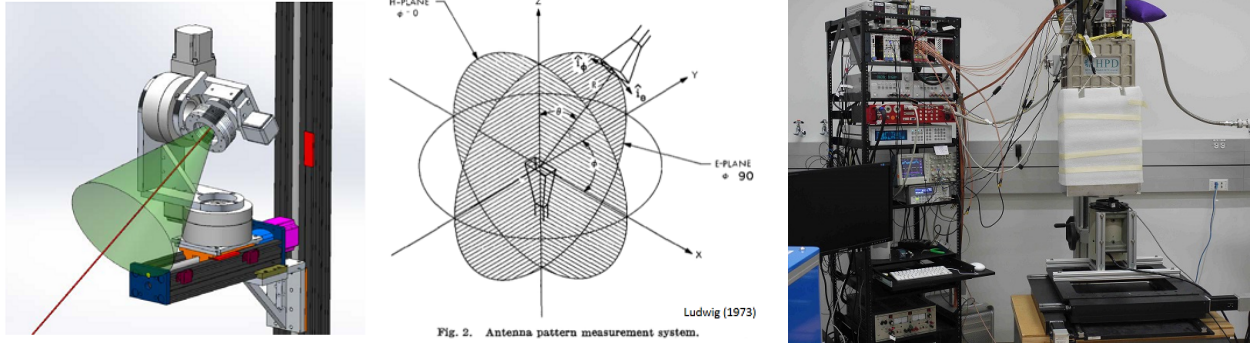


Figure 68: (Left) CAD drawing of multi-axis beam map setup. (Middle) Graphical representation of antenna pattern measurement setup. (Right) Photograph of a 2D beam mapping system at NIST. The detectors look down through the bottom of the dewar, while the chopped source points upward and is mounted on a two axis stage.

**Polarization** Co-polar (E-plane) beam and cross-polar (H-plane) beam of a feed are characterized by attaching a source with a well-defined polarization to beam mapping setup. The multi-axis setup described previously allows accurate mapping of the co-polar and cross-polar response of a feed.

**Spectrum** An FTS is used to characterize the frequency response of each detector. A plastic sheet is often used as a beam splitter for a Michelson FTS, and a wire grid is used as a beam splitter for a Martin-Puplett FTS. A dielectric beam splitter has frequency response that needs to be taken into account in data analysis. Optical coupling between a FTS and a detector needs to be optimized for an accurate spectrum measurement. Inserting an integrating sphere could mitigate the coupling problem at the cost of degradation of signal strength.

**Efficiency** Accurate characterization of detector (feed to detector) efficiency is necessary to optimize the detector design, and consistency in measured detector efficiencies is a good indicator of fabrication repeatability. Efficiency is measured by changing the input temperature of a black body source to known temperatures, and comparing the change in power received versus the total optical power from the source at different input temperatures. For a single-moded detector in the Rayleigh-Jeans limit, the change in optical power from beam-filling black body source is simply  $\Delta P = k_B \Delta T \Delta \nu$  where  $k_B$  is Boltzmann's constant, and  $\Delta \nu$  is the detector's integrated bandwidth. In a case where the temperature modulated source is outside of a dewar, it is important to know the in-band efficiencies of IR filters, attenuator and windows of the dewar. It is also possible to insert a temperature modulated blackbody inside of cryostat, or to inject signal into one polarization channel, route the signal through on-chip RF circuits, and then re-emit directly through the same antenna on the orthogonal channel.

**Prospects and R&D path for CMB-S4** CMB-S4 will deploy an order of magnitude more detectors than Stage-III CMB experiments. Detector characterization throughput needs to keep up with detector

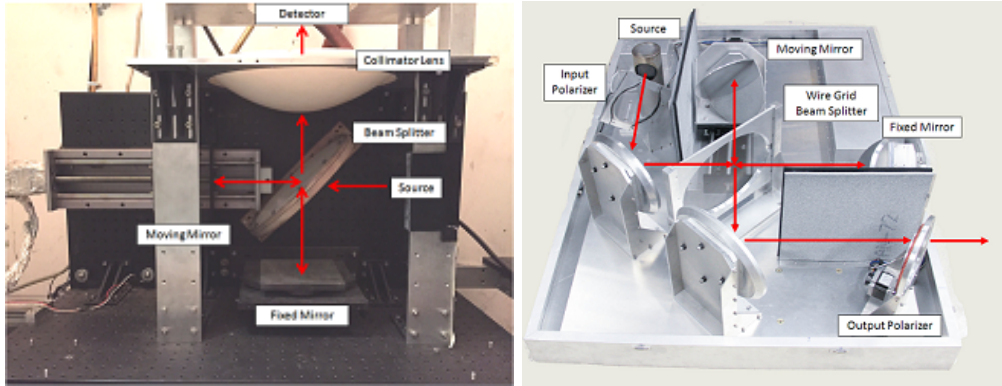


Figure 69: (Left) Photograph of a Michelson FTS with a Mylar beam splitter. UHMWPE lens is placed at output of the FTS to collimate output to a detector. (Right) Photograph of a Martin-Puplett FTS that uses wire grid as a beam splitter.

fabrication. A significant amount of time for detector testing is taken up by cool down time for the test cryostat, so a robust method to shorten cool down time should be demonstrated. Automation of testing procedures allow detector characterization to be done in parallel at multiple places, and standardizing the test setup is important to be able to distribute testing to multiple institutions and still be able to compare test results. As the experiment's sensitivity increases, the requirements on detector systematic errors becomes tighter, and it becomes important to understand details such as characteristics of the attenuating filter used for testing and any reflections that happen between various optical elements in the test setup.

Development of specific RF circuit components would benefit greatly from new measurement techniques. Current practice requires end-to-end measurements, typically with free-space coupling, where the measurement includes only the integrated detector response plus the response from optics external to the device under test. Isolation of a specific RF component in the circuit is challenging. Cryogenic mm-wave VNAs would allow designers to isolate and develop specific circuit elements of the detector design.

We assigned technology status level 4 for characterization. Multiple CMB experiments successfully characterized focal plane system at a level that is good enough for Stage-III experiments. Expected high sensitivity of CMB-S4 will require tighter control of detector systematic errors.

The production status level for characterization is 2. Stage-III experiments characterized large quantity of focal plane units, but characterization needs much higher throughput if we are to test all detectors.

<b>Lab Demonstration:</b>	250/100 mK test bed for TES and MKID at multiple institutions
<b>Sky Demonstration:</b>	N/A
<b>Path to CMB-S4:</b>	Standardization. Improve throughput. Dedicated cryo RF test setup

## 4.7 Conclusion

There are a wealth of promising RF designs for CMB detectors. Given the simultaneous need for high sensitivity and multiple bands to discriminate foregrounds, recent work on implementing multichroic detector designs suggests having two or more frequency bands for each pixel could be a viable path to achieving the total bandwidth and spectral resolution requirements of CMB-S4. Two-channel designs have been successfully implemented in Stage-II and Stage-III experiments, and will soon be deployed in more. Broadband antennas have demonstrated promising performance, and new developments are in place to extend their capabilities. Efficient coupling of millimeter waves to both TES bolometers and MKIDs have been demonstrated.

Scaling up detector fabrication for CMB-S4 requires an increase in production throughput. National labs and universities are exploring ways to expand their production and testing capability. Fabrication facilities with a stable environment are necessary for mass production of CMB-S4 detectors. Groups are studying the feasibility of automating repetitive tasks, simplifying designs by integrating parts, and outsourcing to commercial fabrication foundries. Emerging RF techniques, such as metamaterial lenslet arrays, may facilitate mass production.

Developing dielectric insulators with low loss is essential for boosting detector efficiency and providing flexibility in circuit design. Reduced loss dielectric films make it feasible to build higher order narrow band filter designs that subdivide single atmospheric windows.

Technology to improve detector packing density should be developed, and assembly should be simplified for mass production. Several new developments such as using stepper lithography to shrink wiring real estate, integrating resonators for multiplexing readout on a detector wafer, and new telescope designs that give more design flexibility for detector array are on going.

Detector characterization is an essential part of detector fabrication. Timely feedback with accurate information is necessary to fabricate high performance detectors. The CMB community has many years of experience characterizing detector arrays. Development for high throughput testing is required to meet the demands of CMB-S4. New test cryostat designs, automation of testing and standardization of detector characterization will be necessary to increase detector testing throughput. Systematic error requirements on RF performance will be tighter for a more sensitive future CMB experiment and higher accuracy detector. Detector characterization will be needed to meet these requirements.

Multichroic detectors are deploying in the field, and new ideas are being tested in laboratories. Different designs have unique strengths and short comings. Feedback from up coming Stage-III experiments will allow us to make informed decisions for CMB-S4 development prioritization. Systematic errors that arise from non-ideality in detector performance and cost evaluation were not addressed in this chapter, but they will be addressed in a future iteration of this document. Detector RF design will be decided based on a global optimization that maximizes scientific return.

## 4.8 Summary of detector-RF technologies

	Lab Demonstration	Sky Demonstration	Path to CMB-S4	Section	T/PSL
<b>Antenna and Feed</b>					
<b>Single band</b>					
Feed horn/Planar OMT	✓	90,150 GHz ACTPol/SPTpol	Mass prod of horn	4.3.1.1, 4.3.1.2	5/3
LEKID + Horn	150 GHz dual pol	1.2 THz BLAST-TNG (2017)	On sky demo, fast prod	4.3.1.3	2/3
Lenslet coupled antenna	✓	150 GHz PB-1	Mass prod	4.3.2.1, 4.3.2.2	5/3
Antenna Array	✓	90/150/220/270 GHz BICEPS	Steerable beam	4.3.3	5/4
Multimode Absorber	BUG for PIPER	MBAC, SHARC-II	Pol sensitive det array	4.3.4	3/3
<b>Multi-choice</b>					
Feed horn/Planar OMT	✓	90/150, 150/230 GHz ACTPol	Mass prod, coupling	4.3.1.1, 4.3.1.2	4/3
MKID + Horn	Design completed	-	RF coupling, scalability	4.3.1.3	1/1
Lenslet coupled antenna	5.1, 40 to 350 GHz	90/150, 220/280 GHz SA(2017)	Mass prod, on sky syst	4.3.2.1, 4.3.2.2	3/3
Meta material lenslet	Coupled with antenna	-	Lab study, mass prod	4.3.2.3	1/2
Antenna Array	2:1 bandwidth	-	Total bandwidth	4.3.3	5/4
Multimode Absorber	PSB for PIXIE	-	Pol sensitive det array	4.3.4	3/2
<b>RF Technology</b>					
T-Line	SiNx	SiO <sub>x</sub> & Si	Low loss dielectric	4.4.1	5/5
Filter	3,4,7-channels	2,3 channel humped & stub	Split atm. window	4.4.2	5/5
Cross-over	via & via-less	via & via-less	✓	4.4.3	5/5
Termination	meander & humped	meander & humped	✓	4.4.4	5/5
<b>Array Layout</b>					
Array Layout	90/150/220 GHz	150/23 GHz0, 2,000 ch/wafer	Integ mux, int connect	4.5	4/3
<b>Characterization</b>					
Characterization	✓	mult exp tested & deployed	Std, throughput, syst	4.6	4/2



# 5

---

## Focal plane sensors and readout

### 5.1 Introduction

In this section, we briefly review the state of low-noise sensors and signal readout suitable for CMB polarimetry, focusing on scalable technologies that hold promise for CMB-S4. For each technology described here, we provide (1) an overview and references for further study, (2) a summary of current performance as demonstrated on-sky for technologies with established heritage, and laboratory performance for technologies with promising initial results, and (3) challenges and the requisite R&D path to scale and/or refine the technology for CMB-S4 requirements.

We describe low-noise sensors for detecting the CMB in Sections 5.2 and 5.3, which address transition edge sensor (TES) bolometers and microwave kinetic inductance detectors (MKIDs) respectively. Highly multiplexed readout is crucial for operating large arrays of sensors at sub-Kelvin temperatures. MKIDs were conceived to be read out in a frequency-division multiplexing (FDM) scheme at approximately GHz frequencies, as described in Section 5.3. Several different readout techniques exist for TESs. Sections 5.4 describes time-division multiplexing (TDM), while Sections 5.5 and 5.6 overview two different FDM schemes. All the TES readout methods rely on cold-stage signal amplification using SQUIDs. The FDM techniques using GHz interrogation frequencies use a cold-stage low-noise amplifier such as a high-electron mobility transistor (HEMT) amplifier to read out groups of 500-1000 detectors. Section 5.7 reports on the room-temperature electronics for FDM in its various forms. Finally, Section 5.8 gives conclusions from this sensor and readout review, and Section 5.9 provides summary tables.

The large number of detectors required for CMB-S4 puts a premium on developing robust methods for assembly of the sensors with the cryogenic readout (often called “packaging”) and/or techniques for integrated fabrication of sensors with readout elements. The present work provides context for these assembly and integration issues, but further elaboration is delayed for future work, as are direct performance comparisons and detailed cost discussions.

### 5.2 Transition edge sensor (TES) bolometers

#### Description of the technology

A TES bolometer is a highly sensitive thermometer consisting of a superconducting thin film weakly heat-sunk to a bath at much lower temperature than the superconductor  $T_c$  (see Fig. 70). Arrays of these devices are fabricated via micro-machining of thin films deposited on silicon wafers. When supplied with a

voltage bias, a TES sensor can operate in its superconducting-to-normal transition such that small changes to the TES temperature, arising from changes in the absorbed power, lead to large changes in the TES electrical resistance. The combination of voltage bias and sharp transition (large  $dR/dT$ ) lead the TES to experience strong electrothermal feedback [220]: the TES Joule power dissipation,  $V^2/R$ , opposes changes in the incident power, maintaining the TES at a nearly constant temperature. This negative feedback linearizes the detector's response, expands its bandwidth, and ensures a simple relationship (“self-calibration”) between observed TES current and incident power.

Operationally, a TES is voltage biased using either an AC or DC signal and is read out using a SQUID. SQUIDs have much lower noise than TES or photon noise, enabling multiplexed detector readout schemes (see Sections 5.4, 5.5, and 5.6). Multiplexed readout is important for operating large arrays of detectors at sub-Kelvin temperatures. An important consideration in TES detector design is operational stability of the electrothermal circuit. The detector's operational time constant needs to be fast relative to the sky signal, but slow relative to the per-channel readout bandwidth. Fielded TES detectors have satisfied these constraints with tuned bolometer heat capacities and thermal conductivities, which in combination with the detector transition shapes  $R(T, I)$  have yielded time constants of order 1 ms.

The theoretical foundations for use of TESs in detectors are well developed [221] providing good descriptions of the noise and response for real devices. In CMB applications, the irreducible noise for a TES detector arises from statistical fluctuations in the absorbed photons [222]. For ground-based experiments, this noise is typically  $\mathcal{O}(10)$  aW/ $\sqrt{\text{Hz}}$ , though values vary depending on platform/site, observation frequency/bandwidth, and the instrumental throughput/efficiency. The second source of fundamental noise for TES bolometers comes from fluctuations in the thermal carriers of the TES's weak thermal link to the bath [223]. With appropriate thermal isolation structures and  $T_c$  ranging from 100–500 mK, TES detectors can achieve thermal conductivities of  $\sim$ 50–200 pW/K, where the thermal fluctuation noise becomes comparable or subdominant to the photon noise. Together with sufficiently low-noise readout electronics, TES bolometers have achieved nearly background limited sensitivities.

## Demonstrated performance

TES bolometric detectors have been applied across a diverse set of CMB experimental platforms. Current detector architectures utilize a low-loss superconducting microstrip transmission line coupled to planar structures to realize optical bandpass definition, polarization separation, beam synthesis and radiation coupling (see Chapter 4). Examples of implemented TES architectures include in-phase combined antenna arrays [183] used by the SPIDER, BICEP2, BICEP3, and the Keck Array experiments, lenslet coupled antennas [176] used by the POLARBEAR and SPT-3G experiments, absorber coupled devices used by the EBEX [81, 224] and SPTpol (90 GHz) [225] experiments, and feedhorn coupled devices with planar orthomode transducers used by the ABS, CLASS [199], ACTPol [226], and SPTpol (150 GHz) [218] experiments. For these detector architectures, the RF performance can be modeled and simulated with results in good agreement with measured performance (see Chapter 4).

CMB detector performance is typically reported as a noise equivalent power (NEP) in units of W/ $\sqrt{\text{Hz}}$ , defined as the amount of detected signal power required to obtain a signal-to-noise ratio of unity in a 1 Hz bandwidth. Detector NEP is often converted into a noise equivalent temperature (NET), which refers the noise to the equivalent sky signal in units of K $\sqrt{\text{s}}$ . This conversion requires knowledge of (or assumptions about) the end-to-end optical efficiency of the completed receiver system, as well as the frequency spectrum of the observed power. CMB experiments have deployed TES detectors sensitive to frequencies spanning the entire range envisioned for CMB-S4: 40–300 GHz, with detectors achieving noise equivalent power (NEP)

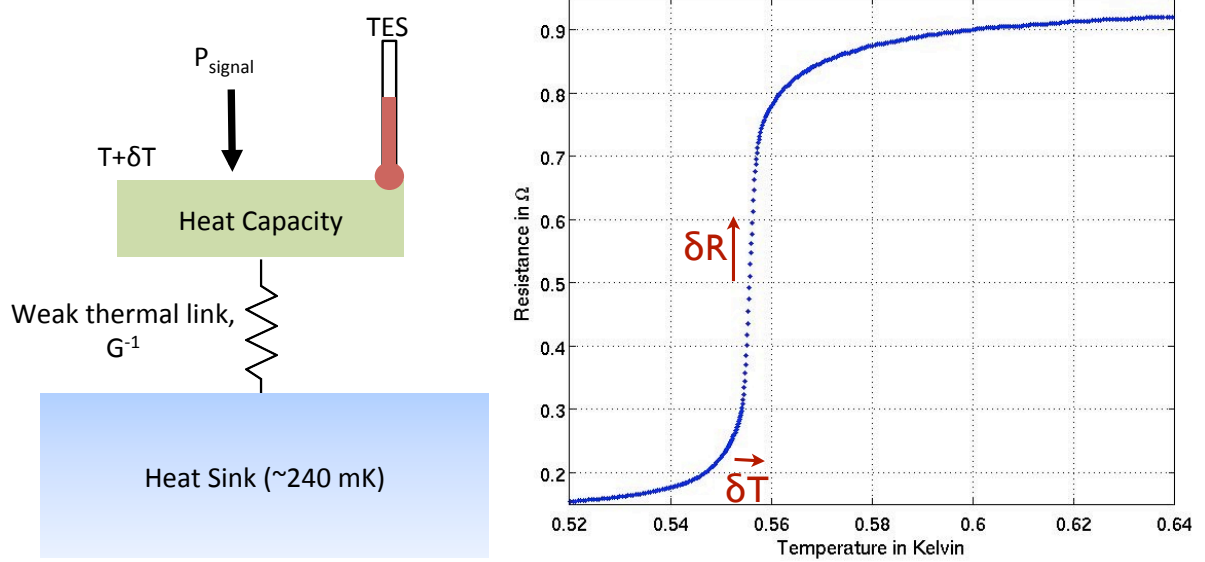


Figure 70: (Left) Illustration of a thermal circuit for a typical TES detector highlighting the principles of signal detection. A weakly thermally sunk heat capacity absorbs power,  $P_{\text{signal}}$ , which is to be measured. Variations in the absorbed power change the heat capacity's temperature, which is measured by a TES operating under strong electrothermal feedback. (Right) Plot of resistance versus temperature for a typical TES illustrating the principles of negative electrothermal feedback [220]. The TES is voltage biased onto its superconducting-to-normal transition. Small changes in the TES temperature produce large changes in the TES resistance. Since the TES is voltage biased, an increase (or decrease) in the temperature produces an increase (or decrease) in the resistance leading to a decrease (or increase) in the Joule heating power supplied by the bias. This canceling effect corresponds to a strong negative electrothermal feedback making the current through the TES nearly proportional to  $P_{\text{signal}}$ .

of (30-50)  $\text{aW}/\sqrt{\text{Hz}}$  (nearly background limited at CMB frequencies). Detectors deployed at low optical frequencies ( $\sim 40 \text{ GHz}$ ) and balloon-borne payloads should realize even lower NEPs of  $\sim 10 \text{ aW}/\sqrt{\text{Hz}}$ . In multiple deployed experiments, the TES noise is consistent with what is predicted from theoretical modeling with realized ground-based experimental sensitivities (array NET) in the range of  $\sim 10\text{--}20 \mu\text{K}\sqrt{\text{s}}$  [63, 226–228].

## Prospects and R&D path for CMB-S4 for TES bolometers

Given the maturity, diversity and demonstrated performance of TES-based CMB detectors, TES detectors are at a high technology status level (see Section 5.9). Multiplexed readouts are required for implementing TES focal planes with thousands of detectors. Current multiplexer technologies (Sections 5.4 and 5.5) already enable arrays of  $\mathcal{O}(10,000)$  detectors, though readout R&D described in Sections 5.5–5.7 could improve scalability and lower cost. The most critical R&D elements needed to advance TES technology for CMB-S4 is that associated with scaling up TES array production for large sensor counts and sufficient quality assurance.

- **Increase production throughput:** Current TES bolometer array fabrication typically involves processing  $\sim$ 10 layers of materials on substrates that are 100-150 mm in diameter. A 150-mm wafer supports  $\sim$ 1,000 detectors at 150 GHz, a density which varies strongly with observing frequency, and which can be multiplied with multichroic optical coupling designs. Arrays are typically fabricated by a team of 2-3 experts producing 5-10 arrays in approximately 3-6 weeks. Improvements in fabrication throughput will come from parallelizing fabrication resources, both person-power and equipment, and by developing modest changes to fabrication techniques and logistics. The primary requirement for increasing TES production is access to micro-fabrication resources with a particular need for dedicated thin film deposition systems to guarantee cleanliness and control of exotic materials.
- **Optimize materials and establish a quality assurance program:** Subsets of TES bolometer arrays for CMB-S4 will by design possess small variations in device parameters to accommodate different operating conditions associated with different observing frequencies, sites and instrument throughput. It is also possible that different RF coupling schemes will be employed to optimize use of different platforms. An important R&D goal is to identify the best materials and processing to accommodate these minor variations in TES designs such as optimal operation temperatures (100 vs 300 mK) and different RF couplings (see Section 4.4). This R&D should proceed in parallel with a program focused on understanding the connection between variations in fabrication processing and superconducting RF circuit performance and thermal properties. In addition to materials and process optimization, it is important to establish test facilities and a quality assurance program among the universities, national labs and fabrication facilities that is commensurate with the increased fabrication throughput. The ultimate goal of this R&D would be an end-to-end production line yielding TES bolometer arrays with uniform properties across each wafer and consistent performance from wafer-to-wafer for a given set of device parameters.

### 5.3 Microwave Kinetic Inductance Detectors

#### Description of the technology

MKIDs are superconducting thin-film GHz resonators that are also designed to be photon absorbers [229]. Absorbed photons with energies greater than the superconducting gap of the film ( $\nu > 2\Delta/h \cong 74 \text{ GHz} \times (T_c/1 \text{ K})$ ) break Cooper pairs, changing the density of quasiparticles in the device. The quasiparticle density affects the dissipation of the superconducting film and the inductance from Cooper pair inertia (kinetic inductance), so that a changing optical signal will cause the resonant frequency and internal quality factor of the resonator to shift. These changes in resonator properties can be detected as changes in the amplitude and phase of a probe tone that drives the resonator at its resonant frequency. This detector technology is particularly well-suited for sub-Kelvin, kilo-pixel detector arrays because each detector element can be dimensioned to have a unique resonant frequency, and the probe tones for hundreds to thousands of detectors can be carried into and out of the cryostat on a single pair of coaxial cables (see Section 5.7).

The total instrument noise is the quadrature sum of the detector noise and the photon noise, and the fundamental performance goal is to achieve a sensitivity that is dominated by the random arrival of background photons. For an MKID, the detector noise includes contributions from three sources: generation-recombination (g-r) noise, two-level system (TLS) noise, and amplifier noise [229]. In general, g-r noise comes from the generation and recombination of quasiparticles. Under typical operating conditions for ground-based CMB observations, any thermal g-r noise is negligible, so the two main noise sources are quasiparticle generation noise from photons (photon noise) and the associated random quasiparticle recombination noise.

TLS noise is produced by dielectric fluctuations due to quantum two level systems in amorphous dielectric surface layers surrounding the MKID. The scaling of TLS noise with operating temperature, resonator geometry, and readout tone power and frequency has been extensively studied experimentally and is well described by a semi-empirical model [230]. Finally, the amplifier noise is the electronic noise of the readout system, which is dominated by the cryogenic microwave low-noise amplifier.

## Demonstrated performance

A range of MKID-based instruments have already shown that MKIDs work at millimeter and sub-millimeter wavelengths. Early MKIDs used antenna coupling [231], and these antenna-coupled MKIDs were demonstrated at the Caltech Submillimeter Observatory (CSO) in 2007 [232] leading to the development of MUSIC, a multichroic antenna-coupled MKID camera [233]. A simpler device design that uses the inductor in a single-layer *LC* resonator to directly absorb the millimeter and sub-millimeter-wave radiation was published in 2008 [234]. This style of MKID, called LEKID, was first demonstrated in 2011 in the 224-pixel NIKA dual-band millimeter-wave camera on the 30 m IRAM telescope in Spain [235]. This pathfinder NIKA instrument led to an upgraded polarization-sensitive NIKA2 receiver with approximately 3,300 detectors [163, 236]. A large format sub-millimeter wavelength camera, called A-MKID, with more than 20,000 pixels and a readout multiplexing factor greater than 1,000 has been built and is currently being commissioned at the APEX telescope in the Atacama Desert in Chile [237].

Photon-noise-limited horn-coupled LEKIDs sensitive to 1.2 THz were recently demonstrated [238] for use in the balloon-borne experiment BLAST-TNG [166, 167]. Laboratory studies have shown that state-of-the-art MKID and LEKID designs can achieve photon noise limited performance [164, 165, 239, 240]. Finally, MKID-based, on-chip spectrometers for sub-millimeter wavelengths (SuperSpec and Micro-Spec) are currently being developed [241, 242].

Two scalable varieties of MKID – using two completely different RF coupling strategies – are currently being developed for CMB polarization studies with CMB-S4 in mind: (i) dual-polarization LEKIDs and (ii) multichroic MKIDs. The details of the RF coupling designs are discussed in Section 4.3.1.3 and Section 4.4.4. The horn-coupled, multichroic devices are based on the polarimeters that were developed for the Advanced ACTPol experiment [9, 150]. However in this new MKID-based version, the TES bolometers are replaced with hybrid coplanar-waveguide (CPW) MKIDs, and the millimeter-wave circuit is fully re-optimized for SOI wafers. The multichroic MKIDs are still in the development stage, and a laboratory performance demonstration is planned for early 2017. The NET, NEP, in-band spectral response, pulse response (time constant), low-frequency noise performance, and multiplexing performance of LEKIDs have all been studied extensively in the laboratory [160, 164, 165]. These studies have revealed that the performance of LEKIDs can be comparable to that of state-of-the-art TES bolometers – especially for ground-based experiments when the optical loading is greater than approximately 1 pW.

Development work is underway to make the sensing element in various MKID architectures out of materials with a tunable transition temperature, such as aluminum manganese (AlMn), titanium nitride (TiN), TiN trilayers, and aluminum-titanium bi-layers [243–245]. With these materials it is possible to decrease the transition temperature below that of thin-film aluminum in a controllable way, which does two critical things. First and foremost, near 150 GHz photons are energetic enough to break multiple Cooper pairs in the sensing element, so that the detector noise will be further suppressed below the photon noise improving the sensitivity. Second, a lower  $T_c$  makes the detector technology sensitive to lower frequencies ( $\sim$ 30 GHz), so that one MKID architecture with a tunable transition temperature could be used for all of the spectral bands in CMB-S4.

## Prospects and R&D Path for CMB-S4 for MKIDs

MKIDs are a new detector option for CMB studies, and they may have appreciable advantages worth considering for CMB-S4. For example, the technology was invented with high multiplexing factors in mind, the readout uses low-power commercially available hardware (see Section 5.7), some device architectures can be made from a single superconducting film, and high-performance prototype LEKIDs have been fabricated in small commercial foundries. Therefore, although MKIDs lack the heritage of TES bolometers in the CMB community, it is reasonable to anticipate that the technology could flourish in a large-scale program like CMB-S4. To make MKIDs a viable candidate for CMB-S4 instruments, research and development work must be done in the following areas:

- **Build deployment-quality arrays:** To date, in the spectral bands for CMB-S4 (30–300 GHz), only comparatively small arrays and scalable prototype arrays of MKIDs have been built, mostly at frequencies of 150 GHz and above. These existing technologies will need to be scaled up and optimized for performance, yield and manufacturability.
- **Demonstrate MKIDs on the sky:** An on-sky test demonstrating that MKIDs can be used for high-precision CMB polarimetry is the critical next step. NIKA2 is starting to make polarization measurements now, and this work will be informative. LEKID-based CMB polarimeter concepts have been considered but not yet funded or built [244, 246, 247]. Dual-polarization LEKID arrays [160] with approximately 500 single-polarization detectors are currently being fabricated, and a demonstration using this array could take place in the next year or two.
- **Increase production throughput:** MKIDs can be fabricated using the tools and techniques currently available in the foundries in national laboratories. However, the number of detectors required for CMB-S4 is unprecedented, so improvements in fabrication throughput will be required. A coordinated effort among existing foundries will likely be needed.

## 5.4 Time-division multiplexing (TDM) using DC SQUIDS

### Description of the technology

In TDM, a group of detectors is arranged into a two-dimensional logical array. Each column of detectors shares a dedicated readout amplifier chain, and only one row of the array is routed to the amplifiers at any given time. The various rows are addressed cyclically in rapid succession to record the entire array.

In the latest generation of the system architecture developed at NIST [248, 249], the current signal from each TES is amplified by a dedicated first-stage SQUID (SQ1)<sup>1</sup>. Each first-stage SQUID is wired in parallel with a Josephson junction switch, and the series voltage sum of all such units in the column is amplified by a series SQUID array (SSA) for transmission to the warm electronics. During multiplexing all but one of the switches are closed to short out the inactive SQUIDS, so that only a single first-stage SQUID feeds the SSA at any given time. This arrangement is shown schematically in Figure 71. This two-stage voltage-summing TDM architecture was first deployed by BICEP3 in 2015 [250]; previous instruments such as SCUBA-2, BICEP2 and ACT employed a three-stage flux-summing architecture [249].

<sup>1</sup>Each first-stage SQUID in the current system is actually itself a small series SQUID array, but we ignore that in this discussion to avoid confusion with each column's SQUID array

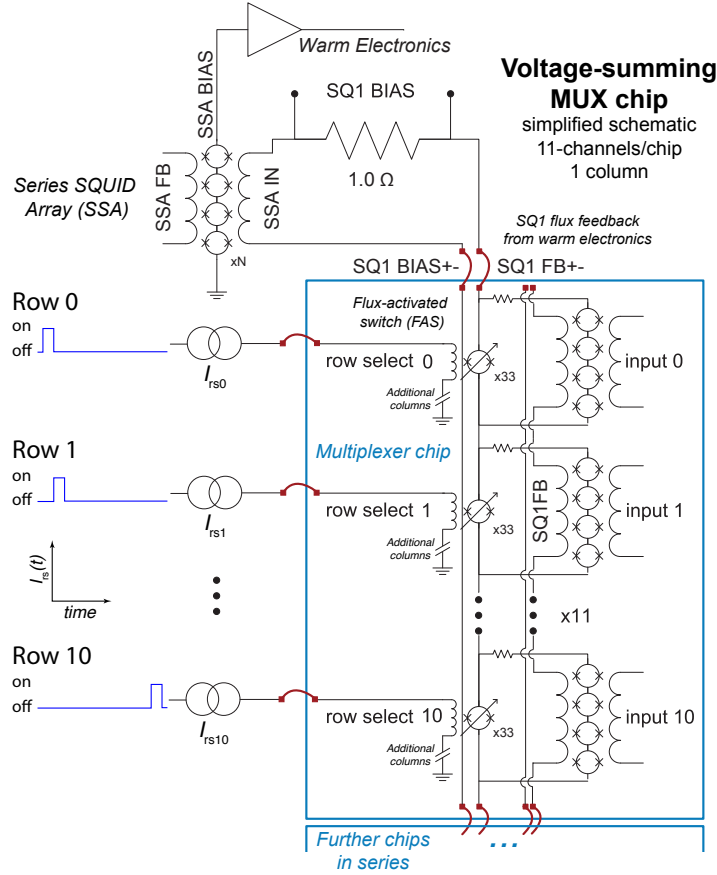


Figure 71: Schematic illustration of a single column of the voltage-summing NIST SQUID multiplexer system. Each TES is coupled inductively to a SQ1. All SQ1s in a column are wired in series to the input of a SSA, but at any given time all but one row of SQ1s is bypassed by a flux-activated switch. The various row-select lines are biased in sequence with low-duty-cycle square waves, as shown at left.

The first-stage SQUIDS and flux-activated switches for 11 rows of a single readout column are patterned on a single “multiplexer chip”. Each multiplexer chip is mated to a corresponding ‘interface chip’, which contains the parallel (shunt) resistors to voltage-bias each TES and series inductors to define the TES bandwidth. The lines connecting the multiplexer and Nyquist chips to the TESs must have low parasitic resistance (typically superconducting), so these chips are typically operated at the detector temperature (0.1-0.3) K.

The Multi-Channel Electronics (MCE), developed for SCUBA-2 [251], provide bias currents and flux offsets for all SQUID stages and switches, thus controlling the shapes and relative alignments of the various modulation curves. The warm electronics linearize this complex response function through flux feedback to the first-stage SQUIDS, keeping each locked at an appropriate point along its modulation curve. This feedback constitutes the recorded signal for each detector. A single MCE crate contains all of the low-noise DACs, ADCs, and digital processing necessary to operate a full TDM array of up to 32 columns and 64 rows. Each circuit board in the crate is controlled by a field-programmable gate array (FPGA), allowing for feature additions and bug fixes through firmware updates. The entire crate communicates with a control computer through a single fiber optic pair, ensuring electrical isolation. Multiple MCEs can be synchronized

with one another (and with external hardware) using a shared “sync box”, which distributes trigger signals and time stamps from a crystal oscillator.

Like all systems in which the multiplexing operation takes place outside the detector wafer, the NIST TDM system makes heavy hybridization demands. The connections between TES and SQ1 must have parasitic resistances that are small compared to the TES shunt resistor (typically a few  $m\Omega$ ), which precludes most connector types. We thus must typically make at least eight superconducting wire bonds per TES: two each from detector to circuit board, from circuit board to multiplexer chip, and between multiplexer and interface chips, plus two for the row select lines. The present division between multiplexer and interface chips is largely to allow interchangeability among instruments with multiple TES architectures; in mass production these chips could easily be integrated, saving one wire bond pair per channel. Connections between the multiplexer chips and SSAs can be made with superconducting Nb wiring for low parasitic resistance and acceptable thermal isolation. The requirements on parasitic resistance are much weaker here, so connectors may be used.

In the TDM system the number of wires to ambient temperature scales roughly as the perimeter of the 2D readout array, while the pixel count scales as the area. It requires one pair per row (row select) and four pairs per column (bias and feedback for the first-stage SQUIDs and SSA). These connections are typically twisted pairs with few-MHz bandwidth.

## Demonstrated performance

The TDM architecture described above is now very mature and has extensive field heritage on a variety of CMB instruments, including ABS [252], ACT [253], ACTPol [136], BICEP2 [201], BICEP3 [19], CLASS [127], Keck Array [254], and SPIDER [110]. As with the other multiplexer systems we describe, the primary figures of merit to consider are (1) wire count per detector, both cold (hybridization effort) and warm (thermal load); (2) thermal loading, both from wiring and amplifier dissipation; and (3) noise, which should be sub-dominant to expected detector and photon noise.

The achievable multiplexing factor is constrained by the ratio of readout bandwidth to TES bandwidth. For a science signal bandwidth of  $\lesssim 100$  Hz, considerations of stability typically demand a TES bandwidth of order a few kHz [221]. This bandwidth is defined by the TES resistance (typically  $< 1 \Omega$ ) and the inductor on the interface chip (typically  $0.1\text{-}2 \mu\text{H}$ ). Readout chain bandwidth is typically defined by the SQUID amplifier and interconnects, notably by the  $L/R$  time constant of the first-stage SQUIDs driving the SSA input coil and (in some cases) by the  $RC$  time constant of the cables to ambient temperature. AdvACT is currently deploying the highest achieved multiplexing factor of 64 TES channels per readout column using the NIST TDM chips and the MCE electronics [9]. There is no intrinsic limit on the number of columns, given sufficient warm readout electronics.

Since the readout chain’s bandwidth must be much higher than the sampling rate of any given TES, noise from the SQUIDs and warm amplifiers is heavily aliased. The aliasing penalty for RMS noise is proportional to the square root of the multiplexing factor. There is some freedom to limit the aliasing impact by reducing detector resistance or adding turns to the SQUID input coil, so in practice the impact from the SQUID/amplifier alone has been small: BICEP2 with a 25 kHz TDM revisit frequency experienced  $\sim 14\%$  aliased noise penalty to its total (photon-noise-dominated) NET, mostly from aliased detector noise [227].

Current instruments dissipate  $\sim 1.8$  nW per readout column at the detector temperature (100-300 mK) [255, 256]. This should not scale strongly with multiplexing factor, since it is dominated by the single first-stage SQUID that is operational at any given time. The SSAs dissipate substantially more power:  $\sim 20$  nW per

readout column. This power may be dissipated at a somewhat higher temperature (typically 1–4 K), and so is typically not a limiting factor.

TDM has several known crosstalk mechanisms, generally of modest amplitude [201, 249]. The largest form of crosstalk is inductive: each SQ1 detects current from neighboring input coils (adjacent rows in the same readout column) inductively at the  $\sim 0.3\%$  level, and at a yet smaller level to more distant rows. In a well-designed system all other forms of crosstalk are subdominant.

A typical full-sized (72-HP) MCE crate serving a  $\sim 2000$  pixel (32 column by 64 row) array consumes 85 watts, supplied by custom linear or switched DC supplies. The crate dimensions are approximately  $40 \times 43 \times 34$  cm (depth / width / height) and it weighs approximately 13 kg, not including separate DC supplies.

## Prospects and R&D path for CMB-S4 for TDM

TDM benefits from almost a decade of field experience in CMB instruments, which has yielded dozens of publications involving more than 10,000 detectors. The hardware and software are well-characterized and well-supported. Systematic errors are controlled and understood for arrays with as many as 64 rows. The interconnect technologies are also relatively simple: twisted-pair cryogenic cables and aluminum wire bonds.

BICEP3 and Advanced ACTPol have successfully deployed CMB receivers using TDM at the  $\sim 2,000$ -detector scale, comparable to the channel counts targeted for CMB-S4’s lower frequency (*e.g.* 30 – 40 GHz) channels. Despite these successes, there are significant development challenges to scaling this technology to the high pixel counts envisioned for CMB-S4’s higher-frequency receivers. TDM is nonetheless a natural back-up alternative to more ambitious multiplexing schemes.

Among other schemes, modified versions of the TDM system known as “code-division multiplexing” (CDM), now under development, may prove to be more viable for larger multiplexing factors [257–259]. Rather than switching among individual detectors, a CDM system switches among measurements of various Walsh code combinations (alternating-sign sums) of the various TES signals. In this configuration all TES signals are sampled at all times, eliminating the  $\sim \sqrt{N_{\text{mux}}}$  amplifier noise aliasing penalty. This allows for much more efficient use of readout bandwidth and thus higher multiplexing factors.

R&D items for CMB-S4 include:

- **Decrease assembly complexity:** Since TDM row-switching is carried out at ambient temperature, wires to room temperature are required for each row as well as each column. That leads to a relatively high wire count per pixel: roughly 264 wire pairs to sub-Kelvin for a  $32 \times 200$  array. This may be ameliorated somewhat through the development of a custom cold switching system [260]. The standard TDM system also has no provision for individually-tuned TES bias values down a common line. Larger multiplexing factors thus make heavier demands on TES fabrication uniformity (in order to use a common bias), or demand additional TES bias lines. Cold hybridization requirements are also substantial: at least eight bonds per TES, plus four per column for SQUID and TES biasing. This hybridization effort may be reduced with fully-automated wire bonding systems or development toward indium bump-bonded systems (*e.g.* [261]). The number of interconnects could be drastically reduced by fabricating the SQUIDs alongside the TESs on the same wafer, though this would require development effort to ensure adequate uniformity and yield.
- **Increase production throughput for cold components** Extrapolating from current technology, a  $32 \times 200$  (6,400 TES) readout array would incorporate more than 70,000 Josephson junctions, 50,000

wire bonds, and  $\sim 60$  nW of power dissipation at detector temperature. The manufacture of large quantities of high-quality Josephson junctions is relatively complex, demanding careful control of superconducting film deposition. Such arrays are now manufactured routinely at *e.g.* NIST, but are rare in industrial fabrication.

- **Increase multiplexing factor** The large number of detectors per telescope envisioned for CMB-S4, particularly for the higher-frequency instruments, will demand a higher multiplexing factor than has been demonstrated thus far. Careful tuning of TES and SQUID properties could potentially double readout bandwidth over Advanced ACTPol while halving TES bandwidth, for a total multiplexing factor of order  $\sim 200$ . Larger factors seem difficult to reconcile with current interconnect bandwidth and TES stability. Significant increases in multiplexing factor may also be achieved in the exploration of hybrid FDM/TDM or modified TDM architectures, including CDM-based systems presently under study.

## 5.5 Frequency-division multiplexing using MHz LC resonators (DfMux)

### Description of the technology

Frequency-division multiplexing (FDM) takes advantage of the relatively large bandwidth of the SQUID amplifier (1–100 MHz) compared to the small bandwidth of CMB signal incident on a TES bolometer. For FDM using in-series MHz LC resonators, each detector is assigned a channel in frequency space, defined by a resonant series RLC circuit, with the bolometer  $R_{\text{TES}}$  acting as a variable resistor. Each detector is AC biased with a unique sinusoidal carrier at its resonant frequency. Sky signals modulate  $R_{\text{TES}}$ , which causes amplitude modulation in the carrier current, encoding the signals as sidebands of the carrier frequency. A key feature of this strategy is that the bias power provided to each detector can be chosen independently, allowing the readout system to compensate somewhat for non-uniformities amongst detector parameters.

The current system of FDM using in-series MHz LC resonators which has been used in CMB experiments is known as DfMux and is described in Reference [262]. A circuit diagram of the DfMux readout system is shown in Figure 72. A bias resistor is wired in parallel with the bolometer LCR circuit, with  $R_{\text{bias}} \ll R_{\text{TES}}$ , creating a voltage bias  $V_{\text{bias}}$  on the bolometers. In the current system, this bias resistor is located at 4 K so that the voltage bias can be supplied by a single pair of wires to the sub-Kelvin focal plane for each comb of bolometers. A current-biased series array of DC SQUIDs [263] (referred to here as a “SQUID”) is used to read out a comb of multiple channels. The current from the bolometers is summed at the SQUID, whose output is modulated by the bolometer currents. To maintain linearity the voltage bias input must be nulled at the amplifier input and the magnitude of the remaining sky signal must also stay within the linear regime of the SQUID. The current generation of DfMux uses a form of baseband feedback known as Digital Active Nulling (DAN) [264], where feedback is applied only around the bolometer carrier frequencies. With DAN the sky signal is also nulled, so that the SQUID acts as an error sensor, and the nulling current is the sky signal.

The readout bandwidth is set by the inductance  $L$  and the resistance  $R_{\text{TES}}$ . The inductance of each channel is constant, and the capacitance is varied to set the resonant frequency. In current implementations of the DfMux system, there is a comfortable margin between the necessary optical time constant, the detector time constant, and the readout time constant ( $L = 60 \mu\text{H}$ ,  $\tau_e \sim 0.5$  ms) [265]. The spacing of the channels in a frequency comb must be large enough so that the off-resonance current from neighboring channels does not interfere with the voltage bias on-resonance, and so that crosstalk between neighboring channels is small.

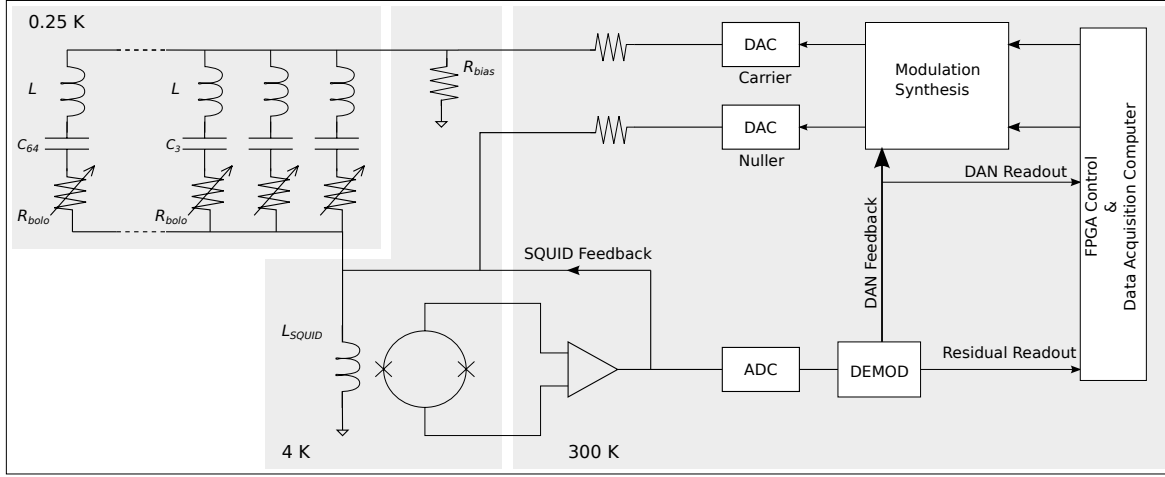


Figure 72: A circuit diagram of the DfMux readout system is shown, with the cryogenic portion at the left, and the room temperature electronics at right. Figure from [266].

To keep crosstalk below 0.5%, minimum spacing between channels are greater than 40 kHz. Crosstalk here is defined as the ratio of power fluctuations from other channels to the expected signal power fluctuation.

The operation of the resonant RLC circuit depends on there being negligible impedance in series with the well-defined components of the circuit. The bolometer resistance  $R_{TES}$  must be the dominant resistance, and there also must be minimal stray inductance from wiring and circuit boards. These components and wiring are all at sub-Kelvin temperatures, which helps to achieve these specifications. The wiring from the SQUID and bias resistor at 4 K to the sub-Kelvin focal plane must be low inductance while acting as a thermal break; this is achieved with broadside-coupled NbTi striplines with lengths  $\sim 50\text{--}100$  cm. For systems where the bias resistor and SQUID input sit at different cryogenic temperatures, the practical lengths and inductances of the current sub-Kelvin wiring and components requires  $R_{TES} \approx 1\Omega$ , to keep the bolometer impedance large compared to other impedances. FDM for much lower  $R_{TES}$  has been implemented by placing the bias resistor and a first stage SQUID at low temperature, such that the wire lengths are short and wiring inductance is negligible [267].

There are two pairs of wirebonds per detector: from detector wafer to cable, and across the LC resonator. There is no power dissipation at the sub-Kelvin stages from readout components. The cryogenic wiring is simple: there is just one pair of wires running to the sub-Kelvin stages for each multiplexed comb of bolometers. There are only two connectors used in the readout chain so as to minimize stray inductance and resistance: after the wafer readout cable, and at the 4 K SQUID. The thermal load on the focal plane from these wires is about  $\sim 1\text{ nW}$  per comb, depending on wire length and the number of thermal interfaces. There is also minimal power dissipated at the other temperature stages from readout wiring. The readout system dissipates power at the 4 K stage in the current system, from SQUIDs and bias resistors,  $\lesssim 1\text{ }\mu\text{W}$  per comb. If the bias resistor is moved to a sub-Kelvin stage with limited cooling power, it could be replaced with an inductive or capacitive divider to reduce power dissipation to zero. The standard twisted-pair cryogenic wiring which runs between the cold components and the room temperature electronics requires three pairs for each multiplexed comb. The length of this wiring is practically limited by its total resistance ( $\sim 20\Omega$ ), since it acts as a voltage divider for the voltage output of the SQUID. Exact total length could be adjusted by varying gauge of low thermal conductivity wire.

The DfMux readout system uses custom warm electronics to synthesize the bolometer voltage biases (labeled “Carrier Bias Comb”), the nulling signal that is applied to the SQUID to increase its dynamic range (labeled “Nulling Comb”), and the demodulators [262, 264, 268]. The SQUID has a transimpedance that is high enough to convert small current through the bolometers into a voltage that can be read out with a room-temperature amplifier. The power and space requirements for the warm electronics are relatively small. The “ICE” room temperature readout electronics [269] being deployed for SPT-3G with a 68x multiplexing factor will operate 8,700 detector channels per 9U crate (40 cm tall, 25 cm deep, 50 cm wide), with less than 1 kW of power draw.

## Demonstrated performance

Stage-II CMB polarization experiments such as POLARBEAR-1 [63, 270], SPTpol [139, 271], and EBEX [81] have demonstrated frequency-division multiplexing factors of 8×–16× on a single pair of cryogenic wires. The Stage-III experiments SPT-3G [266] and POLARBEAR-2 [265, 272, 273] are deploying in 2016 and 2017 with multiplexing factors of 68× and 40×, respectively.

The introduction of DAN feedback (demonstrated on-sky with SPTpol) has extended the usable bandwidth with stable SQUID feedback, allowing channels to be distributed anywhere within the 120 MHz bandwidth of the current SQUID series arrays.

To improve the precision of channel placement and to reduce loss at higher frequencies, superconducting resonator components were developed [265, 273], with an interdigitated capacitor along with a spiral inductor in a single layer of superconducting traces. These developments increased the potential multiplexing factor by a factor of five for the DfMux system used in Stage-III experiments.

Two of the dominant noise sources are related to the SQUID: the current noise of the SQUID itself, and the voltage noise of the SQUID’s first-stage amplifier. Both of these noise sources are far from fundamental limits and could be further reduced. There is also noise associated with the generation of the carrier and nuller signals, dominated by the output current noise of the DAC, presently limited by available off-the-shelf DAC technology. The system can be designed so that the expected noise equivalent current of the dominant readout noise sources is sub-dominant to the bolometer power noise terms ( $\sim 20\text{--}30\text{pA}/\sqrt{\text{Hz}}$ ), and a readout noise equivalent current of  $\sim 7\text{--}10\text{pA}/\sqrt{\text{Hz}}$  has been demonstrated on several experiments [63, 274, 275]. This results in the readout noise being negligible compared to the photon noise for detectors with appropriate parameters.

In the DfMux system, signal crosstalk onto a detector can only occur if the crosstalk signal lies within its frequency bandwidth. Other crosstalk can introduce excess loading on the SQUID and noise, but does not introduce false sky signals. Since the fraction of total SQUID bandwidth that is occupied by detector signals is very small, there is a small amount of crosstalk from its nearest neighbors in frequency space and physical space in the comb. For POLARBEAR-1, the highest level of signal crosstalk came from neighbors in frequency space, with a maximum level of about 1% [270]. Stage-III experiments expect similar low levels of crosstalk, but this remains to be demonstrated on the sky for the larger multiplexing factors used.

## Prospects and R&D path for CMB-S4 for DfMux

Expanding the channel capacity of the current DfMux readout systems, without any improvements to the cold or warm readout electronics and maintaining the present multiplexing factor of 68 per wire-pair, would

mean increasing the number of readout modules needed for a single telescope. The number of readout modules that would be required to read out 50,000 detectors is a factor of  $\sim 4$  larger than the number currently in use by Stage-III experiments (SPT-3G has 15,234 detectors at  $68\times$  multiplexing). The “ICE” readout boards that are used for DfMux are also used in radio astronomy correlators [269]. For example, in 2017, the CHIME telescope started using 128 readout boards (4.5 times more than SPT-3G), demonstrating that systems with this number of boards is tractable.

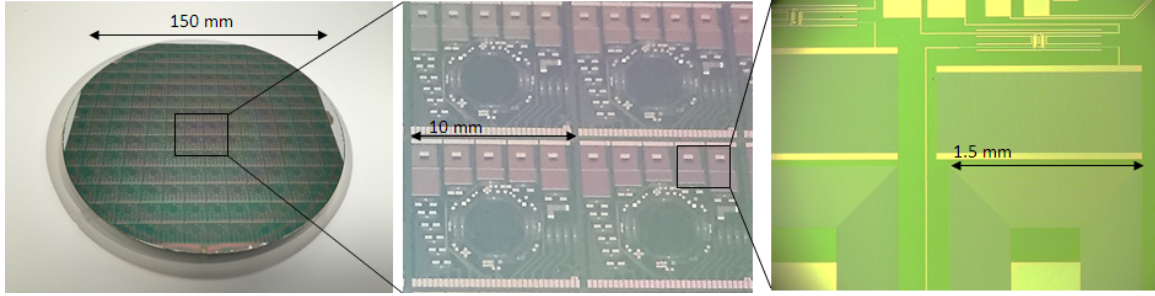


Figure 73: Demonstration of superconducting resonators integrated onto a multichroic detector wafer. Left: Photograph of the device wafer. Center: Close-up view of four multichroic pixels with integrated superconducting resonators at the top of each pixel. Right: Close-up view of a superconducting resonator, with interdigitated capacitor at the top and spiral inductor at the bottom.

To increase the multiplexing factor per readout module, and simplify the complexity of cold component integration, an alternate approach is under development, referred to here as 50 MHz fMUX. Integration of the frequency multiplexing circuit onto the detector wafer simplifies interconnects by reducing the number of required connections by the multiplexing factor. This requires shrinking the physical size of the resonators to a scale smaller than the detector pixel size, which increases the resonant frequencies to  $\sim 50 - 100$  MHz. With this approach, parasitic impedance can be accurately simulated and controlled with standard micro-fabrication techniques used in detector RF circuit design. As a test of this approach, superconducting resonators were integrated on detector wafers as shown in Figure 73. Currently 50 – 100 MHz resonators are being developed for 50 MHz DfMux, but the same method can be used to fabricate  $\sim 1$  GHz resonators for microwave SQUID readout (see Section 5.6).

R&D items for CMB-S4 include:

- **Demonstrate electrothermal design for 5 MHz DfMux for 50,000 detectors**

Scaling to cryogenic FDM circuits up is more challenging. The technology status level of the 5 MHz DfMux system is currently 4/5. Data has been fully analyzed for lower multiplexing factors used in POLARBEAR-1 and SPTpol, and  $68\times$  multiplexing deployed with SPT-3G at the end of 2016, which should advance the TSL to 5 in near future. The overall production status level for the current DfMux system is 4, and could be increased to 5 with R&D effort. Scaling cryogenic DfMux circuits up to the channel densities required by CMB-S4 presents a challenge. One potential issue is that it could require long lengths of wiring to the bolometers (compared to the current lengths of  $\sim 50-100$  cm). The thermal loads on the sub-Kelvin stages from  $\sim 1,500$  readout wires would require a significant portion of the cooling capacity of a three-stage helium sorption fridge. In a dilution refrigerator cooled cryostat, the SQUID and bias resistor could be moved from the 4 K stage to the 1 K buffer stage if it could accommodate the  $\sim 1$  mW of dissipated power, along with the thermal load from three pairs of wires per comb. This would greatly reduce the physical distance and necessary wiring lengths to the bolometers.

- **Increase multiplexing factor**

The issues associated with the cryogenic wiring complexity would be addressed by increasing the multiplexing factor up to 128–256 $\times$ . This can either be achieved by packing the channels closer together by means of narrower inductor-capacitor resonances, or by extending the readout bandwidth to accommodate additional frequency channels. Both strategies are being actively explored. Packing channels more closely together requires high uniformity in the channel spacing, and excellent control of stray impedances in the wiring and interconnects. Control over stray impedances in particular may be improved by keeping all components of the cold-multiplexer at sub-Kelvin temperature, ensuring short wire lengths. Significant increases in system bandwidth may also be achieved with 50 MHz fMUX, as described above. The technology and production status levels (TSL/PSL) for the 50 MHz fMUX system are currently only at 1, since so far only prototypes have been fabricated. There is significant unknown physics involved in operating TES devices at high AC modulation frequencies including increased SQUID backaction noise, high TES kinetic inductance, pair breaking near  $T_c$  at modulation frequencies, and the potential for other new sources of bias instability and noise. If these issues are investigated and overcome, readout R&D efforts can be implemented that would advance to higher TSL levels. Modest R&D efforts then would be expected to advance this technology to TSL/PSL 3, based on their similarity to existing technologies and production methods. If successful, further R&D efforts leading up to CMB-S4 could advance the 50 MHz fMUX system to TSL/PSL 5.

- **Further develop warm electronics** Increasing the backend electronics multiplexing factor is not an issue. Firmware for the “ICE” backend electronics already supports a multiplexing factor of 128x and uses about half the FPGA resources. Exploiting full FPGA resources and optimizing firmware should allow an increase to 256x without warm hardware changes (~32,000 detector channels for a single 9U crate). The ICE backend electronics used with TES detectors with 5 MHz DfMux could also be specialized for higher frequency (100 MHz or 1 GHz) readout of MKIDs or  $\mu$ MUX by using higher frequency digitizer daughter-boards that are available commercially, or by developing custom daughter boards. For telescopes that plan to support deployment of both TES and KID focal planes, a system that can support fMUX at high and low frequencies would allow the same core electronics to be used for the readout of both detector systems. The technology status level of the warm readout electronics is currently 5, and the production status level is 4.

## 5.6 Frequency-division multiplexing using SQUID-coupled GHz resonators ( $\mu$ MUX)

### Description of the technology

The microwave SQUID multiplexer ( $\mu$ MUX) [276, 277] is a readout scheme intended to greatly increase the focal plane pixel count of TES bolometer arrays, using inspiration from the GHz FDM approach of MKIDs [229, 278]. Fig. 74 illustrates the concept.

The TES bias circuit is identical to that of time-division SQUID multiplexing: each TES is voltage-biased with a DC current and parallel shunt resistor, with multiple TESs sharing a single pair of bias wires. The readout mechanism is very different from TDM, however: each TES is inductively coupled to its own resonator and addressed by its unique resonant frequency. Current sourced from a TES produces a frequency shift in a microwave resonator by means of a flux-coupled RF-SQUID. In this manner, many readout channels can be densely packed onto a single superconducting transmission line with a total readout bandwidth of

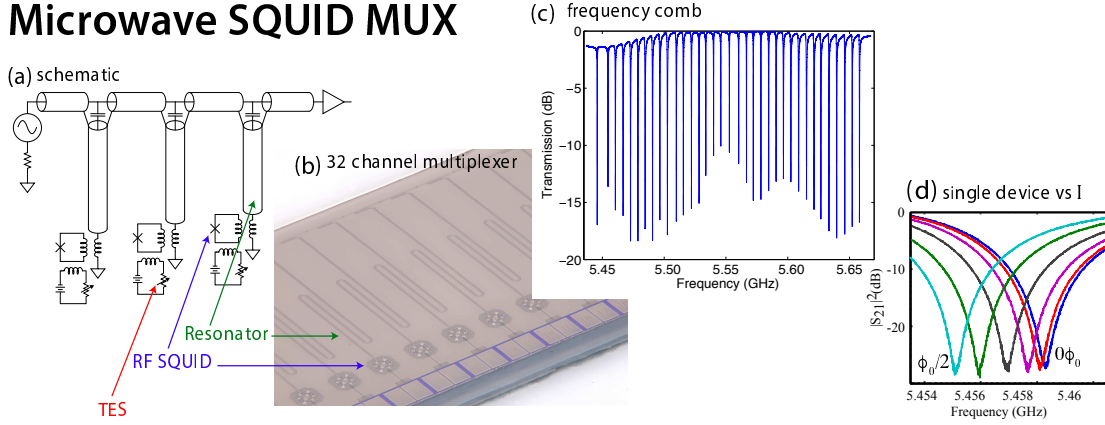


Figure 74: Overview of the the microwave SQUID multiplexer. (a) Schematic of the circuit. (b) Photograph of a 32-channel  $\mu$ MUX chip. (c)  $S_{21}$  transmission measurement of the  $\mu$ MUX with 32 active channels. (d) Variation of single readout channel transmission curves to applied input magnetic flux (or equivalently applied current when inductively coupled).

several GHz. Similar to MKID readout, signals are determined from the transmission properties of microwave resonators, monitored by use of homodyne readout techniques. The only difference in  $\mu$ MUX readout, with respect to MKID readout, is the addition of “flux-ramp demodulation” [279], which linearizes the response and substantially decreases 1/f readout noise. Cabling per module consists of a pair of DC wires and two coaxial cables.

## Demonstrated performance

Performance has been demonstrated through extensive lab-based measurements and with on-sky observations in the MUSTANG2 receiver. Readout noise levels relevant for CMB-S4 have already been demonstrated in the lab. The architecture was used to read out a  $3 \times 10^{-17}$  W/ $\sqrt{\text{Hz}}$  NEP TES bolometer, which was optimized for CMB polarization measurements [277]. In this demonstration, the readout noise was negligible compared to the system noise, to modulation frequencies as low as 1 Hz. Lower modulation frequencies were not investigated. By altering the input coil coupling, the current generation of  $\mu$ MUX chips have achieved an input-referred white current noise level of 17 pA/ $\sqrt{\text{Hz}}$  [280]. This noise level is nearly a factor of 10 below the expected photon noise level in the types of cryogenic receivers envisioned for CMB-S4. (Here we assume 3 pWs of optical load at 150 GHz, and an optimized TES bolometer with  $R_{\text{TES}} \sim 5 \text{ m}\Omega$ .)

On-sky observations have been made in two engineering runs of the MUSTANG2 receiver on the Green Bank Telescope (GBT). In 2015, MUSTANG2 used the architecture in a 32-channel per module configuration to make first-light images [281]. In 2016, on-sky, background-limited sensitivity has been demonstrated in pixels coupled to 64-channel multiplexers.

In addition to bolometric applications, the  $\mu$ MUX is under development for several TES microcalorimeter-based instruments. A DOE-funded, 512-pixel gamma-ray spectrometer demonstration, called SLEDGE-HAMMER, is underway [280], and the readout approach is baselined for a first-light instrument at the Linac Coherent Light Source II (LCLS-II). The current technical state-of-the-art for calorimetric applications is

a successful demonstration of undegraded energy resolution in a 4-pixel array that was read out using the scalable ROACH-II warm electronics.

The total readout bandwidth and resonator frequency spacing set the number of detectors multiplexed on a single coaxial cable. To date, the  $\mu$ MUX development has focused on the (4–8) GHz band since this matches the bandwidth of existing cryogenic HEMT amplifiers. Resonator spacing of 6 MHz has been demonstrated with few resonator collisions. Hence in the implemented approach and using the full HEMT bandwidth, 660 detectors can in principle be multiplexed on a single line.

Multiple generations of 33-channel multiplexers using a standard 3 mm  $\times$  19 mm form factor have been fabricated and tested. Different frequency band 33-channel chips have been wired in series to increase the number of readout channels per multiplexer module. This demonstrates both successful frequency scaling of the devices and the ability to daisy chain chips together, as a means to increase the multiplexing factor. The silicon footprint is currently identical to that of time-division SQUID multiplexing.

The total power dissipated on the cold stage is  $\sim$  10 pW/channel. When resonators are spaced in frequency at least ten times their bandwidth, nearest neighbor crosstalk is measured to be  $< 0.1\%$ . Linearity has been measured to 1 part in 1,000.

## Prospects and R&D path for CMB-S4 for microwave SQUIDs

The  $\mu$ MUX is less mature than time-division SQUID multiplexing (TDM) or MHz frequency-division SQUID multiplexing (FDM), which together have been used to read out  $\sim$ 30,000 deployed TES detectors that observe in the mm/sub-mm/FIR. However, the technology is rapidly gaining maturity through its use in several instruments. The demonstrated multiplexing factor is equal to that of contemporary TDM instruments (x64, AdvACT [9]) and FDM instruments (x68, SPT-3G [11]). The envisioned multiplexing factor is at least an order of magnitude higher than this.

R&D items for CMB-S4 include:

- **Increase multiplexing factor** With current technology, the cold multiplexing density achieves a multiplexing factor of 660. Recent developments in fabrication have reduced the frequency scatter by several factors, and thus the multiplexing density may be increased by this same factor. Near-term efforts to demonstrate  $\sim$  1 MHz frequency spacing would be beneficial, as the quantity of warm readout electronics boards and cryogenic HEMT amplifiers reduces by this same factor.
- **Demonstrate array performance on the sky** The majority of experimental data on the  $\mu$ MUX is at the few pixel demonstration level. On-sky results from MUSTANG2 are promising (which uses a  $\times$ 64 multiplexing factor), but a detailed study of performance, including low frequency noise properties, cross-talk and linearity is needed. MUSTANG2 offers a nice platform for this study, but other instruments or lab-based work will be essential since MUSTANG2 will not probe the target  $\sim$  1 MHz frequency spacing.
- **Shrink cryogenic circuit elements** Smaller circuit elements will reduce the cost of any cryogenic readout technology, since fewer wafer need to be processed for a fixed number of readout channels. The footprint of the circuitry is currently comparable or several factors smaller than the leading TES multiplexing approaches. By moving to a lumped element design, the readout footprint could shrink substantially.

- **Demonstrate integrated sensor and  $\mu$ MUX fabrication** The current  $\mu$ MUX implementation decreases the number of wires running between temperature stages. However, four to six wirebonds per channel are still required at the cold (isothermal) focal plane stage. Placing the readout onto the detector wafer solves this issue, drastically reduces the complexity of focal plane assembly, and eliminates the need for separate SQUID multiplexer chip fabrication. Beam forming elements, such as lenslets or feedhorns, which create space on the wafer for the readout components make integrated fabrication a possibility. In the near term, preliminary designs should be pursued, and steps to demonstrate an integrated fabrication process flow should be taken.
- **Further develop warm electronics** Warm readout for the  $\mu$ MUX has heavily benefitted from the developments in MKID readout. But future R&D is required and discussed in the following section.

Lastly, we note that the  $\mu$ MUX may be developed as a stand-alone multiplexing technique for CMB-S4, or it may find use in a hybrid multiplexing scheme. Hybrid multiplexing is a common way to use available bandwidth more efficiently, e.g. in 3G mobile phone technology. For readout of TES bolometers, a lower bandwidth multiplexing scheme, such as TDM or code-division multiplexing, is embedded within a wider bandwidth GHz resonator. Therefore each GHz tone carries the signals from  $N$  bolometers, where  $N$  may be 32 or 64. A proof-of-concept demonstration was shown in 2008 [282]. In the near term, a design study for hybrid multiplexing should be undertaken to inform CMB-S4, and if determined viable, an R&D path laid out.

## 5.7 Room-temperature electronics for frequency-division-multiplexed readout

### Description of the technology

In the various FDM readout schemes described above for TESs and MKIDs, the response to a tone played at a specified resonant frequency is measured for amplitude and/or phase shift after modulation by a cryogenic detector. A signal in DfMux is an amplitude modulation, in  $\mu$ MUX is a phase shift in the resonance, and in MKIDs is a shift in both phase and amplitude. In this section, we focus on the warm readout electronics for  $\mu$ MUX and MKIDs, which operate in GHz frequencies and enjoy extensive commonality in the architecture of their readout electronics. MHz FDM shares the same overall strategy, albeit at a lower frequency. We will also discuss the possibility of the same backend electronics supporting all three of these techniques.

Figure 75 shows the cryogenic readout schematic for MKID arrays and the  $\mu$ MUX multiplexer. These systems operate at the range of the resonance frequencies of the detectors, which is typically 100 – 8,000 MHz. They are designed to support a sufficiently large bandwidth (500 – 2000 MHz) to read out hundreds or thousands of detectors at once, depending on the resonator quality factors and frequency spacing. The readout noise is much less than the intrinsic detector noise (below  $\sim -90$  dBc/Hz) with frequency resolution to probe resonators with very high quality factors ( $Q \sim 100,000$ ) [283–292].

A common readout design implemented by various MKID experiments including AMKID [232], BLAST-TNG [167], MAKO [293], MUSIC [294], NIKA [295], and NIKA-2 [236] makes use of a homodyne readout technique. A digital tone generator, such as an FPGA, is connected to a DAC to produce the probe tones. The waveforms are generated on the FPGA by taking a length  $N$  inverse fast Fourier transform (IFFT) of a delta function comb. The length of the IFFT sets the frequency resolution of the tones. For example, an FPGA with 500 MHz of bandwidth divided into  $2^{18}$  bins gives a frequency resolution of about 1.9 kHz. The

initial waveform amplitude should be maximal within the range of the DAC and the waveform crest factor (the ratio of peak to r.m.s. amplitudes) should be minimized. This is achieved by randomly generating the probe tone phases (more advanced techniques are unnecessary because the MKID devices themselves will quasi-randomly shift the tone phases) [283]. A mixing circuit is used to bring the signals to the required frequency. For example, to read out devices with resonances between 1000 to 1500 MHz, one would use the FPGA to generate complex tones from -250 to 250 MHz and mix them with a 1250 MHz local oscillator (LO) and IQ modulator to the required frequency. The tones are then fed into the cryostat via coaxial cables and vacuum feedthroughs. The coax is then wired through to the required cold stages and attenuated before interacting with the detectors. The signal is then passed into a cold low noise amplifier and then back out of the cryostat. The signal is again amplified and mixed down before going into an ADC and back into the digital readout. Signals are then demodulated into amplitude and phase shifts, which can be calibrated to intensity variations on the detectors.

The warm electronics currently used for  $\mu$ MUX borrows largely from MKID readout developments. One additional requirement for the  $\mu$ MUX system is a flux modulation applied to the RF SQUID to linearize its response. The demodulation of this signal is typically done in the same FPGA that is used for digital tone generation and readout.

## Demonstrated performance

A combination of the digital readout bandwidth and resonator quality factors determine the maximum number of detectors that can be read out on a single coaxial line. State of the art microwave readout systems can support thousands of resonators [167, 247, 283, 287, 288, 291, 292, 296]. In lab systems have demonstrated multiplexing factors up to 1000 while maintaining the required noise performance [283, 297]. NIKA2 has demonstrated the highest on-sky multiplexing factor of 400 [236, 290].

The readout heat loading in the cryostat is due to the RF signal and LNA power usage. The RF power dissipated at the cold stage depends on the design of the resonators and the input power. For the  $\mu$ MUX system, this turns out to be 10 pW per channel. The LNA dissipates 5–10 milliwatts of power, but it is thermalized at a warmer stage ( $\sim$ 4 K) which has substantially more cooling power. The total power consumption of the system is dominated by the warm electronics and totals around 50–100 W [283, 290, 297].

The readout noise should be sub-dominant to the detector noise at all frequencies, and this has been demonstrated in a variety of MKID instruments at sub-millimeter and millimeter frequencies [163, 236, 283, 290, 297].

## Prospects and R&D path for CMB-S4 for microwave readout

Current tone generation and multiplexing schemes are capable of reading out thousands of detectors on a single pair of coaxial cables. In order to meet the stability, noise, and power requirements for CMB-S4 detectors, the readout systems would benefit from development several following areas. For some of these technology needs (e.g. faster ADCs and more powerful FPGAs) we can expect to benefit from existing massive development efforts for the communications and computation industries. New developments in microwave readout are exploring direct digital synthesis and demodulation to eliminate the tuning parameters necessary for the IQ scheme, oversampled polyphase filter banks as an alternative to long IFFTs, and resonator tone tracking and feedback for improved system linearity.

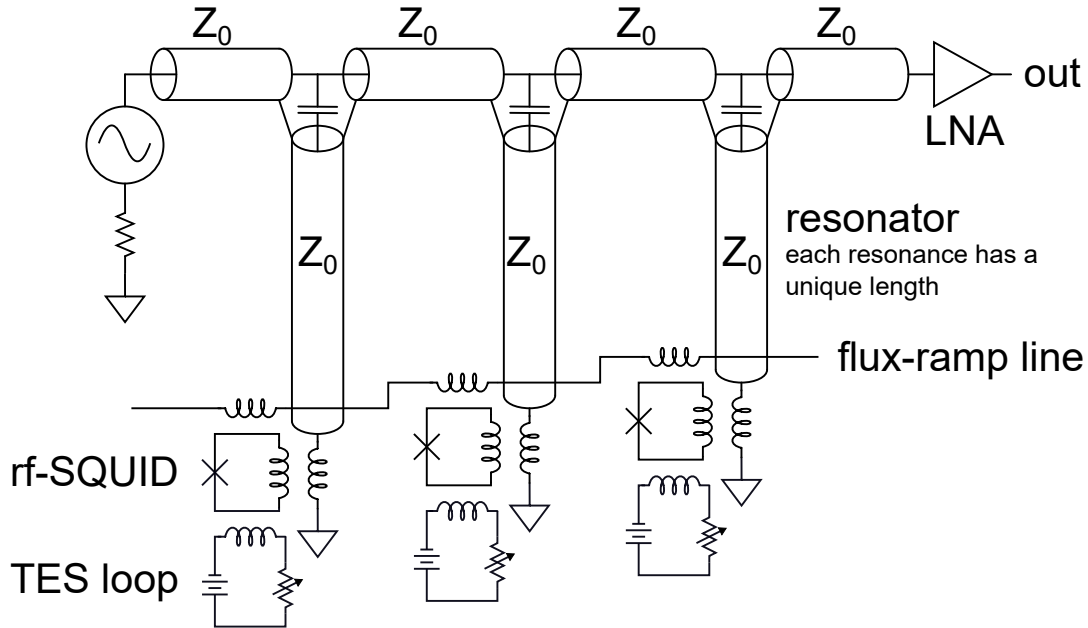
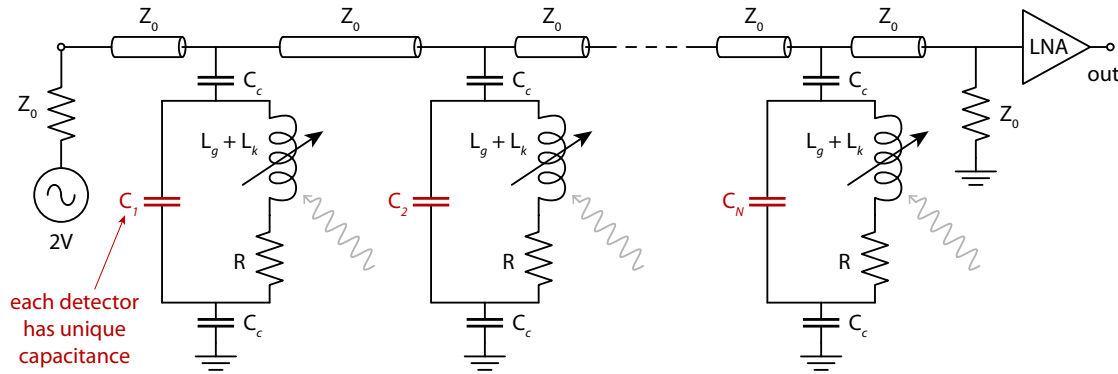


Figure 75: Circuit schematics showing how MKIDs and  $\mu$ MUX TESs are multiplexed. (Top) Each MKID has a unique resonance frequency, which is set by the capacitor coupled to the resonator, for example. A comb of probe tones is routed to the MKID array using a single transmission line, and single cryogenic LNA is used to read out all of the detectors. (Bottom) Each  $\mu$ MUX readout channel has a unique resonance frequency set by the length of the quarter-wavelength resonator. Like MKID readout,  $\mu$ MUX also uses a comb of probe tones and a single LNA to read out many detectors.

- **Implement systems with faster ADC/DACs** Increasing the bandwidth of the digital electronics directly increases the multiplexing factor of the system.
- **Validate and/or improve low-frequency noise performance** Minimizing the low frequency noise of the readout system is critical for CMB-S4. Instability, drift, and jitter in reference clocks

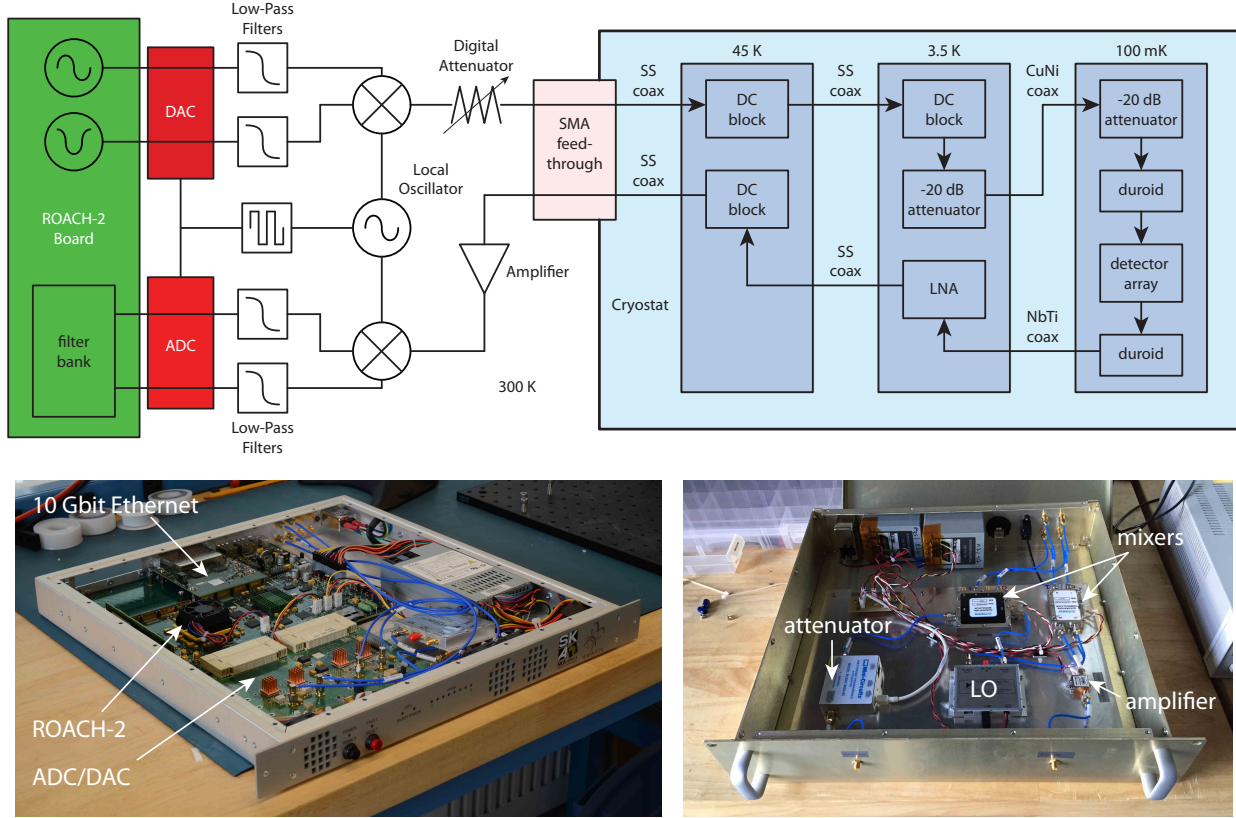


Figure 76: **(Top)** Readout schematic for the ROACH system showing the probe tone path in an MKID readout system. The top left shows the signal generation, digital-to-analog conversion, and IQ mixing. The blue portion shows the cryogenic part of the system. The bottom left shows the demodulation and filtering scheme. **Bottom Left:** The ROACH-2 with the DAC/ADC. **Bottom Right:** The analog signal conditioning hardware. This chassis houses the filters, room-temperature mixers, attenuator, warm amplifier, and the local oscillator shown in the schematic above. Existing hardware has a multiplexing factor of approximately 500 and each readout consumes only 20 W. Figure from [298]

and reference voltages are common sources for such noise. To mitigate the low-frequency noise, readout systems commonly place tones off resonance to characterize correlated electronic noise, which is subsequently subtracted from the detector data [283, 297]. Work should be done to assess if this is sufficient and improve the LNA, ADC, and DAC stability.

- **Increase linearity** The total drive power on a line must be sufficiently low to avoid cross talk between channels caused by intermodulation distortion in the LNA, ADCs and DACs. The drive power for MKIDs is -90 dBm per resonator, allowing for nearly 10,000 detectors on a single line before affecting LNA linearity for instance. However, the  $\mu$ MUX system is driven at a higher power and runs into this limit at  $\sim$ 1,000 detectors. Development of drive systems that track and feedback on a resonator's fundamental frequency (tone following) will greatly relax such limits and are being actively pursued.
- **Investigate universal backend electronics** The readout electronics for DfMux,  $\mu$ MUX and MKIDs rely on similar core electronics but operate at different frequencies. Universal backend electronics with swappable RF daughter boards should be investigated. This will be especially useful if CMB-S4 will

support deployment of both TES and MKID focal planes. A system that can support FDM at high and low frequencies would allow the same core electronics to be used for the readout of both detector systems.

## 5.8 Conclusion

We are in the fortunate situation of having low-noise sensors and associated readout with sufficient performance for CMB-S4’s likely technical specifications already in hand. We also have sufficient time to pursue R&D in areas that have high probability of lowering the overall CMB-S4 detector budget, including the costs of R&D as well as of production, assembly and quality assurance. The existing solution comprises TES bolometers with either of the existing readout methods outlined in Sections 5.4 (TDM) or 5.5 (DfMux with interrogation frequencies  $\lesssim 10$  MHz).

TES bolometers possess a long record of CMB science results from well-characterized kilopixel arrays. In particular their noise properties have been demonstrated to be sufficient for CMB-S4 needs. TES bolometers are ready for R&D investment in scaling up their production rate and expanding quality assurance testing facilities in universities and national labs. All the TES readout techniques would benefit from R&D investment in scaling up the production rate for SQUIDs. Several promising avenues exist for R&D to reduce the assembly complexity and thus the cost and schedule for the readout for TESs, including continued development of  $\mu$ MUX readout at GHz interrogation frequencies (Section 5.6) and exploration of FDM RLC with frequencies  $\gtrsim 50$  MHz (Section 5.5).

Another approach would be to use MKIDs, which were designed for highly multiplexed readout at GHz interrogation frequencies with minimal assembly complexity since the readout is integrated on the detector wafer. Readout of arrays with large multiplexing factors ( $O(1000)$ ) through a single coaxial cable has been demonstrated. Lab tests with MKIDs show nearly comparable noise performance to that from TES bolometers, though adequate low frequency noise performance has been demonstrated only in a lumped element MKID design. However, MKIDs have not yet been deployed in any CMB instrument. An on-sky CMB mapping demonstration is essential to validate MKIDs in the field before considering continuing their development for CMB-S4 production.

The GHz-interrogation readout techniques would all benefit from R&D investment into scaling up production of low-noise, low-dissipation-power 4K IF amplifiers. In all cases, the warm readout electronics appear scalable with R&D. FDM schemes for both TESs and MKIDs use similar room-temperature biasing and readout electronics, enabling common development. In particular, schemes to ensure linearity of these systems at high multiplexing count should be validated.

## 5.9 Summary of sensor and readout technologies

	Lab Demonstration	Sky Demonstration	Path to CMB-S4	Section	T/PSL
<b>Sensors</b>					
Transition edge sensors	-	ACTPol/SPTpol/BICEPS/PB	mass prod material optimization	5.2	5/4
MKID	150 GHz LEKID	1.2THz BLAST-TNG (2017) NIKA2	On sky pol demo, fab uniformity, mass prod	5.3	2/3
<b>Cold Multiplexers</b>					
Time-division	64x mux	ACTPol/BICEPS	interconnects, mux factor	5.4	5/4
Frequency-division: 5MHz DfMux 50 MHz fMux	68x mux	SPT/PB	higher freq resonances, integrated fab	5.5	5/4
Microwave-multiplexed SQUIDs ( $\mu$ MUX)	66x mux	MUSTANG2	Resonator freq density, resonator size, integrated det fab	5.6	1/1
MKID	1000x	400x NIKA2	resonance spacing	5.3	3/3
<b>Room temperature readout</b>					
TDM	64x mux	ACTPol/BICEPS	mux factor	5.4	5/4
DfMUX	256x mux	SPTpol/PB	mux factor	5.5	5/4
Microwave	1000x mux SRON	-	increased linearity, universal back-end	5.7	3/3

# 6

---

## Conclusion and Future Work

The design of the experimental configuration of CMB-S4 will be dictated by technical requirements determined by the science objectives. The top-level requirements will be on 1) the instrumental sensitivity  $\mathcal{S}$  as a function of angular scale (or multipole  $\ell$ ) and frequency  $\nu$ ,  $\mathcal{S}(\ell, \nu)$ ; 2) the suppression of systematic errors that could overwhelm  $\mathcal{S}(\ell, \nu)$ ; and 3) the area of sky and amount of overlap with existing and planned surveys in other wavelength bands. The recent explosion of progress in measuring the CMB, in interpreting data from the CMB, and in designing and deploying new technologies for even better measurement of the CMB has made the ambitious scope of the CMB-S4 science objectives possible. This Technology Book represents an essential first step in planning for the design of CMB-S4: assessing the status and potential of the myriad technical options.

We have presented the progress to date in developing technologies relevant for achieving the science goals of CMB-S4. The book focused on the technical challenges in four broad areas, demonstrated that multiple pathways exist in each area, quantified the readiness of each of the pathways in terms of TSL and PSL, presented pros and cons of competing methods, and indicated the breadth of R&D required to advance each alternative sufficiently for use in the CMB-S4 construction project. A partial list of the elements not yet addressed includes: cryogenics for cooling massive focal planes, instrumental control and monitoring, tools and techniques for in situ calibration and validation during integration and test, data storage and management, and power management for remote sites. These elements do not drive the overall instrument concept.

Armed with the facts tallied here, the CMB-S4 community will now proceed to the next steps required to plan the experimental configuration. These include:

1. Development of good estimates of cost, schedule, performance and risk or the technological alternatives, with the aim of prioritizing R&D needs;
2. Definition of performance and risk metrics for evaluating systematic errors;
3. End-to-end propagation of the performance properties of each subsystem to estimates of  $\mathcal{S}(\ell, \nu)$ ; and
4. Assessment of and planning for the instrumental elements not included in this version of the Technology Book.

This book is the most comprehensive compendium of instrumentation for the CMB ever compiled. It benefited dramatically from the cooperation among instrumentalists from more than a half dozen CMB experiments.

## List of acronyms

<b>ADC</b>	Analog to Digital Converter
<b>ADM</b>	Artificial Dielectric Material
<b>ADR</b>	Adiabatic Demagnetization Refrigerator
<b>AHWP</b>	Achromatic Half Wave Plate
<b>AR</b>	Anti Reflection
<b>ARC</b>	Anti Reflection Coating
<b>AZ</b>	Azimuth
<b>BUG</b>	Backshort-Under-Grid
<b>CAD</b>	Computer Assisted Design
<b>CD</b>	Critical Decision
<b>CDM</b>	code-division multiplexing
<b>CFRP</b>	Carbon Fiber Reinforced Polymer
<b>CMB</b>	Cosmic Microwave Background
<b>CHES</b>	Controlled Heat Extraction System
<b>CLASS</b>	Clear Large Aperture Sapphire Sheets
<b>CMM</b>	Coordinate Measuring Machine
<b>CNC</b>	Computer Numerical Control
<b>CPW</b>	Co-Planar Wave guide
<b>CTE</b>	Coefficient of Thermal Expansion
<b>DAC</b>	Digital to Analog Converter
<b>DAN</b>	Digital Active Nulling
<b>DRIE</b>	Deep Reactive Ion Etching
<b>EFG</b>	Edge-defined Film-fed Growth
<b>EL</b>	Elevation
<b>FDM</b>	Frequency Division Multiplexing
<b>FIR</b>	Far Infrared Radiation
<b>FOV</b>	Field Of View
<b>FP</b>	Fabry-Perot
<b>FTS</b>	Fourier Transform Spectrometer
<b>FWHM</b>	Full Width at Half-Maximum
<b>FPGA</b>	field-programmable gate array
<b>GRIN</b>	GRradient-INdex
<b>GBT</b>	Green Bank Telescope
<b>HDPE</b>	High Density PolyEthylene
<b>HEM</b>	Heat Exchanger Method
<b>HEMT</b>	High-electron-mobility transistor
<b>HF</b>	High-Frequency
<b>HWP</b>	Half Wave Plate

<b>IDC</b>	InterDigitated Capacitor
<b>IGW</b>	Inflationary Gravitational Wave
<b>IR</b>	InfraRed
<b>JFET</b>	Junction gate Field-Effect Transistor
<b>LAIS</b>	Laser Ablated Infrared Shaders
<b>LCLS-II</b>	Linac Coherent Light Source II
<b>LDPE</b>	Low-Density PolyEthylene
<b>LED</b>	Light-Emitting Diode
<b>LEKID</b>	Lumped-Element Kinetic Inductance Detector
<b>LF</b>	Low Frequency
<b>LNA</b>	Low Noise Amplifier
<b>MCE</b>	Multi-Channel Electronics
<b>MEM</b>	Micro-ElectroMechanical
<b>MF</b>	Medium Frequency
<b>MKID</b>	Microwave Kinetic Inductance Detector
<b>MMF</b>	Metal Mesh Filter
<b>MMARC</b>	Meta-Material Anti-Reflection Coating
<b>MML</b>	Meta-Material Lens
<b>NET</b>	Noise Equivalent Temperature
<b>NEP</b>	Noise Equivalent Power
<b>NIR</b>	Near InfraRed
<b>NTD</b>	Neutron Transmutation Doped
<b>OMT</b>	OrthoMode Transducer
<b>PPTFE</b>	Porous PolyTetraFluoroEthylene
<b>PSL</b>	Production Status Level
<b>PTC</b>	Pulse-Tube Cooler
<b>PTFE</b>	PolyTetraFluoroEthylene
<b>QWP</b>	Quarter Wave Plate
<b>R&amp;D</b>	Research and Development
<b>RF</b>	Radio Frequency
<b>RT-MLI</b>	Radio-Transparent Multi-Layer Insulation
<b>SMB</b>	Superconducting Magnetic Bearings
<b>SQUID</b>	Superconducting Quantum Interference Device
<b>SOI</b>	Silicon-on-Insulator
<b>SQ1</b>	first-stage SQUID
<b>SSA</b>	series SQUID array
<b>SWS</b>	SubWavelength Structures
<b>T<sub>c</sub></b>	critical Temperature
<b>TES</b>	Transition Edge Sensor

<b>TL</b>	Transmission Line
<b>TLS</b>	Two-Level System
<b>TDM</b>	Time Division Multiplexing
<b>TOD</b>	Time Ordered Data
<b>TSL</b>	Technology Status Level
<b>UHMWPE</b>	Ultra-High Molecular Weight PolyEthylene
<b>VNA</b>	Vector Network Analyzer
<b>VPM</b>	Variable Polarization Modulator

## References

- [1] K. N. Abazajian, P. Adshead, Z. Ahmed, S. W. Allen, D. Alonso, K. S. Arnold, C. Baccigalupi, J. G. Bartlett, N. Battaglia, B. A. Benson, C. A. Bischoff, J. Borrill, V. Buza, E. Calabrese, R. Caldwell, J. E. Carlstrom, C. L. Chang, T. M. Crawford, F.-Y. Cyr-Racine, F. De Bernardis, T. de Haan, S. di Serego Alighieri, J. Dunkley, C. Dvorkin, J. Errard, G. Fabbian, S. Feeney, S. Ferraro, J. P. Filippini, R. Flauger, G. M. Fuller, V. Gluscevic, D. Green, D. Grin, E. Grohs, J. W. Henning, J. C. Hill, R. Hlozek, G. Holder, W. Holzapfel, W. Hu, K. M. Huffenberger, R. Keskitalo, L. Knox, A. Kosowsky, J. Kovac, E. D. Kovetz, C.-L. Kuo, A. Kusaka, M. Le Jeune, A. T. Lee, M. Lilley, M. Loverde, M. S. Madhavacheril, A. Mantz, D. J. E. Marsh, J. McMahon, P. D. Meerburg, J. Meyers, A. D. Miller, J. B. Munoz, H. N. Nguyen, M. D. Niemack, M. Peloso, J. Peloton, L. Pogosian, C. Pryke, M. Raveri, C. L. Reichardt, G. Rocha, A. Rotti, E. Schaan, M. M. Schmittfull, D. Scott, N. Sehgal, S. Shandera, B. D. Sherwin, T. L. Smith, L. Sorbo, G. D. Starkman, K. T. Story, A. van Engelen, J. D. Vieira, S. Watson, N. Whitehorn, and W. L. Kimmy Wu, “CMB-S4 Science Book, First Edition,” *ArXiv e-prints* (Oct., 2016) , [arXiv:astro-ph/1610.02743](https://arxiv.org/abs/1610.02743).
- [2] S. Hanany, M. D. Niemack, and L. Page, “CMB Telescopes and Optical Systems,” in *Planets, Stars and Stellar Systems. Volume 1: Telescopes and Instrumentation*, T. D. Oswalt and I. S. McLean, eds., p. 431. 2013.
- [3] M. D. Niemack, “Designs for a large-aperture telescope to map the CMB 10x faster,” *Ap. Opt.* **55** (Mar., 2016) 1688.
- [4] H. Tran, A. Lee, S. Hanany, M. Milligan, and T. Renbarger, “Comparison of the crossed and the Gregorian Mizuguchi-Dragone for wide-field millimeter-wave astronomy,” *Ap. Opt.* **47** (Jan., 2008) 103–109.
- [5] T. Essinger-Hileman, J. W. Appel, J. A. Beal, H. M. Cho, J. Fowler, M. Halpern, M. Hasselfield, K. D. Irwin, T. A. Marriage, M. D. Niemack, L. Page, L. P. Parker, S. Pufu, S. T. Staggs, O. Stryzak, C. Visnjic, K. W. Yoon, and Y. Zhao, “The Atacama B-Mode Search: CMB Polarimetry with Transition-Edge-Sensor Bolometers,” in *American Institute of Physics Conference Series*, B. Young, B. Cabrera, and A. Miller, eds., vol. 1185 of *American Institute of Physics Conference Series*, pp. 494–497. Dec., 2009.
- [6] W. A. Imbriale, J. Gundersen, and K. L. Thompson, “The 1.4-m Telescope for the Q/U Imaging Experiment,” *IEEE Transactions on Antennas and Propagation* **59** (June, 2011) 1972–1980.
- [7] A. C. Taylor, A. Challinor, D. Goldie, K. Grainge, M. E. Jones, A. N. Lasenby, S. Withington, G. Yassin, W. K. Gear, L. Piccirillo, P. Ade, P. D. Mauskopf, B. Maffei, and G. Pisano, “CLOVER - A new instrument for measuring the B-mode polarization of the CMB,” *ArXiv e-prints* (July, 2004) , [arXiv:astro-ph/0407148](https://arxiv.org/abs/astro-ph/0407148).
- [8] H. Tran, B. Johnson, M. Dragovan, J. Bock, A. Aljabri, A. Amblard, D. Bauman, M. Betoule, T. Chui, L. Colombo, A. Cooray, D. Crumb, P. Day, C. Dickenson, D. Dowell, S. Golwala, K. Gorski, S. Hanany, W. Holmes, K. Irwin, B. Keating, C.-L. Kuo, A. Lee, A. Lange, C. Lawrence, S. Meyer, N. Miller, H. Nguyen, E. Pierpaoli, N. Ponthieu, J.-L. Puget, J. Raab, P. Richards, C. Satter, M. Seiffert, M. Shimon, B. Williams, and J. Zmuidzinas, “Optical design of the EPIC-IM crossed Dragone telescope,” *Society of Photo-Optical Instrumentation Engineers (SPIE) Conference Series* **7731** (July, 2010) 1.
- [9] S. W. Henderson, R. Allison, J. Austermann, T. Baildon, N. Battaglia, J. A. Beall, D. Becker, F. De Bernardis, J. R. Bond, E. Calabrese, S. K. Choi, K. P. Coughlin, K. T. Crowley, R. Datta, M. J.

Devlin, S. M. Duff, J. Dunkley, R. Dünner, A. van Engelen, P. A. Gallardo, E. Grace, M. Hasselfield, F. Hills, G. C. Hilton, A. D. Hincks, R. Hložek, S. P. Ho, J. Hubmayr, K. Huffenberger, J. P. Hughes, K. D. Irwin, B. J. Koopman, A. B. Kosowsky, D. Li, J. McMahon, C. Munson, F. Nati, L. Newburgh, M. D. Niemack, P. Niraula, L. A. Page, C. G. Pappas, M. Salatino, A. Schillaci, B. L. Schmitt, N. Sehgal, B. D. Sherwin, J. L. Sievers, S. M. Simon, D. N. Spergel, S. T. Staggs, J. R. Stevens, R. Thornton, J. Van Lanen, E. M. Vavagiakis, J. T. Ward, and E. J. Wollack, “Advanced ACTPol Cryogenic Detector Arrays and Readout,” *Journal of Low Temperature Physics* **184** (Aug., 2016) 772–779, [arXiv:astro-ph/1510.02809](https://arxiv.org/abs/1510.02809) [astro-ph.IM].

[10] N. Stebor, P. Ade, Y. Akiba, C. Aleman, K. Arnold, C. Baccigalupi, B. Barch, D. Barron, S. Beckman, A. Bender, D. Boettger, J. Borrill, S. Chapman, Y. Chinone, A. Cukierman, T. de Haan, M. Dobbs, A. Ducout, R. Dnner Planella, T. Elleflot, J. Errard, G. Fabbian, S. Feeney, C. Feng, T. Fujino, G. Fuller, A. J. Gilbert, N. Goeckner-Wald, J. Groh, G. Hall, N. Halverson, T. Hamada, M. Hasegawa, K. Hattori, M. Hazumi, C. Hill, W. L. Holzapfel, Y. Hori, L. Howe, Y. Inoue, F. Irie, G. Jaehnig, A. Jaffe, O. Jeong, N. Katayama, J. P. Kaufman, K. Kazemzadeh, B. G. Keating, Z. Kermish, R. Keskitalo, T. Kisner, A. Kusaka, M. Le Jeune, A. T. Lee, D. Leon, E. V. Linder, L. Lowry, F. Matsuda, T. Matsumura, N. Miller, J. Montgomery, M. Navaroli, H. Nishino, H. Paar, J. Peloton, D. Poletti, G. Puglisi, C. R. Raum, G. M. Rebeiz, C. L. Reichardt, P. L. Richards, C. Ross, K. M. Rotermund, Y. Segawa, B. D. Sherwin, I. Shirley, P. Siritanasak, L. Steinmetz, R. Stompor, A. Suzuki, O. Tajima, S. Takada, S. Takatori, G. P. Teply, A. Tikhomirov, T. Tomaru, B. Westbrook, N. Whitehorn, A. Zahn, and O. Zahn, “The Simons Array CMB polarization experiment,” *Proc. SPIE* **9914** (2016) 99141H–99141H–9. <http://dx.doi.org/10.1117/12.2233103>.

[11] B. A. Benson, P. A. R. Ade, Z. Ahmed, S. W. Allen, K. Arnold, J. E. Austermann, A. N. Bender, L. E. Bleem, J. E. Carlstrom, C. L. Chang, H. M. Cho, J. F. Cliche, T. M. Crawford, A. Cukierman, T. de Haan, M. A. Dobbs, D. Dutcher, W. Everett, A. Gilbert, N. W. Halverson, D. Hanson, N. L. Harrington, K. Hattori, J. W. Henning, G. C. Hilton, G. P. Holder, W. L. Holzapfel, K. D. Irwin, R. Keisler, L. Knox, D. Kubik, C. L. Kuo, A. T. Lee, E. M. Leitch, D. Li, M. McDonald, S. S. Meyer, J. Montgomery, M. Myers, T. Natoli, H. Nguyen, V. Novosad, S. Padin, Z. Pan, J. Pearson, C. Reichardt, J. E. Ruhl, B. R. Saliwanchik, G. Simard, G. Smecher, J. T. Sayre, E. Shirokoff, A. A. Stark, K. Story, A. Suzuki, K. L. Thompson, C. Tucker, K. Vanderlinde, J. D. Vieira, A. Vikhlinin, G. Wang, V. Yefremenko, and K. W. Yoon, “SPT-3G: a next-generation cosmic microwave background polarization experiment on the South Pole telescope,” in *Millimeter, Submillimeter, and Far-Infrared Detectors and Instrumentation for Astronomy VII*, vol. 9153 of *Proc. SPIE*, p. 91531P. July, 2014. [arXiv:astro-ph/1407.2973](https://arxiv.org/abs/1407.2973) [astro-ph.IM].

[12] J. Bock, A. Aljabri, A. Amblard, D. Baumann, M. Betoule, T. Chui, L. Colombo, A. Cooray, D. Crumb, P. Day, C. Dickinson, D. Dowell, M. Dragovan, S. Golwala, K. Gorski, S. Hanany, W. Holmes, K. Irwin, B. Johnson, B. Keating, C.-L. Kuo, A. Lee, A. Lange, C. Lawrence, S. Meyer, N. Miller, H. Nguyen, E. Pierpaoli, N. Ponthieu, J.-L. Puget, J. Raab, P. Richards, C. Satter, M. Seiffert, M. Shimon, H. Tran, B. Williams, and J. Zmuidzinas, “Study of the Experimental Probe of Inflationary Cosmology (EPIC)-Intermediate Mission for NASA’s Einstein Inflation Probe,” *ArXiv e-prints* (Jun, 2009) , [arXiv:astro-ph/0906.1188](https://arxiv.org/abs/0906.1188) [astro-ph.CO].

[13] W. Hu, M. M. Hedman, and M. Zaldarriaga, “Benchmark parameters for CMB polarization experiments,” *Phys. Rev. D* **67** no. 4, (Feb., 2003) 043004, [arXiv:astro-ph/0210096](https://arxiv.org/abs/astro-ph/0210096).

[14] P. A. Fluxa Rojas, R. Dünner, L. Maurin, S. K. Choi, M. J. Devlin, P. A. Gallardo, S.-P. P. Ho, B. J. Koopman, T. Louis, J. J. McMahon, F. Nati, M. D. Niemack, L. Newburgh, L. A. Page, M. Salatino, A. Schillaci, B. L. Schmitt, S. M. Simon, S. T. Staggs, and E. J. Wollack, “Far sidelobe effects from panel gaps of the Atacama Cosmology Telescope.”

[15] R. J. Thornton, P. A. R. Ade, S. Aiola, F. E. Angile, M. Amiri, J. A. Beall, D. T. Becker, H. Cho, S. K. Choi, P. Corlies, K. P. Coughlin, R. Datta, M. J. Devlin, S. R. Dicker, R. Dunner, J. W. Fowler, A. E. Fox, P. A. Gallardo, J. Gao, E. Grace, M. Halpern, M. Hasselfield, S. W. Henderson, G. C. Hilton, A. D. Hincks, S. P. Ho, J. Hubmayr, K. D. Irwin, J. Klein, B. Koopman, D. Li, T. Louis, M. Lungu, L. Maurin, J. McMahon, C. D. Munson, S. Naess, F. Nati, L. Newburgh, J. Nibarger, M. D. Niemack, P. Niraula, M. R. Nolta, L. A. Page, C. G. Pappas, A. Schillaci, B. L. Schmitt, N. Sehgal, J. L. Sievers, S. M. Simon, S. T. Staggs, C. Tucker, M. Uehara, J. van Lanen, J. T. Ward, and E. J. Wollack, “The Atacama Cosmology Telescope: The polarization-sensitive ACTPol instrument,” *ArXiv e-prints* (May, 2016) , [arXiv:astro-ph/1605.06569 \[astro-ph.IM\]](https://arxiv.org/abs/1605.06569).

[16] J. W. Fowler, M. D. Niemack, S. R. Dicker, A. M. Aboobaker, P. A. R. Ade, E. S. Battistelli, M. J. Devlin, R. P. Fisher, M. Halpern, P. C. Hargrave, A. D. Hincks, M. Kaul, J. Klein, J. M. Lau, M. Limon, T. A. Marriage, P. D. Mauskopf, L. Page, S. T. Staggs, D. S. Swetz, E. R. Switzer, R. J. Thornton, and C. E. Tucker, “Optical design of the Atacama Cosmology Telescope and the Millimeter Bolometric Array Camera,” *Ap. Opt.* **46** (June, 2007) 3444–3454, [arXiv:astro-ph/0701020](https://arxiv.org/abs/astro-ph/0701020).

[17] M. D. Niemack, P. A. R. Ade, J. Aguirre, F. Barrientos, J. A. Beall, J. R. Bond, J. Britton, H. M. Cho, S. Das, M. J. Devlin, S. Dicker, J. Dunkley, R. Dünner, J. W. Fowler, A. Hajian, M. Halpern, M. Hasselfield, G. C. Hilton, M. Hilton, J. Hubmayr, J. P. Hughes, L. Infante, K. D. Irwin, N. Jarosik, J. Klein, A. Kosowsky, T. A. Marriage, J. McMahon, F. Menanteau, K. Moodley, J. P. Nibarger, M. R. Nolta, L. A. Page, B. Partridge, E. D. Reese, J. Sievers, D. N. Spergel, S. T. Staggs, R. Thornton, C. Tucker, E. Wollack, and K. W. Yoon, “**ACTPol: a polarization-sensitive receiver for the Atacama Cosmology Telescope**,” in *Millimeter, Submillimeter, and Far-Infrared Detectors and Instrumentation for Astronomy V*, vol. 7741 of *Proc. SPIE*, p. 77411S. July, 2010. [arXiv:astro-ph/1006.5049 \[astro-ph.IM\]](https://arxiv.org/abs/1006.5049).

[18] R. Datta, C. D. Munson, M. D. Niemack, J. J. McMahon, J. Britton, E. J. Wollack, J. Beall, M. J. Devlin, J. Fowler, P. Gallardo, J. Hubmayr, K. Irwin, L. Newburgh, J. P. Nibarger, L. Page, M. A. Quijada, B. L. Schmitt, S. T. Staggs, R. Thornton, and L. Zhang, “Large-aperture wide-bandwidth antireflection-coated silicon lenses for millimeter wavelengths,” *Ap. Opt.* **52** (Dec., 2013) 8747, [arXiv:astro-ph/1307.4715 \[astro-ph.IM\]](https://arxiv.org/abs/1307.4715).

[19] Z. Ahmed, M. Amiri, S. J. Benton, J. J. Bock, R. Bowens-Rubin, I. Buder, E. Bullock, J. Connors, J. P. Filippini, J. A. Grayson, M. Halpern, G. C. Hilton, V. V. Hristov, H. Hui, K. D. Irwin, J. Kang, K. S. Karkare, E. Karpel, J. M. Kovac, C. L. Kuo, C. B. Netterfield, H. T. Nguyen, R. O’Brien, R. W. Ogburn, C. Pryke, C. D. Reintsema, S. Richter, K. L. Thompson, A. D. Turner, A. G. Vieregg, W. L. K. Wu, and K. W. Yoon, “**BICEP3: a 95GHz refracting telescope for degree-scale CMB polarization**,” in *Millimeter, Submillimeter, and Far-Infrared Detectors and Instrumentation for Astronomy VII*, vol. 9153 of *Proc. SPIE*, p. 91531N. Aug., 2014. [arXiv:astro-ph/1407.5928 \[astro-ph.IM\]](https://arxiv.org/abs/1407.5928).

[20] J. A. Grayson, P. A. R. Ade, Z. Ahmed, K. D. Alexander, M. Amiri, D. Barkats, S. J. Benton, C. A. Bischoff, J. J. Bock, H. Boenish, R. Bowens-Rubin, I. Buder, E. Bullock, V. Buza, J. Connors, J. P. Filippini, S. Fliescher, M. Halpern, S. Harrison, G. C. Hilton, V. V. Hristov, H. Hui, K. D. Irwin, J. Kang, K. S. Karkare, E. Karpel, S. Kefeli, S. A. Kernasovskiy, J. M. Kovac, C. L. Kuo, E. M. Leitch, M. Lueker, K. G. Megerian, V. Monticue, T. Namikawa, C. B. Netterfield, H. T. Nguyen, R. O’Brien, R. W. Ogburn, IV, C. Pryke, C. D. Reintsema, S. Richter, R. Schwarz, C. Sorensen, C. D. Sheehy, Z. K. Staniszewski, B. Steinbach, G. P. Teply, K. L. Thompson, J. E. Tolan, C. Tucker, A. D. Turner, A. G. Vieregg, A. Wandui, A. C. Weber, D. V. Wiebe, J. Willmert, W. L. K. Wu, and K. W. Yoon, “BICEP3 performance overview and planned Keck Array upgrade,” *ArXiv e-prints* (July, 2016) , [arXiv:astro-ph/1607.04668 \[astro-ph.IM\]](https://arxiv.org/abs/1607.04668).

[21] R. O'Brient, P. Ade, K. Arnold, J. Edwards, G. Engargiola, W. Holzapfel, A. T. Lee, X. F. Meng, M. Myers, E. Quealy, G. Rebeiz, P. Richards, and A. Suzuki, “[A dual-polarized multichroic antenna-coupled TES bolometer for terrestrial CMB Polarimetry](#),” in *Millimeter, Submillimeter, and Far-Infrared Detectors and Instrumentation for Astronomy V*, vol. 7741 of *Proc. SPIE*, p. 77410J. July, 2010.

[22] BICEP2 Collaboration, P. A. R. Ade, R. W. Aikin, M. Amiri, D. Barkats, S. J. Benton, C. A. Bischoff, J. J. Bock, J. A. Brevik, I. Buder, E. Bullock, G. Davis, P. K. Day, C. D. Dowell, L. Duband, J. P. Filippini, S. Fliescher, S. R. Golwala, M. Halpern, M. Hasselfield, S. R. Hildebrandt, G. C. Hilton, K. D. Irwin, K. S. Karkare, J. P. Kaufman, B. G. Keating, S. A. Kernasovskiy, J. M. Kovac, C. L. Kuo, E. M. Leitch, N. Llombart, M. Lueker, C. B. Netterfield, H. T. Nguyen, R. O'Brient, R. W. Ogburn, IV, A. Orlando, C. Pryke, C. D. Reintsema, S. Richter, R. Schwarz, C. D. Sheehy, Z. K. Staniszewski, K. T. Story, R. V. Sudiwala, G. P. Teply, J. E. Tolan, A. D. Turner, A. G. Vieregg, P. Wilson, C. L. Wong, and K. W. Yoon, “[BICEP2. II. Experiment and three-year Data Set](#),” *ApJ* **792** (Sept., 2014) 62, [arXiv:astro-ph/1403.4302](#).

[23] R. W. Ogburn, IV, P. A. R. Ade, R. W. Aikin, M. Amiri, S. J. Benton, J. J. Bock, J. A. Bonetti, J. A. Brevik, B. Burger, C. D. Dowell, L. Duband, J. P. Filippini, S. R. Golwala, M. Halpern, M. Hasselfield, G. Hilton, V. V. Hristov, K. Irwin, J. P. Kaufman, B. G. Keating, J. M. Kovac, C. L. Kuo, A. E. Lange, E. M. Leitch, C. B. Netterfield, H. T. Nguyen, A. Orlando, C. L. Pryke, C. Reintsema, S. Richter, J. E. Ruhl, M. C. Runyan, C. D. Sheehy, Z. K. Staniszewski, S. A. Stokes, R. V. Sudiwala, G. P. Teply, J. E. Tolan, A. D. Turner, P. Wilson, and C. L. Wong, “[The BICEP2 CMB polarization experiment](#),” in *Millimeter, Submillimeter, and Far-Infrared Detectors and Instrumentation for Astronomy V*, vol. 7741 of *Proc. SPIE*, p. 77411G. July, 2010.

[24] C. D. Sheehy, *Progress toward a detection of inflationary B-modes with the BICEP2 and Keck Array polarimeters*. PhD thesis, The University of Chicago, 2013.

[25] J. R. Eimer, C. L. Bennett, D. T. Chuss, T. Marriage, E. J. Wollack, and L. Zeng, “[The cosmology large angular scale surveyor \(CLASS\): 40 GHz optical design](#),” in *Millimeter, Submillimeter, and Far-Infrared Detectors and Instrumentation for Astronomy VI*, vol. 8452, p. 845220. Sept., 2012. [arXiv:astro-ph/1211.0041 \[astro-ph.IM\]](#).

[26] D. T. Chuss, E. J. Wollack, R. Henry, H. Hui, A. J. Juarez, M. Krejny, S. H. Moseley, and G. Novak, “Properties of a variable-delay polarization modulator,” *Ap. Opt.* **51** (Jan., 2012) 197, [arXiv:astro-ph/1106.5984 \[astro-ph.IM\]](#).

[27] J. Klein, A. Aboobaker, P. Ade, F. Aubin, C. Baccigalupi, C. Bao, J. Borrill, D. Chapman, J. Didier, M. Dobbs, B. Gold, W. Grainger, S. Hanany, J. Hubmayr, S. Hillbrand, J. Grain, A. Jaffe, B. Johnson, T. Jones, T. Kisner, A. Korotkov, S. Leach, A. Lee, L. Levinson, M. Limon, K. MacDermid, T. Matsumura, A. Miller, M. Milligan, E. Pascale, D. Polsgrove, N. Ponthieu, K. Raach, B. Reichborn-Kjennerud, I. Sagiv, R. Stompor, H. Tran, M. Tristram, G. S. Tucker, A. Yadav, M. Zaldarriaga, and K. Zilic, “A cryogenic half-wave plate polarimeter using a superconducting magnetic bearing,” *Proc. SPIE* **8150** (Oct., 2011) 4.

[28] M. Milligan, *The E and B EXperiment: Implementation and Analysis of the 2009 Engineering Flight*. PhD thesis, University of Minnesota, 2011.

[29] C. Dragone, “A first-order treatment of aberrations in Cassegrainian and Gregorian antennas,” *IEEE Transactions on Antennas and Propagation* **30** (May, 1982) 331–339.

[30] Y. Mizuguchi, M. Akagawa, and H. Yokoi, “Offset Gregorian antenna,” *Electronics Communications of Japan* **61** (Mar., 1978) 58–66.

[31] The EBEX Collaboration, A. M. Aboobaker, P. Ade, D. Araujo, F. Aubin, C. Baccigalupi, B. C., D. Chapman, J. Didier, M. Dobbs, C. Geach, W. Grainger, S. Hanany, K. Helson, S. Hillbrand, J. Hubmayr, A. Jaffe, B. Johnson, T. Jones, J. Klein, A. Korotkov, A. Lee, L. Levinson, M. Limon, K. MacDermid, T. Matsumura, A. D. Miller, M. Milligan, K. Raach, B. Reichborn-Kjennerud, I. Sagiv, G. Savini, L. Spencer, C. Tucker, G. S. Tucker, B. Westbrook, K. Young, and K. Zilic, “The EBEX Balloon Borne Experiment - Optics, Receiver, and Polarimetry,” *submitted to The Astrophysical Journal Supplement* (Mar, 2017) , [arXiv:astro-ph/1703.03847 \[astro-ph.IM\]](https://arxiv.org/abs/1703.03847).

[32] R. W. Aikin, P. A. Ade, S. Benton, J. J. Bock, J. A. Bonetti, J. A. Brevik, C. D. Dowell, L. Duband, J. P. Filippini, S. R. Golwala, M. Halpern, V. V. Hristov, K. Irwin, J. P. Kaufman, B. G. Keating, J. M. Kovac, C. L. Kuo, A. E. Lange, C. B. Netterfield, H. T. Nguyen, R. W. Ogburn, IV, A. Orlando, C. Pryke, S. Richter, J. E. Ruhl, M. C. Runyan, C. Sheehy, S. A. Stokes, R. Sudiwala, G. P. Teply, J. E. Tolan, A. D. Turner, P. Wilson, and C. L. Wong, “Optical performance of the BICEP2 Telescope at the South Pole,” in *Millimeter, Submillimeter, and Far-Infrared Detectors and Instrumentation for Astronomy V*, vol. 7741 of *Proc. SPIE*, p. 77410V. July, 2010.

[33] BICEP2 Collaboration, Keck Array Collaboration, SPIDER Collaboration, P. A. R. Ade, R. W. Aikin, M. Amiri, D. Barkats, S. J. Benton, C. A. Bischoff, J. J. Bock, J. A. Bonetti, J. A. Brevik, I. Buder, E. Bullock, G. Chattopadhyay, G. Davis, P. K. Day, C. D. Dowell, L. Duband, J. P. Filippini, S. Fliescher, S. R. Golwala, M. Halpern, M. Hasselfield, S. R. Hildebrandt, G. C. Hilton, V. Hristov, H. Hui, K. D. Irwin, W. C. Jones, K. S. Karkare, J. P. Kaufman, B. G. Keating, S. Kefeli, S. A. Kernasovskiy, J. M. Kovac, C. L. Kuo, H. G. LeDuc, E. M. Leitch, N. Llombart, M. Lueker, P. Mason, K. Megerian, L. Moncelsi, C. B. Netterfield, H. T. Nguyen, R. O'Brient, R. W. Ogburn, IV, A. Orlando, C. Pryke, A. S. Rahlin, C. D. Reintsema, S. Richter, M. C. Runyan, R. Schwarz, C. D. Sheehy, Z. K. Staniszewski, R. V. Sudiwala, G. P. Teply, J. E. Tolan, A. Trangsrud, R. S. Tucker, A. D. Turner, A. G. Vieregg, A. Weber, D. V. Wiebe, P. Wilson, C. L. Wong, K. W. Yoon, and J. Zmuidzinas, “Antenna-coupled TES Bolometers Used in BICEP2, Keck Array, and Spider,” *ApJ* **812** (Oct., 2015) 176, [arXiv:astro-ph/1502.00619 \[astro-ph.IM\]](https://arxiv.org/abs/1502.00619).

[34] K. S. Karkare, P. A. R. Ade, Z. Ahmed, K. D. Alexander, M. Amiri, D. Barkats, S. J. Benton, C. A. Bischoff, J. J. Bock, H. Boenish, R. Bowens-Rubin, I. Buder, E. Bullock, V. Buza, J. Connors, J. P. Filippini, S. T. Fliescher, J. A. Grayson, M. Halpern, S. A. Harrison, G. C. Hilton, V. V. Hristov, H. Hui, K. D. Irwin, J. H. Kang, E. Karpel, S. Kefeli, S. A. Kernasovskiy, J. M. Kovac, C. L. Kuo, E. M. Leitch, M. Lueker, K. G. Megerian, V. Monticue, T. Namikawa, C. B. Netterfield, H. T. Nguyen, R. O'Brient, R. W. Ogburn, IV, C. Pryke, C. D. Reintsema, S. Richter, M. T. St. Germaine, R. Schwarz, C. D. Sheehy, Z. K. Staniszewski, B. Steinbach, G. P. Teply, K. L. Thompson, J. E. Tolan, C. Tucker, A. D. Turner, A. G. Vieregg, A. Wandui, A. Weber, J. Willmert, C. L. Wong, W. L. K. Wu, and K. W. Yoon, “Optical Characterization of the BICEP3 CMB Polarimeter at the South Pole,” *ArXiv e-prints* (July, 2016) , [arXiv:astro-ph/1607.04567 \[astro-ph.IM\]](https://arxiv.org/abs/1607.04567).

[35] A. S. Rahlin, P. A. R. Ade, M. Amiri, S. J. Benton, J. J. Bock, J. R. Bond, S. A. Bryan, H. C. Chiang, C. R. Contaldi, B. P. Crill, O. Doré, M. Farhang, J. P. Filippini, L. M. Fissel, A. A. Fraisse, A. E. Gambrel, N. N. Gandilo, S. Golwala, J. E. Gudmundsson, M. Halpern, M. F. Hasselfield, G. Hilton, W. A. Holmes, V. V. Hristov, K. D. Irwin, W. C. Jones, Z. D. Kermish, C. L. Kuo, C. J. MacTavish, P. V. Mason, K. Megerian, L. Moncelsi, T. A. Morford, J. M. Nagy, C. B. Netterfield, R. O'Brient, C. Reintsema, J. E. Ruhl, M. C. Runyan, J. A. Shariff, J. D. Soler, A. Trangsrud, C. Tucker, R. S. Tucker, A. D. Turner, A. C. Weber, D. V. Wiebe, and E. Y. Young, “Pre-flight integration and characterization of the SPIDER balloon-borne telescope,” in *Millimeter, Submillimeter, and Far-Infrared Detectors and Instrumentation for Astronomy VII*, vol. 9153 of *Proc. SPIE*, p. 915313. July, 2014. [arXiv:astro-ph/1407.2906 \[astro-ph.IM\]](https://arxiv.org/abs/1407.2906).

[36] J. E. Gudmundsson, P. A. R. Ade, M. Amiri, S. J. Benton, J. J. Bock, J. R. Bond, S. A. Bryan, H. C. Chiang, C. R. Contaldi, B. P. Crill, O. Dore, J. P. Filippini, A. A. Fraisse, A. Gambrel, N. N. Gandilo, M. Hasselfield, M. Halpern, G. Hilton, W. Holmes, V. V. Hristov, K. D. Irwin, W. C. Jones, Z. Kermish, C. J. MacTavish, P. V. Mason, K. Megerian, L. Moncelsi, T. E. Montroy, T. A. Morford, J. M. Nagy, C. B. Netterfield, A. S. Rahlin, C. D. Reintsema, J. E. Ruhl, M. C. Runyan, J. A. Shariff, J. D. Soler, A. Trangsrud, C. Tucker, R. S. Tucker, A. D. Turner, D. V. Wiebe, and E. Young, “The thermal design, characterization, and performance of the SPIDER long-duration balloon cryostat,” *Cryogenics* **72** (Dec., 2015) 65–76, [arXiv:astro-ph/1506.06953](https://arxiv.org/abs/1506.06953) [astro-ph.IM].

[37] C. J. MacTavish, P. A. R. Ade, E. S. Battistelli, S. Benton, R. Bihary, J. J. Bock, J. R. Bond, J. Brevik, S. Bryan, C. R. Contaldi, B. P. Crill, O. Doré, L. Fissel, S. R. Golwala, M. Halpern, G. Hilton, W. Holmes, V. V. Hristov, K. Irwin, W. C. Jones, C. L. Kuo, A. E. Lange, C. Lawrie, T. G. Martin, P. Mason, T. E. Montroy, C. B. Netterfield, D. Riley, J. E. Ruhl, M. Runyan, A. Trangsrud, C. Tucker, A. Turner, M. Viero, and D. Wiebe, “Spider Optimization: Probing the Systematics of a Large-Scale B-Mode Experiment,” *ApJ* **689** (Dec., 2008) 655–665, [arXiv:astro-ph/0710.0375](https://arxiv.org/abs/0710.0375).

[38] J. Hubmayr, J. E. Austermann, J. A. Beall, D. T. Becker, S. J. Benton, A. Stevie Bergman, J. R. Bond, S. Bryan, S. M. Duff, A. J. Duivenvoorden, H. K. Eriksen, J. P. Filippini, A. A. Fraisse, M. Galloway, A. E. Gambrel, K. Ganga, A. L. Grigorian, R. Gualtieri, J. E. Gudmundsson, J. W. Hartley, M. Halpern, G. C. Hilton, W. C. Jones, J. J. McMahon, L. Moncelsi, J. M. Nagy, C. B. Netterfield, B. Osherson, I. Padilla, A. S. Rahlin, B. Racine, J. Ruhl, T. M. Ruud, J. A. Shariff, J. D. Soler, X. Song, J. N. Ullom, J. Van Lanen, M. R. Vissers, I. K. Wehus, S. Wen, D. V. Wiebe, and E. Young, “Design of 280 GHz feedhorn-coupled TES arrays for the balloon-borne polarimeter SPIDER,” *ArXiv e-prints* (June, 2016) , [arXiv:astro-ph/1606.09396](https://arxiv.org/abs/1606.09396) [astro-ph.IM].

[39] N. N. Gandilo, P. A. R. Ade, D. Benford, C. L. Bennett, D. T. Chuss, J. L. Dotson, J. R. Eimer, D. J. Fixsen, M. Halpern, G. Hilton, G. F. Hinshaw, K. Irwin, C. Jhabvala, M. Kimball, A. Kogut, L. Lowe, J. J. McMahon, T. M. Miller, P. Mirel, S. H. Moseley, S. Pawlyk, S. Rodriguez, E. Sharp, III, P. Shirron, J. G. Staguhn, D. F. Sullivan, E. R. Switzer, P. Taraschi, C. E. Tucker, and E. J. Wollack, “The Primordial Inflation Polarization Explorer (PIPER),” *ArXiv e-prints* (July, 2016) , [arXiv:astro-ph/1607.06172](https://arxiv.org/abs/1607.06172) [astro-ph.IM].

[40] J. R. Eimer, P. A. R. Ade, D. J. Benford, C. L. Bennett, D. T. Chuss, D. J. Fixsen, A. J. Kogut, P. Mirel, C. E. Tucker, G. M. Voellmer, and E. J. Wollack, “The Primordial Inflation Polarization Explorer (PIPER): optical design,” in *Ground-based and Airborne Telescopes III*, vol. 7733 of *Proc. SPIE*, p. 77333B. July, 2010.

[41] H. Tran, A. Lee, S. Hanany, M. Milligan, and T. Renbarger, “Comparison of the crossed and the Gregorian Mizuguchi-Dragone for wide-field millimeter-wave astronomy,” *Ap. Opt.* **47** no. 2, (Jan, 2008) 103–109. <http://ao.osa.org/abstract.cfm?URI=ao-47-2-103>.

[42] J. Choi, H. Ishitsuka, S. Mima, S. Oguri, K. Takahashi, and O. Tajima, “Radio-transparent multi-layer insulation for radiowave receivers,” *Review of Scientific Instruments* **84** no. 11, (2013) . <http://scitation.aip.org/content/aip/journal/rsi/84/11/10.1063/1.4827081>.

[43] Y. Inoue, T. Matsumura, M. Hazumi, A. T. Lee, T. Okamura, A. Suzuki, T. Tomaru, and H. Yamaguchi, “Cryogenic infrared filter made of alumina for use at millimeter wavelength,” *Ap. Opt.* **53** no. 9, (Mar, 2014) 1727–1733, [arXiv:astro-ph/1311.5388](https://arxiv.org/abs/1311.5388). <http://ao.osa.org/abstract.cfm?URI=ao-53-9-1727>.

[44] C. A. Hill, S. Beckman, Y. Chinone, N. Goeckner-Wald, M. Hazumi, B. Keating, A. Kusaka, A. T. Lee, F. Matsuda, R. Plambeck, A. Suzuki, and S. Takakura, “Design and development of

an ambient-temperature continuously-rotating achromatic half-wave plate for CMB polarization modulation on the POLARBEAR-2 experiment,” *Proc. SPIE* **9914** (2016) 99142U–99142U–18, [arXiv:astro-ph/1607.07399](https://arxiv.org/abs/1607.07399). <http://dx.doi.org/10.1117/12.2232280>.

[45] J. E. Carlstrom, P. A. R. Ade, K. A. Aird, B. A. Benson, L. E. Bleem, S. Busetti, C. L. Chang, E. Chauvin, H.-M. Cho, T. M. Crawford, A. T. Crites, M. A. Dobbs, N. W. Halverson, S. Heimsath, W. L. Holzapfel, J. D. Hrubes, M. Joy, R. Keisler, T. M. Lanting, A. T. Lee, E. M. Leitch, J. Leong, W. Lu, M. Lueker, D. Luong-Van, J. J. McMahon, J. Mehl, S. S. Meyer, J. J. Mohr, T. E. Montroy, S. Padin, T. Plagge, C. Pryke, J. E. Ruhl, K. K. Schaffer, D. Schwan, E. Shirokoff, H. G. Spieler, Z. Staniszewski, A. A. Stark, C. Tucker, K. Vanderlinde, J. D. Vieira, and R. Williamson, “The 10 Meter South Pole Telescope,” *PASP* **123** (May, 2011) 568–581, [arXiv:astro-ph/0907.4445](https://arxiv.org/abs/0907.4445) [astro-ph.IM].

[46] O. Jeong, A. Lee, C. Raum, and A. Suzuki, “Broadband Plasma-Sprayed Anti-reflection Coating for Millimeter-Wave Astrophysics Experiments,” *Journal of Low Temperature Physics* **1573-7357** (2016) 1 – 6.

[47] T. Essinger-Hileman, A. Kusaka, J. W. Appel, S. K. Choi, K. Crowley, S. P. Ho, N. Jarosik, L. A. Page, L. P. Parker, S. Raghunathan, S. M. Simon, S. T. Staggs, and K. Visnjic, “Systematic effects from an ambient-temperature, continuously-rotating half-wave plate,” *ArXiv e-prints* (Jan., 2016) , [arXiv:astro-ph/1601.05901](https://arxiv.org/abs/1601.05901) [astro-ph.IM].

[48] C. Bischoff, A. Brizius, I. Buder, Y. Chinone, K. Cleary, R. N. Dumoulin, A. Kusaka, R. Monsalve, S. K. Næss, L. B. Newburgh, G. Nixon, R. Reeves, K. M. Smith, K. Vanderlinde, I. K. Wehus, M. Bogdan, R. Bustos, S. E. Church, R. Davis, C. Dickinson, H. K. Eriksen, T. Gaier, J. O. Gundersen, M. Hasegawa, M. Hazumi, C. Holler, K. M. Huffenberger, W. A. Imbriale, K. Ishidoshiro, M. E. Jones, P. Kangaslahti, D. J. Kapner, C. R. Lawrence, E. M. Leitch, M. Limon, J. J. McMahon, A. D. Miller, M. Nagai, H. Nguyen, T. J. Pearson, L. Piccirillo, S. J. E. Radford, A. C. S. Readhead, J. L. Richards, D. Samtleben, M. Seiffert, M. C. Shepherd, S. T. Staggs, O. Tajima, K. L. Thompson, R. Williamson, B. Winstein, E. J. Wollack, and J. T. L. Zwart, “The Q/U Imaging Experiment Instrument,” *ApJ* **768** (May, 2013) 9.

[49] R. A. Monsalve, “Beam characterization for the QUIET Q-Band instrument using polarized and unpolarized astronomical sources,” in *Millimeter, Submillimeter, and Far-Infrared Detectors and Instrumentation for Astronomy V*, vol. 7741 of *Proc. SPIE*, p. 77412M. July, 2010.

[50] T. Dumitrescu, “Toward a millimeter-wave antireflection coating for the abs ultra high molecular weight polyethylene cryostat window,” *Princeton University* **55** (May, 2009) 3502, [arXiv:astro-ph/1601.08246](https://arxiv.org/abs/1601.08246).

[51] J. W. Lamb, “Miscellaneous data on materials for millimetre and submillimetre optics,” *International Journal of Infrared and Millimeter Waves* **17** no. 12, (Dec., 1996) 1997 – 2034.

[52] B. Kerr and Boyd *MMA Memorandum #90, NRAO* (Jan., 1992) .

[53] D. Fixsen, E. Wollack, A. Kogut, M. Limon, P. Mirel, and J. Singal, “Compact Radiometric Microwave Calibrator,” *Review of Scientific Instruments* **77** no. 6, (2006) 64905–1–6.

[54] P. A. R. Ade, G. Pisano, C. Tucker, and S. Weaver, “A review of metal mesh filters,” in *Society of Photo-Optical Instrumentation Engineers (SPIE) Conference Series*, vol. 6275 of *Proc. SPIE*, p. 62750U. June, 2006.

[55] N. Marcuvitz, *Waveguide Handbook*. Electromagnetics and Radar Series. P. Peregrinus, 1951. <https://books.google.com/books?id=Ao34iFuNZgIC>.

[56] R. Ulrich, “Far-infrared properties of metallic mesh and its complementary structure,” *Infrared Physics* **7** (Mar., 1967) 37–55.

[57] C. Tucker and P. Ade, “Metal-mesh filters for THz applications,” in *IR/mm Waves and 15th International Conference on THz Electronics, IRMMW-THz*, pp. 973 –975. 2007.

[58] G. Pisano, C. Tucker, P. A. R. Ade, P. Moseley, and M. W. Ng, “Metal mesh based metamaterials for millimetre wave and THz astronomy applications,” in *8th UK, Europe, China Millimeter Waves and THz Technology Workshop (UCMMT)*. 2016.

[59] Z. Ahmed, J. A. Grayson, K. L. Thompson, C.-L. Kuo, G. Brooks, and T. Pothoven, “Large-Area Reflective Infrared Filters for Millimeter/Sub-mm Telescopes,” *Journal of Low Temperature Physics* (Mar., 2014) 1–6. <http://link.springer.com/article/10.1007/s10909-014-1141-5>.

[60] M. Halpern, H. P. Gush, E. Wishnow, and V. de Cosmo, “Far infrared transmission of dielectrics at cryogenic and room temperatures - Glass, Fluorogold, Eccosorb, Styrocast, and various plastics,” *Ap. Opt.* **25** (Feb., 1986) 565–570.

[61] BICEP2 and Keck Array Collaborations, P. A. R. Ade, R. W. Aikin, D. Barkats, S. J. Benton, C. A. Bischoff, J. J. Bock, K. J. Bradford, J. A. Brevik, I. Buder, E. Bullock, C. D. Dowell, L. Duband, J. P. Filippini, S. Fliescher, S. R. Golwala, M. Halpern, M. Hasselfield, S. R. Hildebrandt, G. C. Hilton, H. Hui, K. D. Irwin, J. H. Kang, K. S. Karkare, J. P. Kaufman, B. G. Keating, S. Kefeli, S. A. Kernasovskiy, J. M. Kovac, C. L. Kuo, E. M. Leitch, M. Lueker, K. G. Megerian, C. B. Netterfield, H. T. Nguyen, R. O'Brient, R. W. Ogburn, IV, A. Orlando, C. Pryke, S. Richter, R. Schwarz, C. D. Sheehy, Z. K. Staniszewski, R. V. Sudiwala, G. P. Teply, K. Thompson, J. E. Tolan, A. D. Turner, A. G. Vieregg, A. C. Weber, C. L. Wong, and K. W. Yoon, “BICEP2/Keck Array. IV. Optical Characterization and Performance of the BICEP2 and Keck Array Experiments,” *ApJ* **806** (June, 2015) 206, [arXiv:astro-ph/1502.00596 \[astro-ph.IM\]](https://arxiv.org/abs/1502.00596).

[62] W. L. K. Wu, P. A. R. Ade, Z. Ahmed, K. D. Alexander, M. Amiri, D. Barkats, S. J. Benton, C. A. Bischoff, J. J. Bock, R. Bowens-Rubin, I. Buder, E. Bullock, V. Buza, J. A. Connors, J. P. Filippini, S. Fliescher, J. A. Grayson, M. Halpern, S. A. Harrison, G. C. Hilton, V. V. Hristov, H. Hui, K. D. Irwin, J. Kang, K. S. Karkare, E. Karpel, S. Kefeli, S. A. Kernasovskiy, J. M. Kovac, C. L. Kuo, K. G. Megerian, C. B. Netterfield, H. T. Nguyen, R. O'Brient, R. W. Ogburn, C. Pryke, C. D. Reintsema, S. Richter, C. Sorensen, Z. K. Staniszewski, B. Steinbach, R. V. Sudiwala, G. P. Teply, K. L. Thompson, J. E. Tolan, C. E. Tucker, A. D. Turner, A. G. Vieregg, A. C. Weber, D. V. Wiebe, J. Willmert, and K. W. Yoon, “Initial Performance of Bicep3: A Degree Angular Scale 95 GHz Band Polarimeter,” *Journal of Low Temperature Physics* **184** (Aug., 2016) 765–771, [arXiv:astro-ph/1601.00125 \[astro-ph.IM\]](https://arxiv.org/abs/1601.00125).

[63] Z. D. Kermish, P. Ade, A. Anthony, K. Arnold, D. Barron, D. Boettger, J. Borrill, S. Chapman, Y. Chinone, M. A. Dobbs, J. Errard, G. Fabbian, D. Flanigan, G. Fuller, A. Ghribi, W. Grainger, N. Halverson, M. Hasegawa, K. Hattori, M. Hazumi, W. L. Holzapfel, J. Howard, P. Hyland, A. Jaffe, B. Keating, T. Kisner, A. T. Lee, M. Le Jeune, E. Linder, M. Lungu, F. Matsuda, T. Matsumura, X. Meng, N. J. Miller, H. Morii, S. Moyerman, M. J. Myers, H. Nishino, H. Paar, E. Quealy, C. L. Reichardt, P. L. Richards, C. Ross, A. Shimizu, M. Shimon, C. Shimmin, M. Sholl, P. Siritanasak, H. Spieler, N. Stebor, B. Steinbach, R. Stompor, A. Suzuki, T. Tomaru, C. Tucker, and O. Zahn, “The POLARBEAR experiment,” *Proc. SPIE* **8452** (2012) 84521C–84521C–15, [arXiv:astro-ph/1210.7768](https://arxiv.org/abs/1210.7768). <http://dx.doi.org/10.1117/12.926354>.

[64] A. Rahlin, *The First Flight of the Spider Balloon-Borne Telescope. PhD Thesis*. PhD thesis, Princeton University, 2016.

[65] A. Suzuki, P. Ade, Y. Akiba, C. Aleman, K. Arnold, C. Baccigalupi, B. Barch, D. Barron, A. Bender, D. Boettger, J. Borrill, S. Chapman, Y. Chinone, A. Cukierman, M. Dobbs, A. Ducout, R. Dunner, T. Elleflot, J. Errard, G. Fabbian, S. Feeney, C. Feng, T. Fujino, G. Fuller, A. Gilbert, N. Goeckner-Wald, J. Groh, T. D. Haan, G. Hall, N. Halverson, T. Hamada, M. Hasegawa, K. Hattori, M. Hazumi, C. Hill, W. Holzapfel, Y. Hori, L. Howe, Y. Inoue, F. Irie, G. Jaehnig, A. Jaffe, O. Jeong, N. Katayama, J. Kaufman, K. Kazemzadeh, B. Keating, Z. Kermish, R. Keskitalo, T. Kisner, A. Kusaka, M. L. Jeune, A. Lee, D. Leon, E. Linder, L. Lowry, F. Matsuda, T. Matsumura, N. Miller, K. Mizukami, J. Montgomery, M. Navaroli, H. Nishino, J. Peloton, D. Poletti, G. Puglisi, G. Rebeiz, C. Raum, C. Reichardt, P. Richards, C. Ross, K. Rotermund, Y. Segawa, B. Sherwin, I. Shirley, P. Siritanasak, N. Stebor, R. Stompor, J. Suzuki, O. Tajima, S. Takada, S. Takakura, S. Takatori, A. Tikhomirov, T. Tomaru, B. Westbrook, N. Whitehorn, T. Yamashita, A. Zahn, and O. Zahn, “The Polarbear-2 and the Simons Array Experiments,” *Journal of Low Temperature Physics* **184** (Aug., 2016) 805–810, [arXiv:astro-ph/1512.07299](https://arxiv.org/abs/1512.07299) [astro-ph.IM].

[66] E. R. Dobrovisnkaya, L. A. Lytvynov, and V. Pishchik, *Sapphire: Material, Manufacturing, Applications*. Springer Science + Business Media, 2009.

[67] A. Hadni, J. Claudel, X. Gerbaux, G. Morlot, and J.-M. Munier, “Sur le comportement différent des cristaux et des verres dans l’absorption de l’infrarouge lointain (40–1500 $\mu$ ) à la température de l’hélium liquide,” *Ap. Opt.* **4** no. 4, (Apr, 1965) 487–494. <http://ao.osa.org/abstract.cfm?URI=ao-4-4-487>.

[68] J. Choi, H. Ishitsuka, S. Mima, S. Oguri, K. Takahashi, and O. Tajima, “Radio-transparent multi-layer insulation for radio wave receivers,” *Rev. Sci. Instru.* **84** (2013) 1–6.

[69] S. Oguri, J. Choi, T. Damayanthi, M. Hattori, M. Hazumi, H. Ishitsuka, K. Karatsu, S. Mima, M. Minowa, T. Nagasaki, C. Otani, Y. Sekimoto, O. Tajima, N. Tomita, M. Yoshida, E. Won, and the GroundBIRD group, “Groundbird: Observing cosmic microwave polarization at large angular scale with kinetic inductance detectors and high-speed rotating telescope,” *Journal of Low Temperature Physics* **184** (2016) pp786–792.

[70] T. Nagasaki, K. Araki, H. Ishimoto, K. Kominami, and O. Tajima, “Monitoring system for atmospheric water vapor with a ground-based multi-band radiometer: Meteorological application of radio astronomy technologies,” *Journal of Low Temperature Physics* **184** (2016) pp674–679.

[71] G. Savini, P. A. R. Ade, and J. Zhang, “A new artificial material approach for flat THz frequency lenses,” *Optics Express* **20** (Nov., 2012) 25766, [arXiv:astro-ph/1212.3010](https://arxiv.org/abs/1212.3010) [physics.optics].

[72] G. Pisano, M. W. Ng, F. Ozturk, B. Maffei, and V. Haynes, “Dielectrically embedded flat mesh lens for millimeter waves applications,” *Ap. Opt.* **52** (Apr., 2013) 2218.

[73] R. Corporation, “Ro3000-series bondply data sheet,” 2015.

[74] J. Lau, J. Fowler, T. Marriage, L. Page, J. Leong, E. Wishnow, R. Henry, E. Wollack, M. Halpern, D. Marsden, and G. Marsden, “Millimeter-wave antireflection coating for cryogenic silicon lenses,” *Ap. Opt.* **45** no. 16, (Jun, 2006) 3746–3751. <http://ao.osa.org/abstract.cfm?URI=ao-45-16-3746>.

[75] Y. Inoue, T. Hamada, M. Hasegawa, M. Hazumi, Y. Hori, A. Suzuki, T. Tomaru, T. Matsumura, T. Sakata, T. Minamoto, and T. Hirai, “Two-layer anti-reflection coating with mullite and polyimide foam for large-diameter cryogenic infrared filters,” *Ap. Opt.* **55** (Dec., 2016) D22, [arXiv:1607.02938](https://arxiv.org/abs/1607.02938) [astro-ph.IM].

[76] E. Quealy, *The POLARBEAR Cosmic Microwave Background Polarization Experiment and Anti-Reflection Coatings for Millimeter Wave Observations*. PhD thesis, University of California, Berkeley, 2012.

[77] J. P. Filippini, P. A. R. Ade, M. Amiri, S. J. Benton, R. Bihary, J. J. Bock, J. R. Bond, J. A. Bonetti, S. A. Bryan, B. Burger, H. C. Chiang, C. R. Contaldi, B. P. Crill, O. Doré, M. Farhang, L. M. Fissel, N. N. Gandilo, S. R. Golwala, J. E. Gudmundsson, M. Halpern, M. Hasselfield, G. Hilton, W. Holmes, V. V. Hristov, K. D. Irwin, W. C. Jones, C. L. Kuo, C. J. MacTavish, P. V. Mason, T. E. Montroy, T. A. Morford, C. B. Netterfield, D. T. O'Dea, A. S. Rahlin, C. D. Reintsema, J. E. Ruhl, M. C. Runyan, M. A. Schenker, J. A. Shariff, J. D. Soler, A. Trangsrud, C. Tucker, R. S. Tucker, and A. D. Turner, “SPIDER: a balloon-borne CMB polarimeter for large angular scales,” in *Millimeter, Submillimeter, and Far-Infrared Detectors and Instrumentation for Astronomy V*, vol. 7741 of *Proc. SPIE*, p. 77411N. July, 2010. [arXiv:1106.2158 \[astro-ph.CO\]](https://arxiv.org/abs/1106.2158).

[78] P. C. Hargrave and G. Savini, “Anti-reflection coating of large-format lenses for sub-mm applications,” *Proc. SPIE* **7741** (2010) 77410S–77410S–10. <http://dx.doi.org/10.1117/12.856919>.

[79] A. Kusaka, T. Essinger-Hileman, J. W. Appel, P. Gallardo, K. D. Irwin, N. Jarosik, M. R. Nolta, L. A. Page, L. P. Parker, S. Raghunathan, J. L. Sievers, S. M. Simon, S. T. Staggs, and K. Visnjic, “Modulation of CMB polarization with a warm rapidly-rotating half-wave plate on the Atacama B-Mode Search (ABS) instrument,” *Rev. Sci. Instrum.* **85** (2014) 024501, [arXiv:astro-ph/1310.3711](https://arxiv.org/abs/astro-ph/1310.3711).

[80] S. Bryan, *Half-wave Plates for the Spider Cosmic Microwave Background Polarimeter*. PhD thesis, Case Western Reserve University, 2014.

[81] B. Reichborn-Kjennerud, A. M. Aboobaker, P. Ade, F. Aubin, C. Baccigalupi, C. Bao, J. Borrill, C. Cantalupo, D. Chapman, J. Didier, M. Dobbs, J. Grain, W. Grainger, S. Hanany, S. Hillbrand, J. Hubmayr, A. Jaffe, B. Johnson, T. Jones, T. Kisner, J. Klein, A. Korotkov, S. Leach, A. Lee, L. Levinson, M. Limon, K. MacDermid, T. Matsumura, X. Meng, A. Miller, M. Milligan, E. Pascale, D. Polsgrove, N. Ponthieu, K. Raach, I. Sagiv, G. Smecher, F. Stivoli, R. Stompor, H. Tran, M. Tristram, G. S. Tucker, Y. Vinokurov, A. Yadav, M. Zaldarriaga, and K. Zilic, “EBEX: a balloon-borne CMB polarization experiment,” in *Society of Photo-Optical Instrumentation Engineers (SPIE) Conference Series*, vol. 7741 of *Proc. SPIE*. July, 2010. [arXiv:astro-ph/1007.3672 \[astro-ph.CO\]](https://arxiv.org/abs/1007.3672).

[82] D. Rosen, A. Suzuki, B. Keating, W. Krantz, A. T. Lee, E. Quealy, P. L. Richards, P. Siritanasak, and W. Walker, “Epoxy-based broadband antireflection coating for millimeter-wave optics,” *Ap. Opt.* **52** no. 33, (Nov, 2013) 8102–8105. <http://ao.osa.org/abstract.cfm?URI=ao-52-33-8102>.

[83] K. Young, Q. Wen, S. Hanany, H. Imada, J. Koch, T. Matsumura, O. Suttmann, and V. Schütz, “Broadband Millimeter-Wave Anti-Reflection Coatings on Silicon Using Pyramidal Sub-Wavelength Structures,” *ArXiv e-prints* (Feb., 2017) , [arXiv:astro-ph/1702.01768 \[astro-ph.IM\]](https://arxiv.org/abs/1702.01768).

[84] J. D. Wheeler, B. Koopman, P. Gallardo, P. R. Maloney, S. Brugger, G. Cortes-Medellin, R. Datta, C. D. Dowell, J. Glenn, S. Golwala, C. McKenney, J. J. McMahon, C. D. Munson, M. Niemack, S. Parshley, and G. Stacey, “Antireflection coatings for submillimeter silicon lenses,” in *Millimeter, Submillimeter, and Far-Infrared Detectors and Instrumentation for Astronomy VII*, vol. 9153 of *Proc. SPIE*, p. 91532Z. July, 2014.

[85] P. A. Gallardo, B. J. Koopman, N. Cothard, S. M. M. Bruno, G. Cortes-Medellin, G. Marchetti, K. H. Miller, B. Mockler, M. D. Niemack, G. Stacey, and E. J. Wollack, “Deep Reactive Ion Etched Anti-Reflection Coatings for Sub-millimeter Silicon Optics,” *ArXiv e-prints* (Oct., 2016) , [arXiv:astro-ph/1610.07655 \[astro-ph.IM\]](https://arxiv.org/abs/1610.07655).

[86] T. Matsumura, K. Young, Q. Wen, S. Hanany, H. Ishino, Y. Inoue, M. Hazumi, J. Koch, O. Suttman, and V. Schütz, “Millimeter-wave broadband antireflection coatings using laser ablation of subwavelength structures,” *Ap. Opt.* **55** (May, 2016) 3502, [arXiv:astro-ph/1601.08246](https://arxiv.org/abs/astro-ph/1601.08246) [astro-ph.IM].

[87] J. McMahon, *The 2004–2005 CAPMAP instrument and CMB polarization data*. PhD thesis, Princeton University, June, 2006.

[88] K. Harrington, T. Marriage, A. Ali, J. W. Appel, C. L. Bennett, F. Boone, M. Brewer, M. Chan, D. T. Chuss, F. Colazo, S. Dahal, K. Denis, R. Dünner, J. Eimer, T. Essinger-Hileman, P. Fluxa, M. Halpern, G. Hilton, G. F. Hinshaw, J. Hubmayr, J. Iuliano, J. Karakla, J. McMahon, N. T. Miller, S. H. Moseley, G. Palma, L. Parker, M. Petroff, B. Pradenas, K. Rostem, M. Sagliocca, D. Valle, D. Watts, E. Wollack, Z. Xu, and L. Zeng, “The Cosmology Large Angular Scale Surveyor,” *Proc. SPIE, Millimeter, Submillimeter, and Far-Infrared Detectors and Instrumentation for Astronomy VIII* **9914** (Aug., 2016) , [arXiv:astro-ph/1608.08234](https://arxiv.org/abs/astro-ph/1608.08234) [astro-ph.IM].

[89] J. Zhang, P. A. R. Ade, P. Mauskopf, L. Moncelsi, G. Savini, and N. Whitehouse, “New artificial dielectric metamaterial and its application as a terahertz antireflection coating,” *Ap. Opt.* **48** (Dec., 2009) 6635, [arXiv:astro-ph/1107.3560](https://arxiv.org/abs/astro-ph/1107.3560) [astro-ph.IM].

[90] B. R. Johnson, J. Collins, M. E. Abroe, P. A. R. Ade, J. Bock, J. Borrill, A. Boscaleri, P. de Bernardis, S. Hanany, A. H. Jaffe, T. Jones, A. T. Lee, L. Levinson, T. Matsumura, B. Rabii, T. Renbarger, P. L. Richards, G. F. Smoot, R. Stompor, H. T. Tran, C. D. Winant, J. H. P. Wu, and J. Zuntz, “MAXIPOL: Cosmic Microwave Background Polarimetry Using a Rotating Half-Wave Plate,” *ApJ* **665** (2007) 42–54, [arXiv:astro-ph/0611394](https://arxiv.org/abs/astro-ph/0611394). <http://arxiv.org/abs/astro-ph/0611394>.

[91] S. Moyerman, E. Bierman, P. A. R. Ade, R. Aiken, D. Barkats, C. Bischoff, J. J. Bock, H. C. Chiang, C. D. Dowell, L. Duband, E. F. Hivon, W. L. Holzapfel, V. V. Hristov, W. C. Jones, J. Kaufman, B. G. Keating, J. M. Kovac, C. L. Kuo, E. M. Leitch, P. V. Mason, T. Matsumura, H. T. Nguyen, N. Ponthieu, C. Pryke, S. Richter, G. Rocha, C. Sheehy, Y. D. Takahashi, J. E. Tolan, E. Wollack, and K. W. Yoon, “Scientific verification of Faraday Rotation Modulators: Detection of diffuse polarized Galactic emission,” *ApJ* **765** no. 1, (Feb., 2013) , [astro-ph/1212.0133](https://arxiv.org/abs/1212.0133). <http://arxiv.org/abs/1212.0133>.

[92] A. Ritacco, N. Ponthieu, and R. A. P. A. P. B. A. B. A. B. N. B. O. C. M. C. G. C. B. D. F.-X. D. S. G. J. K. C. L. S. M.-P. J. F. M. P. M. A. M. F. M. A. P. F. P. E. P. L. P. G. R.-I. M. R. V. R. L. R. C. R. F. S. G. S. K. S. A. T. C. T. S. T. C. Z. R. Catalano, A. and Adam, “Polarimetry at millimeter wavelengths with the NIKA camera: calibration and performance,” *A & A* **599** no. A34, (Feb., 2017) 17.

[93] J.-P. Bernard, P. Ade, Y. Andr, J. Aumont, L. Bautista, N. Bray, P. d. Bernardis, O. Boulade, F. Bousquet, M. Bouzit, V. Buttice, A. Caillat, M. Charra, M. Chaigneau, B. Crane, J.-P. Crussaire, F. Douchin, E. Doumayrou, J.-P. Dubois, C. Engel, P. Etcheto, P. Glot, M. Griffin, G. Foenard, S. Grabarnik, P. Hargrave, A. Hughes, R. Laureijs, Y. Lepennec, B. Leriche, Y. Longval, S. Maestre, B. Maffei, J. Martignac, C. Marty, W. Marty, S. Masi, F. Mirc, R. Misawa, J. Montel, L. Montier, B. Mot, J. Narbonne, J.-M. Nicot, F. Pajot, G. Parot, E. Prot, J. Pimentao, G. Pisano, N. Ponthieu, I. Ristorcelli, L. Rodriguez, G. Roudil, M. Salatino, G. Savini, O. Simonella, M. Saccoccia, P. Tapie, J. Tauber, J.-P. Torre, and C. Tucker, “PILOT: a balloon-borne experiment to measure the polarized FIR emission of dust grains in the interstellar medium,” *Experimental Astronomy* **42** (Oct., 2016) 2, 199–227.

[94] A. Tartari, J. Aumont, S. Banfi, P. Battaglia, E. S. Battistelli, A. Baù, B. Bélier, D. Bennett, L. Bergé, J. P. Bernard, M. Bersanelli, M. A. Bigot-Sazy, N. Bleurvacq, G. Bordier, J. Brossard, E. F. Bunn,

D. Buzzi, D. Cammilleri, F. Cavalieri, P. Chanial, C. Chapron, A. Coppolecchia, G. D'Alessandro, P. de Bernardis, T. Decourcelle, F. Del Torto, M. De Petris, L. Dumoulin, C. Franceschet, A. Gault, D. Gayer, M. Gervasi, A. Ghribi, M. Giard, Y. Giraud-Héraud, M. Gradziel, L. Grandsire, J. C. Hamilton, V. Haynes, N. Holtzer, J. Kaplan, A. Korotkov, J. Lande, A. Lowitz, B. Maffei, S. Marnieros, J. Martino, S. Masi, M. McCulloch, S. Melhuish, A. Mennella, L. Montier, A. Murphy, D. Néel, M. W. Ng, C. O'Sullivan, F. Pajot, A. Passerini, C. Perbost, F. Piacentini, M. Piat, L. Piccirillo, G. Pisano, D. Prèle, D. Rambaud, O. Rigaut, M. Salatino, A. Schillaci, S. Scully, M. M. Stolpovskiy, P. Timbie, G. Tucker, D. Viganò, F. Voisin, B. Watson, and M. Zannoni, “QUBIC: A Fizeau Interferometer Targeting Primordial B-Modes,” *Journal of Low Temperature Physics* **184** (Aug., 2016) 3–4, 739–745.

[95] M. Salatino and P. de Bernardis, “On Stokes Polarimeters for high precision CMB measurements and mm Astronomy measurements,” 2010. [arXiv:astro-ph/1006.3225 \[astro-ph.IM\]](https://arxiv.org/abs/1006.3225). <https://arxiv.org/abs/1006.3225>.

[96] S. A. Bryan, T. E. Montroy, and J. E. Ruhl, “Modeling dielectric Half-Wave Plates for Cosmic Microwave Background polarimetry using a Mueller matrix formalism,” *Ap. Opt.* **49** (Nov., 2010) 6313, [arXiv:astro-ph/1006.3359 \[astro-ph.IM\]](https://arxiv.org/abs/1006.3359).

[97] S. Pancharatnam, “Achromatic Combinations of Birefringent Plates,” *Memoir No. 71 of the Raman Research Institute* (March, 1955) 130–136.

[98] G. Savini, G. Pisano, and P. A. R. Ade, “Achromatic half-wave plate for submillimeter instruments in cosmic microwave background astronomy: modelling and simulation,” *Ap. Opt.* **45** no. 35, (Dec, 2006) 8907–8915.

[99] T. Matsumura, S. Hanany, B. R. Johnson, T. J. Jones, and P. Jonnalagadda, “Analysis of performance of three- and five-stack achromatic half-wave plates at millimeter wavelengths,” *Ap. Opt.* **48** no. 19, (Jun, 2008) 3614–3625, [arXiv:astro-ph/0806.1518](https://arxiv.org/abs/0806.1518).

[100] S. Hanany, J. Hubmayr, B. R. Johnson, T. Matsumura, P. Oxley, and M. Thibodeau, “Millimeter-wave achromatic half-wave plate,” *Ap. Opt.* **44** (Aug., 2005) 4666–4670, [arXiv:physics/0503122](https://arxiv.org/abs/physics/0503122).

[101] G. Pisano, G. Savini, P. A. R. Ade, and V. Haynes, “Metal-mesh achromatic half-wave plate for use a submillimeter wavelengths,” *Ap. Opt.* **47** no. 33, (Nov, 2008) 6251–6256.

[102] T. Matsumura, K. Young, Q. Wen, S. Hanany, H. Ishino, Y. Inoue, M. Hazumi, J. Koch, O. Suttman, and V. Schütz, “Millimeter-Wave Broadband Anti-Reflection Coatings Using Laser Ablation of Sub-Wavelength Structures,” *Ap. Opt.* **55** no. 13, (Jan, 2016) 3502–3509, [arXiv:astro-ph/1601.08246](https://arxiv.org/abs/1601.08246).

[103] S. Bryan, P. Ade, M. Amiri, S. Benton, R. Bihary, J. Bock, J. R. Bond, H. C. Chiang, C. Contaldi, B. Crill, O. Dore, B. Elder, J. Filippini, A. Fraisse, A. Gambrel, N. Gando, J. Gudmundsson, M. Hasselfield, M. Halpern, G. Hilton, W. Holmes, V. Hristov, K. Irwin, W. Jones, Z. Kermish, C. Lawrie, C. MacTavish, P. Mason, K. Megerian, L. Moncelsi, T. Montroy, T. Morford, J. Nagy, C. B. Netterfield, I. Padilla, A. S. Rahlin, C. Reintsema, D. C. Riley, J. Ruhl, M. Runyan, B. Saliwanchik, J. Shariff, J. Soler, A. Trangsrud, C. Tucker, R. Tucker, A. Turner, S. Wen, D. Wiebe, and E. Young, “A cryogenic rotation stage with a large clear aperture for the half-wave plates in the Spider instrument,” *Review of Scientific Instruments* **87** no. 1, (Jan., 2016) 014501, [arXiv:1510.01771 \[astro-ph.IM\]](https://arxiv.org/abs/1510.01771).

[104] T. Matsumura, H. Kataza, S. Utsunomiya, R. Yamamoto, M. Hazumi, and N. Katayama, “Design and performance of a prototype polarization modulator rotation system for use in space using a superconducting magnetic bearing,” *IEEE Transactions on Applied Superconductivity* **26** no. 3, (Apr, 2016) .

[105] C. Bao, B. Gold, C. Baccigalupi, J. Didier, S. Hanany, A. Jaffe, B. R. Johnson, S. Leach, T. Matsumura, A. Miller, and D. O'Dea, "The Impact of the Spectral Response of an Achromatic Half-Wave Plate on the Measurement of the Cosmic Microwave Background Polarization," *ApJ* **747** no. 2, (12, 2012) , [arXiv:astro-ph/1112.3057](https://arxiv.org/abs/1112.3057). <http://arxiv.org/abs/1112.3057>.

[106] T. Matsumura, "Mitigation of the spectral dependent polarization angle response for achromatic half-wave plate," *ArXiv e-prints* (Apr, 2014) , [arXiv:astro-ph/1404.5795](https://arxiv.org/abs/1404.5795).

[107] T. Matsumura, Y. Akiba, J. Borrill, Y. Chinone, M. Dobbs, H. Fuke, A. Ghribi, M. Hasegawa, K. Hattori, M. Hattori, M. Hazumi, W. Holzapfel, Y. Inoue, K. Ishidoshiro, H. Ishino, H. Ishitsuka, K. Karatsu, N. Katayama, I. Kawano, A. Kibayashi, Y. Kibe, K. Kimura, N. Kimura, K. Koga, M. Kozu, E. Komatsu, A. Lee, H. Matsuhara, S. Mima, K. Mitsuda, K. Mizukami, H. Morii, T. Morishima, S. Murayama, M. Nagai, R. Nagata, S. Nakamura, M. Naruse, K. Natsume, T. Nishibori, H. Nishino, A. Noda, T. Noguchi, H. Ogawa, S. Oguri, I. Ohta, C. Otani, P. Richards, S. Sakai, N. Sato, Y. Sato, Y. Sekimoto, A. Shimizu, K. Shinozaki, H. Sugita, T. Suzuki, A. Suzuki, O. Tajima, S. Takada, S. Takakura, Y. Takei, T. Tomaru, Y. Uzawa, T. Wada, H. Watanabe, N. Yamasaki, M. Yoshida, T. Yoshida, and K. Yotsumoto, "Mission design of LiteBIRD," *ArXiv e-prints* (Nov, 2013) , [astro-ph/1311.2847](https://arxiv.org/abs/1311.2847).

[108] V. V. Parshin, R. Heidinger, B. A. Andreev, A. V. Gusev, and V. B. Shmagin, "Silicon as an advanced window material for high power gyrotrons," *Journal of Infrared and Millimeter Waves* **16** no. 5, (May, 1995) 863–877.

[109] S. A. Bryan, P. A. R. Ade, M. Amiri, S. Benton, R. Bihary, J. J. Bock, J. R. Bond, J. A. Bonetti, H. C. Chiang, C. R. Contaldi, B. P. Crill, D. O'Dea, O. Dore, M. Farhang, J. P. Filippini, L. Fissel, N. Gandilo, S. Golwala, J. E. Gudmundsson, M. Hasselfield, M. Halpern, K. R. Helson, G. Hilton, W. Holmes, V. V. Hristov, K. D. Irwin, W. C. Jones, C. L. Kuo, C. J. MacTavish, P. Mason, T. Morford, T. E. Montroy, C. B. Netterfield, A. S. Rahlin, C. D. Reintsema, D. Riley, J. E. Ruhl, M. C. Runyan, M. A. Schenker, J. Shariff, J. D. Soler, A. Transrud, R. Tucker, C. Tucker, and A. Turner, "Modeling and characterization of the SPIDER half-wave plate," in *Society of Photo-Optical Instrumentation Engineers (SPIE) Conference Series*, vol. 7741 of *Proceedings of SPIE*. July, 2010. [arXiv:astro-ph/1006.3874](https://arxiv.org/abs/1006.3874) [astro-ph.IM].

[110] A. A. Fraisse, P. A. R. Ade, M. Amiri, S. J. Benton, J. J. Bock, J. R. Bond, J. A. Bonetti, S. Bryan, B. Burger, H. C. Chiang, C. N. Clark, C. R. Contaldi, B. P. Crill, G. Davis, O. Doré, M. Farhang, J. P. Filippini, L. M. Fissel, N. N. Gandilo, S. Golwala, J. E. Gudmundsson, M. Hasselfield, G. Hilton, W. Holmes, V. V. Hristov, K. Irwin, W. C. Jones, C. L. Kuo, C. J. MacTavish, P. V. Mason, T. E. Montroy, T. A. Morford, C. B. Netterfield, D. T. O'Dea, A. S. Rahlin, C. Reintsema, J. E. Ruhl, M. C. Runyan, M. A. Schenker, J. A. Shariff, J. D. Soler, A. Transrud, C. Tucker, R. S. Tucker, A. D. Turner, and D. Wiebe, "SPIDER: probing the early Universe with a suborbital polarimeter," *JCAP* **4** (Apr., 2013) 47, [arXiv:astro-ph/1106.3087](https://arxiv.org/abs/1106.3087) [astro-ph.CO].

[111] K. Zilic, *Calibration and Design of the E and B EXperiment (EBEX) Cryogenic Receiver*. PhD thesis, University of Minnesota, 2014.

[112] D. C. Harris, "A Century of Sapphire Growth," *Proc. SPIE* **7425** (2009) .

[113] GHTOT, "Advanced HEM Sapphire Growth," Sep, 2015. <http://ghtot.com/index.php/technology/advanced-hem-sapphire-growth>.

[114] "Arc-Energy Crystal Technologies,". <http://www.arc-energy.com/pr-new-ches-500-furnace-production-massive-300kg-sapphire-boules.html>.

[115] “Saint-Gobain Crystal Technologies,”. [http://www.crystals.saint-gobain.com/CLASS\\_Sapphire.aspx](http://www.crystals.saint-gobain.com/CLASS_Sapphire.aspx).

[116] “Kyocera Crystal Technologies,”. [http://global.kyocera.com/prdct/fc/product/pdf/s\\_c\\_sapphire.pdf](http://global.kyocera.com/prdct/fc/product/pdf/s_c_sapphire.pdf).

[117] R. L. Gentilman, P. T. McGuire, B. G. Pazol, J. Askinazi, R. Steindl, and J. W. Locher, “High strength edge-bonded sapphire windows,” *Proc. SPIE* **3705** (Jul, 1999) .

[118] G. Pisano, M. W. Ng, V. Haynes, and B. Maffei, “A Broadband Photolithographic Polariser for Millimetre Wave Applications,” in *PIERS Proceedings, Kuala Lumpur, Malaysia*. 2012.

[119] G. Pisano, G. Savini, P. A. R. Ade, and V. Haynes, “Metal-mesh achromatic half-wave plate for use at submillimeter wavelengths,” *Ap. Opt.* **47** (Nov., 2008) 6251.

[120] J. Zhang, P. A. R. Ade, P. Mauskopf, G. Savini, L. Moncelsi, and N. Whitehouse, “Polypropylene embedded metal mesh broadband achromatic half-wave plate for millimeter wavelengths,” *Ap. Opt.* **50** (July, 2011) 3750–3757.

[121] G. Pisano, M. W. Ng, V. Haynes, and B. Maffei, “A broadband metal-mesh half-wave plate for millimetre wave linear polarisation rotation,” *Progress In Electromagnetics Research M* **25** (2012) 101–114.

[122] G. Pisano, B. Maffei, M. W. Ng, V. Haynes, M. Brown, F. Noviello, P. de Bernardis, S. Masi, F. Piacentini, L. Pagano, M. Salatino, B. Ellison, M. Henry, P. de Maagt, and B. Shortt, “Development of large radii half-wave plates for CMB satellite missions,” in *Millimeter, Submillimeter, and Far-Infrared Detectors and Instrumentation for Astronomy VII*, vol. 9153 of *Proc. SPIE*, p. 915317. July, 2014. [arXiv:astro-ph/1409.8516 \[astro-ph.IM\]](https://arxiv.org/abs/1409.8516).

[123] M. Houde, R. L. Akeson, J. E. Carlstrom, J. W. Lamb, D. A. Schleuning, and D. P. Woody, “Polarizing Grids, Their Assemblies, and Beams of Radiation,” *PASP* **113** (May, 2001) 622–638, [astro-ph/0311414](https://arxiv.org/abs/astro-ph/0311414).

[124] D. T. Chuss, E. J. Wollack, S. H. Moseley, and G. Novak, “Interferometric polarization control,” *Ap. Opt. IP* **45** no. 2, (July, 2006) 5107–5117.

[125] D. T. Chuss, E. J. Wollack, G. Pisano, S. Ackiss, K. U-Yen, and M. w. Ng, “A translational polarization rotator,” *Ap. Opt.* **51** (Oct., 2012) 6824, [arXiv:astro-ph/1206.2284 \[astro-ph.IM\]](https://arxiv.org/abs/1206.2284).

[126] D. T. Chuss, P. A. R. Ade, D. J. Benford, C. L. Bennett, J. L. Dotson, J. R. Eimer, D. J. Fixsen, M. Halpern, G. Hilton, J. Hinderks, G. Hinshaw, K. Irwin, M. L. Jackson, M. A. Jah, N. Jethava, C. Jhabvala, A. J. Kogut, L. Lowe, N. McCullagh, T. Miller, P. Mirel, S. H. Moseley, S. Rodriguez, K. Rostem, E. Sharp, J. G. Staguhn, C. E. Tucker, G. M. Voellmer, E. J. Wollack, and L. Zeng, “The Primordial Inflation Polarization Explorer (PIPER),” in *Millimeter, Submillimeter, and Far-Infrared Detectors and Instrumentation for Astronomy V*, vol. 7741 of *Proc. SPIE*, p. 77411P. July, 2010.

[127] T. Essinger-Hileman, A. Ali, M. Amiri, J. W. Appel, D. Araujo, C. L. Bennett, F. Boone, M. Chan, H.-M. Cho, D. T. Chuss, F. Colazo, E. Crowe, K. Denis, R. Dünner, J. Eimer, D. Gothe, M. Halpern, K. Harrington, G. C. Hilton, G. F. Hinshaw, C. Huang, K. Irwin, G. Jones, J. Karakla, A. J. Kogut, D. Larson, M. Limon, L. Lowry, T. Marriage, N. Mehrle, A. D. Miller, N. Miller, S. H. Moseley, G. Novak, C. Reintsema, K. Rostem, T. Stevenson, D. Towner, K. U-Yen, E. Wagner, D. Watts, E. J. Wollack, Z. Xu, and L. Zeng, “CLASS: the Cosmology Large Angular Scale Surveyor,” in *Millimeter, Submillimeter, and Far-Infrared Detectors and Instrumentation for Astronomy VII*, vol. 9153 of *Proc. SPIE*, p. 91531I. July, 2014. [arXiv:astro-ph/1408.4788 \[astro-ph.IM\]](https://arxiv.org/abs/1408.4788).

[128] M. Krejny, D. Chuss, C. D. D'Aubigny, D. Golish, M. Houde, H. Hui, C. Kulesa, R. F. Loewenstein, S. H. Moseley, G. Novak, G. Voellmer, C. Walker, and E. Wollack, “The Hertz/VPM polarimeter: design and first light observations,” *Ap. Opt.* **47** (Aug., 2008) 4429, [arXiv:astro-ph/0803.3759](https://arxiv.org/abs/0803.3759).

[129] G. M. Voellmer, D. T. Chuss, M. Jackson, M. Krejny, S. H. Moseley, G. Novak, and E. J. Wollack, “A kinematic flexure-based mechanism for precise parallel motion for the Hertz variable-delay polarization modulator (VPM),” *Proc. SPIE* **6273** (July, 2006) 62733P.

[130] G. M. Voellmer, C. Bennett, D. T. Chuss, J. Eimer, H. Hui, S. H. Moseley, G. Novak, E. J. Wollack, and L. Zeng, “[A large free-standing wire grid for microwave variable-delay polarization modulation](#),” in *Ground-based and Airborne Instrumentation for Astronomy II*, vol. 7014 of *Proc. SPIE*, p. 70142A. July, 2008.

[131] N. N. Gandilo, P. A. R. Ade, D. Benford, C. L. Bennett, D. T. Chuss, J. L. Dotson, J. R. Eimer, D. J. Fixsen, M. Halpern, G. Hilton, G. F. Hinshaw, K. Irwin, C. Jhabvala, M. Kimball, A. Kogut, L. Lowe, J. J. McMahon, T. M. Miller, P. Mirel, S. H. Moseley, S. Pawlyk, S. Rodriguez, E. Sharp, III, P. Shirron, J. G. Staguhn, D. F. Sullivan, E. R. Switzer, P. Taraschi, C. E. Tucker, and E. J. Wollack, “The Primordial Inflation Polarization Explorer (PIPER),” *ArXiv e-prints* (July, 2016) , [arXiv:astro-ph/1607.06172 \[astro-ph.IM\]](https://arxiv.org/abs/1607.06172).

[132] D. T. Chuss, J. R. Eimer, D. J. Fixsen, J. Hinderks, A. J. Kogut, J. Lazear, P. Mirel, E. Switzer, G. M. Voellmer, and E. J. Wollack, “Variable-delay polarization modulators for cryogenic millimeter-wave applications,” *Review of Scientific Instruments* **85** no. 6, (June, 2014) 064501.

[133] N. J. Miller, D. T. Chuss, T. A. Marriage, E. J. Wollack, J. W. Appel, C. L. Bennett, J. Eimer, T. Essinger-Hileman, D. J. Fixsen, K. Harrington, S. H. Moseley, K. Rostem, E. R. Switzer, and D. J. Watts, “Recovery of Large Angular Scale CMB Polarization for Instruments Employing Variable-delay Polarization Modulators,” *ApJ* **818** no. 2, (Feb., 2016) 1–12.

[134] J. Eimer, C. Bennett, D. Chuss, and E. Wollack, “Vector Reflectometry in a Beam Waveguide,” *Review of Scientific Instruments* **82** (2011) 086101.

[135] A. Murk, J. Reveles, R. Wylde, G. Bell, I. Zivkovic, A. McNamara, and P. de Maagt, “Low Mass Calibration Target for MM-Wave Remote Sensing Instruments,” *IEEE Transactions on Antennas and Propagation* **61** no. 4, (Apr., 2013) 1547–1556, [arXiv:astro-ph/1207.5562 \[astro-ph.IM\]](https://arxiv.org/abs/1207.5562).

[136] M. D. Niemack, P. A. R. Ade, J. Aguirre, F. Barrientos, J. A. Beall, J. R. Bond, J. Britton, H. M. Cho, S. Das, M. J. Devlin, S. Dicker, J. Dunkley, R. Dunner, J. W. Fowler, A. Hajian, M. Halpern, M. Hasselfield, G. C. Hilton, M. Hilton, J. Hubmayr, J. P. Hughes, L. Infante, K. D. Irwin, N. Jarosik, J. Klein, A. Kosowsky, T. A. Marriage, J. McMahon, F. Menanteau, K. Moodley, J. P. Nibarger, M. R. Nolta, L. A. Page, B. Partridge, E. D. Reese, J. Sievers, D. N. Spergel, S. T. Staggs, R. Thornton, C. Tucker, E. Wollack, and K. W. Yoon, “ACTPol: A polarization-sensitive receiver for the Atacama Cosmology Telescope,” *Proc. SPIE 7741, Millimeter, Submillimeter, and Far-Infrared Detectors and Instrumentation for Astronomy V* **7714** no. 771411S, (Jun, 2010) , [astro-ph/1006.5049](https://arxiv.org/abs/1006.5049).

[137] K. Array, B. Collaborations, P. A. R. Ade, Z. Ahmed, R. W. Aikin, K. D. Alexander, D. Barkats, S. J. Benton, C. A. Bischoff, J. J. Bock, R. Bowens-Rubin, J. A. Brevik, I. Buder, E. Bullock, V. Buza, J. Connors, B. P. Crill, L. Duband, C. Dvorkin, J. P. Filippeni, S. Fliescher, J. Grayson, M. Halpern, S. Harrison, G. C. Hilton, H. Hui, K. D. Irwin, K. S. Karkare, E. Karpel, J. P. Kaufman, B. G. Keating, S. Kefeli, S. A. Kernasovskiy, J. M. Kovac, C. L. Kuo, E. M. Leitch, M. Lueker, K. G. Megerian, C. B. Netterfield, H. T. Nguyen, R. O'Brient, R. W. O. IV, A. Orlando, C. Pryke, S. Richter, R. Schwarz, and et al. (16 additional authors not shown), “BICEP2 / Keck Array VI: Improved Constraints On Cosmology and Foregrounds When Adding 95 GHz Data From Keck Array,” *Phys. Rev. Lett.* **116** no. 031302, (Oct, 2016) , [arXiv:astro-ph/1510.09217](https://arxiv.org/abs/1510.09217).

[138] J. A. Grayson, P. A. R. Ade, Z. Ahmed, K. D. Alexander, M. Amiri, D. Barkats, S. J. Benton, C. A. Bischoff, J. J. Bock, H. Boenish, R. Bowens-Rubin, I. Buder, E. Bullock, V. Buza, J. Connors, J. P. Filippini, S. Fliescher, M. Halpern, S. Harrison, G. C. Hilton, V. V. Hristov, H. Hui, K. D. Irwin, J. Kang, K. S. Karkare, E. Karpel, S. Kefeli, S. A. Kernasovskiy, J. M. Kovac, C. L. Kuo, E. M. Leitch, M. Lueker, K. G. Megerian, V. Monticue, T. Namikawa, C. B. Netterfield, H. T. Nguyen, R. O'Brient, R. W. O. IV, C. Pryke, C. D. Reintsema, S. Richter, R. Schwarz, C. Sorensen, C. D. Sheehy, Z. K. Staniszewski, B. Steinbach, G. P. Teply, K. L. Thompson, J. E. Tolan, C. Tucker, A. D. Turner, A. G. Vieregg, A. Wandui, A. C. Weber, D. V. Wiebe, J. Willmert, W. L. K. Wu, and K. W. Yoon, “BICEP3 performance overview and planned Keck Array upgrade,” *Proc. SPIE 9914, Millimeter, Submillimeter, and Far-Infrared Detectors and Instrumentation for Astronomy VIII* **9914** (07, 2016) , [arXiv:astro-ph/1607.04668](https://arxiv.org/abs/1607.04668).

[139] J. E. Austermann, K. A. Aird, J. A. Beall, D. Becker, A. Bender, B. A. Benson, L. E. Bleem, J. Britton, J. E. Carlstrom, C. L. Chang, H. C. Chiang, H. M. Cho, T. M. Crawford, A. T. Crites, A. Datesman, T. de Haan, M. A. Dobbs, E. M. George, N. W. Halverson, N. Harrington, J. W. Henning, G. C. Hilton, G. P. Holder, W. L. Holzapfel, S. Hoover, N. Huang, J. Hubmayr, K. D. Irwin, R. Keisler, J. Kennedy, L. Knox, A. T. Lee, E. Leitch, D. Li, M. Lueker, D. P. Marrone, J. J. McMahon, J. Mehl, S. S. Meyer, T. E. Montroy, T. Natoli, J. P. Nibarger, M. D. Niemack, V. Novosad, S. Padin, C. Pryke, C. L. Reichardt, J. E. Ruhl, B. R. Saliwanchik, J. T. Sayre, K. K. Schaffer, E. Shirokoff, A. A. Stark, K. Story, K. Vanderlinde, J. D. Vieira, G. Wang, R. Williamson, V. Yefremenko, K. W. Yoon, and O. Zahn, “SPTpol: an instrument for CMB polarization measurements with the South Pole Telescope,” *Proc. SPIE 8452, Millimeter, Submillimeter, and Far-Infrared Detectors and Instrumentation for Astronomy VI* **8452** no. 84520E, (Oct, 2012) , [arXiv:astro-ph/1210.4970](https://arxiv.org/abs/1210.4970).

[140] P. Léna, F. Lebrun, and F. Mignard, *Observational Astrophysics*. Springer, Berlin, 1998.

[141] **Planck** Collaboration, R. Adam *et al.*, “Planck 2015 results. X. Diffuse component separation: Foreground maps,” *ArXiv* (2015) , [arXiv:astro-ph/1502.01588 \[astro-ph.CO\]](https://arxiv.org/abs/1502.01588).

[142] S. Paine, “am Atmospheric Model,” 2016. <https://www.cfa.harvard.edu/~spaine/am/>.

[143] Planck Collaboration, R. Adam, P. A. R. Ade, N. Aghanim, M. Arnaud, J. Aumont, C. Baccigalupi, A. J. Banday, R. B. Barreiro, J. G. Bartlett, *et al.*, “Planck intermediate results. XXX. The angular power spectrum of polarized dust emission at intermediate and high Galactic latitudes,” *A&A* **586** (Feb., 2016) A133, [arXiv:astro-ph/1409.5738](https://arxiv.org/abs/1409.5738).

[144] Planck Collaboration, N. Aghanim, M. Ashdown, J. Aumont, C. Baccigalupi, M. Ballardini, A. J. Banday, R. B. Barreiro, N. Bartolo, *et al.*, “Planck intermediate results. L. Evidence for spatial variation of the polarized thermal dust spectral energy distribution and implications for CMB  $B$ -mode analysis,” *ArXiv e-prints* (June, 2016) , [arXiv:astro-ph/1606.07335](https://arxiv.org/abs/1606.07335).

[145] M. J. Griffin, J. J. Bock, and W. K. Gear, “Relative Performance of Filled and Feedhorn-Coupled Focal-Plane Architectures,” *Ap. Opt.* **41** no. 31, (2002) 6543 – 6554.

[146] P. J. B. Clarricoats and A. D. Olver, *Corrugated horns for microwave antennas*. Peter Peregrinus Ltd., London, UK, 1984.

[147] L. Zeng, C. L. Bennett, D. T. Chuss, and E. J. Wollack, “A low cross-polarization smooth-walled horn with improved bandwidth,” *IEEE Transactions on Antennas and Propagation* **58** no. 4, (April, 2010) 1383–1387.

[148] S. M. Simon, J. Austermann, J. A. Beall, S. K. Choi, K. P. Coughlin, S. M. Duff, P. A. Gallardo, S. W. Henderson, F. B. Hills, S. P. Ho, J. Hubmayr, A. Josaitis, B. Koopman, J. McMahon, F. Nati,

L. Newburgh, M. D. Niemack, M. Salatino, A. Schillaci, B. L. Schmitt, S. T. Staggs, E. M. Vavagiakis, J. T. Ward, and E. J. Wollack, “The design and characterization of wideband spline-profiled feedhorns for Advanced ACTPol,”.

[149] C. Granet, G. L. James, R. Bolton, and G. Moorey, “A smooth-walled spline-profile horn as an alternative to the corrugated horn for wide band millimeter-wave applications,” *IEEE Transactions on Antennas and Propagation* **52** no. 3, (March, 2004) 848–854.

[150] R. Datta, J. Hubmayr, C. Munson, J. Austermann, J. Beall, D. Becker, H. M. Cho, N. Halverson, G. Hilton, K. Irwin, D. Li, J. McMahon, L. Newburgh, J. Nibarger, M. Niemack, B. Schmitt, H. Smith, S. Staggs, J. Van Lanen, and E. Wollack, “Horn Coupled Multichroic Polarimeters for the Atacama Cosmology Telescope Polarization Experiment,” *Journal of Low Temperature Physics* **176** (Sept., 2014) 670–676, [arXiv:astro-ph/1401.8029 \[astro-ph.IM\]](https://arxiv.org/abs/1401.8029).

[151] J. Hubmayr, “Advances in Multichroic Feedhorn-Coupled TES Polarimeter Arrays for CMB Measurements,” in *16th Low Temperature Detector Conference*. 2015.

[152] R. Knochel and B. Mayer, “Broadband printed circuit 0 degrees /180 degrees couplers and high power inphase power dividers,” in *Microwave Symposium Digest, 1990., IEEE MTT-S International*, pp. 471–474 vol.1. May, 1990.

[153] P. A. R. Ade, D. T. Chuss, S. Hanany, V. Haynes, B. G. Keating, A. Kogut, J. E. Ruhl, G. Pisano, G. Savini, and E. J. Wollack, “Polarization modulators for cmbpol,” *Journal of Physics: Conference Series* **155** no. 1, (2009) 012006. <http://stacks.iop.org/1742-6596/155/i=1/a=012006>.

[154] K. U-yen, E. J. Wollack, J. Papapolymerou, and J. Laskar, “A broadband planar magic-t using microstrip-slotline transitions,” *IEEE Transactions on Microwave Theory and Techniques* **56** no. 1, (Jan, 2008) 172–177.

[155] J. McMahon, J. Beall, D. Becker, H. M. Cho, R. Datta, A. Fox, N. Halverson, J. Hubmayr, K. Irwin, J. Nibarger, M. Niemack, and H. Smith, “Multi-chroic Feed-Horn Coupled TES Polarimeters,” *Journal of Low Temperature Physics* **167** no. 5, (2012) 879–884. <http://dx.doi.org/10.1007/s10909-012-0612-9>.

[156] K. Rostem, C. L. Bennett, D. T. Chuss, N. Costen, E. Crowe, K. L. Denis, J. R. Eimer, N. Lourie, T. Essinger-Hileman, T. A. Marriage, S. H. Moseley, T. R. Stevenson, D. W. Towner, G. Voellmer, E. J. Wollack, and L. Zeng, “Detector architecture of the cosmology large angular scale surveyor,” *Proc. SPIE* **8452** (2012) 84521N–84521N–7.

[157] K. Rostem, A. Ali, J. W. Appel, C. L. Bennett, D. T. Chuss, F. A. Colazo, E. Crowe, K. L. Denis, T. Essinger-Hileman, T. A. Marriage, S. H. Moseley, T. R. Stevenson, D. W. Towner, K. U-Yen, and E. J. Wollack, “Scalable background-limited polarization-sensitive detectors for mm-wave applications,” *Proc. SPIE* **9153** (2014) 91530B–91530B–7.

[158] K. Rostem, A. Ali, J. W. Appel, C. L. Bennett, A. Brown, M.-P. Chang, D. T. Chuss, F. A. Colazo, N. Costen, K. L. Denis, T. Essinger-Hileman, R. Hu, T. A. Marriage, S. H. Moseley, T. R. Stevenson, K. U-Yen, E. J. Wollack, and Z. Xu, “Silicon-based antenna-coupled polarization-sensitive millimeter-wave bolometer arrays for cosmic microwave background instruments,” *Proc. SPIE* **9914** (2016) 99140D–99140D–10.

[159] D. T. Chuss, A. Ali, M. Amiri, J. Appel, C. L. Bennett, F. Colazo, K. L. Denis, R. Dünnner, T. Essinger-Hileman, J. Eimer, P. Fluxa, D. Gothe, M. Halpern, K. Harrington, G. Hilton, G. Hinshaw, J. Hubmayr, J. Iuliano, T. A. Marriage, N. Miller, S. H. Moseley, G. Mumby, M. Petroff, C. Reintsema,

K. Rostem, K. U-Yen, D. Watts, E. Wagner, E. J. Wollack, Z. Xu, and L. Zeng, “Cosmology Large Angular Scale Surveyor (CLASS) Focal Plane Development,” *Journal of Low Temperature Physics* **184** no. 3, (2016) 759–764. <http://dx.doi.org/10.1007/s10909-015-1368-9>.

[160] H. McCarrick, M. H. Abitbol, P. A. R. Ade, P. Barry, S. Bryan, G. Che, P. Day, S. Doyle, D. Flanigan, B. R. Johnson, G. Jones, H. G. LeDuc, M. Limon, P. Mauskopf, A. Miller, C. Tucker, and J. Zmuidzinas, “Development of dual-polarization LEKIDs for CMB observations,” [arXiv:1607.03448](https://arxiv.org/abs/1607.03448) [astro-ph.IM].

[161] L. Zeng, C. L. Bennett, D. T. Chuss, and E. J. Wollack, “A Low Cross-Polarization Smooth-Walled Horn With Improved Bandwidth,” *IEEE Transactions on Antennas and Propagation* **58** (Apr., 2010) 1383–1387.

[162] S. Bryan, K. Bradford, G. Che, P. Day, D. Flanigan, B. R. Johnson, G. Jones, B. Kjellstrand, M. Limon, P. Mauskopf, H. McCarrick, A. Miller, and B. Smiley, “Design of Dual-Polarization Horn-Coupled Kinetic Inductance Detectors for Cosmic Microwave Background Polarimetry,” *ArXiv e-prints* (Mar., 2015) , [arXiv:astro-ph/1503.04684](https://arxiv.org/abs/1503.04684) [astro-ph.IM].

[163] A. Ritacco, N. Ponthieu, A. Catalano, R. Adam, P. Ade, P. André, A. Beelen, A. Benoît, A. Bideaud, N. Billot, O. Bourrion, M. Calvo, G. Coiffard, B. Comis, F.-X. Désert, S. Doyle, J. Goupy, C. Kramer, S. Leclercq, J. F. Macías-Pérez, P. Mauskopf, A. Maury, F. Mayet, A. Monfardini, F. Pajot, E. Pascale, L. Perotto, G. Pisano, M. Rebolo-Iglesias, V. Revéret, L. Rodriguez, C. Romero, F. Ruppin, G. Savini, K. Schuster, A. Sievers, C. Thum, S. Triqueneaux, C. Tucker, and R. Zylka, “Polarimetry at millimeter wavelengths with the NIKA camera: calibration and performance,” *A & A* **599** no. A34, (Feb., 2017) 17, [arXiv:astro-ph/1609.02042](https://arxiv.org/abs/1609.02042) [astro-ph.IM].

[164] D. Flanigan, H. McCarrick, G. Jones, B. R. Johnson, M. H. Abitbol, P. Ade, D. Araujo, K. Bradford, R. Cantor, G. Che, P. Day, S. Doyle, C. B. Kjellstrand, H. Leduc, M. Limon, V. Luu, P. Mauskopf, A. Miller, T. Mroczkowski, C. Tucker, and J. Zmuidzinas, “Photon noise from chaotic and coherent millimeter-wave sources measured with horn-coupled, aluminum lumped-element kinetic inductance detectors,” *Applied Physics Letters* **108** no. 8, (Feb., 2016) 083504, [arXiv:astro-ph/1510.06609](https://arxiv.org/abs/1510.06609) [astro-ph.IM].

[165] H. McCarrick, D. Flanigan, G. Jones, B. R. Johnson, P. Ade, D. Araujo, K. Bradford, R. Cantor, G. Che, P. Day, S. Doyle, H. Leduc, M. Limon, V. Luu, P. Mauskopf, A. Miller, T. Mroczkowski, C. Tucker, and J. Zmuidzinas, “Horn-coupled, commercially-fabricated aluminum lumped-element kinetic inductance detectors for millimeter wavelengths,” *Review of Scientific Instruments* **85** no. 12, (Dec., 2014) 123117, [arXiv:astro-ph/1407.7749](https://arxiv.org/abs/1407.7749) [astro-ph.IM].

[166] N. Galitzki, P. A. R. Ade, F. E. Angilè, P. Ashton, J. A. Beall, D. Becker, K. J. Bradford, G. Che, H.-M. Cho, M. J. Devlin, B. J. Dober, L. M. Fissel, Y. Fukui, J. Gao, C. E. Groppi, S. Hillbrand, G. C. Hilton, J. Hubmayr, K. D. Irwin, J. Klein, J. van Lanen, D. Li, Z.-Y. Li, N. P. Lourie, H. Mani, P. G. Martin, P. Mauskopf, F. Nakamura, G. Novak, D. P. Pappas, E. Pascale, G. Pisano, F. P. Santos, G. Savini, D. Scott, S. Stanchfield, C. Tucker, J. N. Ullom, M. Underhill, M. R. Vissers, and D. Ward-Thompson, “The Next Generation BLAST Experiment,” *Journal of Astronomical Instrumentation* **3** (2014) 1440001, [arXiv:astro-ph/1409.7084](https://arxiv.org/abs/1409.7084) [astro-ph.IM].

[167] B. J. Dober, P. A. R. Ade, P. Ashton, F. E. Angilè, J. A. Beall, D. Becker, K. J. Bradford, G. Che, H.-M. Cho, M. J. Devlin, L. M. Fissel, Y. Fukui, N. Galitzki, J. Gao, C. E. Groppi, S. Hillbrand, G. C. Hilton, J. Hubmayr, K. D. Irwin, J. Klein, J. Van Lanen, D. Li, Z.-Y. Li, N. P. Lourie, H. Mani, P. G. Martin, P. Mauskopf, F. Nakamura, G. Novak, D. P. Pappas, E. Pascale, F. P. Santos, G. Savini, D. Scott, S. Stanchfield, J. N. Ullom, M. Underhill, M. R. Vissers, and D. Ward-Thompson,

“The next-generation BLASTPol experiment,” in *Society of Photo-Optical Instrumentation Engineers (SPIE) Conference Series*, vol. 9153 of *Society of Photo-Optical Instrumentation Engineers (SPIE) Conference Series*, p. 91530H. July, 2014. [arXiv:astro-ph/1407.3756 \[astro-ph.IM\]](https://arxiv.org/abs/1407.3756).

[168] G. Rebeiz, “Millimeter-wave and terahertz integrated circuit antennas,” *Proceedings of the IEEE* **80** no. 11, (1992) 1748–1770.

[169] P. Siritanasak, C. Aleman, K. Arnold, A. Cukierman, M. Hazumi, K. Kazemzadeh, B. Keating, T. Matsumura, A. T. Lee, C. Lee, E. Quealy, D. Rosen, N. Stebor, and A. Suzuki, “The Broadband Anti-reflection Coated Extended Hemispherical Silicon Lenses for Polarbear-2 Experiment,” *Journal of Low Temperature Physics* **184** no. 3, (2016) 553–558. <http://dx.doi.org/10.1007/s10909-015-1386-7>.

[170] D. Filipovic, S. Gearhart, and G. Rebeiz, “Double-slot antennas on extended hemispherical and elliptical silicon dielectric lenses,” *Microwave Theory and Techniques, IEEE Transactions on* **41** no. 10, (1993) 1738–1749.

[171] J. Edwards, R. O’Brien, A. Lee, and G. Rebeiz, “Dual-Polarized Sinuous Antennas on Extended Hemispherical Silicon Lenses,” *Antennas and Propagation, IEEE Transactions on* **60** no. 9, (2012) 4082–4091.

[172] R. O’Brien *et al.*, “A dual-polarized broadband planar antenna and channelizing filter bank for millimeter wavelengths,” *Applied Physics Letters* **102** no. 6, (2013) 063506. <http://link.aip.org/link/?APL/102/063506/1>.

[173] A. Suzuki, K. Arnold, J. Edwards, G. Engargiola, W. Holzapfel, B. Keating, A. T. Lee, X. F. Meng, M. J. Myers, R. O’Brien, E. Quealy, G. Rebeiz, P. L. Richards, D. Rosen, and P. Siritanasak, “Multi-Chroic Dual-Polarization Bolometric Detectors for Studies of the Cosmic Microwave Background,” *Journal of Low Temperature Physics* **176** no. 5, (2014) 650–656. <http://dx.doi.org/10.1007/s10909-013-1049-5>.

[174] C. Bao, B. Gold, C. Baccigalupi, J. Didier, S. Hanany, A. Jaffe, B. R. Johnson, S. Leach, T. Matsumura, A. Miller, and D. O’Dea, “The Impact of the Spectral Response of an Achromatic Half-wave Plate on the Measurement of the Cosmic Microwave Background Polarization,” *ApJ* **747** (Mar., 2012) 97, [arXiv:astro-ph/1112.3057 \[astro-ph.IM\]](https://arxiv.org/abs/1112.3057).

[175] C. Bao, B. Gold, C. Baccigalupi, J. Didier, S. Hanany, A. Jaffe, B. R. Johnson, S. Leach, T. Matsumura, A. Miller, and D. O’Dea, “Erratum: “The Impact of the Spectral Response of an Achromatic Half-wave Plate on the Measurement of the Cosmic Microwave Background Polarization”,” *ApJ* **818** (Feb., 2016) 205.

[176] K. Arnold, P. A. R. Ade, A. E. Anthony, D. Barron, D. Boettger, J. Borrill, S. Chapman, Y. Chinone, M. A. Dobbs, J. Errard, G. Fabbian, D. Flanigan, G. Fuller, A. Ghribi, W. Grainger, N. Halverson, M. Hasegawa, K. Hattori, M. Hazumi, W. L. Holzapfel, J. Howard, P. Hyland, A. Jaffe, B. Keating, Z. Kermish, T. Kisner, M. Le Jeune, A. T. Lee, E. Linder, M. Lungu, F. Matsuda, T. Matsumura, N. J. Miller, X. Meng, H. Morii, S. Moyerman, M. J. Myers, H. Nishino, H. Paar, E. Quealy, C. Reichardt, P. L. Richards, C. Ross, A. Shimizu, C. Shimmin, M. Shimon, M. Sholl, P. Siritanasak, H. Speiler, N. Stebor, B. Steinbach, R. Stompor, A. Suzuki, T. Tomaru, C. Tucker, and O. Zahn, “The bolometric focal plane array of the POLARBEAR CMB experiment,” *Proc. SPIE* **8452** (2012) 84521D–84521D–12. <http://dx.doi.org/10.1117/12.927057>.

[177] B. Westbrook, A. Cukierman, A. Lee, A. Suzuki, C. Raum, and W. Holzapfel, “Development of the Next Generation of Multi-chroic Antenna-Coupled Transition Edge Sensor Detectors for CMB

Polarimetry,” *Journal of Low Temperature Physics* **184** no. 1, (2016) 74–81. <http://dx.doi.org/10.1007/s10909-016-1508-x>.

[178] A. Suzuki, *Multichroic Bolometric Detector Architecture for Cosmic Microwave Background Polarimetry Experiments*. PhD thesis, University of California, Berkeley, 2013.

[179] G. Pisano, M. W. Ng, F. Ozturk, B. Maffei, and V. Haynes, “Dielectrically embedded flat mesh lens for millimeter waves applications,” *Ap. Opt.* **52** (Apr., 2013) 2218.

[180] L. J. Swenson, P. K. Day, C. D. Dowell, B. H. Eom, M. I. Hollister, R. Jarnot, A. Kovács, H. G. Leduc, C. M. McKenney, R. Monroe, T. Mroczkowski, H. T. Nguyen, and J. Zmuidzinas, “MAKO: a pathfinder instrument for on-sky demonstration of low-cost 350 micron imaging arrays,” in *Society of Photo-Optical Instrumentation Engineers (SPIE) Conference Series*, vol. 8452 of *Society of Photo-Optical Instrumentation Engineers (SPIE) Conference Series*. Sept., 2012. [arXiv:astro-ph/1211.0315](https://arxiv.org/abs/1211.0315) [astro-ph.IM].

[181] S.-G. Park, K. Lee, D. Han, J. Ahn, and K.-H. Jeong, “Subwavelength silicon through-hole arrays as an all-dielectric broadband terahertz gradient index metamaterial,” *Applied Physics Letters* **105** no. 9, (Sept., 2014) 091101.

[182] G. Pisano, M. W. Ng, V. Haynes, and B. Maffei, “A broadband metal-mesh half wave plate for millimetre wave linear polarisation rotation,” *Progress In Electromagnetics Research M* **25** (2012) 101.

[183] C. L. Kuo, J. J. Bock, J. A. Bonetti, J. Brevik, G. Chattopadhyay, P. K. Day, S. Golwala, M. Kenyon, A. E. Lange, H. G. LeDuc, H. Nguyen, R. W. Ogburn, A. Orlando, A. Transgrud, A. Turner, G. Wang, and J. Zmuidzinas, “Antenna-coupled TES bolometer arrays for CMB polarimetry,” *Proc. SPIE* **7020** (2008) 70201I–70201I-14. <http://dx.doi.org/10.1117/12.788588>.

[184] R. C. O'Brient, J. J. Bock, J. Bonnetti, P. Day, H. Hui, C. L. Kuo, N. Llombert, M. Lueker, H. Ngyen, Z. Stanizewski, G. Teply, A. Turner, and K. Yoon, “Suppressing Beam Systematics in Antenna-Coupled TES Bolometers for CMB Polarimetry,” *Journal of Low Temperature Physics* **167** no. 3, (2012) 497–503. <http://dx.doi.org/10.1007/s10909-011-0435-0>.

[185] D. S. Swetz, P. A. R. Ade, M. Amiri, J. W. Appel, E. S. Battistelli, B. Burger, J. Chervenak, M. J. Devlin, S. R. Dicker, W. B. Doriese, R. Dnner, T. Essinger-Hileman, R. P. Fisher, J. W. Fowler, M. Halpern, M. Hasselfield, G. C. Hilton, A. D. Hincks, K. D. Irwin, N. Jarosik, M. Kaul, J. Klein, J. M. Lau, M. Limon, T. A. Marriage, D. Marsden, K. Martocci, P. Mauskopf, H. Moseley, C. B. Netterfield, M. D. Niemack, M. R. Nolta, L. A. Page, L. Parker, S. T. Staggs, O. Stryzak, E. R. Switzer, R. Thornton, C. Tucker, E. Wollack, and Y. Zhao, “Overview of the Atacama Cosmology Telescope: Receiver, Instrumentation, and Telescope Systems,” *The Astrophysical Journal Supplement Series* **194** no. 2, (2011) 41. <http://stacks.iop.org/0067-0049/194/i=2/a=41>.

[186] C. D. Dowell, C. A. Allen, R. S. Babu, M. M. Freund, M. Gardner, J. Groseth, M. D. Jhabvala, A. Kovacs, D. C. Lis, S. H. Moseley, Jr., T. G. Phillips, R. F. Silverberg, G. M. Voellmer, and H. Yoshida, “SHARC II: a Caltech submillimeter observatory facility camera with 384 pixels,” *Proc. SPIE* **4855** (2003) 73–87. <http://dx.doi.org/10.1117/12.459360>.

[187] D. A. Schleuning, C. D. Dowell, R. H. Hildebrand, S. R. Platt, and G. Novak, “HERTZ, A Submillimeter Polarimeter,” *PASP* **109** (Mar., 1997) 307–318.

[188] P. Bastien, T. Jenness, and J. Molnar, “A Polarimeter for SCUBA-2,” *Astronomical Society of the Pacific Conference Series* **343** (Dec., 2005) 69.

[189] H. Li, M. Attard, C. D. Dowell, R. H. Hildebrand, M. Houde, L. Kirby, G. Novak, and J. E. Vaillancourt, “SHARP: the SHARC-II polarimeter for CSO,” *Proc. SPIE* **6275** (June, 2006) 62751H.

[190] D. J. Benford, D. T. Chuss, G. C. Hilton, K. D. Irwin, N. S. Jethava, C. A. Jhabvala, A. J. Kogut, T. M. Miller, P. Mirel, S. H. Moseley, K. Rostem, E. H. Sharp, J. G. Staguhn, G. M. Stiehl, G. M. Voellmer, and E. J. Wollack, “5,120 superconducting bolometers for the PIPER balloon-borne CMB polarization experiment,” *Proc. SPIE* **7741** (July, 2010) 77411Q.

[191] A. Kogut, D. J. Fixsen, D. T. Chuss, J. Dotson, E. Dwek, M. Halpern, G. F. Hinshaw, S. M. Meyer, S. H. Moseley, M. D. Seiffert, D. N. Spergel, and E. J. Wollack, “The Primordial Inflation Explorer (PIXIE): a nulling polarimeter for cosmic microwave background observations,” *JCAP* **7** (July, 2011) 025, [arXiv:astro-ph/1105.2044](https://arxiv.org/abs/astro-ph/1105.2044).

[192] A. Kusaka, D. J. Fixsen, A. J. Kogut, S. S. Meyer, S. T. Staggs, and T. R. Stevenson, “MuSE: a novel experiment for CMB polarization measurement using highly multimoded bolometers,” *Proc. SPIE* **8452** (Sept., 2012) 84521L.

[193] A. Kusaka, E. J. Wollack, and T. R. Stevenson, “Angular and polarization response of multimode sensors with resistive-grid absorbers,” *Journal of the Optical Society of America A* **31** (July, 2014) 1557, [arXiv:astro-ph/1401.1859](https://arxiv.org/abs/astro-ph/1401.1859) [astro-ph.IM].

[194] P. C. Nagler, K. T. Crowley, K. L. Denis, A. M. Devasia, D. J. Fixsen, A. J. Kogut, G. Manos, S. Porter, and T. R. Stevenson, “Multimode bolometer development for the PIXIE instrument,” *Proc. SPIE* **9914** (2016) 99141A–99141A–10. <http://dx.doi.org/10.1117/12.2231082>.

[195] K. U-yen, D. Chuss, and E. Wollack, “Planar Transmission Line Technologies,” 2008.

[196] D. Li, J. Gao, J. E. Austermann, J. A. Beall, D. Becker, H. M. Cho, A. E. Fox, N. Halverson, J. Henning, G. C. Hilton, J. Hubmayr, K. D. Irwin, J. V. Lanen, J. Nibarger, and M. Niemack, “Improvements in Silicon Oxide Dielectric Loss for Superconducting Microwave Detector Circuits,” *IEEE Transactions on Applied Superconductivity* **23** no. 3, (June, 2013) 1501204–1501204.

[197] H. Paik and K. D. Osborn, “Reducing quantum-regime dielectric loss of silicon nitride for superconducting quantum circuits,” *Applied Physics Letters* **96** no. 7, (2010) . <http://scitation.aip.org/content/aip/journal/apl/96/7/10.1063/1.3309703>.

[198] E. J. Crowe, C. L. Bennett, D. T. Chuss, K. L. Denis, J. Eimer, N. Lourie, T. Marriage, S. H. Moseley, K. Rostem, T. R. Stevenson, D. Towner, K. U-yen, and E. J. Wollack, “Fabrication of a Silicon Backshort Assembly for Waveguide-Coupled Superconducting Detectors,” *IEEE Transactions on Applied Superconductivity* **23** no. 3, (June, 2013) 2500505–2500505.

[199] K. L. Denis, A. Ali, J. Appel, C. L. Bennett, M. P. Chang, D. T. Chuss, F. A. Colazo, N. Costen, T. Essinger-Hileman, R. Hu, T. Marriage, K. Rostem, K. U-Yen, and E. J. Wollack, “Fabrication of Feedhorn-Coupled Transition Edge Sensor Arrays for Measurement of the Cosmic Microwave Background Polarization,” *Journal of Low Temperature Physics* **184** (Aug., 2016) 668–673, [arXiv:astro-ph/1511.05036](https://arxiv.org/abs/astro-ph/1511.05036) [astro-ph.IM].

[200] G. Cataldo, E. J. Wollack, E. M. Barrentine, A. D. Brown, S. H. Moseley, and K. U-Yen, “Analysis and calibration techniques for superconducting resonators,” *Review of Scientific Instruments* **86** no. 1, (2015) . <http://scitation.aip.org/content/aip/journal/rsi/86/1/10.1063/1.4904972>.

[201] **BICEP2** Collaboration, P. A. R. Ade *et al.*, “BICEP2 II: Experiment and Three-Year Data Set,” *ApJ* **792** no. 1, (2014) 62, [arXiv:astro-ph/1403.4302](https://arxiv.org/abs/astro-ph/1403.4302) [astro-ph.CO].

[202] **BICEP2, SPIDER, KECK ARRAY** Collaboration, P. A. R. Ade *et al.*, “Antenna-coupled TES bolometers used in BICEP2, Keck array, and SPIDER,” *ApJ* **812** no. 2, (2015) 176, [arXiv:astro-ph/1502.00619 \[astro-ph.IM\]](https://arxiv.org/abs/1502.00619).

[203] R. Datta, J. Austermann, J. A. Beall, D. Becker, K. P. Coughlin, S. M. Duff, P. A. Gallardo, E. Grace, M. Hasselfield, S. W. Henderson, G. C. Hilton, S. P. Ho, J. Hubmayr, B. J. Koopman, J. V. Lanen, D. Li, J. McMahon, C. D. Munson, F. Nati, M. D. Niemack, L. Page, C. G. Pappas, M. Salatino, B. L. Schmitt, A. Schillaci, S. M. Simon, S. T. Staggs, J. R. Stevens, E. M. Vavagiakis, J. T. Ward, and E. J. Wollack, “Design and Deployment of a Multichroic Polarimeter Array on the Atacama Cosmology Telescope,” *Journal of Low Temperature Physics* **184** no. 3, (2016) 568–575. <http://dx.doi.org/10.1007/s10909-016-1553-5>.

[204] C. M. Posada, P. A. R. Ade, Z. Ahmed, K. Arnold, J. E. Austermann, A. N. Bender, L. E. Bleem, B. A. Benson, K. Byrum, J. E. Carlstrom, C. L. Chang, H. M. Cho, S. T. Ciocys, J. F. Cliche, T. M. Crawford, A. Cukierman, D. Czaplewski, J. Ding, R. Divan, T. de Haan, M. A. Dobbs, D. Dutcher, W. Everett, A. Gilbert, N. W. Halverson, N. L. Harrington, K. Hattori, J. W. Henning, G. C. Hilton, W. L. Holzapfel, J. Hubmayr, K. D. Irwin, O. Jeong, R. Keisler, D. Kubik, C. L. Kuo, A. T. Lee, E. M. Leitch, S. Lendinez, S. S. Meyer, C. S. Miller, J. Montgomery, M. Myers, A. Nadolski, T. Natoli, H. Nguyen, V. Novosad, S. Padin, Z. Pan, J. Pearson, J. E. Ruhl, B. R. Saliwanchik, G. Smecher, J. T. Sayre, E. Shirokoff, L. Stan, A. A. Stark, J. Sobrin, K. Story, A. Suzuki, K. L. Thompson, C. Tucker, K. Vanderlinde, J. D. Vieira, G. Wang, N. Whitehorn, V. Yefremenko, K. W. Yoon, and K. E. Ziegler, “Fabrication of large dual-polarized multichroic TES bolometer arrays for CMB measurements with the SPT-3G camera,” *Superconductor Science and Technology* **28** no. 9, (2015) 094002. <http://stacks.iop.org/0953-2048/28/i=9/a=094002>.

[205] S. M. Simon, S. Raghunathan, J. W. Appel, D. T. Becker, L. E. Campusano, H. M. Cho, T. Essinger-Hileman, S. P. Ho, K. D. Irwin, N. Jarosik, A. Kusaka, M. D. Niemack, G. W. Nixon, M. R. Nolta, L. A. Page, G. A. Palma, L. P. Parker, J. L. Sievers, S. T. Staggs, and K. Visnjic, “Characterization of the Atacama B-mode Search,” in *Millimeter, Submillimeter, and Far-Infrared Detectors and Instrumentation for Astronomy VII*, vol. 9153 of *Proc. SPIE*, p. 91530Y. July, 2014.

[206] A. Suzuki, P. Ade, Y. Akiba, C. Aleman, K. Arnold, M. Atlas, D. Barron, J. Borrill, S. Chapman, Y. Chinone, A. Cukierman, M. Dobbs, T. Elleflot, J. Errard, G. Fabbian, G. Feng, A. Gilbert, W. Grainger, N. Halverson, M. Hasegawa, K. Hattori, M. Hazumi, W. Holzapfel, Y. Hori, Y. Inoue, G. Jaehnig, N. Katayama, B. Keating, Z. Kermish, R. Keskitalo, T. Kisner, A. Lee, F. Matsuda, T. Matsumura, H. Morii, S. Moyerman, M. Myers, M. Navaroli, H. Nishino, T. Okamura, C. Reichart, P. Richards, C. Ross, K. Rotermund, M. Sholl, P. Siritanasak, G. Smecher, N. Stebor, R. Stompor, J. Suzuki, S. Takada, S. Takakura, T. Tomaru, B. Wilson, H. Yamaguchi, and O. Zahn, “The POLARBEAR-2 Experiment,” *Journal of Low Temperature Physics* **176** (Sept., 2014) 719–725.

[207] R. O’Brient, P. Ade, K. Arnold, J. Edwards, G. Engargiola, W. L. Holzapfel, A. T. Lee, M. J. Myers, E. Quealy, G. Rebeiz, P. Richards, and A. Suzuki, “A dual-polarized broadband planar antenna and channelizing filter bank for millimeter wavelengths,” *Applied Physics Letters* **102** no. 6, (Feb., 2013) 063506, [arXiv:astro-ph/1302.0325 \[astro-ph.IM\]](https://arxiv.org/abs/1302.0325).

[208] B. Westbrook, A. Cukierman, A. Lee, A. Suzuki, C. Raum, and W. Holzapfel, “Development of the Next Generation of Multi-chroic Antenna-Coupled Transition Edge Sensor Detectors for CMB Polarimetry,” *Journal of Low Temperature Physics* **184** (July, 2016) 74–81.

[209] S. Hailey-Dunsheath, E. Shirokoff, P. S. Barry, C. M. Bradford, S. Chapman, G. Che, J. Glenn, M. Hollister, A. Kovács, H. G. LeDuc, P. Mauskopf, C. McKenney, R. O’Brient, S. Padin, T. Reck, C. Shiu, C. E. Tucker, J. Wheeler, R. Williamson, and J. Zmuidzinas, “Low Noise Titanium Nitride

KIDs for SuperSpec: A Millimeter-Wave On-Chip Spectrometer," *Journal of Low Temperature Physics* **184** (July, 2016) 180–187, [arXiv:astro-ph/1511.04488 \[astro-ph.IM\]](https://arxiv.org/abs/1511.04488).

[210] A. Endo, J. J. A. Baselmans, P. P. van der Werf, B. Knoors, S. M. H. Javadzadeh, S. J. C. Yates, D. J. Thoen, L. Ferrari, A. M. Baryshev, Y. J. Y. Lankwarden, P. J. de Visser, R. M. J. Janssen, and T. M. Klapwijk, "Development of DESHIMA: a redshift machine based on a superconducting on-chip filterbank," in *Millimeter, Submillimeter, and Far-Infrared Detectors and Instrumentation for Astronomy VI*, vol. 8452 of *Proc. SPIE*, p. 84520X. Sept., 2012.

[211] R. O'Brient, J. J. Bock, C. M. Bradford, A. Crites, R. Duan, S. Hailey-Dunsheath, J. Hunacek, R. LeDuc, E. Shirokoff, Z. Staniszewski, A. Turner, and M. Zemcov, "Lithographed spectrometers for tomographic line mapping of the Epoch of Reionization," in *Millimeter, Submillimeter, and Far-Infrared Detectors and Instrumentation for Astronomy VII*, vol. 9153 of *Proc. SPIE*, p. 91530F. Aug., 2014.

[212] G. Cataldo, W.-T. Hsieh, W.-C. Huang, S. H. Moseley, T. R. Stevenson, and E. J. Wollack, "Micro-Spec: an integrated direct-detection spectrometer for far-infrared space telescopes," in *Space Telescopes and Instrumentation 2014: Optical, Infrared, and Millimeter Wave*, vol. 9143 of *Proc. SPIE*, p. 91432C. Aug., 2014.

[213] S. M. Duff, J. Austermann, J. A. Beall, D. Becker, R. Datta, P. A. Gallardo, S. W. Henderson, G. C. Hilton, S. P. Ho, J. Hubmayr, B. J. Koopman, D. Li, J. McMahon, F. Nati, M. D. Niemack, C. G. Pappas, M. Salatino, B. L. Schmitt, S. M. Simon, S. T. Staggs, J. R. Stevens, J. Van Lanen, E. M. Vavagiakis, J. T. Ward, and E. J. Wollack, "Advanced ACTPol Multichroic Polarimeter Array Fabrication Process for 150 mm Wafers," *Journal of Low Temperature Physics* **184** no. 3, (2016) 634–641. <http://dx.doi.org/10.1007/s10909-016-1576-y>.

[214] K. U-yen, E. J. Wollack, S. H. Moseley, T. R. Stevenson, W. T. Hsieh, and N. T. Cao, "Via-less microwave crossover using microstrip-CPW transitions in slotline propagation mode," *Microwave Symposium Digest, 2009. MTT '09. IEEE MTT-S International* (June, 2009) 1029–1032.

[215] K. L. Denis, A. D. Brown, M. P. Chang, R. Hu, K. Rostem, K. U-Yen, and E. J. Wollack, "Fabrication of superconducting vacuum-gap crossovers for high performance microwave applications," *IEEE Transactions on Applied Superconductivity* **27** no. 4, (June, 2017) 1–4.

[216] H. Surdi, *Applications of Kinetic Inductance: Parametric Amplifier & Phase Shifter, 2DEG Coupled Co-planar Structures & Microstrip to Slotline Transition at RF Frequencies*. PhD thesis, ARIZONA STATE UNIVERSITY, 2016.

[217] E. Grace, J. Beall, J. R. Bond, H. M. Cho, R. Datta, M. J. Devlin, R. Dünnner, A. E. Fox, P. Gallardo, M. Hasselfield, S. Henderson, G. C. Hilton, A. D. Hincks, R. Hlozek, J. Hubmayr, K. Irwin, J. Klein, B. Koopman, D. Li, M. Lungu, L. Newburgh, J. P. Nibarger, M. D. Niemack, L. Maurin, J. McMahon, S. Naess, L. A. Page, C. Pappas, B. L. Schmitt, J. Sievers, S. T. Staggs, R. Thornton, J. Van Lanen, and E. J. Wollack, "ACTPol: on-sky performance and characterization," in *Millimeter, Submillimeter, and Far-Infrared Detectors and Instrumentation for Astronomy VII*, vol. 9153 of *Proc. SPIE*, p. 915310. Aug., 2014.

[218] J. W. Henning, P. Ade, K. A. Aird, J. E. Austermann, J. A. Beall, D. Becker, B. A. Benson, L. E. Bleem, J. Britton, J. E. Carlstrom, C. L. Chang, H.-M. Cho, T. M. Crawford, A. T. Crites, A. Datesman, T. de Haan, M. A. Dobbs, W. Everett, A. Ewall-Wice, E. M. George, N. W. Halverson, N. Harrington, G. C. Hilton, W. L. Holzapfel, J. Hubmayr, K. D. Irwin, M. Karfunkle, R. Keisler, J. Kennedy, A. T. Lee, E. Leitch, D. Li, M. Lueker, D. P. Marrone, J. J. McMahon, J. Mehl, S. S. Meyer, J. Montgomery, T. E. Montroy, J. Nagy, T. Natoli, J. P. Nibarger, M. D. Niemack,

V. Novosad, S. Padin, C. Pryke, C. L. Reichardt, J. E. Ruhl, B. R. Saliwanchik, J. T. Sayre, K. K. Schaffer, E. Shirokoff, K. Story, C. Tucker, K. Vanderlinde, J. D. Vieira, G. Wang, R. Williamson, V. Yefremenko, K. W. Yoon, and E. Young, “Feedhorn-coupled TES polarimeter camera modules at 150 GHz for CMB polarization measurements with SPTpol,” in *Millimeter, Submillimeter, and Far-Infrared Detectors and Instrumentation for Astronomy VI*, vol. 8452 of *Proc. SPIE*, p. 84523A. Sept., 2012. [arXiv:astro-ph/1210.4969 \[astro-ph.IM\]](https://arxiv.org/abs/1210.4969).

[219] S. P. Ho, C. G. Pappas, J. Austermann, J. A. Beall, D. Becker, S. K. Choi, R. Datta, S. M. Duff, P. A. Gallardo, E. Grace, M. Hasselfield, S. W. Henderson, G. C. Hilton, J. Hubmayr, B. J. Koopman, J. V. Lanen, D. Li, J. McMahon, F. Nati, M. D. Niemack, P. Niraula, M. Salatino, A. Schillaci, B. L. Schmitt, S. M. Simon, S. T. Staggs, J. R. Stevens, J. T. Ward, E. J. Wollack, and E. M. Vavagiakis, “The First Multichroic Polarimeter Array on the Atacama Cosmology Telescope: Characterization and Performance,” *Journal of Low Temperature Physics* **184** (Aug., 2016) 559–567.

[220] K. D. Irwin, “An application of electrothermal feedback for high resolution cryogenic particle detection,” *Applied Physics Letters* **66** (Apr., 1995) 1998–2000.

[221] K. D. Irwin and G. C. Hilton, “Transition-Edge Sensors,” in *Cryogenic Particle Detection*, C. Enss, ed., vol. 99 of *Topics in Applied Physics*, pp. 63–150. Springer Berlin Heidelberg, 2005. [http://dx.doi.org/10.1007/10933596\\_3](http://dx.doi.org/10.1007/10933596_3).

[222] J. Zmuidzinas, “Thermal noise and correlations in photon detection,” *Ap. Opt.* **42** (Sept., 2003) 4989–5008.

[223] J. C. Mather, “Bolometer noise: nonequilibrium theory,” *Ap. Opt.* **21** (Mar., 1982) 1125–1129.

[224] The EBEX Collaboration, A. M. Aboobaker, P. Ade, D. Araujo, F. Aubin, C. Baccigalupi, B. C., D. Chapman, J. Didier, M. Dobbs, C. Geach, W. Grainger, S. Hanany, K. Helson, S. Hillbrand, J. Hubmayr, A. Jaffe, B. Johnson, T. Jones, J. Klein, A. Korotkov, A. Lee, L. Levinson, M. Limon, K. MacDermid, T. Matsumura, A. D. Miller, M. Milligan, K. Raach, B. Reichborn-Kjennerud, I. Sagiv, G. Savini, L. Spencer, C. Tucker, G. Tucker, B. Westbrook, K. Young, and K. Zilic, “The EBEX Balloon-Borne Experiment - Gondola, Attitude Control, and Control Software,” *Accepted for publication in ApJ Supp.* (Feb, 2017) , [arXiv:astro-ph/1702.07020 \[astro-ph.IM\]](https://arxiv.org/abs/1702.07020).

[225] J. T. Sayre, P. Ade, K. A. Aird, J. E. Austermann, J. A. Beall, D. Becker, B. A. Benson, L. E. Bleem, J. Britton, J. E. Carlstrom, C. L. Chang, H.-M. Cho, T. M. Crawford, A. T. Crites, A. Datesman, T. de Haan, M. A. Dobbs, W. Everett, A. Ewall-Wice, E. M. George, N. W. Halverson, N. Harrington, J. W. Henning, G. C. Hilton, W. L. Holzapfel, J. Hubmayr, K. D. Irwin, M. Karfunkle, R. Keisler, J. Kennedy, A. T. Lee, E. Leitch, D. Li, M. Lueker, D. P. Marrone, J. J. McMahon, J. Mehl, S. S. Meyer, J. Montgomery, T. E. Montroy, J. Nagy, T. Natoli, J. P. Nibarger, M. D. Niemack, V. Novosad, S. Padin, C. Pryke, C. L. Reichardt, J. E. Ruhl, B. R. Saliwanchik, K. K. Schaffer, E. Shirokoff, K. Story, C. Tucker, K. Vanderlinde, J. D. Vieira, G. Wang, R. Williamson, V. Yefremenko, K. W. Yoon, and E. Young, “Design and characterization of 90 GHz feedhorn-coupled TES polarimeter pixels in the SPTPol camera,” in *Millimeter, Submillimeter, and Far-Infrared Detectors and Instrumentation for Astronomy VI*, vol. 8452 of *Proc. SPIE*, p. 845239. Sept., 2012. [arXiv:astro-ph/1210.4968 \[astro-ph.IM\]](https://arxiv.org/abs/1210.4968).

[226] R. J. Thornton, P. A. R. Ade, S. Aiola, F. E. Angile, M. Amiri, J. A. Beall, D. T. Becker, H. Cho, S. K. Choi, P. Corlies, K. P. Coughlin, R. Datta, M. J. Devlin, S. R. Dicker, R. Dunner, J. W. Fowler, A. E. Fox, P. A. Gallardo, J. Gao, E. Grace, M. Halpern, M. Hasselfield, S. W. Henderson, G. C. Hilton, A. D. Hincks, S. P. Ho, J. Hubmayr, K. D. Irwin, J. Klein, B. Koopman, D. Li, T. Louis, M. Lungu, L. Maurin, J. McMahon, C. D. Munson, S. Naess, F. Nati, L. Newburgh, J. Nibarger, M. D.

Niemack, P. Niraula, M. R. Nolta, L. A. Page, C. G. Pappas, A. Schillaci, B. L. Schmitt, N. Sehgal, J. L. Sievers, S. M. Simon, S. T. Staggs, C. Tucker, M. Uehara, J. van Lanen, J. T. Ward, and E. J. Wollack, “The Atacama Cosmology Telescope: The polarization-sensitive ACTPol instrument,” *ArXiv e-prints* (May, 2016) , [arXiv:astro-ph/1605.06569 \[astro-ph.IM\]](https://arxiv.org/abs/1605.06569).

[227] BICEP2 Collaboration, Keck Array Collaboration, SPIDER Collaboration, P. A. R. Ade, R. W. Aikin, M. Amiri, D. Barkats, S. J. Benton, C. A. Bischoff, J. J. Bock, J. A. Bonetti, J. A. Brevik, I. Buder, E. Bullock, G. Chattopadhyay, G. Davis, P. K. Day, C. D. Dowell, L. Duband, J. P. Filippini, S. Fliescher, S. R. Golwala, M. Halpern, M. Hasselfield, S. R. Hildebrandt, G. C. Hilton, V. Hristov, H. Hui, K. D. Irwin, W. C. Jones, K. S. Karkare, J. P. Kaufman, B. G. Keating, S. Kefeli, S. A. Kernasovskiy, J. M. Kovac, C. L. Kuo, H. G. LeDuc, E. M. Leitch, N. Llombart, M. Lueker, P. Mason, K. Megerian, L. Moncelsi, C. B. Netterfield, H. T. Nguyen, R. O'Brient, R. W. Ogburn, IV, A. Orlando, C. Pryke, A. S. Rahlin, C. D. Reintsema, S. Richter, M. C. Runyan, R. Schwarz, C. D. Sheehy, Z. K. Staniszewski, R. V. Sudiwala, G. P. Teply, J. E. Tolan, A. Trangsrud, R. S. Tucker, A. D. Turner, A. G. Vieregg, A. Weber, D. V. Wiebe, P. Wilson, C. L. Wong, K. W. Yoon, and J. Zmuidzinas, “Antenna-coupled TES Bolometers Used in BICEP2, Keck Array, and Spider,” *ApJ* **812** (Oct., 2015) 176, [arXiv:astro-ph/1502.00619 \[astro-ph.IM\]](https://arxiv.org/abs/1502.00619).

[228] E. M. George, P. Ade, K. A. Aird, J. E. Austermann, J. A. Beall, D. Becker, A. Bender, B. A. Benson, L. E. Bleem, J. Britton, J. E. Carlstrom, C. L. Chang, H. C. Chiang, H.-M. Cho, T. M. Crawford, A. T. Crites, A. Datesman, T. de Haan, M. A. Dobbs, W. Everett, A. Ewall-Wice, N. W. Halverson, N. Harrington, J. W. Henning, G. C. Hilton, W. L. Holzapfel, S. Hoover, N. Huang, J. Hubmayr, K. D. Irwin, M. Karfunkle, R. Keisler, J. Kennedy, A. T. Lee, E. Leitch, D. Li, M. Lueker, D. P. Marrone, J. J. McMahon, J. Mehl, S. S. Meyer, J. Montgomery, T. E. Montroy, J. Nagy, T. Natoli, J. P. Nibarger, M. D. Niemack, V. Novosad, S. Padin, C. Pryke, C. L. Reichardt, J. E. Ruhl, B. R. Saliwanchik, J. T. Sayre, K. K. Schaffer, E. Shirokoff, K. Story, C. Tucker, K. Vanderlinde, J. D. Vieira, G. Wang, R. Williamson, V. Yefremenko, K. W. Yoon, and E. Young, “Performance and on-sky optical characterization of the SPTpol instrument,” in *Millimeter, Submillimeter, and Far-Infrared Detectors and Instrumentation for Astronomy VI*, vol. 8452 of *Proc. SPIE*, p. 84521F. Sept., 2012. [arXiv:astro-ph/1210.4971 \[astro-ph.IM\]](https://arxiv.org/abs/1210.4971).

[229] J. Zmuidzinas, “Superconducting Microresonators: Physics and Applications,” *Annual Review of Condensed Matter Physics* **3** no. 1, (2012) 169–214, <http://www.annualreviews.org/doi/pdf/10.1146/annurev-conmatphys-020911-125022>. <http://www.annualreviews.org/doi/abs/10.1146/annurev-conmatphys-020911-125022>.

[230] J. Gao, M. Daal, J. M. Martinis, A. Vayonakis, J. Zmuidzinas, B. Sadoulet, B. A. Mazin, P. K. Day, and H. G. Leduc, “A semiempirical model for two-level system noise in superconducting microresonators,” *Applied Physics Letters* **92** no. 21, (May, 2008) 212504, [arXiv:astro-ph/0804.0467 \[cond-mat.supr-con\]](https://arxiv.org/abs/0804.0467).

[231] P. K. Day, H. G. Leduc, A. Goldin, T. Vayonakis, B. A. Mazin, S. Kumar, J. Gao, and J. Zmuidzinas, “Antenna-coupled microwave kinetic inductance detectors,” *Nuclear Instruments and Methods in Physics Research A* **559** (Apr., 2006) 561–563.

[232] J. Schlaerth, A. Vayonakis, P. Day, J. Glenn, J. Gao, S. Golwala, S. Kumar, H. Leduc, B. Mazin, J. Vaillancourt, and J. Zmuidzinas, “A Millimeter and Submillimeter Kinetic Inductance Detector Camera,” *Journal of Low Temperature Physics* **151** (May, 2008) 684–689.

[233] S. R. Golwala, C. Bockstiegel, S. Brugger, N. G. Czakon, P. K. Day, T. P. Downes, R. Duan, J. Gao, A. K. Gill, J. Glenn, M. I. Hollister, H. G. LeDuc, P. R. Maloney, B. A. Mazin, S. G. McHugh, D. Miller, O. Noroozian, H. T. Nguyen, J. Sayers, J. A. Schlaerth, S. Siegel, A. K. Vayonakis, P. R.

Wilson, and J. Zmuidzinas, “Status of MUSIC, the Multiwavelength Sub/millimeter Inductance Camera,” in *Society of Photo-Optical Instrumentation Engineers (SPIE) Conference Series*, vol. 8452. Sept., 2012. [arXiv:astro-ph/1211.0595 \[astro-ph.IM\]](https://arxiv.org/abs/1211.0595).

[234] S. Doyle, P. Mauskopf, J. Naylor, A. Porch, and C. Duncombe, “Lumped Element Kinetic Inductance Detectors,” *Journal of Low Temperature Physics* **151** (Apr., 2008) 530–536.

[235] A. Monfardini, A. Benoit, A. Bideaud, L. Swenson, A. Cruciani, P. Camus, C. Hoffmann, F. X. Désert, S. Doyle, P. Ade, P. Mauskopf, C. Tucker, M. Roesch, S. Leclercq, K. F. Schuster, A. Endo, A. Baryshev, J. J. A. Baselmans, L. Ferrari, S. J. C. Yates, O. Bourrion, J. Macias-Perez, C. Vescovi, M. Calvo, and C. Giordano, “A Dual-band Millimeter-wave Kinetic Inductance Camera for the IRAM 30 m Telescope,” *ApJ Suppl.* **194** (June, 2011) 24, [arXiv:astro-ph/1102.0870 \[astro-ph.IM\]](https://arxiv.org/abs/1102.0870).

[236] M. Calvo, A. Benoît, A. Catalano, J. Goupy, A. Monfardini, N. Ponthieu, E. Barria, G. Bres, M. Grollier, G. Garde, J.-P. Leggeri, G. Pont, S. Triqueneaux, R. Adam, O. Bourrion, J.-F. Macías-Pérez, M. Rebolo, A. Ritacco, J.-P. Scordilis, D. Tourres, A. Adane, G. Coiffard, S. Leclercq, F.-X. Désert, S. Doyle, P. Mauskopf, C. Tucker, P. Ade, P. André, A. Beelen, B. Belier, A. Bideaud, N. Billot, B. Comis, A. D’Addabbo, C. Kramer, J. Martino, F. Mayet, F. Pajot, E. Pascale, L. Perotto, V. Revéret, A. Ritacco, L. Rodriguez, G. Savini, K. Schuster, A. Sievers, and R. Zylka, “The NIKA2 Instrument, A Dual-Band Kilopixel KID Array for Millimetric Astronomy,” *Journal of Low Temperature Physics* **184** (Aug., 2016) 816–823, [arXiv:astro-ph/1601.02774 \[astro-ph.IM\]](https://arxiv.org/abs/1601.02774).

[237] A. Baryshev, J. Baselmans, S. Yates, L. Ferrari, L. Bisigello, R. Janssen, A. Endo, T. Klapwijk, B. Klein, S. Heyminck, and R. Güsten, “Large Format Antenna Coupled Microwave Kinetic Inductance Detector Arrays for Radio Astronomy,” in *IRMMW-THz 39*. Sept., 2014. <http://www.irmmw-thz2014.org/topic-sessions/164>.

[238] J. Hubmayr, J. Beall, D. Becker, H.-M. Cho, M. Devlin, B. Dober, C. Groppi, G. C. Hilton, K. D. Irwin, D. Li, P. Mauskopf, D. P. Pappas, J. Van Lanen, M. R. Vissers, Y. Wang, L. F. Wei, and J. Gao, “Photon-noise limited sensitivity in titanium nitride kinetic inductance detectors,” *Applied Physics Letters* **106** no. 7, (Feb., 2015) 073505, [arXiv:astro-ph/1406.4010 \[astro-ph.IM\]](https://arxiv.org/abs/1406.4010).

[239] P. D. Mauskopf, S. Doyle, P. Barry, S. Rowe, A. Bidead, P. A. R. Ade, C. Tucker, E. Castillo, A. Monfardini, J. Goupy, and M. Calvo, “Photon-Noise Limited Performance in Aluminum LEKIDs,” *Journal of Low Temperature Physics* **176** no. 3, (2014) 545–552. <http://dx.doi.org/10.1007/s10909-013-1069-1>.

[240] C. McKenney, H. G. Leduc, L. J. Swenson, P. K. Day, B. H. Eom, and J. Zmuidzinas, “Design considerations for a background limited 350 micron pixel array using lumped element superconducting microresonators,” in *Society of Photo-Optical Instrumentation Engineers (SPIE) Conference Series*, vol. 8452, pp. 84520S–84520S–10. July, 2012. <http://dx.doi.org/10.1117/12.925759>.

[241] A. Kovács, P. S. Barry, C. M. Bradford, G. Chattopadhyay, P. Day, S. Doyle, S. Hailey-Dunsheath, M. Hollister, C. McKenney, H. G. LeDuc, N. Llombart, D. P. Marrone, P. Mauskopf, R. C. O’Brien, S. Padin, L. J. Swenson, and J. Zmuidzinas, “SuperSpec: design concept and circuit simulations,” in *Society of Photo-Optical Instrumentation Engineers (SPIE) Conference Series*, vol. 8452 of *Society of Photo-Optical Instrumentation Engineers (SPIE) Conference Series*. Sept., 2012. [arXiv:astro-ph/1211.0934 \[astro-ph.IM\]](https://arxiv.org/abs/1211.0934).

[242] A. Patel, A. Brown, W. Hsieh, T. Stevenson, S. Moseley, K. U-yen, N. Ehsan, E. Barrentine, G. Manos, and E. Wollack, “Fabrication of MKIDS for the MicroSpec Spectrometer,” *Applied Superconductivity, IEEE Transactions on* **23** no. 3, (June, 2013) 2400404–2400404.

[243] S. W. Deiker, W. Doriese, G. C. Hilton, K. D. Irwin, W. H. Rippard, J. N. Ullom, L. R. Vale, S. T. Ruggiero, A. Williams, and B. A. Young, “Superconducting transition edge sensor using dilute AlMn alloys,” *Applied Physics Letters* **85** (Sept., 2004) 2137.

[244] A. E. Lowitz, A. D. Brown, V. Mikula, T. R. Stevenson, P. T. Timbie, and E. J. Wollack, “Design, Fabrication, and Testing of a TiN/Ti/TiN Trilayer KID Array for 3 mm CMB Observations,” *Journal of Low Temperature Physics* **184** (Aug., 2016) 627–633.

[245] A. Catalano, R. Adam, P. Ade, P. André, H. Aussel, A. Beelen, A. Benoît, A. Bideaud, N. Billot, O. Bourrion, M. Calvo, G. Coiffard, B. Comis, F.-X. Désert, S. Doyle, J. Goupy, C. F. Kramer, G. Lagache, S. Leclercq, J. F. Lestrade, J. F. Macías-Pérez, A. Maury, P. Mauskopf, F. Mayet, A. Monfardini, F. Pajot, E. Pascale, L. Perotto, G. Pisano, N. Ponthieu, V. Revéret, A. Ritacco, L. Rodriguez, C. Romero, H. Roussel, F. Ruppin, K. Schuster, A. Sievers, J. Soler, S. Truqueneaux, C. Tucker, and R. Zylka, “The NIKA2 commissioning campaign: performance and first results,” *ArXiv e-prints* (May, 2016) , [arXiv:astro-ph/1605.08628 \[astro-ph.IM\]](https://arxiv.org/abs/1605.08628).

[246] B. R. Johnson, P. A. R. Ade, D. Araujo, K. J. Bradford, D. Chapman, P. K. Day, J. Didier, S. Doyle, H. K. Eriksen, D. Flanigan, C. Groppi, S. Hillbrand, G. Jones, M. Limon, P. Mauskopf, H. McCarrick, A. Miller, T. Mroczkowski, B. Reichborn-Kjennerud, B. Smiley, J. Sobrin, I. K. Wehus, and J. Zmuidzinas, “The Detector System for the Stratospheric Kinetic Inductance Polarimeter (Skip),” *Journal of Low Temperature Physics* **176** (Sept., 2014) 741–748, [arXiv:astro-ph/1308.0235 \[astro-ph.IM\]](https://arxiv.org/abs/1308.0235).

[247] D. C. Araujo, P. A. R. Ade, J. R. Bond, K. J. Bradford, D. Chapman, G. Che, P. K. Day, J. Didier, S. Doyle, H. K. Eriksen, D. Flanigan, C. E. Groppi, S. N. Hillbrand, B. R. Johnson, G. Jones, M. Limon, A. D. Miller, P. Mauskopf, H. McCarrick, T. Mroczkowski, B. Reichborn-Kjennerud, B. Smiley, J. Sobrin, I. K. Wehus, and J. Zmuidzinas, “A LEKID-based CMB instrument design for large-scale observations in Greenland,” in *Society of Photo-Optical Instrumentation Engineers (SPIE) Conference Series*, vol. 9153 of *Society of Photo-Optical Instrumentation Engineers (SPIE) Conference Series*, p. 0. Aug., 2014. [arXiv:astro-ph/1407.6249 \[astro-ph.IM\]](https://arxiv.org/abs/1407.6249).

[248] K. D. Irwin, L. R. Vale, N. E. Bergren, S. Deiker, E. N. Grossman, G. C. Hilton, S. W. Nam, C. D. Reintsema, D. A. Rudman, and M. E. Huber, “Time-division SQUID multiplexers,” *AIP Conference Proceedings* **605** no. 1, (2002) 301–304.

[249] P. A. J. de Korte *et al.*, “Time-division superconducting quantum interference device multiplexer for transition-edge sensors,” *Review of Scientific Instruments* **74** no. 8, (2003) 3807–3815. <http://link.aip.org/link/?RSI/74/3807/1>.

[250] H. Hui *et al.*, “BICEP3 focal plane design and detector performance,” *Proc. SPIE* **9914** (2016) .

[251] E. S. Battistelli, M. Amiri, B. Burger, M. Halpern, S. Knotek, M. Ellis, X. Gao, D. Kelly, M. MacIntosh, K. Irwin, and C. Reintsema, “Functional Description of Read-out Electronics for Time-Domain Multiplexed Bolometers for Millimeter and Sub-millimeter Astronomy,” *Journal of Low Temperature Physics* **151** no. 3, (2008) 908–914. <http://dx.doi.org/10.1007/s10909-008-9772-z>.

[252] T. Essinger-Hileman, J. W. Appel, J. A. Beal, H. M. Cho, J. Fowler, M. Halpern, M. Hasselfield, K. D. Irwin, T. A. Marriage, M. D. Niemack, L. Page, L. P. Parker, S. Pufu, S. T. Staggs, O. Stryzak, C. Visnjic, K. W. Yoon, and Y. Zhao, “The Atacama B-Mode Search: CMB Polarimetry with Transition-Edge-Sensor Bolometers,” *AIP Conference Proceedings* **1185** no. 1, (2009) 494–497.

[253] D. S. Swetz *et al.*, “Overview of the Atacama Cosmology Telescope: Receiver, instrumentation, and telescope systems,” *ApJ Suppl.* **194** (2011) 41, [arXiv:astro-ph/1007.0290 \[astro-ph.IM\]](https://arxiv.org/abs/1007.0290).

[254] **BICEP2, Keck Array** Collaboration, P. A. R. Ade *et al.*, “BICEP2 / Keck Array V: Measurements of B-mode Polarization at Degree Angular Scales and 150 GHz by the Keck Array,” *ApJ* **811** (2015) 126, [arXiv:astro-ph/1502.00643 \[astro-ph.CO\]](https://arxiv.org/abs/1502.00643).

[255] W. B. Doriese, K. M. Morgan, D. A. Bennett, E. V. Denison, C. P. Fitzgerald, J. W. Fowler, J. D. Gard, J. P. Hays-Wehle, G. C. Hilton, K. D. Irwin, Y. I. Joe, J. A. B. Mates, G. C. O’Neil, C. D. Reintsema, N. O. Robbins, D. R. Schmidt, D. S. Swetz, H. Tatsuno, L. R. Vale, and J. N. Ullom, “Developments in Time-Division Multiplexing of X-ray Transition-Edge Sensors,” *Journal of Low Temperature Physics* **184** no. 1, (2016) 389–395. <http://dx.doi.org/10.1007/s10909-015-1373-z>.

[256] W. B. Doriese, K. M. Morgan, D. A. Bennett, E. V. Denison, C. P. Fitzgerald, J. W. Fowler, J. D. Gard, J. P. Hays-Wehle, G. C. Hilton, K. D. Irwin, Y. I. Joe, J. A. B. Mates, G. C. O’Neil, C. D. Reintsema, N. O. Robbins, D. R. Schmidt, D. S. Swetz, H. Tatsuno, L. R. Vale, and J. N. Ullom, “Erratum to: Developments in Time-Division Multiplexing of X-ray Transition-Edge Sensors,” *Journal of Low Temperature Physics* **184** no. 1, (2016) 396–396. <http://dx.doi.org/10.1007/s10909-016-1608-7>.

[257] J. W. Fowler, W. B. Doriese, G. C. Hilton, K. D. Irwin, D. R. Schmidt, G. M. Stiehl, D. S. Swetz, J. N. Ullom, and L. R. Vale., “Optimization and analysis of code-division multiplexed TES microcalorimeters,” *Journal of Low Temperature Physics* **167** (2012) 713–720, [arXiv:astro-ph/1110.2531 \[physics.ins-det\]](https://arxiv.org/abs/1110.2531).

[258] K. D. Irwin, H. M. Cho, W. B. Doriese, J. W. Fowler, G. C. Hilton, M. D. Niemack, C. D. Reintsema, D. R. Schmidt, J. N. Ullom, and L. R. Vale, “Advanced code-division multiplexers for superconducting detector arrays,” *Journal of Low Temperature Physics* **167** (2012) 588–594, [arXiv:astro-ph/1110.1608 \[astro-ph.IM\]](https://arxiv.org/abs/1110.1608).

[259] G. M. Stiehl, W. B. Doriese, J. W. Fowler, G. C. Hilton, K. D. Irwin, C. D. Reintsema, D. R. Schmidt, D. S. Swetz, J. N. Ullom, and L. R. Vale., “Code-division multiplexing for x-ray microcalorimeters,” *Appl. Phys. Lett.* **100** (2012) 072601, [arXiv:astro-ph/1201.6289 \[physics.ins-det\]](https://arxiv.org/abs/1201.6289).

[260] D. Prèle, F. Voisin, M. Piat, T. Decourcelle, C. Perbost, C. Chapron, D. Rambaud, S. Maestre, W. Marty, and L. Montier, “A 128 Multiplexing Factor Time-Domain SQUID Multiplexer,” *Journal of Low Temperature Physics* **184** no. 1, (2016) 363–368. <http://dx.doi.org/10.1007/s10909-015-1449-9>.

[261] C. A. Jhabvala *et al.*, “Kilopixel backshort-under-grid arrays for the Primordial Inflation Polarization Explorer,” *Proc. SPIE* **9153** (2014) 91533C.

[262] M. A. Dobbs, M. Lueker, K. A. Aird, A. N. Bender, B. A. Benson, L. E. Bleem, J. E. Carlstrom, C. L. Chang, H.-M. Cho, J. Clarke, T. M. Crawford, A. T. Crites, D. I. Flanigan, T. de Haan, E. M. George, N. W. Halverson, W. L. Holzapfel, J. D. Hrubes, B. R. Johnson, J. Joseph, R. Keisler, J. Kennedy, Z. Kermish, T. M. Lanting, A. T. Lee, E. M. Leitch, D. Luong-Van, J. J. McMahon, J. Mehl, S. S. Meyer, T. E. Montroy, S. Padin, T. Plagge, C. Pryke, P. L. Richards, J. E. Ruhl, K. K. Schaffer, D. Schwan, E. Shirokoff, H. G. Spieler, Z. Staniszewski, A. A. Stark, K. Vanderlinde, J. D. Vieira, C. Vu, B. Westbrook, and R. Williamson, “Frequency multiplexed superconducting quantum interference device readout of large bolometer arrays for cosmic microwave background measurements,” *Rev. Sci. Instrum.* **83** no. 7, (2012) 073113. <http://link.aip.org/link/?RSI/83/073113/1>.

[263] M. E. Huber, P. A. Neil, R. G. Benson, D. A. Burns, A. M. Corey, C. S. Flynn, Y. Kitaygorodskaya, O. Massihzadeh, J. M. Martinis, and G. C. Hilton, “DC SQUID series array amplifiers with 120 MHz bandwidth,” *IEEE Transactions on Applied Superconductivity* **11** no. 1, (Mar, 2001) 1251–1256.

[264] T. de Haan, G. Smecher, and M. Dobbs, “Improved performance of TES bolometers using digital feedback,” *Proc. SPIE* **8452** (2012) 84520E–84520E-10. <http://dx.doi.org/10.1117/12.925658>.

[265] K. Rotermund, B. Barch, S. Chapman, K. Hattori, A. Lee, N. Palaio, I. Shirley, A. Suzuki, and C. Tran, “Planar Lithographed Superconducting LC Resonators for Frequency-Domain Multiplexed Readout Systems,” *Journal of Low Temperature Physics* **184** (July, 2016) 486–491.

[266] A. N. Bender, P. A. R. Ade, A. J. Anderson, J. Avva, Z. Ahmed, K. Arnold, J. E. Austermann, R. Basu Thakur, B. A. Benson, L. E. Bleem, K. Byrum, J. E. Carlstrom, F. W. Carter, C. L. Chang, H. M. Cho, J. F. Cliche, T. M. Crawford, A. Cukierman, D. A. Czapelewski, J. Ding, R. Divan, T. de Haan, M. A. Dobbs, D. Dutcher, W. Everett, A. Gilbert, J. C. Groh, R. Guyser, N. W. Halverson, A. Harke-Hosemann, N. L. Harrington, K. Hattori, J. W. Henning, G. C. Hilton, W. L. Holzapfel, N. Huang, K. D. Irwin, O. Jeong, T. Khaire, M. Korman, D. Kubik, C. L. Kuo, A. T. Lee, E. M. Leitch, S. Lendinez, S. S. Meyer, C. S. Miller, J. Montgomery, A. Nadolski, T. Natoli, H. Nguyen, V. Novosad, S. Padin, Z. Pan, J. Pearson, C. M. Posada, A. Rahlin, C. L. Reichardt, J. E. Ruhl, B. R. Saliwanchik, J. T. Sayre, J. A. Shariff, I. Shirley, E. Shirokoff, G. Smecher, J. Sobrin, L. Stan, A. A. Stark, K. Story, A. Suzuki, Q. Y. Tang, K. L. Thompson, C. Tucker, K. Vanderlinde, J. D. Vieira, G. Wang, N. Whitehorn, V. Yefremenko, and K. W. Yoon, “Integrated performance of a frequency domain multiplexing readout in the SPT-3G receiver,” vol. 9914, pp. 99141D–99141D–11. 2016. <http://dx.doi.org/10.1117/12.2232146>.

[267] M. P. Bruijn, L. Gottardi, R. H. den Hartog, H. F. C. Hoevers, M. Kiviranta, P. A. J. de Korte, and J. van der Kuur, “High-Q LC Filters for FDM Read out of Cryogenic Sensor Arrays,” *Journal of Low Temperature Physics* **167** no. 5, (2012) 695–700. <http://dx.doi.org/10.1007/s10909-011-0422-5>.

[268] A. N. Bender, J.-F. Cliche, T. de Haan, M. A. Dobbs, A. J. Gilbert, J. Montgomery, N. Rowlands, G. M. Smecher, K. Smith, and A. Wilson, “Digital frequency domain multiplexing readout electronics for the next generation of millimeter telescopes,” vol. 9153, pp. 91531A–91531A–15. 2014. <http://dx.doi.org/10.1117/12.2054949>.

[269] K. Bandura *et al.*, “ICE: a scalable, low-cost FPGA-based telescope signal processing and networking system,” *ArXiv e-prints* (2016) , [arXiv:astro-ph/1608.06262 \[astro-ph.IM\]](https://arxiv.org/abs/1608.06262).

[270] P. A. R. Ade, Y. Akiba, A. E. Anthony, K. Arnold, M. Atlas, D. Barron, D. Boettger, J. Borrill, S. Chapman, Y. Chinone, M. Dobbs, T. Ellefot, J. Errard, G. Fabbian, C. Feng, D. Flanigan, A. Gilbert, W. Grainger, N. W. Halverson, M. Hasegawa, K. Hattori, M. Hazumi, W. L. Holzapfel, Y. Hori, J. Howard, P. Hyland, Y. Inoue, G. C. Jaehnig, A. H. Jaffe, B. Keating, Z. Kermish, R. Keskitalo, T. Kisner, M. L. Jeune, A. T. Lee, E. M. Leitch, E. Linder, M. Lungu, F. Matsuda, T. Matsumura, X. Meng, N. J. Miller, H. Morii, S. Moyerman, M. J. Myers, M. Navaroli, H. Nishino, A. Orlando, H. Paar, J. Peloton, D. Poletti, E. Quealy, G. Rebeiz, C. L. Reichardt, P. L. Richards, C. Ross, I. Schanning, D. E. Schenck, B. D. Sherwin, A. Shimizu, C. Shimmin, M. Shimon, P. Siritanasak, G. Smecher, H. Spieler, N. Stebor, B. Steinbach, R. Stompor, A. Suzuki, S. Takakura, T. Tomaru, B. Wilson, A. Yadav, and O. Zahn, “A Measurement of the Cosmic Microwave Background B-mode Polarization Power Spectrum at Sub-degree Scales with POLARBEAR,” *ApJ* **794** no. 2, (2014) 171. <http://stacks.iop.org/0004-637X/794/i=2/a=171>.

[271] D. Hanson, S. Hoover, A. Crites, P. A. R. Ade, K. A. Aird, J. E. Austermann, J. A. Beall, A. N. Bender, B. A. Benson, L. E. Bleem, J. J. Bock, J. E. Carlstrom, C. L. Chang, H. C. Chiang, H.-M. Cho, A. Conley, T. M. Crawford, T. de Haan, M. A. Dobbs, W. Everett, J. Gallicchio, J. Gao, E. M. George, N. W. Halverson, N. Harrington, J. W. Henning, G. C. Hilton, G. P. Holder, W. L. Holzapfel, J. D. Hrubes, N. Huang, J. Hubmayr, K. D. Irwin, R. Keisler, L. Knox, A. T. Lee, E. Leitch, D. Li, C. Liang, D. Luong-Van, G. Marsden, J. J. McMahon, J. Mehl, S. S. Meyer, L. Mocanu, T. E. Montroy, T. Natoli, J. P. Nibarger, V. Novosad, S. Padin, C. Pryke, C. L. Reichardt, J. E. Ruhl, B. R. Saliwanchik, J. T. Sayre, K. K. Schaffer, B. Schulz, G. Smecher, A. A. Stark, K. T. Story, C. Tucker, K. Vanderlinde, J. D. Vieira, M. P. Viero, G. Wang, V. Yefremenko, O. Zahn, and M. Zemcov,

“Detection of  $B$ -Mode Polarization in the Cosmic Microwave Background with Data from the South Pole Telescope,” *PRL* **111** no. 14, (Oct., 2013) 141301, [arXiv:astro-ph/1307.5830](https://arxiv.org/abs/1307.5830) [astro-ph.CO].

[272] D. Barron, P. A. R. Ade, Y. Akiba, C. Aleman, K. Arnold, M. Atlas, A. Bender, J. Borrill, S. Chapman, Y. Chinone, A. Cukierman, M. Dobbs, T. Ellefot, J. Errard, G. Fabbian, G. Feng, A. Gilbert, N. W. Halverson, M. Hasegawa, K. Hattori, M. Hazumi, W. L. Holzapfel, Y. Hori, Y. Inoue, G. C. Jaehnig, N. Katayama, B. Keating, Z. Kermish, R. Keskitalo, T. Kisner, M. Le Jeune, A. T. Lee, F. Matsuda, T. Matsumura, H. Morii, M. J. Myers, M. Navroli, H. Nishino, T. Okamura, J. Peloton, G. Rebeiz, C. L. Reichardt, P. L. Richards, C. Ross, M. Sholl, P. Siritanasak, G. Smecher, N. Stebor, B. Steinbach, R. Stompor, A. Suzuki, J. Suzuki, S. Takada, T. Takakura, T. Tomaru, B. Wilson, H. Yamaguchi, and O. Zahn, “Development and characterization of the readout system for POLARBEAR-2,” vol. 9153, pp. 915335–915335–8. 2014. <http://dx.doi.org/10.1117/12.2055611>.

[273] K. Hattori, K. Arnold, D. Barron, M. Dobbs, T. de Haan, N. Harrington, M. Hasegawa, M. Hazumi, W. L. Holzapfel, B. Keating, A. T. Lee, H. Morii, M. J. Myers, G. Smecher, A. Suzuki, and T. Tomaru, “Adaptation of frequency-domain readout for Transition Edge Sensor bolometers for the POLARBEAR-2 Cosmic Microwave Background experiment,” *Nuclear Instruments and Methods in Physics Research Section A: Accelerators, Spectrometers, Detectors and Associated Equipment* **732** no. 0, (2013) 299 – 302. <http://www.sciencedirect.com/science/article/pii/S0168900213010619>. Vienna Conference on Instrumentation 2013.

[274] F. Aubin, A. M. Aboobaker, P. Ade, C. Baccigalupi, C. Bao, J. Borrill, C. Cantalupo, D. Chapman, J. Didier, M. Dobbs, W. Grainger, S. Hanany, J. Hubmayr, P. Hyland, S. Hillbrand, A. Jaffe, B. Johnson, T. Jones, T. Kisner, J. Klein, A. Korotkov, S. Leach, A. Lee, M. Limon, K. MacDermid, T. Matsumura, X. Meng, A. Miller, M. Milligan, D. Polsgrove, N. Ponthieu, K. Raach, B. Reichborn-Kjennerud, I. Sagiv, G. Smecher, H. Tran, G. S. Tucker, Y. Vinokurov, A. Yadav, M. Zaldarriaga, and K. Zilic, “First implementation of TES bolometer arrays with SQUID-based multiplexed readout on a balloon-borne platform,” in *Millimeter, Submillimeter, and Far-Infrared Detectors and Instrumentation for Astronomy V*, vol. 7741 of *Proc. SPIE*, p. 77411T. July, 2010.

[275] J. Ruhl, P. A. R. Ade, J. E. Carlstrom, H.-M. Cho, T. Crawford, M. Dobbs, C. H. Greer, N. w. Halverson, W. L. Holzapfel, T. M. Lanting, A. T. Lee, E. M. Leitch, J. Leong, W. Lu, M. Lueker, J. Mehl, S. S. Meyer, J. J. Mohr, S. Padin, T. Plagge, C. Pryke, M. C. Runyan, D. Schwan, M. K. Sharp, H. Spieler, Z. Staniszewski, and A. A. Stark, “The South Pole Telescope,” in *Z-Spec: a broadband millimeter-wave grating spectrometer: design, construction, and first cryogenic measurements*, C. M. Bradford, P. A. R. Ade, J. E. Aguirre, J. J. Bock, M. Dragovan, L. Duband, L. Earle, J. Glenn, H. Matsuura, B. J. Naylor, H. T. Nguyen, M. Yun, and J. Zmuidzinas, eds., vol. 5498 of *Proc. SPIE*, pp. 11–29. Oct., 2004. [arXiv:astro-ph/0411122](https://arxiv.org/abs/astro-ph/0411122).

[276] K. Irwin and K. W. Lehnert, “Microwave SQUID multiplexer,” *Applied Physics Letters* **85** no. 11, (2004) 2107–2109.

[277] J. A. B. Mates, *The microwave SQUID multiplexer*. PhD thesis, University of Colorado, 2011.

[278] P. K. Day, H. G. LeDuc, B. A. Mazin, A. Vayonakis, and J. Zmuidzinas, “A broadband superconducting detector suitable for use in large arrays,” *Nature* **425** (Oct., 2003) 817–821.

[279] J. Mates, K. Irwin, L. Vale, G. Hilton, J. Gao, and K. Lehnert, “Flux-ramp modulation for squid multiplexing,” *Journal of Low Temperature Physics* **167** no. 5–6, (2012) 707–712.

[280] D. A. Bennett, J. A. B. Mates, J. D. Gard, A. S. Hoover, M. W. Rabin, C. D. Reintsema, D. R. Schmidt, L. R. Vale, and J. N. Ullom, “Integration of TES Microcalorimeters With Microwave SQUID Multiplexed Readout,” *IEEE Transactions on Applied Superconductivity* **25** no. 3, (June, 2015) 1–5.

[281] S. Stanchfield, P. Ade, J. Aguirre, J. Brevik, H. Cho, R. Datta, M. Devlin, S. Dicker, B. Dober, D. Egan, *et al.*, “Development of a Microwave SQUID-Multiplexed TES Array for MUSTANG-2,” *Journal of Low Temperature Physics* (2016) 1–6.

[282] C. Reintsema, J. Beall, W. Doriese, W. Duncan, L. Ferreira, G. Hilton, K. Irwin, D. Schmidt, J. Ullom, L. Vale, *et al.*, “A TDMA Hybrid SQUID Multiplexer,” *Journal of Low Temperature Physics* **151** no. 3-4, (2008) 927–933.

[283] J. van Rantwijk, M. Grim, D. van Loon, S. Yates, A. Baryshev, and J. Baselmans, “Multiplexed Readout for 1000-Pixel Arrays of Microwave Kinetic Inductance Detectors,” *IEEE Transactions on Microwave Theory and Techniques* **64** no. 6, (June, 2016) 1876–1883.

[284] O. Bourrion, A. Bideaud, A. Benoit, A. Cruciani, J. F. Macias-Perez, A. Monfardini, M. Roesch, L. Swenson, and C. Vescovi, “Electronics and data acquisition demonstrator for a kinetic inductance camera,” *Journal of Instrumentation* **6** (June, 2011) 6012, [arXiv:astro-ph/1102.1314](https://arxiv.org/abs/astro-ph/1102.1314) [astro-ph.IM].

[285] B. A. Mazin, “Microwave Kinetic Inductance Detectors: The First Decade,” in *American Institute of Physics Conference Series*, B. Young, B. Cabrera, and A. Miller, eds., vol. 1185 of *American Institute of Physics Conference Series*, pp. 135–142. Dec., 2009.

[286] O. Bourrion, C. Vescovi, A. Catalano, M. Calvo, A. D’Addabbo, J. Goupy, N. Boudou, J. F. Macias-Perez, and A. Monfardini, “High speed readout electronics development for frequency-multiplexed kinetic inductance detector design optimization,” *Journal of Instrumentation* **8** (Dec., 2013) C12006, [arXiv:astro-ph/1310.5891](https://arxiv.org/abs/astro-ph/1310.5891) [astro-ph.IM].

[287] R. Duan, S. McHugh, B. Serfass, B. A. Mazin, A. Merrill, S. R. Golwala, T. P. Downes, N. G. Czakon, P. K. Day, J. Gao, J. Glenn, M. I. Hollister, H. G. Leduc, P. R. Maloney, O. Noroozian, H. T. Nguyen, J. Sayers, J. A. Schlaerth, S. Siegel, J. E. Vaillancourt, A. Vayonakis, P. R. Wilson, and J. Zmuidzinas, “An open-source readout for MKIDs,” in *Millimeter, Submillimeter, and Far-Infrared Detectors and Instrumentation for Astronomy V*, vol. 7741 of *Proc. SPIE*, p. 77411V. July, 2010.

[288] S. McHugh, B. A. Mazin, B. Serfass, S. Meeker, K. O’Brien, R. Duan, R. Raffanti, and D. Werthimer, “A readout for large arrays of microwave kinetic inductance detectors,” *Review of Scientific Instruments* **83** no. 4, (Apr., 2012) 044702, [arXiv:astro-ph/1203.5861](https://arxiv.org/abs/astro-ph/1203.5861) [astro-ph.IM].

[289] O. Bourrion, C. Vescovi, J. L. Bouly, A. Benoit, M. Calvo, L. Gallin-Martel, J. F. Macias-Perez, and A. Monfardini, “NIKEL: Electronics and data acquisition for kilopixels kinetic inductance camera,” *Journal of Instrumentation* **7** (July, 2012) 7014, [arXiv:astro-ph/1204.1415](https://arxiv.org/abs/astro-ph/1204.1415) [astro-ph.IM].

[290] O. Bourrion, A. Benoit, J. L. Bouly, J. Bouvier, G. Bosson, M. Calvo, A. Catalano, J. Goupy, C. Li, J. F. Macías-Pérez, A. Monfardini, D. Tourres, N. Ponchard, and C. Vescovi, “NIKEL\_AMC: Readout electronics for the NIKA2 experiment,” *ArXiv e-prints* (Feb., 2016) , [arXiv:astro-ph/1602.01288](https://arxiv.org/abs/astro-ph/1602.01288) [astro-ph.IM].

[291] K. Hattori, S. Ariyoshi, M. Hazumi, H. Ishino, A. Kibayashi, S. Mima, C. Otani, N. Satoh, T. Tomaru, M. Yoshida, and H. Watanabe, “Novel Frequency-Domain Multiplexing MKID Readout for the LiteBIRD Satellite,” *Journal of Low Temperature Physics* **167** (June, 2012) 671–677.

[292] S. J. C. Yates, A. M. Baryshev, J. J. A. Baselmans, B. Klein, and R. Güsten, “Fast Fourier transform spectrometer readout for large arrays of microwave kinetic inductance detectors,” *Applied Physics Letters* **95** no. 4, (July, 2009) 042504.

[293] L. J. Swenson, P. K. Day, C. D. Dowell, B. H. Eom, M. I. Hollister, R. Jarnot, A. Kovács, H. G. Leduc, C. M. McKenney, R. Monroe, T. Mroczkowski, H. T. Nguyen, and J. Zmuidzinas, “MAKO: a pathfinder instrument for on-sky demonstration of low-cost 350 micron imaging arrays,” in *Millimeter, Submillimeter, and Far-Infrared Detectors and Instrumentation for Astronomy VI*, vol. 8452 of *Proc. SPIE*, p. 84520P. Sept., 2012. [arXiv:astro-ph/1211.0315 \[astro-ph.IM\]](https://arxiv.org/abs/1211.0315).

[294] S. R. Golwala, C. Bockstiegel, S. Brugger, N. G. Czakon, P. K. Day, T. P. Downes, R. Duan, J. Gao, A. K. Gill, J. Glenn, M. I. Hollister, H. G. LeDuc, P. R. Malone, B. A. Mazin, S. G. McHugh, D. Miller, O. Noroozian, H. T. Nguyen, J. Sayers, J. A. Schlaerth, S. Siegel, A. K. Vayonakis, P. R. Wilson, and J. Zmuidzinas, “Status of MUSIC, the Multiwavelength Sub/millimeter Inductance Camera,” in *Millimeter, Submillimeter, and Far-Infrared Detectors and Instrumentation for Astronomy VI*, vol. 8452 of *Proc. SPIE*, p. 845205. Sept., 2012. [arXiv:astro-ph/1211.0595 \[astro-ph.IM\]](https://arxiv.org/abs/1211.0595).

[295] A. Catalano, M. Calvo, N. Ponthieu, R. Adam, A. Adane, P. Ade, P. André, A. Beelen, B. Belier, A. Benoît, A. Bideaud, N. Billot, N. Boudou, O. Bourrion, G. Coiffard, B. Comis, A. D’Addabbo, F.-X. Désert, S. Doyle, J. Goupy, C. Kramer, S. Leclercq, J. F. Macías-Pérez, J. Martino, P. Mauskopf, F. Mayet, A. Monfardini, F. Pajot, E. Pascale, L. Perotto, V. Revéret, L. Rodriguez, G. Savini, K. Schuster, A. Sievers, C. Tucker, and R. Zylka, “Performance and calibration of the NIKA camera at the IRAM 30 m telescope,” *A & A* **569** (Sept., 2014) A9, [arXiv:astro-ph/1402.0260 \[astro-ph.IM\]](https://arxiv.org/abs/1402.0260).

[296] B. A. Mazin, P. K. Day, K. D. Irwin, C. D. Reintsema, and J. Zmuidzinas, “Digital readouts for large microwave low-temperature detector arrays,” *Nuclear Instruments and Methods in Physics Research A* **559** (Apr., 2006) 799–801.

[297] J. J. A. Baselmans, J. Bueno, S. J. C. Yates, O. Yurduseven, N. Llombart, K. Karatsu, A. M. Baryshev, L. Ferrari, A. Endo, D. J. Thoen, P. J. de Visser, R. M. J. Janssen, V. Murugesan, E. F. C. Driessens, G. Coiffard, J. Martin-Pintado, P. Hargrave, and M. Griffin, “A kilo-pixel imaging system for future space based far-infrared observatories using microwave kinetic inductance detectors,” *ArXiv e-prints* (Sept., 2016) , [arXiv:astro-ph/1609.01952 \[astro-ph.IM\]](https://arxiv.org/abs/1609.01952).

[298] B. R. Johnson, D. Flanigan, M. H. Abitbol, P. A. R. Ade, S. Bryan, H. Cho, R. Datta, P. Day, S. Doyle, K. Irwin, G. Jones, S. Kernasovskiy, D. Li, P. Mauskopf, H. McCarrick, J. McMahon, A. Miller, G. Pisano, Y. Song, H. Surdi, and C. Tucker, “Polarization sensitive Multi-Chroic MKIDs,” *Proc. SPIE* **9914** (July, 2016) 99140X, [arXiv:astro-ph/1607.03796 \[astro-ph.IM\]](https://arxiv.org/abs/1607.03796).